

Photoproduction of the $b_1(1235)$ Meson
off the proton at $E_{\gamma} = 6-12$ GeV

A Thesis

Submitted to the Faculty of Graduate Studies and Research

In Partial Fulfillment of the Requirements

for the Degree of

Doctor of Philosophy

in

Physics

University of Regina

by

Ahmed Marwan Abdelrahman Foda

Regina, Saskatchewan

January, 2021

© Copyright 2021: A. M. Foda

Abstract

The GlueX Experiment at Jefferson Lab directs a linearly polarized photon beam on a liquid hydrogen target surrounded by an almost hermetic detector. The experiment aims to study the meson spectrum in the light-quark sector and search for exotic spin-parity states predicted by lattice QCD calculations. The lightest exotic candidate is the π_1 meson, which is predicted to decay dominantly to $b_1\pi$. In this thesis, we present efforts to characterize the $\omega\pi^0$ decay channel of the b_1 meson as precursor to an analysis of the sought-after π_1 exotic state.

We present an introduction to the physics involved and an overview of the detector subsystems with a focus on the Barrel Calorimeter gain monitoring system, as part of the service work expected by the GlueX Collaboration.

We discuss the data analysis method used and present two frameworks, for angular moments and partial waves analyses. Details of the simulation used to calculate the detector acceptance. A proof of concept partial wave analysis is presented along with experimental angular moments as first step to a full analysis of the angular distribution. Our partial wave analysis indicates that both S- and D-waves are needed, in qualitative agreement with theoretical expectations. The cross-section of the $\omega\pi^0$

channel is extracted to be of the scale of $1 \mu\text{b}$ in agreement with previous measurements. The differential cross-section indicates the presence of two production processes with $p_1 = -5.24 \pm 0.04$ for $0.25 < -t < 0.95 \text{ GeV}^2/c^2$ and $p_2 = -1.24 \pm 0.05$ for $0.95 < -t < 2.0 \text{ GeV}^2/c^2$, which does not agree with results from previous experiments. The s-channel helicity conservation and helicity amplitudes of the b_1 meson are presented as additional experimental observables. Our results confirm that the b_1 photoproduction process does not conserve s-channel helicity though they do not align with previous measurements. The helicity amplitude of the ω are extracted to be $|F_1|^2 = 0.3037 \pm 0.0003$ which does not agree with the expected value of a b_1 decay or results from a previous experiment. Future steps in all these analyses will be continued by a new graduate student in the group, culminating in a publication.

Acknowledgements

I would like to thank my family for their support, devotion and understanding. Specially my mother.

I would like to deeply thank my supervisor, Dr. Zisis Papandreou, for his help with everything: providing financial support, explaining physics concepts, editing this thesis along with many other documents, and organizing useful discussions with detector and analysis experts. Thanks to Dr. Dave Mack, for helping me understand physical concepts and answering many questions, and for guiding my analysis. I would like to thank Dr. Jon Zarling for the analysis insights. To the rest of my advisory committee, Dr. Aram Teymurazyan, Dr. George Lolos, Dr. Malek Mouhoub and Dr. Nader Mobed: thank you for reviewing my work, pinpointing errors, suggesting additions, and helping to clarify my understanding of certain topics. Thanks to Dr. Elton Smith and Dr. Matthew Shepherd, and the rest of the Hall D staff at JLab, for many discussions regarding analysis and software. A special thanks to Dr. Adam Szczepaniak for providing the analysis model and helping me understand the underlying physics.

I would like to thank Dr. Beattie. Also, I would like to give my sincere gratitude to the majority of the Physics Department and my colleagues at University of Regina.

غض عينيك وارقص بخفة ودلع
الدنيا هي الشابة وانت البدرع
تشوف رشاقة خطواتك تعبدك
لكن انت لو بصيت لرجليك تقع

Close your eyes & dance lightly & indulgently
The world is the damsel & you are the prodigy
Seeing the agility of your steps, she worships you
but gaze at your feet & you shall fall

Salah Jahin, Egyptian Poet, (1930-1986)

Contents

Abstract	i
Acknowledgements	iii
Quote	iv
Table of Contents	v
List of Figures	viii
List of Tables	xxiii
Glossary	xxiv
1 Introduction	1
1.1 The Standard Model	2
1.2 Quark Model	4
1.3 Quantum Chromodynamics	6
1.3.1 LQCD	9
1.3.2 Exotic States	10
1.4 Exclusive b_1 Photoproduction	12
1.4.1 History of the $b_1(1235) \rightarrow \omega\pi^0$	13
1.4.2 Helicity frame of $\omega\pi^0$	13
1.4.3 Angular Distribution	17
1.4.3.1 Angular Moments	18
1.4.3.2 Partial Wave Amplitudes	23
1.4.4 s-Channel Helicity Conservation	25
1.4.5 Helicity Amplitudes of the ω	25
1.5 Summary	26
2 The GlueX Experiment	27
2.1 Photon Beamline	30
2.1.1 Photon Tagger	31
2.1.2 Triplet Polarimeter	32
2.1.3 Pair Spectrometer	34
2.2 Liquid Hydrogen Target	36

2.3	Charged Particle Tracking	37
2.3.1	Central Drift Chamber	38
2.3.2	Forward Drift Chamber	39
2.4	Calorimetry	40
2.4.1	Barrel Calorimeter	41
2.4.2	Forward Calorimeter	46
2.5	Particle Identification Detectors	48
2.5.1	Start Counter	48
2.5.2	Time of Flight	49
2.6	Summary	51
3	BCAL Gain Monitoring System	52
3.1	BCAL LED Readout	56
3.1.1	BCAL_LED Events Selection	57
3.2	LED Monitoring Plugin	63
3.3	Monitoring Phases	68
3.3.1	Online Monitoring	71
3.4	Known Problems	74
3.4.1	Drifting BCAL Channels	74
3.4.2	Failing Quadrants	79
3.5	Pedestal Study	80
3.6	Conclusions	84
4	Data Analysis	86
4.1	Event Selection	87
4.1.1	Stage I	88
4.1.2	Stage II	91
4.2	Analysis Methodology	98
4.2.1	Accidental Subtraction	99
4.2.2	ω Side-Band Subtraction	100
4.3	Fit Models	103
4.3.1	Angular Moments	104
4.3.2	Partial Waves Amplitudes	104
4.4	Summary	106
5	Monte Carlo Simulations	107
5.1	MC Generators	107
5.1.1	genr8	108
5.1.2	gen_amp	108
5.1.3	gen_omegapi	110
5.2	Amplitudes	111
5.2.1	Angular Moments Model	111
5.2.2	Partial Waves Amplitudes Model	112
5.3	Acceptance	113
5.4	Summary	119

6	Results	120
6.1	Moments	120
6.2	Additional Experimental Observables	126
6.2.1	S-Channel Helicity Conservation	127
6.2.2	Helicity Amplitudes of the ω	132
6.3	Partial Wave Amplitudes	135
6.4	Inclusive Cross-section for $\omega\pi^0$	145
6.5	Differential Cross-section for $\omega\pi^0$	148
6.6	Summary	152
7	Systematic Studies	154
7.1	Potential Sources of Systematic Error	155
7.2	$\omega\pi$ Cross-section Systematic Studies	157
7.2.1	Kinematic Fit FOM Cut Study	157
7.2.2	$\pi^+\pi^-\pi^0$ Invariant Mass Cut Study	159
7.2.3	$\omega\pi^0$ Invariant Mass Cut Study	161
7.2.4	$\omega\pi$ Cross-section Combined Systematic Error	163
7.3	$\omega\pi$ Differential Cross-section Systematic Studies	165
7.3.1	Kinematic Fit FOM Cut Study	165
7.3.2	$\pi^+\pi^-\pi^0$ Invariant Mass Cut Study	168
7.3.3	$\omega\pi^0$ Invariant Mass Cut Study	173
7.3.4	Combined Systematic Error for the $\omega\pi$ Differential Cross-section . .	177
7.4	Summary	181
8	Conclusions and Future Work	182
	References	186
A	Extracted Angular Moments from 2017 GlueX Data	191
B	Angular Moments Extracted by The Omega-Photon Collaboration	194
C	Invariant Masses	197
D	Particle Identification Timing Cuts	199
E	Invariant Mass Plots	204

List of Figures

1.1	Fundamental particles according to the SM. Each particle's mass, spin, and electric charge are noted. Particles with colour charge are also indicated.	3
1.2	Possible configurations of quarks to form a colour neutral hadron according to the quark model. Quarks are represented by solid colour rubber ducks with the letter (q), while antiquarks are represented by upside down rubber ducks with the letter (\bar{q}). From left to right, a quark antiquark pair forms a meson and three quarks of different colours form a baryon. Two quark antiquark pairs form a tetraquark and a quark antiquark pair with three quarks of different colours form a pentaquark (colour online).	5
1.3	Diagram showing the 16-plets (SU(4) flavour symmetry) for the pseudo-scalar (a) and vector mesons (b) made of the up, down, strange, and charm quarks as a function of isospin I_z , charm C, and hypercharge ($Y = B + S - C$). The nonets of light mesons occupy the central planes to which the charm states have been added [5].	6
1.4	The strong coupling constant (α_s) measured as a function of the energy scale Q [5] (colour online).	8
1.5	Isoscalar (green and black) and isovector (blue) spectrum as a function of mass, shown on the y-axis label. States are labeled J^{PC} . The quark mass is heavier than its "conventionally" assigned bound mass; leading to a pion mass $m_\pi=524$ MeV, much heavier than its physical mass. The vertical height of each box indicates the statistical uncertainty in the mass. Black and green indicate relative nonstrange and strange composition. Orange outlines interpreted as hybrid states. Note the exotic states in the three rightmost columns [6] (colour online). . . .	9
1.6	Hadrons which are not predicted by the simple quark model. Quarks are represented by solid colour rubber ducks with the letter (q), gluons are represented by striped rubber ducks with the letter (g) while antiquarks are represented by upside down rubber ducks with the letter (\bar{q}). From left to right, a quark antiquark pair in which a gluon contributes to the quantum numbers is called a hybrid, while a group of gluons forms a "glueball". Due to limitations of this representation, a gluon could carry a color-anti-color charge, yet there no direct way of representing this case (colour online).	10

1.7	Invariant mass of $\pi^+\pi^-2\pi^0$ and $\omega\pi^0$ from the Omega-Photon [17] (right) and SLAC-H-Photon experiments [18] (left).	13
1.8	Helicity frame for the $\omega\pi^0$ decay channel. Angles (θ, ϕ) describe the ω meson in the b_1 meson helicity frame. Angles (θ_H, ϕ_H) describe the normal to decay plane (\hat{n}) in the ω meson helicity frame.	16
1.9	The production angle Φ is defined as the angle between the polarization vector $\vec{\epsilon}$ of the incident beam photon and the normal to the production plane formed by the recoil proton and the $\omega\pi^0$ resonance.	17
2.1	An overview of the 12 GeV upgrade of the CEBAF accelerator [24]. .	28
2.2	An illustration of the GlueX experimental setup [25].	29
2.3	These plots show the enhancement of collimation on the distribution of the energy and the polarization fraction of the beam. These are simulated for a 15 μm thick diamond-radiator with a 1 μA electron beam current [28] (colour online).	31
2.4	An illustration of the Hall D tagger. Electrons passing through the diamond-radiator are deflected by the magnetic field into the electron beam dump (for full energy electrons) or onto one of the scintillator counters on the focal plane [29].	32
2.5	A picture of the triplet polarimeter detector. The beam enters from the right, some of the photons interact with electrons in the beryllium foil, and the beam proceeds into the experimental hall. The silicon strip detector (the doughnut-shape in the middle right of the photo) detects the recoil electron while the e^+e^- pair is detected by the Pair Spectrometer.	33
2.6	Plot showing the polarization fraction of the photon beam as a function of energy, as measured by the triplet polarimeter for two polarization orientations PARA (0° , parallel to the floor), PERP (90° , perpendicular to the floor) on the right and PARA (135°), PERP (45°) on the left, with data points offset horizontally by 0.015 GeV for clarity [32].	34
2.7	An illustration of the PS detector. The beam enters from triplet polarimeter on the left. The dipole magnet deflects the e^+ and e^- to opposite directions where an array of scintillating detectors measure the deflection and therefore the energy of the particles [34].	35
2.8	Photon beam flux as a function of energy as measured by the PS in coincidence with a TAGH or TAGM hit for the four beam polarization orientations (PARA 0° , PERP 90° , PARA 135° and PERP 45°). The coherent peak of the lowest photon energy can be seen around 8-9 GeV while other coherent photon peaks, corresponding to different lattice vectors in the diamond-radiator, can be seen on the higher energy side [33] (colour online).	35
2.9	The liquid hydrogen target cell for the GlueX experiment. Beam enters from the left of the image. The target cell is surrounded by a ROHACELL support structure and the ST [34].	36

2.10	Schematic of the layout of the baseline GlueX detectors. The dashed region indicates the location of the DIRC (Direct Internal Cherenkov Detector) whose principal objective is to improve particle identification between pions and kaons to higher momenta ($\sim 4 \text{ GeV}/c$) than currently achievable ($\sim 2 \text{ GeV}/c$). The DIRC was installed in 2018, commissioned in 2019 and now forms a subsystem of the base GlueX detector.	37
2.11	Schematic drawing of the CDC straw configuration. The diagram shows the radial layers of axial (straight) straws (black dots) and stereo straws (red and blue dots) (colour online) [34].	38
2.12	Energy deposition per unit length in the CDC as a function of the reconstructed particle momentum for positively charged particles. The horizontal band represents the pions, kaons and positrons which can be distinguished from the proton band for momentum up to 1 GeV [25] (colour online).	39
2.13	(a) Front view of an FDC package. Vertical lines represent the wires with the two cathode (U and V) strip planes on either side of the wires rotated by $\pm 75^\circ$ with respect to the vertical. (b) Side view of an FDC package. Solid green lines represent (U and V) cathode strip planes while wire planes are shown as dashed lines. A package is made up of six sets of cathode strip detectors, each rotated 60° around the beamline axis with respect to the previous set [37] (colour online). . .	40
2.14	Sketch of Barrel Calorimeter readout. (a) A three-dimensional rendering of the BCAL; (b) top-half cutaway (partial side view) of a BCAL module showing its polar angle coverage and location with respect to the GlueX LH_2 target; (c) end view of the BCAL depicting all 48 azimuthal modules and (d) an end view of a single module showing the readout segmentation. More details can be found in the text and in reference [38] (colour online).	43
2.15	The ratio of the particle speed to the speed of light in vacuum β (measured by the BCAL) for positively charged particles as a function of the reconstructed particle momentum. The three curves show expected distributions of pions (top), kaons (middle), and protons (bottom). The lower band represents protons (speed much lower than speed of light) while the upper band represents positrons/pions (speed very close to the speed of light $\beta \approx 1$), this can be used to distinguish protons from positrons/pions for momentum less than 2 GeV (colour online).	45
2.16	An illustration showing the conceptual design of the FCAL as a circular array of lead glass blocks with a diameter of 1 m. Light from LEDs located on the edges of the acrylic planes illuminates the lead-glass blocks for monitoring the PMTs' timing and energy characteristics. The opaque cover prevents ambient light of entering the detector (colour online).	47
2.17	A representation of the ST mounted to the target cell [40]. The target cell is not visible in this schematic, as it is inside the ST (colour online).	48

2.18	The TOF detector mounted on its support frame. Its surface area is approximately $250 \times 250 \text{ cm}^2$ [42].	50
2.19	The ratio of the particle speed to the speed of light in vacuum β as a function of the reconstructed particle momentum, measured by the TOF detector for positively charged particles [25]. The different particle species identified fall on bands, as denoted by the symbols (colour online).	51
3.1	Pulser Configuration of the BCAL LED monitoring system [38], showing the four LED strings per module.	54
3.2	One end of a prototype BCAL module, showing two of its four sectors of light guides. The LED pulsers are mounted on the side of the light guides attached to a common flexible cable. The free end of the flexible cable connects to its control board (shown in Fig. 3.1) [38].	54
3.3	A pocket is shown on the side of a light guide where the LED is to be mounted [38]. Each LED is inserted at an angle, so as to mostly point to the opposite end of its BCAL cell.	54
3.4	An example of LED pulsing event from run 11450, where Sector 1 is pulsed red/magenta indicating higher amplitude, and optical crosstalk can be seen in the Sector 2 orange/yellow indicating lower amplitude [43] (colour online).	54
3.5	Histogram showing triggers for a sample of run 51262. (Top left) Triggers from all events. Yellow bars represent GTP triggers (FCAL, BCAL and PS) while red ones represent FP triggers (FCAL LED, BCAL LED and random). The BCAL LED triggers are represented by triggers 9 and 10 (upstream and downstream respectively), which correspond to "lane" values of 8 and 9 in the trigger/DAQ configuration file. (top right) Triggers of events which do not have an FP LED trigger yet they satisfy the 200-hits cut. (bottom left) Triggers of events which do not have an FP LED trigger yet they satisfy the 12 GeV-energy cut. (bottom right) Triggers of events are shown which do not have a FP LED trigger yet they satisfy either the 200-hits or the 12 GeV-energy cuts (colour online).	59
3.6	An example leaked event identified as an LED event by the skim plugin. Such an event is likely due to a hadronic shower by a cosmic muon, striking the upper right quadrant in this view.	60
3.7	Example plots for number of hits versus energy deposition in the BCAL per event, for events identified as LED events by the skim (left) and real LED events (right). The leaked events can be seen in the left panel with relatively lower energies and number of hits. Also, they do not follow the linear relation we see between number of hits and energy for LED events in the right panel (colour online).	60

3.8	The number of hits for events identified as LED events by the skim plugin; this is a projection of the plot in the left panel of Fig. 3.7. The real LED events are indicated by the peak around 1536. The distribution at lower number of hits shows the GTP events leaking into the LED skim.	61
3.9	Example plot comparing the use of front panel triggers alone (red) and the inclusion of the 1200 hits as an alternative trigger (blue). In this particular run the FP triggers agree with the pseudo-trigger (colour online).	62
3.10	(Left) Stack of PSPP over six pulser cycles for all four downstream sectors for run 11436. (Right) A single pulser cycle is shown composed of four groups [43] (colour online).	64
	65figure.caption.48	
3.12	A sample normalized pulse peak vs channel ID is shown for the bias of 6.25 V and the upstream pulser configuration over run 11445. [47] . .	66
3.13	(Left) Normalized pulse peak to average ratio vs run number for channel 0 (module 1, layer 1, sector 1 downstream). The ratio is clustered around 1, demonstrating stability over a large number of runs taken over 12 days [47]. (Right) A Gaussian fit of the Y-axis projection of Fig. 3.13 is shown. From this fit the standard deviation and mean are obtained to calculate the fractional variation [47].	67
3.14	(Left) The standard deviation of the normalized pulse peak fit for each channel over spring 2016 runs [47]. (Right) The fractional variance of the normalized pulse peak fit for each channel over spring 2016 runs [47].	67
3.15	An example of Phase A online relative gain monitoring histograms for experts over fall 2018 runs. The relative gain is plotted versus the run number for each channel. Each row represents the change in relative gain for a pair of BCAL channels. The two columns on the left represent the downstream channel relative gain when pulsed by the upstream LED (leftmost column) and downstream LED (middle left column). Similarly, the two columns on the right show the relative gain for the conjugate channel (same module, sector and layer) on the upstream end of the BCAL. In this format, all 1536 channels of the BCAL are summarized in a 96 page file. Phase B monitoring uses an extended version of these plots to study a complete run period.	70

3.16	An example of the third-tier essentially-online relative gain monitoring histograms for shift takers from run 61624 (spring 2019). This tier was decided unfeasible by the CALWG for reasons mentioned in the text. The color scheme is used to make it easy to see if a channel is behaving as expected or not. Well-behaved channels will have a stable gain over the run period, leading to a relative gain of unity (when compared to the average over the run period) (green). Channels with lower than expected gain will have a relative gain lower than unity (violet - blue). Channels with higher than expected relative gain will be larger than unity (yellow - red). White blocks indicate channels where the LED did not pulse or the channel is dead (colour online).	72
3.17	(Left) The 16 ratio histograms (a sample is shown in Fig. 3.12) are superimposed into four histograms with four colours indicating different sectors. (Right) Channels with ratios deviating from unity can be visually detected (colour online).	74
3.18	The normalized pulse peak profile of five channel pairs is plotted over the spring 2017 run period. Each row represents a pair of channels. The two leftmost columns show the downstream channel while the two rightmost columns show the upstream channel of the same module, layer and sector. Each channel was pulsed by the upstream pulser on left and the downstream pulser on the right [50]. The top four rows show that the downstream channels are relatively stable around the unity, while the upstream channels show clear deviations from the unity. The drift is persistent when pulsed by either the upstream and downstream pulsers, which indicates that the drift is in the SiPM gains and not in the pulser signal. The bottom row shows a clear drift in the downstream channel for the upstream pulser while the same channel is stable with the downstream pulser. The upstream channel is stable with both pulsers which indicates the drift is in the downstream SiPM gain.	76
3.19	A general drift is observed in the pulse peak for the BCAL LED response over spring 2018. The first row represents a downstream channel normalized pulse peak exhibiting the drift which largely cancels in the second row upon dividing over the normalized pulse peak of the upstream conjugate channel [51].	77
3.20	The PSPP profile of four channel pairs over spring 2018 run period is graphed. Each row represents the ratio between a pair of channels (downstream/upstream) over the four pulser modes (6 V upstream, 6 V downstream, 6.25 V upstream, 6.25 V downstream). The first row represents a well behaved pair for reference. Rows 2-4 show three pairs with misbehaving channels, yet all within 2% from the unit baseline. [51].	78

3.21	Evolution of the number of hits for LED events over the fall 2018 run period. The peak around 1536 indicates that all channels are being pulsed. The tail on the right indicates that sometime few LEDs fail to fire. A second peak at lower number of hits indicates a quadrant is failing to produce a signal.	79
3.22	Example plots showing the occupancy of different quadrants in the BCAL from run 61580. Occupancy is calculated as the ratio between the number of pulser triggers to the number of events where at least 192 channels (half) in the quadrant record a pulse when a trigger is found for the upstream (blue) and downstream (red) pulsers. As we can see the downstream pulser is failing to pulse all quadrants in $\sim 40\%$ of the events (colour online).	80
3.23	Example pedestal distribution and fitting for all channels in layer 4 at 1.2 V overbias and 18° [54] (colour online).	81
3.24	Pedestal distribution width and mean versus SiPM overbias at 10° . The top two panels show the width and mean for LEDs on runs while the bottom two panels show LEDs off (pedestal only) runs. The left-most point indicates LV runs and therefore is excluded from the fits [54] (colour online).	83
3.25	Pedestal distribution width (left) and mean (right) versus SiPM overbias at 10 and 18° according the study carried out in 2015 [52] (colour online).	84
4.1	Time of flight distribution for the proton, $\pi^+\pi^-$ and γ versus their linear momenta in the BCAL, FCAL and TOF detector subsystems. These plots are produced for with spring 2017 data. The red lines indicate the PIDT selection cuts used in our analysis.	92
4.2	The invariant mass of $\omega\pi^0$ after accidentals and ω background subtraction versus the KinFit CL (colour online).	94
4.3	(left) The z-position, (right) the x-position versus the y-position of the kinematically-fit vertex. The red lines and the red circle indicate the cut limits (colour online).	95
4.4	A side-view of the GlueX detector representing only the target, BCAL and FCAL. The red regions represent fiducial cuts applied around the beam hole in the FCAL, the edges of the FCAL and the downstream edge of the BCAL. Reconstruction is unreliable in these regions (colour online).	96
4.5	The number of events passing through each of the selection cuts in spring 2017 run period.	97
4.6	Invariant mass spectra of the $\omega\pi^0$. The effect of various cuts on the invariant mass spectra is shown, with the cut names listed on the legend (colour online).	97

4.7	Δt_{RF} distribution from data. The prompt peak at 0 ns represents events reconstructed with correct beam bunch with contribution from accidentals. The peaks on either side are used for accidental subtraction, as described in Section 4.2.1. The peaks at ± 4 ns are excluded from the plot and the subtraction to avoid leakage from the prompt peak (colour online).	100
4.8	Invariant mass of $\gamma\gamma$ (left) after event selection cuts, $\pi^+\pi^-\pi^0$ (middle) after subtracting accidentals and $\omega\pi^0$ (right) after subtracting the accidentals and ω background. The top row is produced with spring 2017 data and the bottom row is produced with MC simulation. The red lines indicate the selection cuts for π^0 , ω and $\omega\pi^0$. The blue lines indicate the side-bands used to calculate the background under the ω peak. The $\omega\pi^0$ range is defined by 8.7σ above and below the b_1 peak.	101
4.9	Invariant mass of the $\omega\pi^0$. The black curve represents events reconstructed from the ω peak including contribution from the ω side bands. The green curve represents events reconstructed with contribution from the ω side bands. The red curve represents the black curve after side band subtraction (colour online).	102
5.1	Helicity frame angles of the phase-space for the $\omega\pi$ channel as generated by gen_amp (red) and gen_omegapi (blue). Being in the decaying particle rest frame, the phase-space angular distribution is expected to be flat. We can see the non-flat $\cos\theta_H$ distribution generated by gen_amp as a result of the four pion phase-space.	109
5.2	Invariant mass of the four-pion (left) and three pions (right) as generated by gen_amp (red) and gen_omegapi (blue). gen_amp produces a wider invariant mass distribution for the three pions with a shoulder around the mass of the η' meson. gen_omegapi produces realistic shapes for both distributions.	111
5.3	Invariant mass of the $\omega\pi^0$ for the thrown (left) and accepted (right) MC sample.	114
5.4	The acceptance as a function of the $\omega\pi^0$ invariant mass.	115
5.5	Invariant mass of the $\omega\pi^0$ from data before (left) and after applying acceptance correction (right). The red lines define the b_1 peak cut used to extract the angular distribution.	115
5.6	Thrown helicity frame angles of the phase-space for the $\omega\pi$ channel as generated by gen_omegapi. The phase-space angular distribution is uniform as expected in the decaying particle rest frame.	116
5.7	Accepted helicity frame angles for the b_1 peak for the $\omega\pi$ channel as generated by gen_omegapi.	117
5.8	Acceptance as a function of the helicity frame angles for the b_1 peak for the $\omega\pi$ channel.	117
5.9	Helicity frame angles for the b_1 peak for the $\omega\pi$ channel from data.	118
5.10	Acceptance-corrected helicity frame angles for the b_1 peak for the $\omega\pi$ channel.	118

6.1	Extracted moments of the $\omega\pi$ channel as a function of the $\omega\pi$ invariant mass and Mandelstam-t.	123
6.2	Extracted moments of the $\omega\pi$ channel as a function of the $\omega\pi$ invariant mass and Mandelstam-t.	124
6.3	Extracted moments of the $\omega\pi$ channel as a function of the $\omega\pi$ invariant mass and Mandelstam-t.	125
6.4	Yield of the $b_1(1235)$ meson as a function of the production angle Φ . SLAC-H collaboration data and fit [18].	128
6.5	Yield of the $b_1(1235)$ meson as a function of the production angle Φ based on spring 2017 data and fit over the coherent peak ($8.2 < E_{beam} < 8.8 \text{ GeV}$). (top left) 0° polarization beam. (top right) 90° polarization beam. (bottom left) -45° polarization beam. (bottom right) 45° polarization beam. The red line represents the helicity conservation assumption. Error bars represent only statistical error. (color online)	129
6.6	Yield of the $b_1(1235)$ meson as a function of the production angle Φ based on spring 2018 data and fit over the coherent peak ($8.2 < E_{beam} < 8.8 \text{ GeV}$). (top left) 0° polarization beam. (top right) 90° polarization beam. (bottom left) -45° polarization beam. (bottom right) 45° polarization beam. The red line represents the helicity conservation assumption. Error bars represent only statistical error. (color online)	130
6.7	Yield of the $b_1(1235)$ meson as a function of the production angle Φ based on fall 2018 data and fit over the coherent peak ($8.2 < E_{beam} < 8.8 \text{ GeV}$). (top left) 0° polarization beam. (top right) 90° polarization beam. (bottom left) -45° polarization beam. (bottom right) 45° polarization beam. The red line represents the helicity conservation assumption. Error bars represent only statistical error. (color online)	131
6.8	Yield and fit of the $b_1(1235)$ meson as a function of θ_H , the polar decay angle of the ω meson. (left) Spring 2017, (middle) Spring 2018, (right) fall 2018.	134
6.9	Yield of the $b_1(1235)$ meson as a function of θ_H , the polar angle of the ω meson decay plane. SLAC-H collaboration Data, fit (solid curve) and results from the Omega-Photon collaboration (dashed curve) [17, 18].	135
6.10	Combined S, D and uniform components of the AmpTools fit. The points represent the data, yellow histograms represent generated MC scaled by the physics model while green histograms represent accepted MC scaled by the physics model.	139
6.11	S-wave component of the AmpTools fit. The points represent the data, yellow histograms represent generated MC scaled by the physics model while green histograms represent accepted MC scaled by the physics model.	140
6.12	D-wave component of the AmpTools fit. The points represent the data, yellow histograms represent generated MC scaled by the physics model while green histograms represent accepted MC scaled by the physics model.	141

6.13	Generated phase space MC scaled by the the S-wave component of the physics model.	142
6.14	Generated phase space MC scaled by the the D-wave component of the physics model.	143
6.15	Generated phase space MC (yellow) and accepted phase space MC (green) scaled by the physics model.	144
6.16	Calculating total cross-section of the $\omega\pi^0$ based on data from spring 2017 (Δ), spring 2018 (\square) and fall 2018 (\bigcirc) run periods. Starting from top left the graphs show generated MC, accepted MC, efficiency, yield, tagged beam flux and flux normalized yield. Error bars represent only statistical error. (color online)	146
6.17	Our $\omega\pi^0$ total cross-section results calculated based on data from spring 2017 (Δ), spring 2018 (\square) and fall 2018 (\bigcirc) run periods. Results from previous experiments: (green) Ballam et al. and references therein [16]Error bars represent only statistical error. (color online)	147
6.18	Our $\omega\pi^0$ total cross-section results calculated based on data from spring 2017 (Δ), spring 2018 (\square) and fall 2018 (\bigcirc) run periods. Results from previous experiments: (green) Ballam et al. and references therein [16], (purple) Barber et al. [66], (black) Aston et al. [67], (red) The Omega-Photon collaboration [17]. Error bars represent only statistical error. (color online)	147
6.19	Our $\omega\pi^0$ total cross-section results calculated based on data from spring 2017 (Δ), spring 2018 (\square) and fall 2018 (\bigcirc) run periods. Results from previous experiments: (green) Ballam et al. and references therein [16], (purple) Barber et al. [66], (black) Aston et al. [67], (red) The Omega-Photon collaboration [17]. Error bars represent only statistical error. (color online)	148
6.20	Our $\omega\pi^0$ differential cross-section results in different beam energy bins. Calculated based on data from spring 2017 (black), spring 2018 (red) and fall 2018 (blue) run periods. Our results from different runs periods do not align, specially at low Mandelstam-t. We see a spike in the differential cross-section in the 11 GeV beam energy bin at low t. Error bars represent only statistical error. (color online)	150
6.21	Exponential fit of our $\omega\pi^0$ differential cross-section results on semi-log plots are shown in different beam energy bins, calculated based on data from spring 2017 (black), spring 2018 (red) and fall 2018 (blue) run periods. Our results from different runs periods do not align. The distribution is fitted to the sum of two exponential functions. The mean slope is -5.24 ± 0.04 for $0.25 < t < 0.95 \text{ } GeV^2/c^2$ and -1.24 ± 0.05 for $0.95 < t < 2.0 \text{ } GeV^2/c^2$. A summary of the fit results is presented in Table. 6.5. Error bars represent only statistical error. (color online)	151

7.1	The efficiency ratio of our analysis cuts on the yield of $\omega\pi^0$ in data and signal MC. Least efficient cuts are the particular KinFit FOM cut and the invariant mass cuts on the $\pi^+\pi^-\pi^0$ and $\omega\pi^0$ respectively. The rest of the cut have $100 \pm 1\%$ efficiency.	156
7.2	(top) The $\omega\pi^0$ cross-section with the systematic error calculated for the three run periods by changing the KinFit FOM cut from 10^{-5} to 10^{-4} . The systematic error is added in quadrature to the statistical error to form the total error for each bin. The systematic error is drawn in violet while total error is shown in green. (bottom left) The relative statistical (blue) and systematic (violet) errors for the $\omega\pi^0$ cross-section. Data points for spring 2018 and fall 2018 run periods are shifted along the x-axis for clarification. (bottom right) A zoomed portion of the lower side of the energy range showing the relative statistical and systematic errors.	158
7.3	(top) The $\omega\pi^0$ cross-section with systematic error calculated for the three run periods by changing the width of the ω peak from 2.6σ to 3.43σ above and below the ω peak. The systematic error is added in quadrature to the statistical error to form the total error for each bin. The systematic error is drawn in violet while total error is shown in green. (bottom left) The relative statistical (blue) and systematic (violet) errors for the $\omega\pi^0$ cross-section. Data points for spring 2018 and fall 2018 run periods are shifted along the x-axis for clarification. (bottom right) A zoomed portion of the lower side of the energy range showing the relative statistical and systematic errors.	160
7.4	(top) The $\omega\pi^0$ cross-section with systematic error calculated for the three run periods by changing the $\omega\pi^0$ invariant mass cut. The systematic error is added in quadrature to the statistical error to form the total error for each bin. The systematic error is drawn in violet while total error is shown in green. (bottom left) The relative statistical (blue) and systematic (violet) errors for the $\omega\pi^0$ cross-section. Data points for spring 2018 and fall 2018 run periods are shifted along the beam energy axis for clarification. (bottom right) A zoomed portion of the lower side of the energy range showing the relative statistical and systematic errors.	162
7.5	(top) The $\omega\pi^0$ cross-section with combined systematic error calculated for the three run periods by linearly adding the systematic errors for the KinFit FOM, $\pi^+\pi^-\pi^0$ and the $\omega\pi^0$ invariant mass cuts. The combined systematic error is added in quadrature to the statistical error to form the total error for each bin. The systematic error is drawn in violet while total error is shown in green. (bottom left) The relative statistical (blue) and combined systematic (violet) errors for the $\omega\pi^0$ cross-section. Data points for spring 2018 and fall 2018 run periods are shifted along the x-axis for clarification. (bottom right) A zoomed portion of the lower side of the energy range showing the relative statistical and combined systematic errors.	164

7.6	The $\omega\pi^0$ differential cross-section with systematic error calculated for changing the KinFit FOM cut from 10^{-5} to 24×10^{-5} . The systematic error is added in quadrature to the statistical error to form the total error for each bin. The systematic error is drawn in violet while total error is shown in green. Spring 2018 and Fall 2018 data points are shifted along the beam energy axis for clarification.	166
7.7	The $\omega\pi^0$ differential cross-section with systematic error calculated by changing the KinFit FOM cut from 10^{-5} to 24×10^{-5} . The systematic error is added in quadrature to the statistical error to form the total error for each bin. The systematic error is drawn in violet while total error is shown in green. Spring 2018 and Fall 2018 data points are shifted along the beam energy axis for clarification.	167
7.8	The relative statistical (blue) and systematic (violet) error for the $\omega\pi^0$ differential cross-section over the three run periods in five beam energy bins. The systematic error is calculated by changing the KinFit FOM cut from 10^{-5} to 24×10^{-5}	168
7.9	The $\omega\pi^0$ differential cross-section with systematic error calculated for the three run periods in five beam energy bins by changing the $\pi^+\pi^-\pi^0$ invariant mass cut. The systematic error is added in quadrature to the statistical error to form the total error for each bin. The systematic error is drawn in violet while total error is shown in green. Spring 2018 and Fall 2018 data points are shifted along the beam energy axis for clarification.	170
7.10	The $\omega\pi^0$ differential cross-section with systematic error calculated for the three run periods in five beam energy bins by changing the $\pi^+\pi^-\pi^0$ invariant mass cut. The systematic error is added in quadrature to the statistical error to form the total error for each bin. The systematic error is drawn in violet while total error is shown in green. Spring 2018 and Fall 2018 data points are shifted along the beam energy axis for clarification.	171
7.11	The relative statistical (blue) and systematic (violet) error for the $\omega\pi^0$ differential cross-section over the three run periods in five beam energy bins. The relative systematic error is calculated by changing the $\pi^+\pi^-\pi^0$ invariant mass cut.	172
7.12	The $\omega\pi^0$ differential cross-section with systematic error calculated for the three run periods in five beam energy bins by changing the $\omega\pi^0$ invariant mass cut. The systematic error is added in quadrature to the statistical error to form the total error for each bin. The systematic error is drawn in violet while total error is shown in green. Spring 2018 and Fall 2018 data points are shifted along the beam energy axis for clarification.	174

7.13	The $\omega\pi^0$ differential cross-section with systematic error calculated for the three run periods in five beam energy bins by changing the $\omega\pi^0$ invariant mass cut. The systematic error is added in quadrature to the statistical error to form the total error for each bin. The systematic error is drawn in violet while total error is shown in green. Spring 2018 and Fall 2018 data points are shifted along the beam energy axis for clarification.	175
7.14	The relative statistical (blue) and systematic (violet) error for the $\omega\pi^0$ differential cross-section over the three run periods in five beam energy bins. The systematic error is calculated by changing the $\omega\pi^0$ invariant mass cut.	176
7.15	The $\omega\pi^0$ differential cross-section with combined systematic error calculated for the three run periods in five beam energy bins by linearly adding the systematic errors for the KinFit FOM, $\pi^+\pi^-\pi^0$ and the $\omega\pi^0$ invariant mass cuts. The combined systematic error is added in quadrature to the statistical error to form the total error for each bin. The combined systematic error is drawn in violet while total error is shown in green. Spring 2018 and Fall 2018 data points are shifted along the beam energy axis for clarification.	178
7.16	The $\omega\pi^0$ differential cross-section with combined systematic error calculated for the three run periods in five beam energy bins by linearly adding the systematic errors for the KinFit FOM, $\pi^+\pi^-\pi^0$ and the $\omega\pi^0$ invariant mass cuts. The combined systematic error is added in quadrature to the statistical error to form the total error for each bin. The combined systematic error is drawn in violet while total error is shown in green. Spring 2018 and Fall 2018 data points are shifted along the beam energy axis for clarification.	179
7.17	The relative statistical (blue) and combined systematic (violet) errors for the $\omega\pi^0$ differential cross-section over the three run periods in five beam energy bins. The combined systematic error is calculated by linearly adding the systematic errors for the KinFit FOM, $\pi^+\pi^-\pi^0$ and the $\omega\pi^0$ invariant mass cuts for each bin.	180
A.1	Extracted moments of the $\omega\pi$ channel as a function of the $\omega\pi$ invariant mass.	191
A.2	Extracted moments of the $\omega\pi$ channel as a function of the $\omega\pi$ invariant mass.	192
A.3	Extracted moments of the $\omega\pi$ channel as a function of the $\omega\pi$ invariant mass.	193
B.1	Moments of the $\omega\pi$ channel as a function of the $\omega\pi$ invariant mass. Markers represent acceptance corrected moments. Lines represent the fit.	194

B.2	Moments of the $\omega\pi$ channel as a function of the $\omega\pi$ invariant mass. Markers represent acceptance corrected moments. Lines represent the fit.	195
B.3	Moments of the $\omega\pi$ channel as a function of the $\omega\pi$ invariant mass. Markers represent acceptance corrected moments. Lines represent the fit.	196
C.1	Invariant mass of $\gamma\gamma$ (left) after event selection cuts, $\pi^+\pi^-\pi^0$ (middle) after subtracting accidentals and $\omega\pi^0$ (right) after subtracting the accidentals and ω background. The top row is produced with spring 2018 data and the bottom row is produced with MC simulation. The red lines indicate the selection cuts for π^0 , ω and $\omega\pi^0$. The blue lines indicate the side-bands used to calculate the background under the ω peak. The $\omega\pi^0$ range is defined by 8.7σ above and below the b_1 peak.	197
C.2	Invariant mass of $\gamma\gamma$ (left) after event selection cuts, $\pi^+\pi^-\pi^0$ (middle) after subtracting accidentals and $\omega\pi^0$ (right) after subtracting the accidentals and ω background. The top row is produced with fall 2018 data and the bottom row is produced with MC simulation. The red lines indicate the selection cuts for π^0 , ω and $\omega\pi^0$. The blue lines indicate the side-bands used to calculate the background under the ω peak. The $\omega\pi^0$ range is defined by 8.7σ above and below the b_1 peak.	198
D.1	Time of flight distribution for the proton, $\pi^+\pi^-$ and γ versus their linear momenta in the BCAL, FCAL and TOF detector subsystems. These plots are produced for with data from spring 2018 run period. The red lines indicate the PIDT selection cuts used in our analysis.	199
D.2	Time of flight distribution for the proton, $\pi^+\pi^-$ and γ versus their linear momenta in the BCAL, FCAL and TOF detector subsystems. These plots are produced for with data from fall 2018 run period. The red lines indicate the PIDT selection cuts used in our analysis.	200
D.3	Time of flight distribution for the proton, $\pi^+\pi^-$ and γ versus their linear momenta in the BCAL, FCAL and TOF detector subsystems. These plots are produced for with MC simulation for spring 2017 run period. The red lines indicate the PIDT selection cuts used in our analysis.	201
D.4	Time of flight distribution for the proton, $\pi^+\pi^-$ and γ versus their linear momenta in the BCAL, FCAL and TOF detector subsystems. These plots are produced for with MC simulation for spring 2018 run period. The red lines indicate the PIDT selection cuts used in our analysis.	202
D.5	Time of flight distribution for the proton, $\pi^+\pi^-$ and γ versus their linear momenta in the BCAL, FCAL and TOF detector subsystems. These plots are produced for with MC simulation for fall 2018 run period. The red lines indicate the PIDT selection cuts used in our analysis.	203

E.1	The invariant mass of $\gamma\gamma$ versus the invariant mass of $\pi^+\pi^-\pi^0$ (right) and their projection on the both axes, before applying our selection cuts (top row) and after applying our selection cuts (bottom row). No background (accidentals or ω side-band) subtractions were applied on these plots. These plots are produced with spring 2017 data. Significant background to the ω peak is present, as clear by the $\eta(548)$ peak.	204
E.2	The invariant mass of $\gamma\gamma$ versus the invariant mass of $\pi^+\pi^-\pi^0$ (right) and their projection on the both axes, before applying our selection cuts (top row) and after applying our selection cuts (bottom row). No background (accidentals or ω side-band) subtractions were applied on these plots. These plots are produced with spring 2018 data. Significant background to the ω peak is present, as clear by the $\eta(548)$ peak.	205
E.3	The invariant mass of $\gamma\gamma$ versus the invariant mass of $\pi^+\pi^-\pi^0$ (right) and their projection on the both axes, before applying our selection cuts (top row) and after applying our selection cuts (bottom row). No background (accidentals or ω side-band) subtractions were applied on these plots. These plots are produced with fall 2018 data. Significant background to the ω peak is present, as clear by the $\eta(548)$ peak. . .	206
E.4	The invariant mass of $\gamma\gamma$ versus the invariant mass of $\pi^+\pi^-\pi^0$ (right) and their projection on the both axes, before applying our selection cuts (top row) and after applying our selection cuts (bottom row). No background (accidentals or ω side-band) subtractions were applied on these plots. These plots are produced with spring 2017 MC simulation. Only $\omega\pi^0$ events are include in the simulation. The background is significantly lower compared to data and arises from wrongly reconstructed events.	207
E.5	The invariant mass of $\gamma\gamma$ versus the invariant mass of $\pi^+\pi^-\pi^0$ (right) and their projection on the both axes, before applying our selection cuts (top row) and after applying our selection cuts (bottom row). No background (accidentals or ω side-band) subtractions were applied on these plots. These plots are produced with spring 2018 MC simulation. Only $\omega\pi^0$ events are include in the simulation. The background is significantly lower compared to data and arises from wrongly reconstructed events.	208
E.6	The invariant mass of $\gamma\gamma$ versus the invariant mass of $\pi^+\pi^-\pi^0$ (right) and their projection on the both axes, before applying our selection cuts (top row) and after applying our selection cuts (bottom row). No background (accidentals or ω side-band) subtractions were applied on these plots. These plots are produced with fall 2018 MC simulation. Only $\omega\pi^0$ events are include in the simulation. The background is significantly lower compared to data and arises from wrongly reconstructed events.	209

List of Tables

1.1	Meson states that can be formed following the quark-antiquark model and considering only S and P waves ($L=0,1$).	7
1.2	A compilation of exotic quantum number hybrid approximate masses, widths, and decay predictions [11]. Masses are estimated from dynamical LQCD calculations with $m_\pi = 396$ MeV [12]. The PSS (Page, Swanson and Szczepaniak) and IKP (Isgur, Kokoski and Paton) model widths are from [13], with the IKP calculation based on the model in [14].	11
1.3	Properties of the $b_1(1235)$ meson [5].	12
2.1	Summary of BCAL properties [39].	44
4.1	Selection cuts on $ \Delta t_{\text{RF}} $ for different particle species in ST, TOF, BCAL, and FCAL detector subsystems. A larger cut is used for photons in calorimeters (FCAL and BCAL) due to the time needed for the electromagnetic showers to evolve, shower fluctuations, and the light produced to travel to the photosensors, which could result in a larger $ \Delta t_{\text{RF}} $; inspection of the BCAL $ \Delta t $ versus momentum plot in Fig. 4.1 indicates that 1.5 ns is a conservative cut. Typical timing resolutions of the detector subsystems are presented below [57, 58]. In the case of the BCAL, the number shown is the resolution at $E_\gamma=1$ GeV.	91
5.1	A summary of the algorithms of the two MC generators gen_omegapi and gen_amp.	110
6.1	Fit results of the b_1 meson yield as a function of production angle. . .	128
6.2	Helicity amplitudes as calculated through a fit over the distribution of the decay angle $\cos(\theta_H)$	133
6.3	Comparison of helicity amplitudes as calculated through different models and data, as reported by the SLAC-H group [18].	133
6.4	Parameters and constants used in the fit.	136
6.5	Fit results of the $\omega\pi^0$ differential cross-section in different bins of photon beam energy for Spring 2017, Spring 2018 and Fall 2018 run periods. The mean fit slope and error are calculated over all beam energies and run periods.	152

Glossary

LH_2 Liquid Hydrogen. x, 1, 27, 36, 43, 63, 108

ADC Analog-to-Digital Converter. 55, 63, 81

AM Angular Moment. 18, 87, 104, 106, 107, 111, 112, 119–121, 152, 183, 185

BCAL Barrel Calorimeter. x–xiv, xxi, xxiii, 41–45, 52, 54, 56–60, 65, 68, 70, 71, 73–75, 77, 80, 84–86, 91, 92, 96, 182, 199–203

CALWG Calorimetry Working Group. xiii, 55, 68, 71, 72, 75

CDC Central Drift Chamber. x, 37–39, 89, 96

CEBAF Continuous Electron Beam Accelerator Facility. ix, 27, 28, 30, 86

CL Confidence Level. xiv, 93, 94

CM Center of Mass. 14

DIRC Detection of Internally Reflected Cherenkov Light. x, 37

FCAL Forward Calorimeter. x, xi, xiv, xxi, xxiii, 41, 46, 47, 49, 57, 59, 86, 91, 92, 96, 199–203

FDC Forward Drift Chamber. x, 37, 39, 40

FP Front Panel. xi, xii, 57–59, 62, 84

GTP Global Trigger Processor. xi, xii, 57–59, 61, 84

JLab Thomas Jefferson National Accelerator Facility. 2, 27, 87

JPAC Joint Physics Analysis Center. 23, 104, 112

KinFit Kinematic Fit. xiv, xviii–xx, 91, 93, 94, 106, 156–158, 163–168, 177–182

LED Light Emitting Diode. x–xiv, 42, 47, 52–61, 63, 65, 66, 68–72, 74, 75, 77, 79–81, 83, 84

LQCD Lattice Quantum Chromodynamics. xxiii, 8–12, 26, 137

LV Low Voltage. xiv, 81–83

MC Monte Carlo. vi, xv, xxi–xxiii, 90, 100, 101, 104, 107, 108, 110–116, 119, 145, 149, 155, 156, 183, 197, 198, 201–203, 207–209

MM Missing Mass. 89

PDF Probability Density Function. 93, 104, 108–112

PID Particle Identification. 88, 96

PIDT Particle Identification Timing. xiv, xxi, 90, 92, 199–203

PMT Photomultiplier Tube. x, 41, 47, 49

PS Pair Spectrometer. ix, xi, 34–36, 57, 59, 86, 145

PSPP Pedestal Subtracted Pulse Peak. xii, xiii, 63–65, 78, 182

PWA Partial Wave Analysis. 13, 17, 20, 22, 23, 29, 87, 104, 106, 107, 112, 119, 120, 183, 185

QCD Quantum Chromodynamics. 6–8, 26

QED Quantum Electrodynamics. 3, 6

QFD Quantum Flavordynamics. 4

SDME Spin Density Matrix Element. 13, 18, 107, 112, 121

SiPM Silicon Photomultiplier. xiii, xiv, 41, 42, 48, 52, 53, 55, 56, 63, 66, 69, 71, 74–77, 80–85, 182

SM Standard Model. viii, 2, 3

ST Start Counter. ix, x, xxiii, 36, 44, 48, 91

TAGH Tagger Hodoscope. ix, 32, 35, 86

TAGM Tagger Microscope. ix, 31, 35, 86

TOF Time-of-Flight. xi, xiv, xxi, xxiii, 48–51, 91, 92, 199–203

TPOL Triplet Polarimeter. 33, 34

Chapter 1

Introduction

The GlueX experiment is designed to help understand how quarks and gluons interact inside hadrons. Quarks are the building blocks of protons and neutrons (formed of quark triplets), which form the bulk of our universe's matter, along with a large number of other strongly interacting particles, termed hadrons, ranging from light mesons (quark-antiquark pairs) to heavy pentaquarks (consisting of five quarks). Gluons form the "glue" which holds quarks together. The experiment is studying the spectrum of hadrons produced by directing a linearly polarized photon beam on a liquid hydrogen (LH_2) target with the aim of collecting experimental evidence toward the existence of exotic and hybrid mesons. These are particles that are predicted to exist by theory but so far the evidence presented by other experiments in the past for the existence of these states has been scarce, and GlueX is designed to produce many of these states at a relatively high rate, which it is hoped will provide guidance to expand our current understanding of the strong interaction.

A brief overview of the current understanding of particle physics is given in this chapter, along with experimental evidence for hybrid or exotic states, the physics goals of GlueX, including the motivation for the work presented in this thesis on the data analysis of the $b_1(1235)$ meson. Chapters 2 and 3 provide a description of

the accelerator facility at Thomas the Thomas Jefferson National Accelerator Facility JLab, the GlueX detector and the gain monitoring system for the barrel calorimeter subsystem. Chapters 4 through 7 describe the data analysis, simulations, results, and systematic studies for the $b_1(1235)$ data analysis. Finally, Chapter 8 contains the conclusions and future directions of this line of research.

1.1 The Standard Model

The current understanding of particle physics is summarized in the Standard Model (SM) in which fundamental particles are categorized according to their intrinsic spin into particles with half-integer spin denoted as fermions which are the building blocks of matter, and particles with integer spin termed bosons which act as mediators of different forces acting between particles. Each particle is identified by a unique set of quantum numbers that include the aforementioned intrinsic spin, along with flavour, and electric and colour charge. The SM describes three of the four forces that govern these particles: the electromagnetic, the strong, and the weak forces. The gravitational force is not included in the current description of the SM.

Fermions are further divided into quarks which possess a colour charge and so are affected by the strong force, and leptons which are not affected by the strong force as shown in Fig 1.1. In the following sections, we will discuss the different ways quarks are grouped to form hadrons. As mentioned before, bosons are the mediators of the forces, which means that any observed repulsive or attractive interaction between two particles is described by the exchange of a mediator boson (exchange boson) between the two particles. This is because the SM is a gauge theory, a type of field theory in which the Lagrangian (equations of motion) is invariant under certain local transformations. This invariance is manifested by including a corresponding (the gauge field) term in the Lagrangian. When such a theory is quantized, the quanta of the gauge field arise as the force mediating particles and are called gauge bosons. In

addition to these particles, an antiparticle counterpart for each fermion with opposite charges exists while bosons are their own antiparticles except for the w^+ and w^- bosons which are each other's anti-particle.

	Gen. I	Gen. II	Gen. III		
<i>Quarks</i>	u up coloured 1/2 2/3 ~2.2 MeV/c ²	c charm coloured 1/2 2/3 ~1.28 GeV/c ²	t top coloured 1/2 2/3 ~173.1 GeV/c ²	g gluon coloured 1 0 massless	<i>Exchange Bosons</i>
	d down coloured 1/2 -1/3 ~4.7 MeV/c ²	s strange coloured 1/2 -1/3 ~96 MeV/c ²	b bottom coloured 1/2 -1/3 ~4.18 GeV/c ²	γ photon 1 0 massless	
<i>Leptons</i>	e electron 1/2 -1 ~0.511 MeV/c ²	μ muon 1/2 -1 ~105.7 MeV/c ²	τ tau 1/2 -1 ~1.768 GeV/c ²	Z Z boson 1 0 ~91.19 GeV/c ²	<i>Scalar Boson</i>
	ν_e e neutrino 1/2 0 <2.2 eV/c ²	ν_μ μ neutrino 1/2 0 <1.7 MeV/c ²	ν_τ τ neutrino 1/2 0 ~15.5 MeV/c ²	W W boson 1 ±1 ~80.39 GeV/c ²	
				H Higgs 0 0 ~125.09 GeV/c ²	

Figure 1.1: Fundamental particles according to the SM. Each particle's mass, spin, and electric charge are noted. Particles with colour charge are also indicated.

It is probably clear already that not all particles are affected by all forces. A mediator boson can only be exchanged between two particles which possess the charge corresponding to that force. For example, the electromagnetic force acts on electrically charged particles and the gauge boson for that field is the electrically neutral photon. This means that an electrically neutral fundamental particle like the neutrino cannot exchange a photon. The electromagnetic force is the best understood force, and the gauge theory used to describe it is known as Quantum Electrodynamics (QED). The weak force acts on all fundamental fermions. The gauge bosons of this field are the W^\pm (electrically charged) and Z^0 (electrically neutral) bosons.

The mathematical framework describing the weak force is Quantum Flavordynamics (QFD). At high energies, the weak and electromagnetic interactions converge into the electroweak theory, in which they are described as a single force with four massless gauge bosons and a Higgs boson that is responsible for the mass of fundamental particles. The strong force is described as the exchange of massless colour charged gluons between colour-charged quarks. In addition to gluons, quarks are the only fundamental particles that have a colour charge. The fact that gluons are colour charged and massless makes the gauge theory for the strong force quite different from the electroweak theory as we will detail in the following sections.

1.2 Quark Model

The multitude of hadrons that kept being discovered in experiments was a troubling issue for the models of the time until the proposal of the "Eightfold Way" by Gell-Mann in 1961 [1], followed by the quark model which was proposed independently by Gell-Mann [2] and Zweig [3] in 1964. The model is based on an $SU(3)$ flavour symmetry. As electroweak interactions are independent of the colour quantum numbers, the original quark model did not include a colour charge. However, the Δ^{++} baryon required three up quarks with parallel spins and vanishing orbital angular momentum, which considering the set of quantum numbers known at the time could not have an anti-symmetric wave function, which is a requirement for any system of Fermions¹ by the Pauli exclusion principle. The concept of colour charge as we know it today was presented by Bardeen, Fritzsche, and Gell-Mann in 1973 to solve that problem and became the charge for the strong interaction [4]. The extra quantum number allows the three up quarks inside the Δ^{++} baryon to occupy three distinct quantum states corresponding to colours red, green and blue.

¹Half-integer intrinsic spin particles. Quarks are spin 1/2 particles.

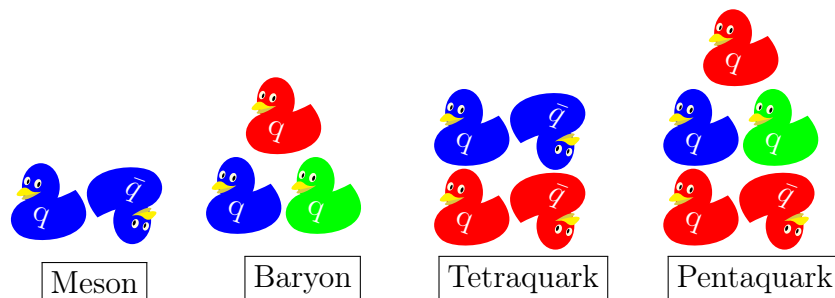


Figure 1.2: Possible configurations of quarks to form a colour neutral hadron according to the quark model. Quarks are represented by solid colour rubber ducks with the letter (q), while antiquarks are represented by upside down rubber ducks with the letter (\bar{q}). From left to right, a quark antiquark pair forms a meson and three quarks of different colours form a baryon. Two quark antiquark pairs form a tetraquark and a quark antiquark pair with three quarks of different colours form a pentaquark (colour online).

Due to the specific nature of the strong force, experimentally observed hadrons are colour neutral. As shown in Fig 1.2, this dictates the configurations allowed by the quark model to generate colour neutral states; mesons, which are composed of quark-anti-quark pairs (e.g. a red and an anti-red quark), and baryons, which are made of three quarks (i.e. a red, a green and a blue quark). More complex systems could be imagined as combinations of these two possibilities and have been observed². The quark model groups mesons of the three lightest flavours³ into nonets⁴ of mesons sharing the same intrinsic spin and parity. The model has been extended to higher flavour symmetry to take into account heavier flavours discovered since (i.e. charm, bottom, top). Fig 1.3 shows the 16-plets for pseudo-scalar and vector mesons made of up, down, strange and charm quarks. The nonets of light mesons occupy the central planes.

²Two quark-anti-quark pairs would form a tetraquark. A meson and a baryon would form a pentaquark.

³Up, down and strange flavours.

⁴Groups of nine particles.

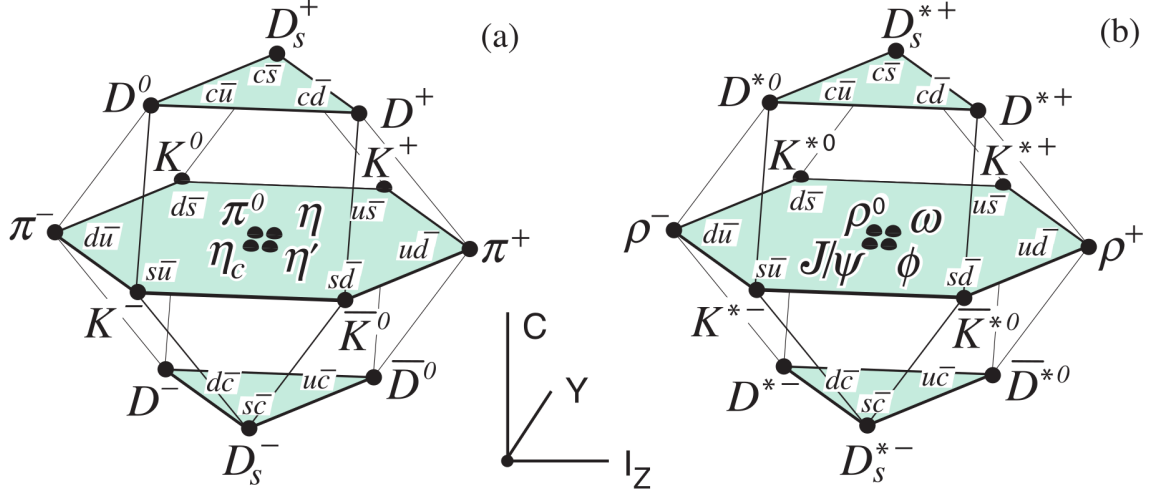


Figure 1.3: Diagram showing the 16-plets (SU(4) flavour symmetry) for the pseudo-scalar (a) and vector mesons (b) made of the up, down, strange, and charm quarks as a function of isospin I_z , charm C, and hypercharge ($Y = B + S - C$). The nonets of light mesons occupy the central planes to which the charm states have been added [5].

As mesons comprise the main focus of GlueX experiment and this thesis, we will focus on them. The allowed quantum numbers for a meson in the quark model can be deduced following few rules which we will discuss here. The quark-antiquark pair could have their spins aligned and adding up to ($S = 1$) or anti-aligned and canceling ($S = 0$). Assuming the orbital angular momentum between the two quarks to be L, the total angular momentum of the meson is $\vec{J} = \vec{L} + \vec{S}$. Such a meson would have parity $P = (-1)^{L+1}$. The charge parity of that system would be⁵ $C = (-1)^{L+S}$. Table 1.1 enumerates the different meson spin parity states which can be formed according to the quark model with only S and P waves ($l=0,1$).

1.3 Quantum Chromodynamics

Motivated by the success of QED, a gauge theory of the strong interaction, named Quantum Chromo-Dynamics (QCD), was formulated. As a gauge theory it introduced gluons as the massless mediating bosons of the strong force. However, as mentioned

⁵Flavoured mesons are not eigenstates of charge parity.

State	Name	Alignment (S)	Wave (L)	J^{PC}	Mesons
1S_0	pseudoscalar	anti-aligned (0)	S (0)	0^{-+}	$\pi \eta \eta' \kappa$
3S_1	vector	aligned (1)	S (0)	1^{--}	$\rho \omega \phi \kappa^*$
1P_1	pseudo-vector	anti-aligned (0)	P (1)	1^{+-}	$b_1 h_1 h'_1 \kappa_1$
3P_0	scalar	aligned (1)	P (1)	0^{++}	$a_0 f_0 f'_0 \kappa^*_0$
3P_1	axial-vector	aligned (1)	P (1)	1^{++}	$a_1 f_1 f'_1 \kappa_1$
3P_2	tensor	aligned (1)	P (1)	2^{++}	$a_2 f_2 f'_2 \kappa^*_2$

Table 1.1: Meson states that can be formed following the quark-antiquark model and considering only S and P waves (L=0,1).

earlier, gluons carry colour charges of their own. Unlike photons (the mediator of electroweak force), gluons can exchange gluons with other gluons, an effect termed "self interaction". These properties stemmed from the experimental fact that no isolated colour charge has ever been observed. This observation guided the formulation of the QCD Lagrangian. The coupling constant for strong interaction increases at the lower end of the energy scale (i.e. long distances). This means that the system becomes more and more bound as the colour charges are pulled away from each other, and decreases at the high end of the energy scale (i.e. short distances). This formulation lead to the "asymptotic freedom" ⁶ of colour charged particles inside a hadron and aligns with the restriction of all experimentally observed states to be colour neutral.

⁶Asymptotic freedom is the property of some gauge theories that result in particle interactions to become weaker as energy and length scales increase.

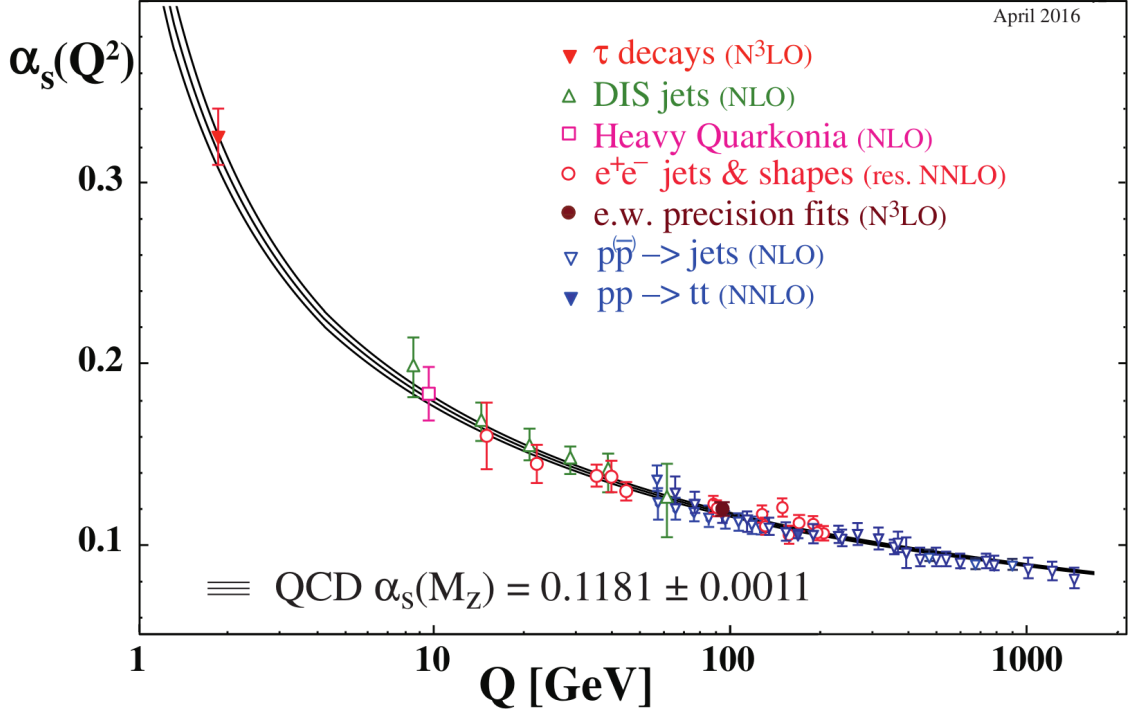


Figure 1.4: The strong coupling constant (α_s) measured as a function of the energy scale Q [5] (colour online).

Fig 1.4 represents the coupling strength of the strong interaction as a function of the energy scale. Therefore, a perturbative⁷ approach to theory where calculations are expanded in orders of the coupling constant is only possible at the high energy limit when the coupling constant is much less than unity⁸. Other methods must be employed at lower energies as the significance of each term increases with increasing powers of the coupling constant. A brief description of one of these methods, namely Lattice QCD (LQCD), will be given in the following section.

⁷Perturbation theory is a set of mathematical methods for finding an approximate solution to a problem, by starting from the exact solution of a related solvable problem. The total solution is found by adding a relatively small perturbation term to the exactly solvable problem.

⁸When the coupling constant is close to or larger than unity, truncating high order terms in the expansion is not possible.

1.3.1 LQCD

LQCD replaces continuous space-time with a discretized lattice, which translates into a discretized reciprocal momentum-energy space. This regularizes the theory by cutting off states not allowed by the lattice spacing. A shorter lattice spacing in space or time means more momentum-energy states are allowed and leads to a more precise prediction, at the expense of more computing power. Fig 1.5 presents the spectrum of isovector and isoscalar mesons as predicted by LQCD [6]. LQCD predicts several states which do not follow the simple quark model rules for J^{PC} . That is to say, they can not be formed by combining quarks and assuming that gluons do not play a role. Such states are called "exotic states".

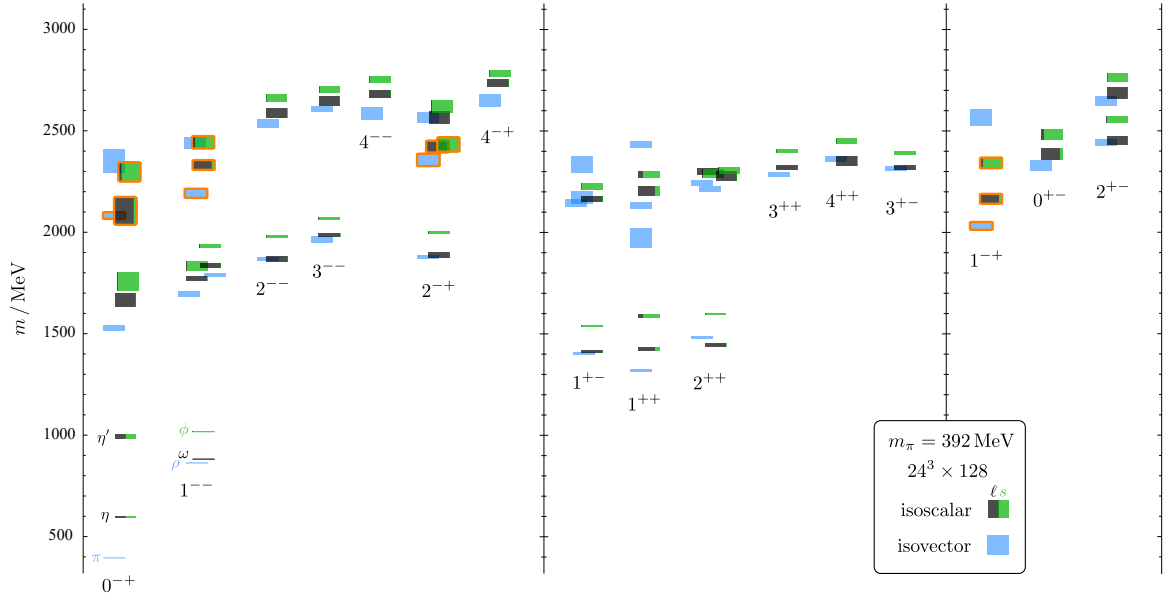


Figure 1.5: Isoscalar (green and black) and isovector (blue) spectrum as a function of mass, shown on the y-axis label. States are labeled J^{PC} . The quark mass is heavier than its "conventionally" assigned bound mass; leading to a pion mass $m_\pi=524$ MeV, much heavier than its physical mass. The vertical height of each box indicates the statistical uncertainty in the mass. Black and green indicate relative nonstrange and strange composition. Orange outlines interpreted as hybrid states. Note the exotic states in the three rightmost columns [6] (colour online).

1.3.2 Exotic States

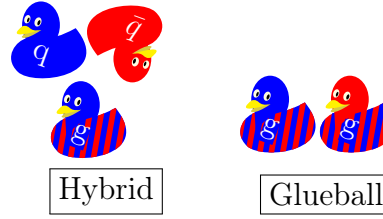


Figure 1.6: Hadrons which are not predicted by the simple quark model. Quarks are represented by solid colour rubber ducks with the letter (q), gluons are represented by striped rubber ducks with the letter (g) while antiquarks are represented by upside down rubber ducks with the letter (\bar{q}). From left to right, a quark antiquark pair in which a gluon contributes to the quantum numbers is called a hybrid, while a group of gluons forms a "glueball". Due to limitations of this representation, a gluon could carry a color-anti-color charge, yet there no direct way of representing this case (colour online).

Several states predicted by LQCD cannot be interpreted in the simple quark model: no combination of valence quarks would make up the quantum numbers of these states, as they require contributions from the gluons and/or sea quarks. Thus they serve as a confirmation on the incompleteness of the simple quark model. States comprised of a quark-antiquark pair with contributions from gluons are known as "hybrid" mesons. We only viewed predictions from LQCD calculations in the previous section. It is important to note that different models predict different quantum numbers. This is why identifying all mesons of the lightest hybrid multiplet (outlined in orange in Fig 1.5) must be measured and studied to decide which model predicts the meson spectra. Here we list few models along with their predictions (boldface represents exotic states):

- Flux-Tube Model: The gluonic field in a meson is a tube between the quark and antiquark. Hybrid mesons are described in terms of transverse oscillations of the tube [7].

$$(0, \mathbf{1}, 2)^{-+}, (\mathbf{0}, 1, \mathbf{2})^{+-}, 1^{--}, 1^{++}$$

- Bag Model: It confines quarks inside a cavity. Gluonic excitations correspond to gluonic field modes allowed by the boundary conditions on the cavity walls [8].

$(0, \mathbf{1}, 2)^{-+}, 1^{--}$

- Constituent Gluons Model: Predicts that gluons may have a dynamically generated mass. Light 0^{--} exotic is a prediction essentially unique to this model [9].

S-Wave $(0, \mathbf{1}, 2)^{++}, 1^{+-}$

P-Wave $\mathbf{0}^{--}, 1^{--}, 2^{--}, 3^{--}, 0^{-+}, \mathbf{1}^{-+}, 2^{-+}$

- Repulsive Three-Body ($q\bar{q}g$) Forces Model [10].

S-Wave $(0, \mathbf{1}, 2)^{-+}, 1^{+-}$

P-Wave $\mathbf{0}^{+-}, 1^{+-}, \mathbf{2}^{+-}, 3^{+-}, (0, \mathbf{1}, 2)^{++}$

A few predicted exotic states along with their predicted allowed decay modes and width are listed in table 1.2. As shown in the table, the b_1 meson is one of the daughters in the allowed decay modes of the lightest exotic multiplet π_1 and other exotic states (b_0 , h_0 , b_2 and h_2).

Name	J^{PC}	Total Width MeV		Allowed Decay Modes
		PSS	IKP	
π_1	1^{-+}	81 – 168	117	$b_1\pi, \pi\rho, \pi f_1, \pi\eta, \pi\eta', \eta a_1, \pi\eta(1295)$
η_1	1^{-+}	59 – 158	107	$\pi a_1, \pi a_2, \eta f_1, \eta f_2, \pi\pi(1300), \eta\eta', KK_1^A, KK_1^B$
η_1'	1^{-+}	95 – 216	172	$KK_1^B, KK_1^A, KK^*, \eta\eta'$
b_0	0^{+-}	247 – 429	665	$\pi\pi(1300), \pi h_1, \rho f_1, \eta b_1$
h_0	0^{+-}	59 – 262	94	$\pi b_1, \eta h_1, KK(1460)$
h_0'	0^{+-}	259 – 490	426	$KK(1460), KK_1^A, \eta h_1$
b_2	2^{+-}	5 – 11	248	$\pi a_1, \pi a_2, \pi h_1, \eta\rho, \eta b_1, \rho f_1$
h_2	2^{+-}	4 – 12	166	$\pi\rho, \pi b_1, \eta\omega, \omega b_1$
h_2'	2^{+-}	5 – 18	79	$KK_1^B, KK_1^A, KK_2^*, \eta h_1$

Table 1.2: A compilation of exotic quantum number hybrid approximate masses, widths, and decay predictions [11]. Masses are estimated from dynamical LQCD calculations with $m_\pi = 396$ MeV [12]. The PSS (Page, Swanson and Szczepaniak) and IKP (Isgur, Kokoski and Paton) model widths are from [13], with the IKP calculation based on the model in [14].

1.4 Exclusive b_1 Photoproduction

The search for exotic hybrid mesons with the GlueX detector will require a thorough understanding of the experimental apparatus. In order to reconstruct more complicated states, we need to show that we can measure basic photoproduction processes well. The decay of the exotic mesons $\pi_1(1600)$ ⁹, $\pi_1(2015)$ ¹⁰, $h_0(2400)$ ¹¹ and $b_2(2500)$ ¹² to $b_1\pi$ would be measured through the dominant decay $b_1 \rightarrow \omega\pi$. Thus, to precisely measure these states, the experiment needs to demonstrate that it is capable of measuring the b_1 meson. Also, a measurement of the D/S amplitude ratio is of interest to validate LQCD calculations [15]. Exclusive b_1 photoproduction is one of the more copious reactions at GlueX photon energies of 8.4-9.0 GeV. Properties of the b_1 meson are found in Table 1.3.

$b_1(1235)$	$I^G(J^{PC}) = 1^+(1^{+-})$
Mass	1229.5 ± 3.2 MeV (S = 1.6)
Width	142 ± 9 MeV (S = 1.2)
D/S Amplitude Ratio ($b_1(1235) \rightarrow \omega\pi$)	0.277 ± 0.027 (S = 2.4)
D/S Amplitude Phase Difference ($b_1(1235) \rightarrow \omega\pi$)	$10 \pm 5^\circ$
Decay Modes	Branching Fraction (Γ_i/Γ)
$\omega\pi$	dominant
$\pi^\pm\gamma$	$(1.6 \pm 0.4) \times 10^{-3}$
$\eta\rho$	seen
$\pi^+\pi^+\pi^-\pi^0$	$< 50\%$
$K^*(892)^\pm K^\mp$	seen
π^0	$< 8\%$
$K_S^0 K_L^0 \pi^\pm$	$< 6\%$
$K_S^0 K_S^0 \pi^\pm$	$< 2\%$
$\phi\pi$	$< 1.5\%$

Table 1.3: Properties of the $b_1(1235)$ meson [5].

⁹Observed by experiments E852, VES, COMPASS and CBAR.

¹⁰Observed by E852 experiment.

¹¹Predicted.

¹²Predicted.

1.4.1 History of the $b_1(1235) \rightarrow \omega\pi^0$

The $\omega\pi^0$ decay channel for the $b_1(1235)$ has been observed in several experiments using pion, anti-proton or photon beams on a proton target. The spin density matrix elements (SDMEs) and partial wave amplitudes (PWAs) depend on the production mechanism¹³. We will focus on the Omega-Photon [17] and SLAC-H-Photon [18] experiments as they are the only two experiments that observed the photoproduction of the b_1 , and as such are the most relevant ones for GlueX measurements. Also, photoproduction is predicted to have up to ten times higher yield for exotic mesons due to the vector nature of the photon [19]. Fig. 1.7 shows the invariant mass of the $\pi^+\pi^-\pi^0$ final state and the $\omega\pi^0$ as observed by the Omega-Photon and SLAC-H-Photon experiments. The GlueX Experiment has already collected significantly more statistics (factor of 400) than these early experiments. Such spectra, from our work will be shown in Chapter 6.

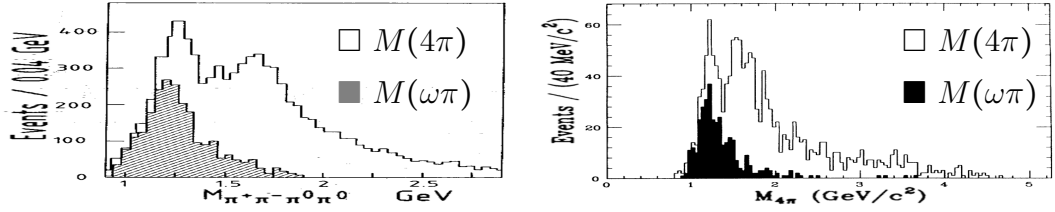


Figure 1.7: Invariant mass of $\pi^+\pi^-\pi^0$ and $\omega\pi^0$ from the Omega-Photon [17] (right) and SLAC-H-Photon experiments [18] (left).

1.4.2 Helicity frame of $\omega\pi^0$

The angular distribution of the $\omega\pi^0$ decay channel is analyzed in the helicity¹⁴ frame of the decaying particle. The use of helicity frame has advantages in this case [20]:

¹³Detailed explanation of SDMEs or PWAs will be presented in Section 1.4.3.

¹⁴Helicity is defined for a particle as the projection of its intrinsic spin onto the direction of its momentum.

1. It avoids the need to separate the total angular momentum J into orbital and spin parts which complicates the treatment of relativistic particles.
2. Helicity is invariant under rotations and so states can be constructed with definite J and helicity.
3. Helicity states are directly related to individual polarization properties of the particles and hence convenient for the polarization study over the conventional formalism of choosing a reference frame with a fixed quantization axis, say z -axis. In the conventional scheme, one has to shuttle back and forth between two representations, one in which the scattering or reaction is conveniently described and the other in which the states are labeled with individual spin components.

We are following the method used in past studies to describe the decay [17, 21]. Angles $\Omega = (\theta, \phi)$ describe the direction of the ω meson in the helicity frame of the $\omega\pi^0$ system. In order to define them, in the γp center-of-mass (C.M) system, we define \vec{z} as the unit vector along the $\omega\pi^0$ direction (as shown in Fig. 1.8), while \hat{k} (not shown in Fig. 1.8) is the unit vector in the beam γ direction. We define the x and y -axes of a right-handed coordinate system by the following two equations:

$$\vec{y} = \frac{\vec{k} \times \vec{z}}{|\vec{k} \times \vec{z}|} \quad (1.1)$$

$$\vec{x} = \vec{y} \times \vec{z} \quad (1.2)$$

Being in the γp CM frame, a Lorentz boost along the direction of the b_1 meson momentum (the \vec{z} axis), places us in the rest frame of the $\omega\pi^0$ system and we obtain $\vec{\omega}$, the momentum vector of the omega meson in the $\omega\pi^0$ system rest frame. The angles are then defined as:

$$\cos \theta = \frac{\vec{\omega} \cdot \vec{z}}{|\vec{\omega}|} \quad (1.3)$$

$$\phi = \tan^{-1} \left(\frac{\vec{\omega} \cdot \vec{y}}{\vec{\omega} \cdot \vec{x}} \right) \quad (1.4)$$

Next, the angles $\Omega_H = (\theta_H, \phi_H)$ describe the direction of the normal to the $\omega \rightarrow \pi^+ \pi^- \pi^0$ decay plane in the helicity frame of the ω . For these in the γp C.M. system, we define \vec{z}_H as the unit vector along the ω direction, which then yields the following:

$$\vec{y} = \frac{\vec{z} \times \vec{z}_H}{|\vec{z} \times \vec{z}_H|} \quad (1.5)$$

$$\vec{x}_H = \vec{y}_H \times \vec{z}_H \quad (1.6)$$

By a Lorentz transformation along the \vec{z}_H axis we obtain $\vec{\pi}_1$ and $\vec{\pi}_2$, the momentum vectors of the charged pions in the ω rest frame. The normal to the decay plane is then defined as:

$$\vec{n} = \frac{\vec{\pi}_1 \times \vec{\pi}_2}{|\vec{\pi}_1 \times \vec{\pi}_2|} \quad (1.7)$$

Finally, angles θ_H and ϕ_H are defined as:

$$\cos \theta_H = \vec{n} \cdot \vec{z}_H \quad (1.8)$$

$$\phi_H = \tan^{-1} \left(\frac{\vec{n} \cdot \vec{y}_H}{\vec{n} \cdot \vec{x}_H} \right) \quad (1.9)$$

Fig. 1.8 shows the definition of the four angles and the momentum vectors of all particles.

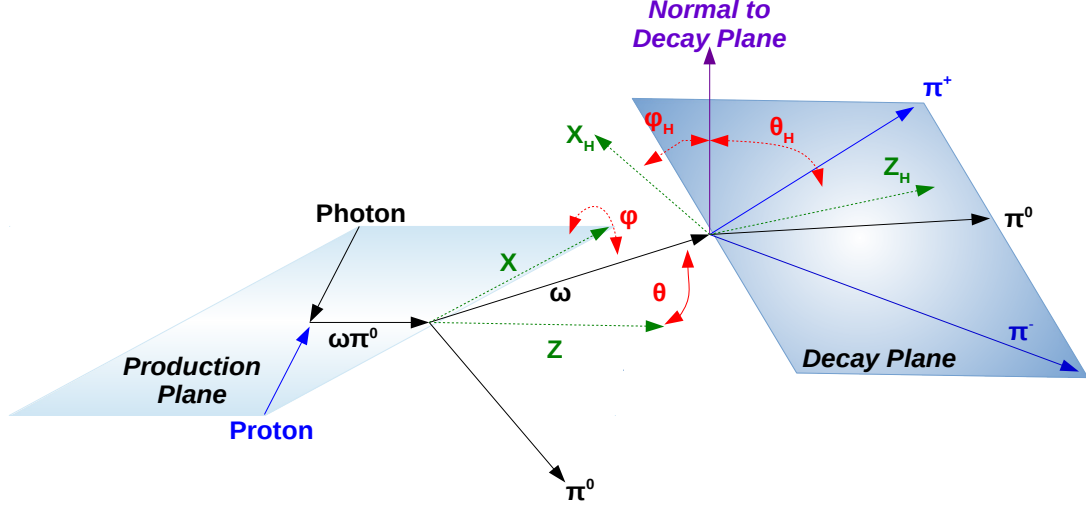


Figure 1.8: Helicity frame for the $\omega\pi^0$ decay channel. Angles (θ, ϕ) describe the ω meson in the b_1 meson helicity frame. Angles (θ_H, ϕ_H) describe the normal to decay plane (\hat{n}) in the ω meson helicity frame.

The production angle Φ is defined as the angle between the polarization vector $\vec{\epsilon}$ of the incident beam photon and the normal to the production plane formed by the recoil proton and the $\omega\pi^0$ resonance as shown in Fig. 1.9. Using the production angle, the polarization vector $\vec{\epsilon}$ of the incident photon can be defined with respect to the production plane as:

$$\epsilon = (\cos \Phi, \sin \Phi, 0) \quad (1.10)$$

The spin density matrix of the incident, partially linearly polarized beam photon is given by [17]:

$$\rho(\gamma) = 1/2 \begin{bmatrix} 1 & -P_\gamma e^{-2i\Phi} \\ -P_\gamma e^{2i\Phi} & 1 \end{bmatrix} \quad (1.11)$$

where $0 \leq P_\gamma \leq 1$ is the polarization fraction.

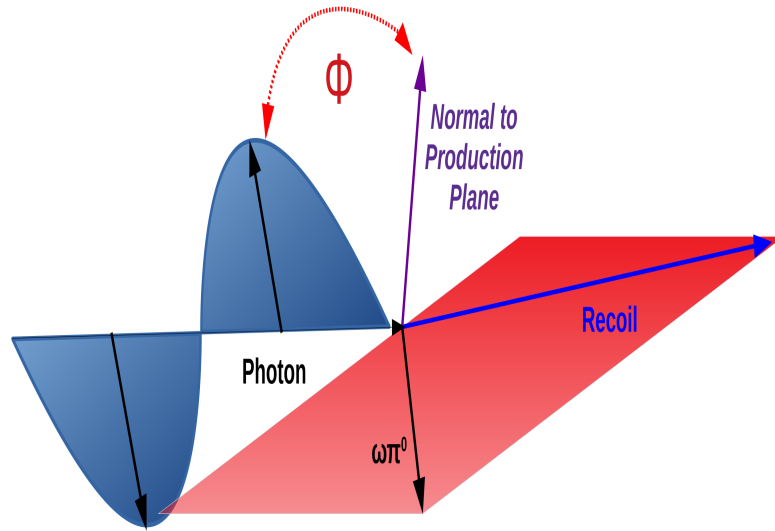


Figure 1.9: The production angle Φ is defined as the angle between the polarization vector $\vec{\epsilon}$ of the incident beam photon and the normal to the production plane formed by the recoil proton and the $\omega\pi^0$ resonance.

1.4.3 Angular Distribution

There are three main methods to analyze the angular distribution of a decay channel:

- A PWA analysis breaks down the decay channel to the contributing resonances as a function of their spin and parity quantum numbers through the application of a set of waves, allowing the identification of exotic meson resonances. A PWA analysis, involves technique for solving scattering problems by decomposing each quantum mechanical wave into its constituent angular momentum components

and solving using boundary conditions.

- An SDME-analysis quantifies the contributions of different reaction channels into the decay channel, providing a detailed description of the physics involved. SDMEs are an alternate way of expressing polarization observables of non-zero spin objects. The density matrix, ρ , represents the state (pure, mixed or both) of a particle with non-zero spin.
- An angular-moments (AMs) analysis projects the distribution on a set of spherical harmonics and describes the final distribution as an accumulation of these spherical harmonics with tuned contribution factors.

In the following sections, we will introduce the angular moments and the partial wave amplitudes analysis methods we are using in this thesis.

1.4.3.1 Angular Moments

The angular moments analysis method is the closest of the three to experimental data, as the expansion in spherical harmonics is done in a model-independent manner. In this method, the most general parameterization expression for the angular distribution of the $\omega\pi^0$ system is:

$$\frac{dN}{d\Omega d\Omega_H d\Phi} = \frac{N}{2\pi} [W_0(\Omega, \Omega_H) - PW_1(\Omega, \Omega_H) \cos 2\Phi - PW_2(\Omega, \Omega_H) \sin 2\Phi] \quad (1.12)$$

Where α is the quantum state defined by lmLM, where L is the total angular momentum of the $\omega\pi^0$ system and M is its z-component, l and m are the total angular momentum and z component of the quantum state basis on which the $\omega\pi^0$ state is projected [22]; $\frac{N}{2\pi}$ is an overall normalization factor, P is the mean polarization of the beam, Φ is the angle between the polarization vector of the photon and the

production plane. Each of the decay distributions $W_k(\Omega, \Omega_H)$ can be expanded in terms of orthogonal moments $H_\alpha^\pm(\Omega, \Omega_H)$:

$$W_k(\Omega, \Omega_H) = \sum_{\alpha, \pm} \frac{H_s^{k, \pm}(\alpha) H_\alpha^\pm(\Omega, \Omega_H)}{C_\alpha} \quad (1.13)$$

$$\iint H_\alpha^\pm(\Omega, \Omega_H) H_\beta^\pm(\Omega, \Omega_H) d\Omega d\Omega_H = \delta_{\alpha, \beta} C_\alpha \quad (1.14)$$

$$H_s^{k, \pm}(\alpha) = \iint W_k(\Omega, \Omega_H) H_\alpha^\pm(\Omega, \Omega_H) d\Omega d\Omega_H \quad (1.15)$$

The orthogonality of $\cos 2\Phi$ and $\sin 2\Phi$ functions over the interval $(0 < \Phi < 2\pi)$, allows us to define an extended set of orthogonal moments $H_\alpha^{k, \pm}(\Omega, \Omega_H, \Phi)$ as [17]:

$$\begin{aligned} H_\alpha^{0, \pm}(\Omega, \Omega_H, \Phi) &= H_\alpha^\pm(\Omega, \Omega_H) \\ H_\alpha^{1, \pm}(\Omega, \Omega_H, \Phi) &= \sqrt{2} \cos 2\Phi H_\alpha^\pm(\Omega, \Omega_H) \\ H_\alpha^{2, \pm}(\Omega, \Omega_H, \Phi) &= \sqrt{2} \sin 2\Phi H_\alpha^\pm(\Omega, \Omega_H) \end{aligned} \quad (1.16)$$

These moments can be expanded in terms of the contributions from different spin-parity states $J_i^{\eta_i}$ and their interferences [17].

$$\begin{aligned} H_s^+(\alpha) &= \sum_i \text{Re}\{H_{ii}(\alpha)\} \\ H_s^-(\alpha) &= 2 \sum_{i>j} \text{Re}\{H_{ij}(\alpha)\}, \quad \eta_i \eta_j = -1 \end{aligned} \quad (1.17)$$

These sums can be expressed in terms of the production density matrix $\rho_{\Lambda\Lambda'}^{ij}$ ¹⁵ and the decay amplitudes F_λ^i [17]:

¹⁵The production density matrix $\rho_{\Lambda\Lambda'}^{ij}$, reduces to the spin-density matrix $\rho_{\Lambda\Lambda'}$ for $i = j$ [21].

$$\begin{aligned}
H_{ij}(\alpha) &= t_{LM}^{ij*} f_{LM}^{ij} \langle 10l0|10 \rangle \\
\text{where } t_{LM}^{ij*} &= \left(\frac{2J_j+1}{2J_i+1}\right)^{1/2} \sum_{\Lambda\Lambda'} \rho_{\Lambda\Lambda'}^{ij} \langle J_j\Lambda'LM|J_i\Lambda \rangle \\
\text{and } f_{LM}^{ij} &= \sum_{\lambda\lambda'} F_{\lambda}^i F_{\lambda'}^{j*} \langle J_j\lambda'LM|J_i\lambda \rangle \langle 1\lambda'lm|1\lambda \rangle
\end{aligned} \tag{1.18}$$

t_{LM}^{ij*} is the generalized multipole parameter which depends entirely on the production of the $\omega\pi$ system. f_{LM}^{ij} describes the decay of the $\omega\pi$ system into two-particle states of $\omega + \pi$. The Clebsch-Gordan coefficient $\langle 10l0|10 \rangle$ describes the decay of the ω into three pions. Parity conservation in the production and decay of the $\omega\pi$ system requires [17]:

$$\begin{aligned}
\rho_{\Lambda\Lambda'}^{ij} &= \eta_i \eta_j (-1)^{J_i-J_j} (-1)^{\Lambda-\Lambda'} \rho_{-\Lambda-\Lambda'}^{ij} \\
\text{and } F_{\lambda}^i &= \eta_i (-1)^{J_i-1} F_{-\lambda}^i
\end{aligned} \tag{1.19}$$

while time reversal invariance, for a fixed spin parity state requires that $F_{\lambda}^i F_{\lambda'}^{i*}$ is real. Thus, the decay helicity amplitudes F_{λ}^i can be expanded in terms of the PWAs C_l^i :

$$F_{\lambda}^i = \sum_l \left(\frac{2l+1}{2J_i+1}\right)^{1/2} \langle J_i\lambda|l01\lambda \rangle C_l^i, \text{ and } \sum_l (C_l^i)^2 = 1 \tag{1.20}$$

The orthogonal functions $H_{\alpha}^{\pm}(\Omega, \Omega_H)$ are defined in terms of Wigner D-functions¹⁶.

¹⁶Moments $H_{\alpha}^{\pm}(\Omega, \Omega_H)$ are the experimental averages of the product of two Wigner D-functions [22]

$$H_{\alpha}^{\pm}(\Omega, \Omega_H) = 1/2 \operatorname{Re}\{D_{Mm}^L(\theta, \phi, 0)D_{m0}^l(\theta_H, \phi_H, 0) \pm (-1)^{L+M}D_{Mm}^L(\theta, \phi, 0)D_{m0}^l(\theta_H, \phi_H, 0)\} \quad (1.21)$$

$$C_{\alpha} = \iint [H_{\alpha}^{\pm}(\Omega, \Omega_H)]^2 d\Omega d\Omega_H = \frac{(4\pi)^2}{(2l+1)(2L+1)(2-\delta_{m0})(2-\delta_{M0})} \quad (1.22)$$

The unpolarized production density matrix can be parameterized as

$$\rho_{\Lambda\Lambda'}^{\alpha\beta} = f_{\Lambda}^{\alpha}f_{\Lambda'}^{\beta*} + \eta_{\alpha}\eta_{\beta}(-1)^{J_{\alpha}-J_{\beta}}(-1)^{\Lambda-\Lambda'}f_{-\Lambda}^{\alpha}f_{-\Lambda'}^{\beta*} \quad (1.23)$$

where η_{α} , Λ and J_{α} are the parity, helicity and spin of state α , respectively. For $J = 1$ states, the complex amplitudes f_{Λ}^{α} are defined by five real numbers, denoted by the angles $\theta_{\alpha}, \Psi_{\alpha}, \phi_0, \phi_+, \phi_-$.

$$\begin{aligned} f_0^{\alpha} &= \frac{\cos \theta_{\alpha}}{\sqrt{2}} e^{i\phi_0^{\alpha}}, \quad \pi/2 \geq \theta_{\alpha} \geq 0 \\ f_+^{\alpha} &= \frac{\sin \theta_{\alpha}}{\sqrt{2}} \cos \psi_{\alpha} e^{i\phi_+^{\alpha}}, \quad 2\pi > \phi_{\Lambda}^{\alpha} \geq 0 \\ f_-^{\alpha} &= \frac{\sin \theta_{\alpha}}{\sqrt{2}} \sin \psi_{\alpha} e^{i\phi_-^{\alpha}}, \quad 2\pi \geq \Psi_{\alpha} \geq 0 \end{aligned} \quad (1.24)$$

These five angles are assumed to be independent of the $M_{\omega\pi^0}$, so that the density matrix elements themselves are independent of $M_{\omega\pi^0}$, and satisfy

$$\begin{aligned}
\rho_{\Lambda\Lambda'}^{\alpha\beta} &= \eta_\alpha \eta_\beta (-1)^{J_\alpha - J_\beta} (-1)^{\Lambda - \Lambda'} \rho_{-\Lambda - \Lambda'}^{\alpha\beta} \\
\rho_{\Lambda\Lambda'}^{\alpha\beta} &= \rho_{\Lambda'\Lambda}^{\beta\alpha*} \\
\sum_{\Lambda} \rho_{\Lambda\Lambda}^{\alpha\alpha} &= 1 \\
|\rho_{\Lambda\Lambda'}^{\alpha\beta}| &\leq (|\rho_{\Lambda\Lambda}^{\alpha\alpha}| \cdot |\rho_{\Lambda'\Lambda'}^{\beta\beta}|)^{1/2}
\end{aligned} \tag{1.25}$$

Since the density matrix is unchanged by the transformation $\phi_\Lambda^\alpha \rightarrow \phi_\Lambda^\alpha + \delta$, we must fix one of these angles, and have chosen to fix ϕ_0^{1+} .

The decay amplitudes are parameterized as a function of mass in terms of a resonant Breit-Wigner amplitude $D_\alpha(m)$, and a coupling (normalization) constant G_α . The decay amplitudes can be expanded using the real PWAs C_l^α :

$$F_\lambda^\alpha(m) = D_\alpha(m) G_\alpha \sum_l \left(\frac{2l+1}{2J_\alpha+1} \right)^{1/2} \langle J_\alpha \lambda | l 0 1 \lambda \rangle C_l^\alpha \frac{B_l(m)}{B_l(m_\alpha)} \tag{1.26}$$

where $B_l(m, R)$ are barrier penetration factors, $C_l = 0$ for $J^P = 1^-, 0^-$, $C_l = 1$ for $J^P = 1^+$, $C_2/C_0 = D/S$. The parameterization of the Breit-Wigner amplitudes are:

$$\begin{aligned}
D_\alpha(m) &= \frac{m_\alpha \Gamma_\alpha}{(m^2 - m_\alpha^2) - i m_\alpha \Gamma_\alpha(m)} \\
\Gamma_\alpha(m) &= \Gamma_\alpha \left(\frac{q}{q_\alpha} \right) \left[\frac{B_l(m)}{B_l(m_\alpha)} \right]^2
\end{aligned} \tag{1.27}$$

where q is the ω momentum in the C.M. of the $\omega\pi$ system with total mass m . This projection of the angular distribution into moments was implemented in the analysis algorithm and used to fit the data to obtain the five angles corresponding to each quantum state J^P . These fitted values were then used in the simulation to create the Monte-Carlo sample used to study the acceptance, as will be detailed in Chapter 5.

1.4.3.2 Partial Wave Amplitudes

The PWA analysis model we are using in this thesis was provided through private communications with members of the Joint Physics Analysis Center (JPAC). This model can be used to analyze the angular distribution of the $\omega\pi^0$ system in the helicity frame. In this model the intensity of the $\omega\pi^0$ final state can be expressed as

$$I = N \sum_{\lambda'_\gamma, \lambda_\gamma} A_{\lambda'_\gamma}^* \rho_{\lambda'_\gamma, \lambda_\gamma}^\gamma(\Phi) A_{\lambda_\gamma} \quad (1.28)$$

where N is the number of events, $\rho_{\lambda'_\gamma, \lambda_\gamma}^\gamma(\Phi)$ is the spin density matrix of the beam photon with a production angle Φ (as presented in Eq. 1.11) and A_{λ_γ} is the amplitude for beam photon helicity λ_γ . The four terms corresponding to the beam photon spin density matrix elements $(\lambda'_\gamma, \lambda_\gamma) = (-, -), (-, +), (+, -), (+, +)$ are rewritten as the sum of two terms as follows

$$I = \frac{1}{2}(1 - P_\gamma) |e^{i\Phi} A_+ + e^{-i\Phi} A_-|^2 + \frac{1}{2}(1 + P_\gamma) |e^{i\Phi} A_+ - e^{-i\Phi} A_-|^2$$

where P_γ is the beam polarization fraction and A_{λ_γ} is calculated as

$$A_{\lambda_\gamma} = \sum_{J_i=0,1,2}^{\omega\pi \text{ Spin}} \sum_{\eta_i=-1,+1}^{\omega\pi \text{ Parity}} \sum_{\Lambda=-J_i \dots J_i}^{\omega\pi \text{ Spin Proj.}} V_{\lambda_\gamma, \Lambda}^i \sum_{\lambda=-1,0,+1}^{\omega \text{ Helicity}} D_{\Lambda, \lambda}^{J_i}(\Omega) F_\lambda^i D_{\lambda, 0}^1(\Omega_H) G \quad (1.29)$$

where $V_{\lambda_\gamma, \Lambda}^i$ are complex vertices describing the probability of a beam photon with helicity λ_γ to produce an $\omega\pi^0$ spin parity system i with a spin projection Λ , $D_{\Lambda, \lambda}^{J_i}(\Omega)$ and $D_{\lambda, 0}^1(\Omega_H)$ are Wigner-D functions of the decay angles Ω and Ω_H in the helicity frame (as detailed in Sec. 1.4.2). G is the Dalitz function of the $\omega \rightarrow \pi^+\pi^-\pi^0$ decay and F_λ^i is the decay amplitude of an ω with helicity λ from an $\omega\pi^0$ spin-parity state i and is expanded in terms of the partial waves amplitudes C_l^i as

$$F_{\lambda}^i = \sum_{l=0,1,2}^{Partial\ Waves} \langle J_i \lambda | l 0, 1 \lambda \rangle C_l^i \quad (1.30)$$

The Dalitz function of the ω decay G is parameterized in powers of Z and Sin(3 θ)

$$G(Z, \theta) = \sqrt{1 + 2\alpha Z + 2\beta Z^{3/2} \sin(3\theta) + 2\gamma Z^2 + 2\delta Z^{5/2} \sin(3\theta)} \quad (1.31)$$

where α , β , γ and δ are fit parameters, $Z = \sqrt{x^2 + y^2}$, $\theta = \frac{y}{\sqrt{Z}}$ and The Dalitz plot axes are rotated by using the parameterization

$$x = \frac{\sqrt{3}(t - u)}{2M(M - 3m_{\pi})}, \quad y = \frac{3(s_c - s)}{2M(M - 3m_{\pi})} \quad (1.32)$$

where $s_c = \frac{1}{3}(M^2 + 3m_{\pi}^2)$ and the Mandelstam variables of the ω decay are defined as

$$s = (\omega - p^0)^2, \quad t = (\omega - p^-)^2, \quad u = (\omega - p^+)^2 \quad (1.33)$$

where ω , p^+ , p^- and p^0 are the energy-momentum four vectors of the ω and its daughters.

In this model the fitting parameters are the vertices $V_{\lambda_{\gamma}, \Lambda}^i$, the partial waves amplitudes C_l^i , the beam polarization fraction P_{γ} and the Dalitz function parameters α , β , γ and δ .

The vertices are governed by the symmetry $V_{\lambda_{\gamma}, \Lambda}^i = -\tau_e \tau_i (-1)^{\Lambda} V_{-\lambda_{\gamma}, -\Lambda}^i$. Where $\tau_i = \eta_i (-1)^{J_i}$ is the naturality of the $\omega \pi^0$ state, and τ_e is the naturality of the exchange (assumed to be +1). While the partial waves amplitudes vanish ($C_l^i = 0$) for odd l when $\eta_i = +1$, and for even l when $\eta_i = -1$.

1.4.4 s-Channel Helicity Conservation

The most general form for the Φ distribution is

$$I(\Phi) = \frac{2}{\pi} [1 + a \cos(2\Phi) + b \sin(2\Phi)] \quad (1.34)$$

and it follows from parity conservation [23] that $b = 0$. By imposing this constraint and fitting the distribution of Φ for a , and comparing that to flat distribution which is a necessary condition of s-channel helicity conservation [23], we can test the conservation of the helicity in the s-channel. Details are given in work done by the Omega-Photon collaboration [17].

1.4.5 Helicity Amplitudes of the ω

The angular distribution of $\cos(\theta_H)$ depends only on the decay properties of a given spin-parity state and not on the details of its production [18]. This offers a direct measurement of the contribution of each helicity amplitude by fitting the distribution using the function

$$\frac{dN}{d\cos(\theta_H)} = \frac{3N}{2} (|F_0|^2 \cos^2 \theta_H + |F_1|^2 \sin^2 \theta_H) \quad (1.35)$$

where F_λ is the decay amplitude for an ω of helicity λ (as shown in Eq. 1.20 and Eq. 1.30), N is the number of events and unitarity requires that $|F_0|^2 + 2|F_1|^2 = 1$. This means that for a pure $J^P = 1^\pm$ state we would have $|F_1|^2 = 0.5$ and $|F_0|^2 = 0$. For the b_1 meson with $D/S = 0.26$, we expected $|F_1|^2 = 0.437 \pm 0.012$ [18].

1.5 Summary

In this chapter we presented an overview of the theoretical framework for hadron spectroscopy through quark model, QCD and LQCD introducing exotic states. Then a brief synopsis of the $b_1(1235) \rightarrow \omega\pi^0$ channel as a potential gateway to the lightest exotic multiplet π_1 . Consequently, we presented the significance of the D/S ratio as a test for recent LQCD calculations. We discussed two methods to analyse the angular distribution of the $\omega\pi^0$ final state based on angular moments and partial waves amplitudes. We also demonstrated a test for s-channel helicity conservation in the $b_1(1235)$ photoproduction and presented a method to extract the helicity amplitudes of the ω based on the angular distribution.

Chapter 2

The GlueX Experiment

The GlueX experiment is housed in Hall D, which was built as part of the 12 GeV upgrade [24] to the Continuous Electron Beam Accelerator Facility (CEBAF) at (JLab) in Newport News, Virginia, USA. A schematic of the upgrade project is shown in Fig 2.1. The race-track-design accelerator in JLab can deliver a high-frequency beam of electron pulses to all four experimental halls simultaneously. The beam electrons are electrons accelerated through superconducting electromagnetic cavities up to 12 GeV. Before entering Hall D, the electron beam is scattered off a diamond-radiator producing a linearly polarized photon beam, which then enters the hall hitting the LH_2 target. A brief summary of the beam line and GlueX experiment detectors is presented in the following sections.

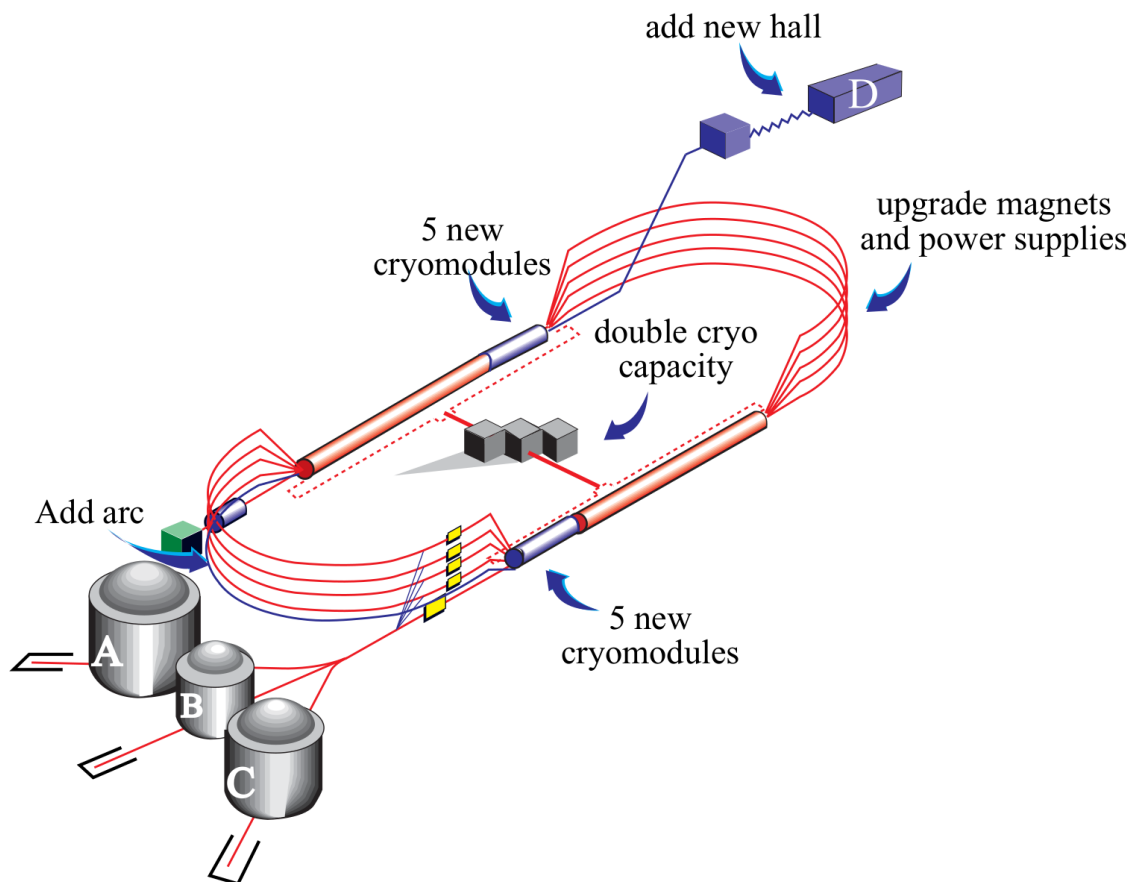


Figure 2.1: An overview of the 12 GeV upgrade of the CEBAF accelerator [24].

The GlueX experimental setup is designed to detect and identify both neutral and charged particles with almost full 4π solid angle coverage; and this along with photon tagging allows exclusive reconstruction of events. The nearly hermetic detector design is essential for PWA analysis, which is a comprehensive deconvolution of reaction amplitudes and angular distributions required to definitely associate those with the quantum numbers of the exchanged particles.

The experimental setup in Hall D and this chapter can be divided into four main sectors: beamline instrumentation, calorimetry, particle identification, and charged particle tracking. A schematic overview of the key beamline and detector elements is shown in Fig 2.2.

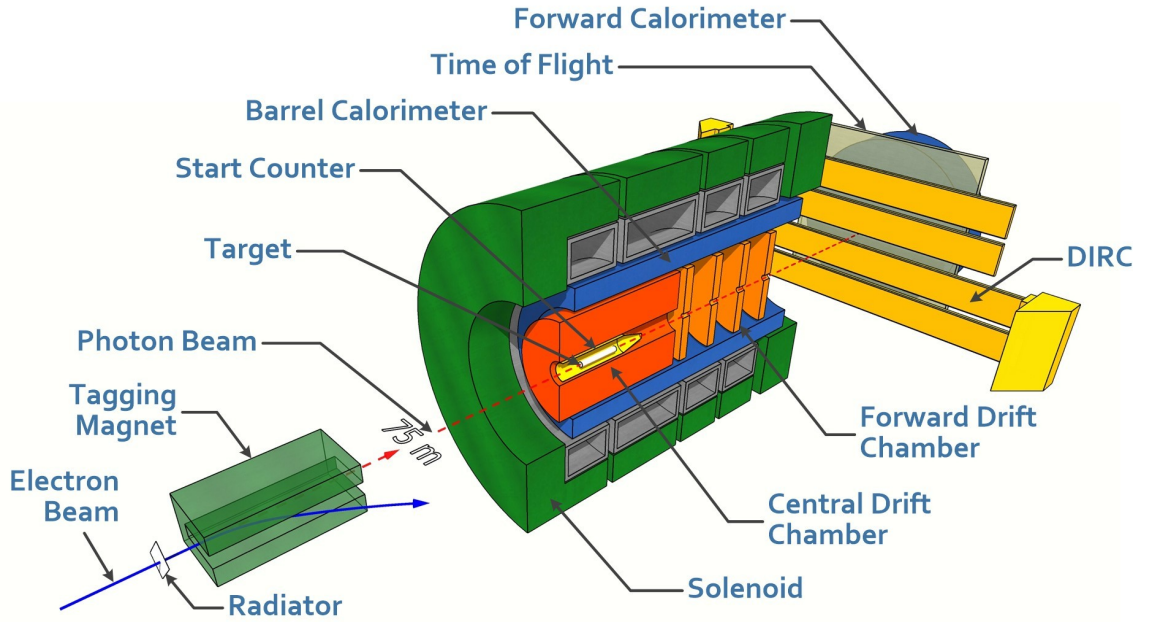


Figure 2.2: An illustration of the GlueX experimental setup [25].

2.1 Photon Beamline

CEBAF delivers 250 million electron pulses to the Hall D tagger every second. In the tagger hall, the electron beam passes through a diamond-radiator¹ emitting coherent bremsstrahlung photons where the incident electron interacts with the Coulomb field surrounding the nuclei in the diamond-radiator and produces high-energy photons. The photons produced are coherent because the lattice structure of the diamond produces an interference between the emitted photons, amplifying photons with discrete energies corresponding to the lattice structure and suppressing others [26]. The orientation of the diamond is adjusted further to enhance the lowest-energy photon peak in the spectra². The bremsstrahlung photons emitted are partially linearly polarized. The direction of the linear polarization can be controlled by rotating the crystal [27]. Linear polarization parallel to the floor are referred to as PARA (0°) and perpendicular to the floor as PERP (90°). Two more polarization orientations were introduced in spring 2017, namely the PARA II (135°)³ and PERP II (45°).

The coherent component of the photon beam is predominantly along the beam direction at small angles ($< 25 \mu\text{rad}$) while the incoherent component of the photon beam has a broader angular distribution. The coherent component of the radiation peaks at an energy dependent on the orientation of the diamond-radiator crystal plane relative to the electron beam. As the emitted photon beam enters the collimator cave, a 3.4 mm or 5.0 mm diameter tungsten collimator allows only photons with small angles relative to the electron beam to pass through, therefore, enhancing the coherent component of the beam entering the experimental hall. Simulations of the tagged photon beam are presented in Fig. 2.3. Note that the principal peak of interest lies between 8 and 9 GeV, with secondary peaks appearing higher in energy.

¹A thin film window is milled by UV laser ablation in an artificially grown single crystal diamond.

²As shown in Fig 2.8.

³The collaboration now calls 135° orientation as -45°.

Those correspond to different lattice vectors in the diamond-radiator.

The instruments in the beamline measure the energy, polarization and flux of the incoming photon beam. These variables are measured by three detectors: the photon tagger, triplet polarimeter, and pair spectrometer, which are explained below.

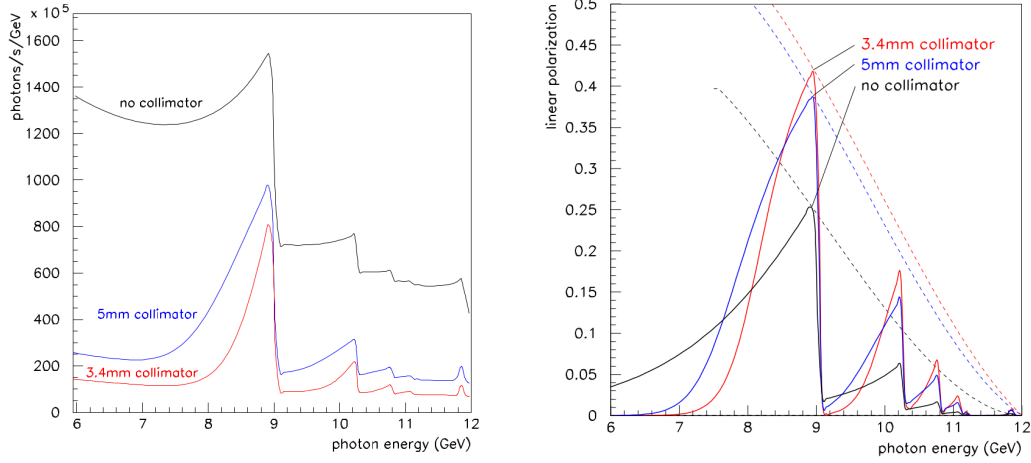


Figure 2.3: These plots show the enhancement of collimation on the distribution of the energy and the polarization fraction of the beam. These are simulated for a $15 \mu\text{m}$ thick diamond-radiator with a $1 \mu\text{A}$ electron beam current [28] (colour online).

2.1.1 Photon Tagger

Most of the electrons in a beam pulse pass through the diamond-radiator without interacting. These electrons are then deflected to the electron beam dump by the 1.5 T field of the tagger dipole magnet. If an electron interacts with the radiator and loses more than 25% of its energy, the same magnetic field bends it into one of the scintillator counters at the focal plane of the tagger. The Hall D tagger system is divided into two detectors:

1. The tagger microscope (TAGM) which covers the energy range from 8.1-9.1 GeV with high energy resolution of 0.1% (8-9 MeV) over the coherent peak region.

2. The tagger hodoscope (TAGH) which covers the rest of the energy range from 3-12 GeV with high energy resolution of 30 MeV [29].

An illustration of the tagger system is shown in Fig 2.4 [30].

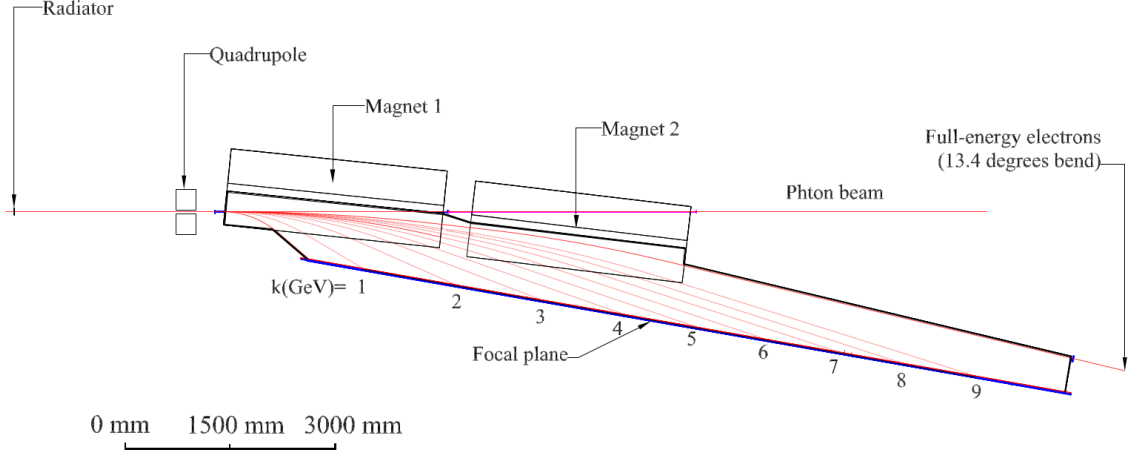


Figure 2.4: An illustration of the Hall D tagger. Electrons passing through the diamond-radiator are deflected by the magnetic field into the electron beam dump (for full energy electrons) or onto one of the scintillator counters on the focal plane [29].

2.1.2 Triplet Polarimeter

In Hall D, the polarization fraction of the photon beam is measured by measuring the angular distribution of triplet photoproduction on a nuclear target. In triplet production, the photon interacts with one of the electrons of the atom: the reaction is represented by $\gamma e^- \rightarrow e^- e^+ e^-$. The angular distribution of the recoil electron encodes information about the polarization of the incident photon. The cross section for the triplet photoproduction is given by

$$\sigma_t(\phi) = \sigma_0[1 + P\Sigma\cos(2\phi)] \quad (2.1)$$

where σ_0 is the unpolarized cross section, P is the degree of polarization of the photon beam, ϕ is the azimuthal angle of the recoil electron with respect to the polarization plane of the photon, and Σ is the beam asymmetry for the triplet photoproduction,

which can be calculated through perturbative QED methods and is determined to be about 0.2 [31]. In order to extract the beam polarization, the cross section needs to be measured as a function of the azimuthal angle ϕ .

The Triplet Polarimeter (TPOL) is a flat, doughnut-shaped silicon strip detector broken into 32 azimuthal segments and measures the angle and energy of the recoil electron and is triggered by the coincident e^+e^- pair in the Pair Spectrometer (see Subsection 2.1.3). The triplet polarimeter target is a 75 μm beryllium foil. The TPOL system is placed in the photon beamline downstream of the collimator and upstream of the pair spectrometer. The entire device is operated under vacuum. Fig 2.5 shows the interior of the TPOL vacuum enclosure. A plot showing the polarization fraction of the photon beam as measured by the triplet polarimeter is shown in Fig 2.6.



Figure 2.5: A picture of the triplet polarimeter detector. The beam enters from the right, some of the photons interact with electrons in the beryllium foil, and the beam proceeds into the experimental hall. The silicon strip detector (the doughnut-shape in the middle right of the photo) detects the recoil electron while the e^+e^- pair is detected by the Pair Spectrometer.

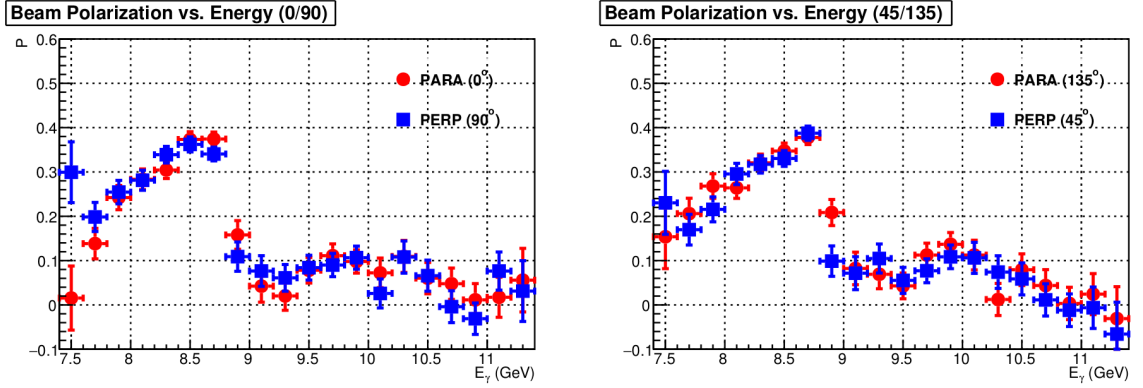


Figure 2.6: Plot showing the polarization fraction of the photon beam as a function of energy, as measured by the triplet polarimeter for two polarization orientations PARA (0° , parallel to the floor), PERP (90° , perpendicular to the floor) on the right and PARA (135°), PERP (45°) on the left, with data points offset horizontally by 0.015 GeV for clarity [32].

2.1.3 Pair Spectrometer

As mentioned in the previous section, the Pair Spectrometer (PS) detects e^+e^- pairs produced from the triplet photoproduction reaction between the beam photons and the TPOL target. In doing that, it measures the flux of the incoming photon beam as a function of energy and acts as a trigger for the TPOL measurement. The pair spectrometer consists of a set of scintillating detectors that determine the energy of the e^+ and e^- . A dipole magnet with 1.8 T field deflects the particles in opposite directions based on their charge and the pair spectrometer measures the amount of deflection experienced in the dipole by the particles and therefore their energies. An illustration of the pair spectrometer detector is shown in Fig 2.7. An example plot of the energy spectrum measured by the PS is shown in Fig 2.8 [33].

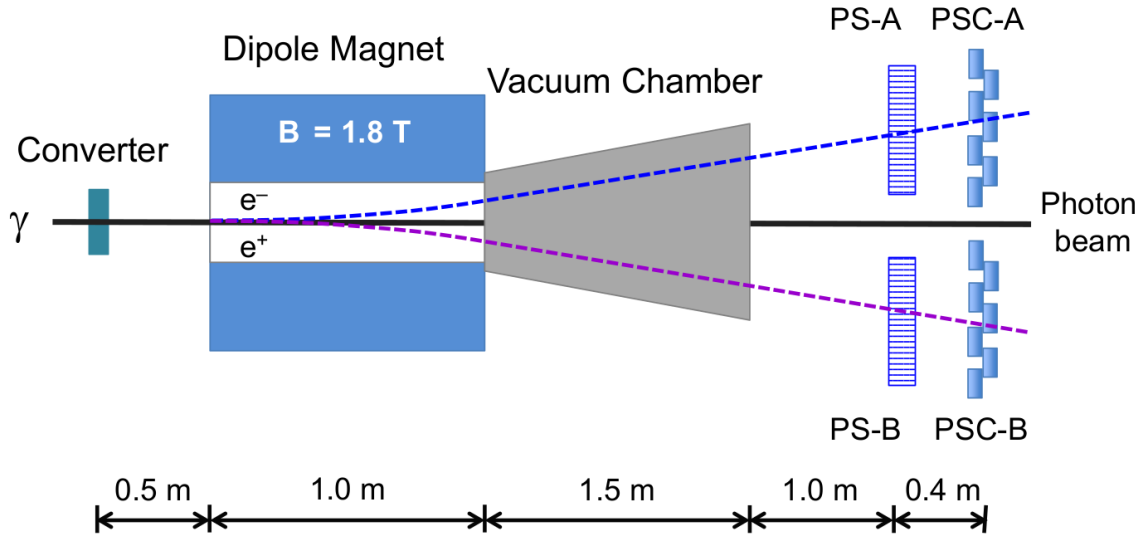


Figure 2.7: An illustration of the PS detector. The beam enters from triplet polarimeter on the left. The dipole magnet deflects the e^+ and e^- to opposite directions where an array of scintillating detectors measure the deflection and therefore the energy of the particles [34].

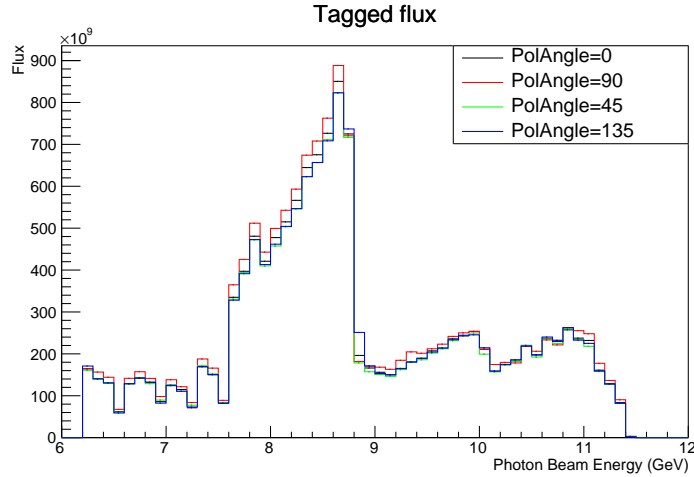


Figure 2.8: Photon beam flux as a function of energy as measured by the PS in coincidence with a TAGH or TAGM hit for the four beam polarization orientations (PARA 0° , PERP 90° , PARA 135° and PERP 45°). The coherent peak of the lowest photon energy can be seen around 8-9 GeV while other coherent photon peaks, corresponding to different lattice vectors in the diamond-radiator, can be seen on the higher energy side [33] (colour online).

2.2 Liquid Hydrogen Target

Downstream of the PS lies the GlueX detector, situated in the Hall D experimental hall. The beam enters the detector and interacts with the LH_2 target first. The target cell is 30 cm long and has a conical shape. The diameter decreases from 2.42 cm on the upstream end to 1.56 cm on the downstream end. The cell is filled with LH_2 and kept at a temperature of $\sim 20^\circ$ K. The target cell is surrounded by a support structure of ROHACELL [®] and the Start Counter (ST). This assembly is inserted into the centre of the Central Drift Chamber. An illustration of the target cell is shown in Fig 2.9 [34].

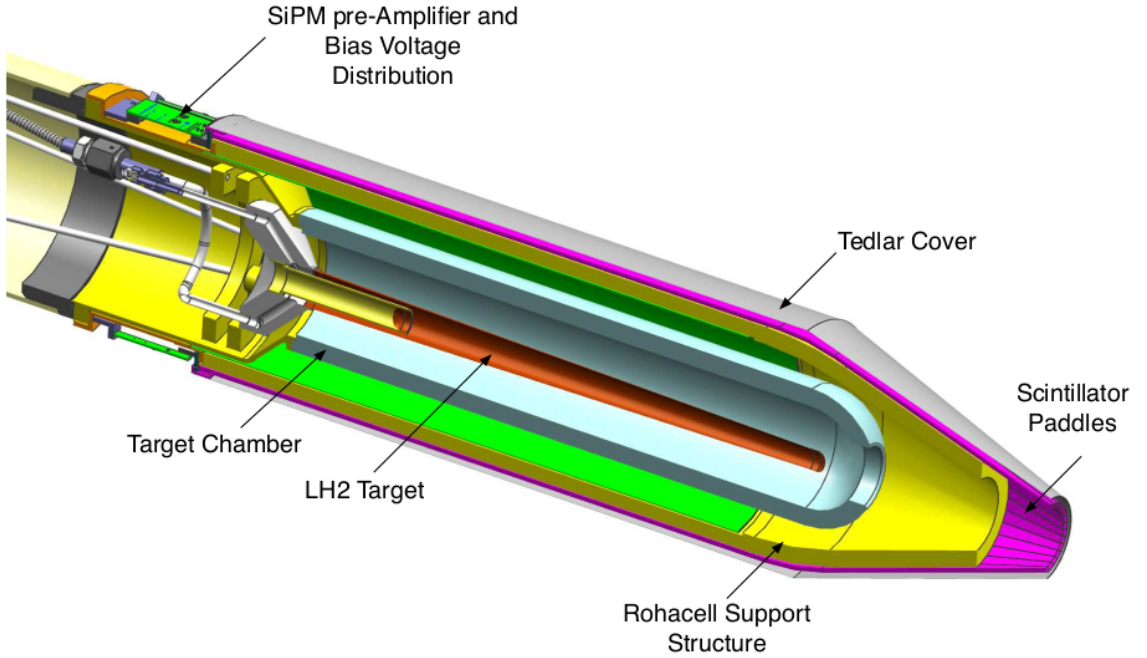


Figure 2.9: The liquid hydrogen target cell for the GlueX experiment. Beam enters from the left of the image. The target cell is surrounded by a ROHACELL support structure and the ST [34].

2.3 Charged Particle Tracking

The almost hermetic charged particle tracking is one of the primary capabilities of the GlueX detector. Two detectors are employed to achieve that, namely the Central Drift Chamber (CDC), which is a straw-tube cylindrical chamber, and the Forward Drift Chamber (FDC), which is a cathode-strip chamber. The CDC covers polar angles between 6° and 168° while the FDC covers polar angles below 20° . Fig 2.10 shows the entire layout of the GlueX detector, including the tracking detectors. The following sections discuss these detectors in more detail.

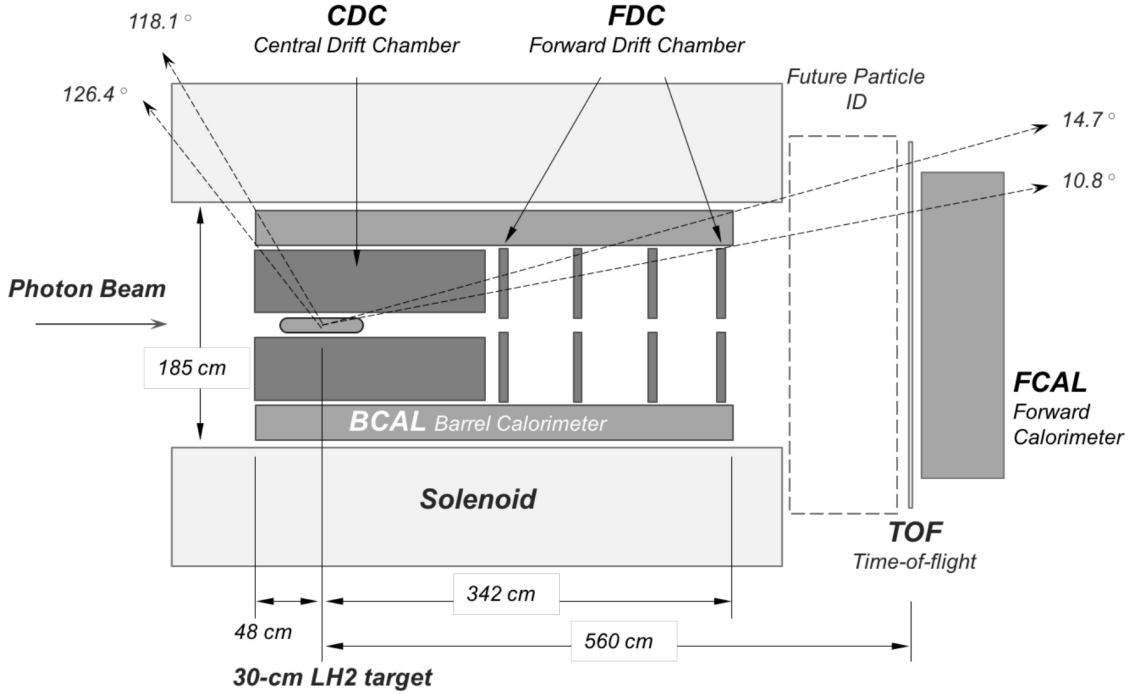


Figure 2.10: Schematic of the layout of the baseline GlueX detectors. The dashed region indicates the location of the DIRC (Direct Internal Cherenkov Detector) whose principal objective is to improve particle identification between pions and kaons to higher momenta ($\sim 4 \text{ GeV}/c$) than currently achievable ($\sim 2 \text{ GeV}/c$). The DIRC was installed in 2018, commissioned in 2019 and now forms a subsystem of the base GlueX detector.

2.3.1 Central Drift Chamber

The CDC is comprised of 3522 straws. The straws are each 0.775 cm in radius and 150 cm long. A 20 μm diameter wire runs down the center of each tube. This wire is held at a voltage of +2125V relative to the tube surrounding it. The volume inside each straw is filled with a 50:50 mixture of Argon and CO_2 [35]. When a charged particle passes through the straw it ionizes the gas and the free electrons drift towards the wire. The high-field gradient near the wire accelerates the electrons causing more ionizations and these electrons deposit their charge as a pulse on the wire and can be measured by the readout electronics. The CDC measures the distance of closest approach of the track to the wire by measuring the shortest drift time for ionization clusters to reach the wire. The CDC covers the polar angles between 6° and 168° .

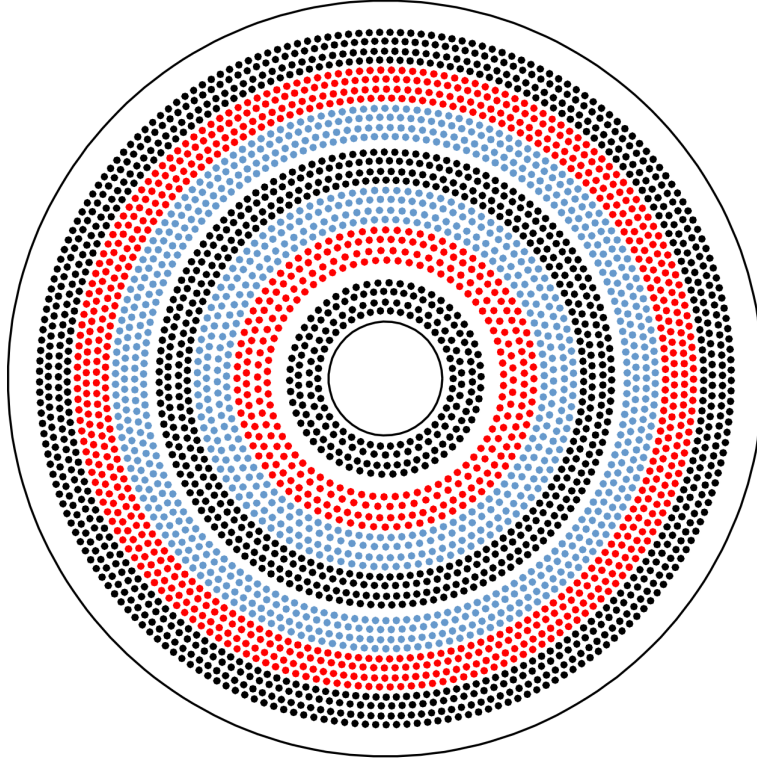


Figure 2.11: Schematic drawing of the CDC straw configuration. The diagram shows the radial layers of axial (straight) straws (black dots) and stereo straws (red and blue dots) (colour online) [34].

The energy deposition per unit track length by a particle depends on the momentum and the particle type. At low momentum, the CDC can distinguish between protons, on one hand, and pions, kaons and electrons on the other, roughly up to 1 GeV. Fig 2.12 shows the energy deposition per unit length as measured by the CDC. Protons can be clearly identified in the positively-charged sample.

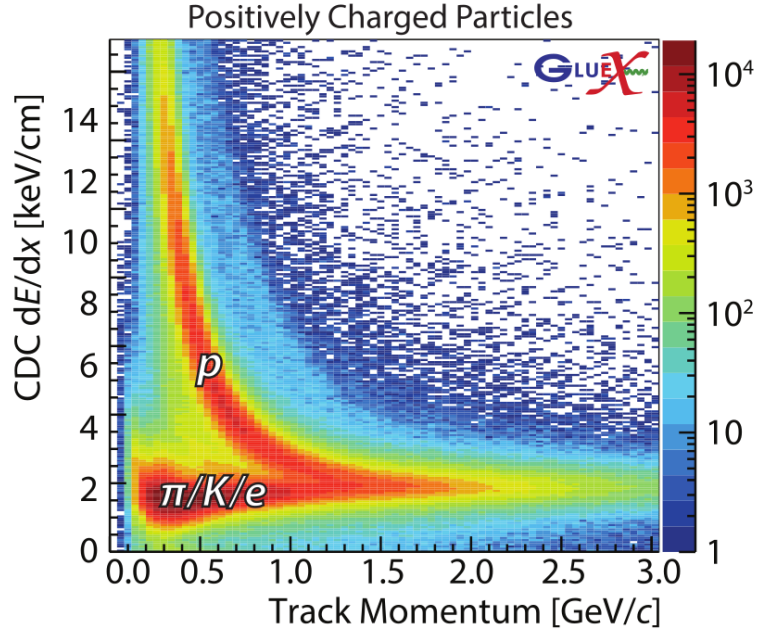


Figure 2.12: Energy deposition per unit length in the CDC as a function of the reconstructed particle momentum for positively charged particles. The horizontal band represents the pions, kaons and positrons which can be distinguished from the proton band for momentum up to 1 GeV [25] (colour online).

2.3.2 Forward Drift Chamber

The FDC detector is made up of four groups (packages) of cathode strip detectors each having six cells for a total of 24 cells placed downstream of the CDC. Each cell is rotated by 60° relative to its neighbor around the beam axis. In each cell, a plane of two alternating sets of wires is held between two grounded cathode planes. The first set, termed sense wires, is held at a bias of +2200 V, and connected to readout

electronics that record the arrival time for signals caused by ionization of the gas by charged particles. The second set, termed field wires, is designed to improve the circular symmetry of the field surrounding the sense wires. The field wires are set to a negative voltage. A 40:60 gas mixture of Argon and CO_2 fills the cells. The cathode planes are made of copper strips rotated by 75° and 105° relative to the wires. Each cell is rotated by 60° relative to the preceding cell. The charge recorded on the cathode strips determines the position on each cathode plane. An illustration of the FDC cells structure is shown in Fig. 2.13 [36].

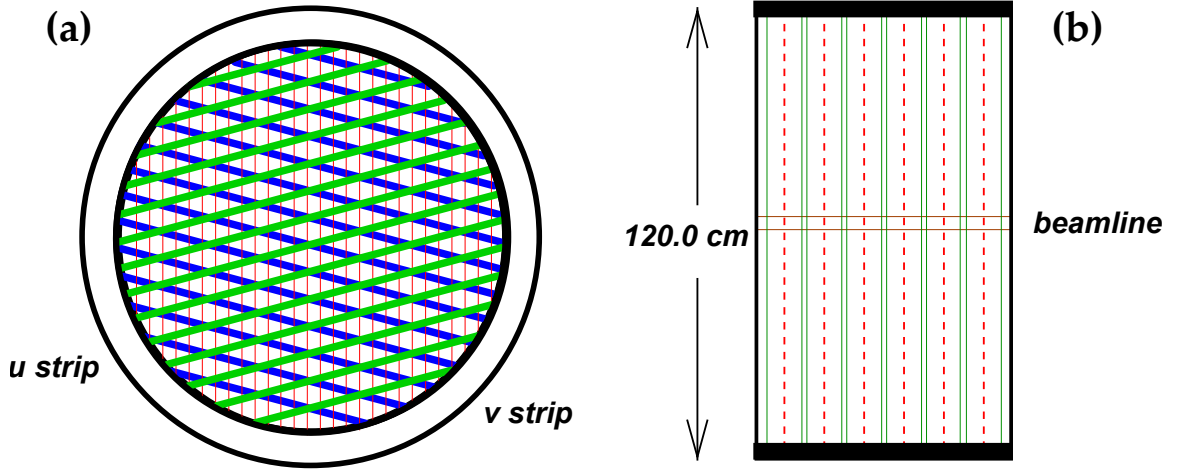


Figure 2.13: (a) Front view of an FDC package. Vertical lines represent the wires with the two cathode (U and V) strip planes on either side of the wires rotated by $\pm 75^\circ$ with respect to the vertical. (b) Side view of an FDC package. Solid green lines represent (U and V) cathode strip planes while wire planes are shown as dashed lines. A package is made up of six sets of cathode strip detectors, each rotated 60° around the beamline axis with respect to the previous set [37] (colour online).

2.4 Calorimetry

Calorimeters are devices (detectors) that measure the energy deposited by particles traversing or stopping in the calorimeter volume. In GlueX, the main purpose of the calorimeters is to detect photons present in the final-state of a majority of channels targeted for hybrid meson searches in the experiment. In order to achieve

4π solid angle coverage GlueX employs two calorimeters: the Barrel Calorimeter (BCAL) which covers polar angles from 11° to 126° , and the Forward Calorimeter (FCAL) which covers forward polar angles down to 1° where a square hole of 12 cm side allows the beam photons to pass through to the beam dump. A fiducial-cut is applied to exclude particles near the transition region between the FCAL and the BCAL ($10.3^\circ < \theta < 11.5^\circ$) and the beam dump hole at the center of the FCAL ($\theta < 2.5^\circ$) due to the reduced reconstruction efficiency in these regions⁴. These detectors will be discussed in more detail in the following sections.

2.4.1 Barrel Calorimeter

The BCAL is a hollow cylindrical shell made up of 48 modules, with the geometry as depicted in Fig. 2.14. Each module is made of 185 alternating layers of scintillating fibers and lead and covers roughly 7.5° in ϕ . It has an inner radius of 65 cm and outer radius of 90 cm, which roughly translates to 15 radiation lengths in the radial direction at normal incidence (rises to 67 radiation length at the downstream corner of the BCAL). In the presence of lead, photons generate electromagnetic showers by pair production. These showers deposit energy in the scintillating fibers. The fibers produce photons with intensity proportional to the deposited shower energy. The light travels through to the upstream and downstream ends of the BCAL where light guides funnel the light from a $\sim 2 \text{ cm}^2$ area of fibers and deliver it to a silicon photomultiplier (SiPM)⁵. Each module is divided into a matrix of four sectors (each covering roughly 1.875° in ϕ) by ten layers and connected on either ends by the same matrix made of light guides, for a total of 3840 SiPMs. The readout channels are summed over consecutive SiPM layers with layer 1 made of the first inner layer of

⁴A recent study concluded that a cut on the radial position of the neutral shower in the FCAL ($25 \text{ cm} < r_\gamma < 10 \text{ cm}$) combined with a cut on the z position of the neutral shower in the BCAL ($z < 380 \text{ cm}$) is more robust and achieves the same reconstruction efficiency.

⁵SiPMs were chosen over standard photomultiplier tubes (PMTs) as the performance of the latter suffers significantly under the intense magnetic field of the solenoid.

SiPMs. Layer 2 is summed over the next two layers, layer 3 is summed over the following three layers and layer 4 represents the sum over the outer four layers, for a total of 16 readout channels per module as shown with different colours in panel (d) of Fig. 2.14. Each of these readout channels records the energy and timing information for energy deposited in the corresponding segment. The time difference of the signal arrival at each BCAL end allows measurement of the position along the length of the BCAL. A shower is reconstructed by grouping nearby (in time and space) depositions. As information provided by the BCAL on the detected particle's energy is directly dependent on the amount of light detected by each SiPM, it is vital that the SiPM gains are understood and continuously monitored for stability. The latter is accomplished by employing a Light Emitting Diode LED pulser system which is discussed in more detail in Chapter 3.

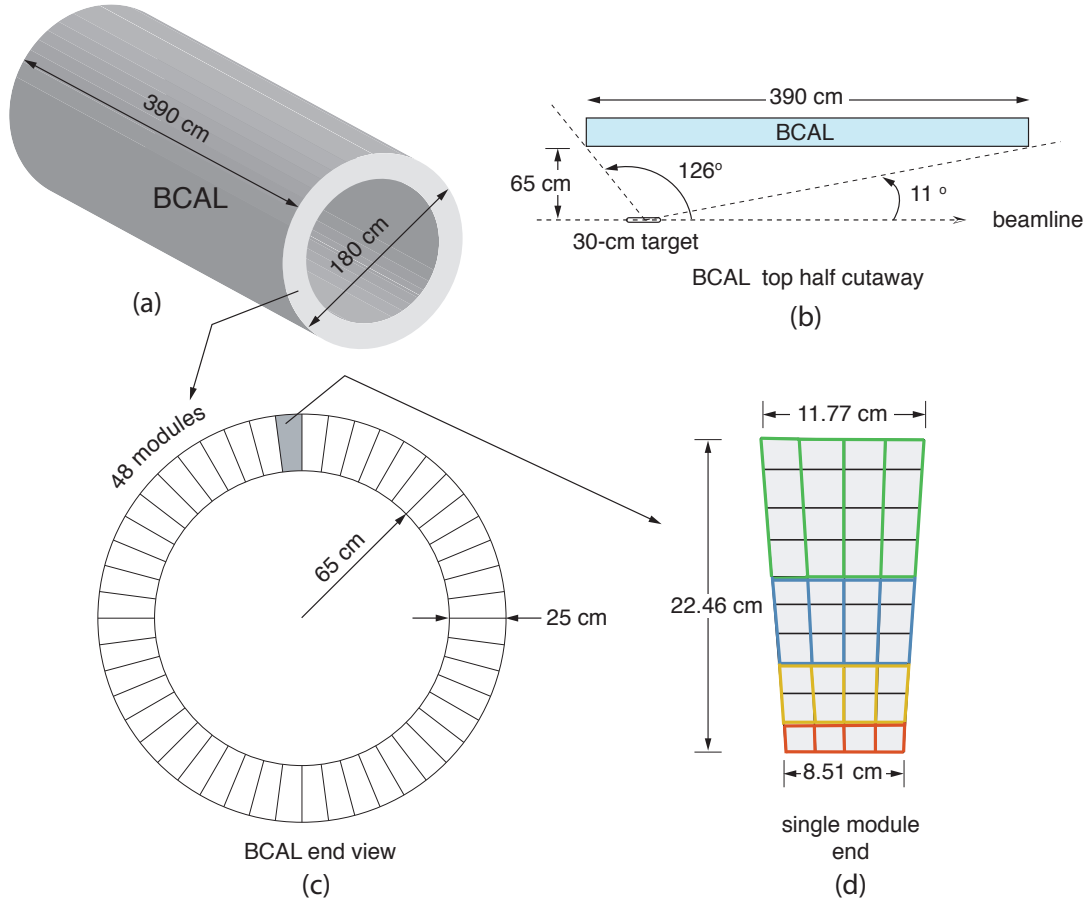


Figure 2.14: Sketch of Barrel Calorimeter readout. (a) A three-dimensional rendering of the BCAL; (b) top-half cutaway (partial side view) of a BCAL module showing its polar angle coverage and location with respect to the GlueX LH_2 target; (c) end view of the BCAL depicting all 48 azimuthal modules and (d) an end view of a single module showing the readout segmentation. More details can be found in the text and in reference [38] (colour online).

In addition to position and energy information, the BCAL can also use the flight times of charged particles (accessed by the time difference between the BCAL hit and a hit in the ST, for instance) to distinguish between different species of particle. This is limited by the timing resolution of the BCAL⁶ of 150 ps at 1 GeV, which leads to an upper limit of 2 GeV to distinguish between protons and electrons/pions as shown in Figure 2.15. A summary of the the BCAL properties is presented in Table 2.1.

Property	Value
Number of modules	48
Module length	390 cm
Module inner/outer widths	84.0 mm/118.3 mm
Lead-scintillator matrix thickness	221.9 mm
Inner/outer Al plates thickness	8 mm/31.75 mm
Module azimuthal bite	7.5°
Total number of fibers	685000
Lead sheet thickness	0.5 mm
Kuraray SCSF-78MJ multi-clad fiber	1.0 mm
Fiber pitch radial/lateral	1.22 mm/1.35 mm
Weight fractions (% Pb:SF:Glue)	86.1: 10.5: 3.4
Effective density	4.88 g/cm ³
Effective Radiation Length	1.45 cm
Effective Molière radius	3.63 cm
Effective Atomic Weight	71.4
Effective Atomic Number	179.9
Sampling fraction	0.095
Total weight	28 t

Table 2.1: Summary of BCAL properties [39].

⁶Since higher momentum translates to shorter flight time between the target and the BCAL.

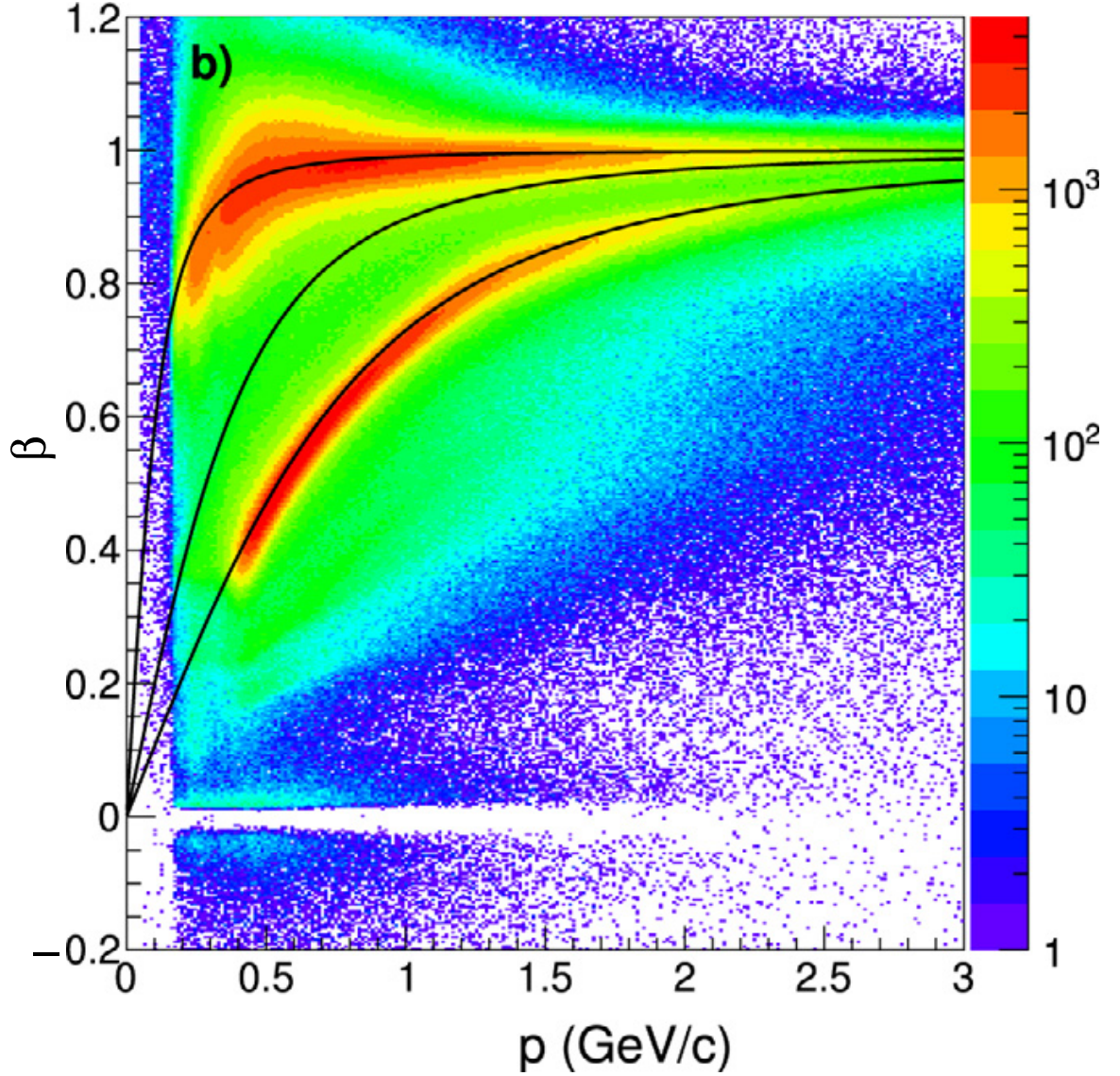


Figure 2.15: The ratio of the particle speed to the speed of light in vacuum β (measured by the BCAL) for positively charged particles as a function of the reconstructed particle momentum. The three curves show expected distributions of pions (top), kaons (middle), and protons (bottom). The lower band represents protons (speed much lower than speed of light) while the upper band represents positrons/pions (speed very close to the speed of light $\beta \approx 1$), this can be used to distinguish protons from positrons/pions for momentum less than 2 GeV (colour online).

2.4.2 Forward Calorimeter

The FCAL is wall made of 2800 lead-glass blocks, arranged in a roughly circular pattern with a radius of 2.4 m. Each block is a $4 \times 4 \times 45$ cm and covers roughly 30° in polar angle. Particles incident on the lead-glass blocks produce electromagnetic showers which then produce Cherenkov light that is detected by a photomultiplier attached to the back of each block. The amount of light produced in the block is proportional to the energy deposited in the block, and therefore can be used to measure the energy of the incident particle. A square of 3 blocks a side (12 cm) is omitted from center of the FCAL to allow the beam photons to pass through to the beam dump, this corresponds to the 1° polar angle fiducial cut mentioned in section 2.4. The design of the FCAL is shown in Fig. 2.16.

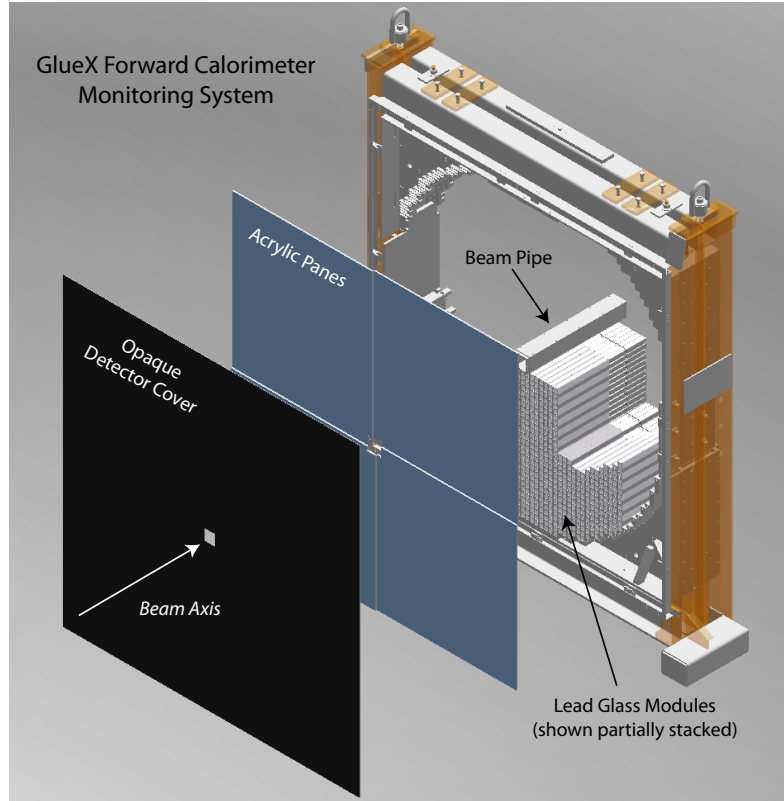


Figure 2.16: An illustration showing the conceptual design of the FCAL as a circular array of lead glass blocks with a diameter of 1 m. Light from LEDs located on the edges of the acrylic planes illuminates the lead-glass blocks for monitoring the PMTs' timing and energy characteristics. The opaque cover prevents ambient light of entering the detector (colour online).

2.5 Particle Identification Detectors

While the identity of reconstructed particles could be inferred from measurements by other detectors in Hall D, GlueX has two detectors with the main purpose of identifying reconstructed particles, namely: the ST and the Time of flight (TOF) detectors. We will discuss these detectors in the following sections.

2.5.1 Start Counter

The ST is an array of 30 plastic scintillators surrounding the target cell, with the main purpose of identifying the photon beam bucket associated with the reaction event. This is done by measuring the start time for charged tracks originating from the target. The scintillators are 3 mm thick and form a cylinder of 39.5 cm length and 15.5 cm inner diameter before they are tapered around the target cell for another 19 cm in length to cover the polar angle range $7.5 - 149^\circ$. When a charged particle passes through one of plastic scintillator segments, it produces light which is then detected by an array of 4 SiPMs at the upstream end of that segment. A representation of the ST construction is shown in Fig. 2.17 [40].

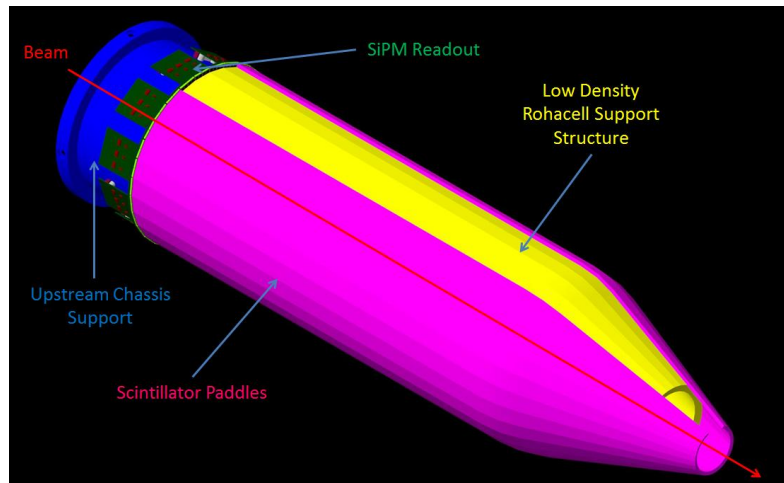


Figure 2.17: A representation of the ST mounted to the target cell [40]. The target cell is not visible in this schematic, as it is inside the ST (colour online).

2.5.2 Time of Flight

A wall of scintillating bars comprise the TOF detector in GlueX. The TOF detector is placed upstream of the FCAL, as shown in Fig 2.18, and provides a timing measurement for forward-going particles. The detector is made of two layers of 42 bars each, with dimensions $250 \times 6 \times 1.25 \text{ cm}^3$. The bars are arranged horizontally in one layer and vertically in the other to allow the reconstruction of the particle position in the plane. Each paddle is read out on both ends except for the two innermost paddles of each plane where a $12 \times 12 \text{ cm}^2$ square hole allows the beam photons to pass through to the beam dump and aligns with the beam dump hole in the FCAL mentioned in section 2.4.2. On all sides of the beam hole, half-length bars are attached to only one PMT. This leads to a total of 164 readout channels for the full TOF detector. When charged particles pass through a scintillating bar they produce light, which is then detected by photomultiplier tubes attached to either side of the bar. Measuring the time difference between the PMTs ⁷ on either side allows the calculation of the position of the particle hit on the bar. The path length of the particle track and the timing information from the TOF are used to calculate the TOF and compare it to the expected flight time for a given particle species with a timing resolution of 70 ps. This allows identification of different particle species as shown in Fig. 2.19 [42].

⁷The magnetic field strength at the location of the TOF PMTs is low enough to allow their operation.

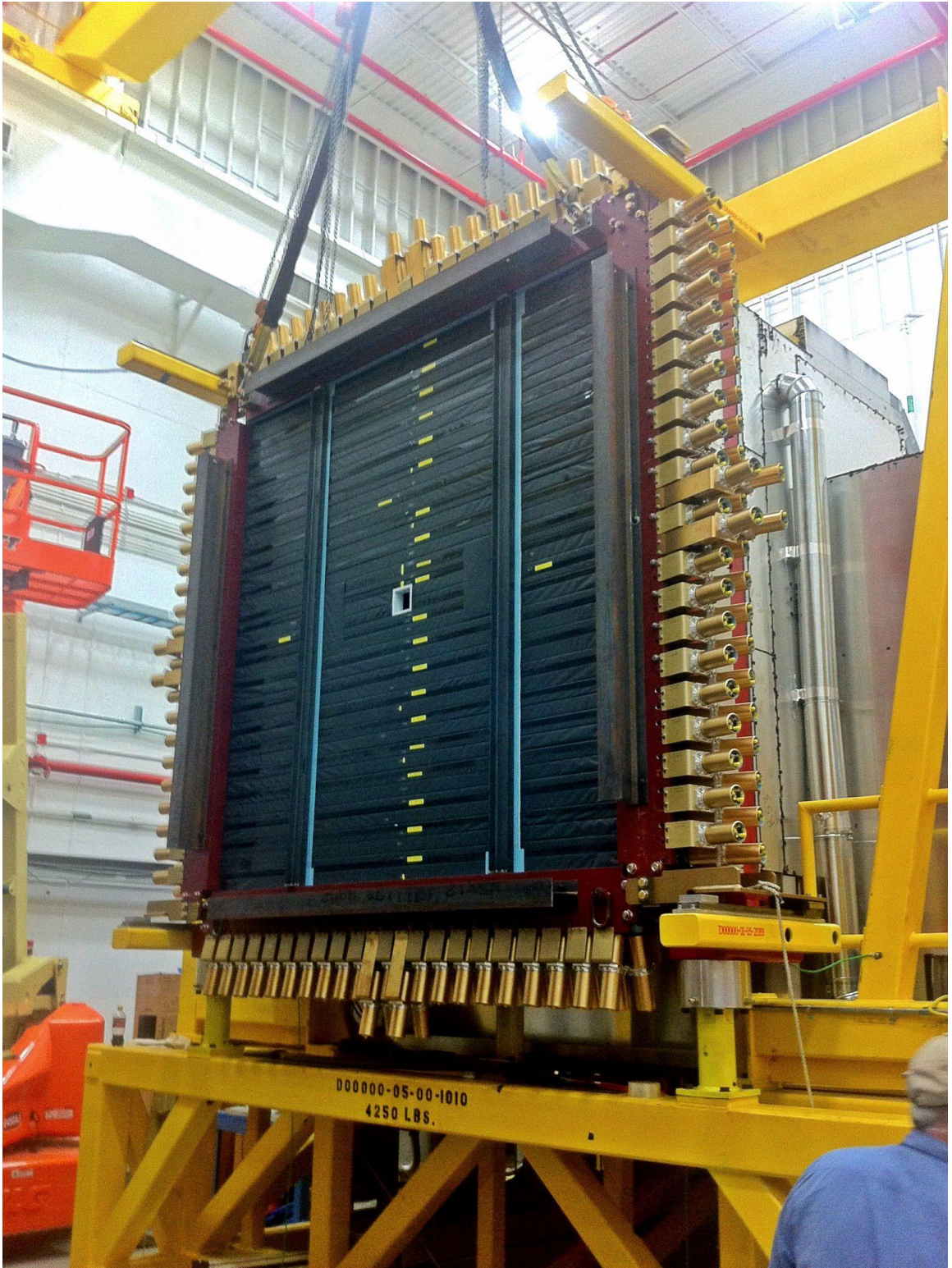


Figure 2.18: The TOF detector mounted on its support frame. Its surface area is approximately $250 \times 250 \text{ cm}^2$ [42].

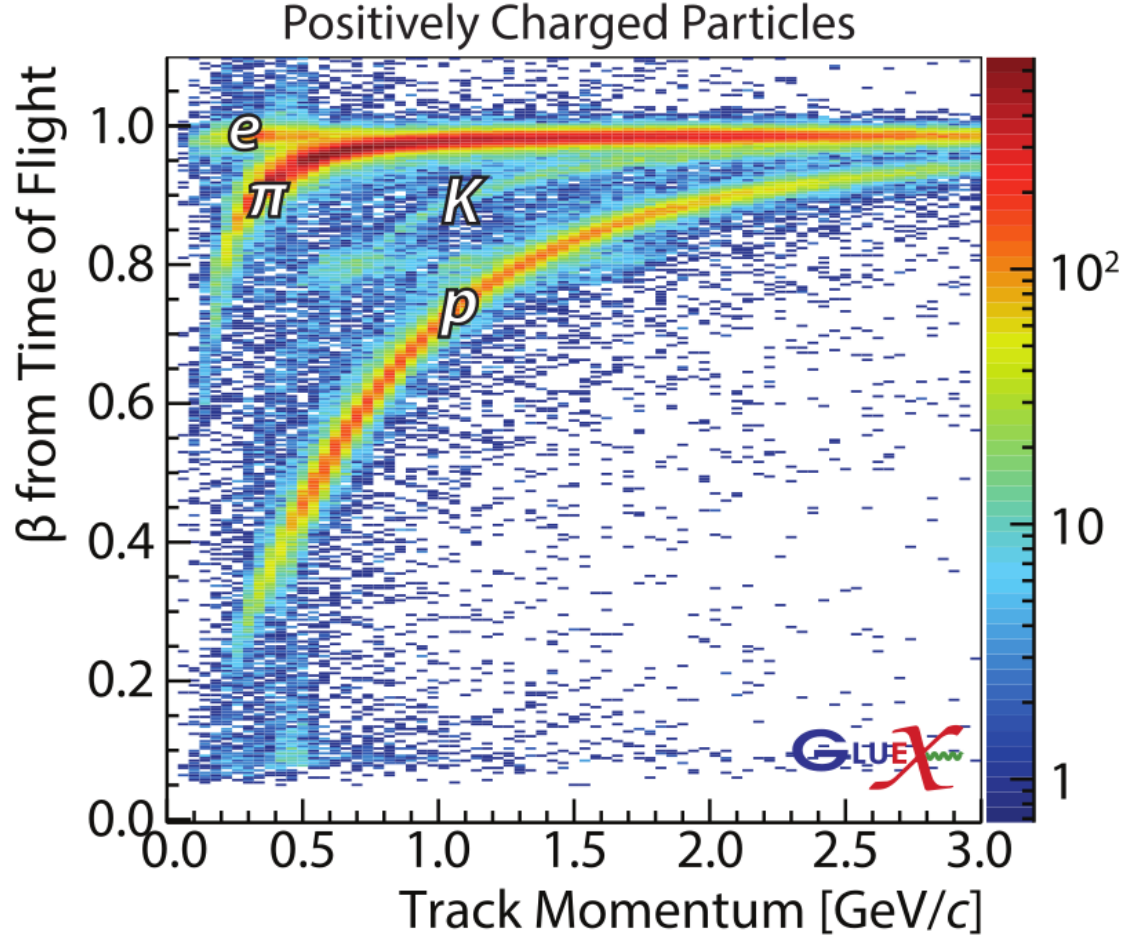


Figure 2.19: The ratio of the particle speed to the speed of light in vacuum β as a function of the reconstructed particle momentum, measured by the TOF detector for positively charged particles [25]. The different particle species identified fall on bands, as denoted by the symbols (colour online).

2.6 Summary

In this chapter, the key components of the CEBAF accelerator, the Hall D beam-line and the GlueX detector were presented.

Chapter 3

BCAL Gain Monitoring System

As detailed in section 2.4.1, the BCAL provides information towards the reconstruction of detected particle's energy, which is directly related to the amount of light detected by each SiPM. Therefore, it is vital that the SiPM gains are known accurately and continuously monitored for stability. The latter is accomplished by employing an LED pulser system¹. The work in this chapter details the author's service contribution to the GlueX Collaboration, as expected from all members of the collaboration.

Implemented in each module of the BCAL, the LED pulser system [38] consists of four strings (one per sector) each of ten LEDs, as shown in Fig. 3.1. The LEDs in each string are pulsed by providing a bias voltage typically in the 5-7 V range and can be pulsed separately. The LEDs are glued to light guides at an angle so that they mostly point to the opposite side of the BCAL (e.g. LEDs on the downstream side mostly face the upstream side) as can be seen in Figures 3.2 and 3.3: when LEDs are pulsed, pulses can be observed by respective BCAL channels upstream and downstream with higher pulse amplitudes observed on the opposite side, in principle ².

¹"The objectives underlying this system are to provide continuous online monitoring and relative offline gain and timing calibration for the Barrel Calorimeter (BCAL)..." G.Voulgaris, P. Ioannou, C. Kourkouvelis, Development of a Calibration System for the GlueX Calorimeter and TOF Detectors, DocDB-1285.

²In practice, accurate angling of the LEDs proved to be difficult. The resultant amplitude ratio of far to near ranged from 1 to 3, after taking attenuation into account, instead of the hoped for 1.

Observing the same LED by channels on both ends allows us to diagnose problems with the LED where opposite channels will show the same damage, versus one channel exhibiting degradation due to either SiPM or light collector. This design also allows us to observe radiation degradation of either SiPM and or the light collector, since the upstream SiPMs are much less likely to be damaged as much or as soon as the downstream ones. Fig. 3.4 shows an example of an LED pulsing event, where the first sector of every module is pulsed and optical crosstalk can be seen in the adjacent sector.

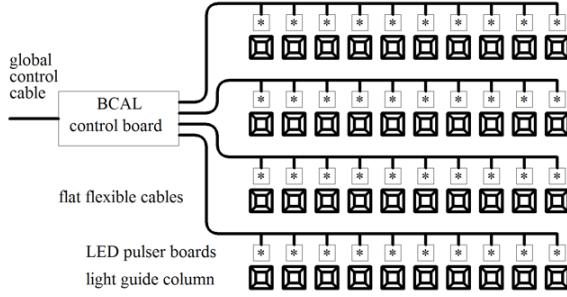


Figure 3.1: Pulser Configuration of the BCAL LED monitoring system [38], showing the four LED strings per module.



Figure 3.2: One end of a prototype BCAL module, showing two of its four sectors of light guides. The LED pulsers are mounted on the side of the light guides attached to a common flexible cable. The free end of the flexible cable connects to its control board (shown in Fig. 3.1) [38].

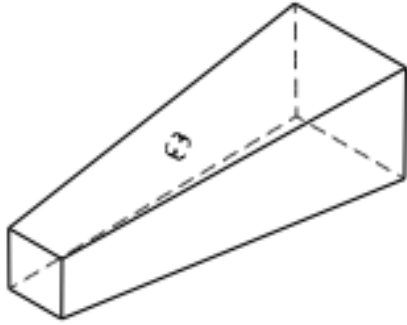


Figure 3.3: A pocket is shown on the side of a light guide where the LED is to be mounted [38]. Each LED is inserted at an angle, so as to mostly point to the opposite end of its BCAL cell.

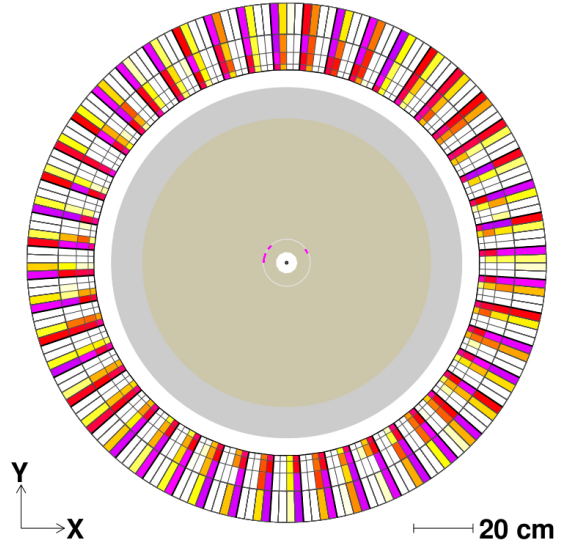


Figure 3.4: An example of LED pulsing event from run 11450, where Sector 1 is pulsed red/magenta indicating higher amplitude, and optical crosstalk can be seen in the Sector 2 orange/yellow indicating lower amplitude [43] (colour online).

The bias values used must be chosen taking into account low and high light levels from the LEDs³, so that the corresponding pulses from the SiPMs fall within the Analog-to-Digital-Converter's (ADC's) range. The LED pulser system was ran into two different global configurations, one from the start of the experiment in 2016 and up to fall 2018, and a simpler one since then, as explained in the following. The initial system was based on a 5 to 7 V bias scan, the pulser cycle was chosen with 6.25 V as the high bias and 6 V as the low bias setting [45]. Sectors and sides are triggered separately. This leads to 16 pulser configurations (e.g. "high bias sector 1 upstream" means pulsing strings of LEDs in Sector 1 in all upstream modules with 6.25 V). A script was written to run on the slow controls system cycling through the 16 configurations with 60 pulses in each configuration. This number of pulses was chosen to allow enough statistics in each pulsing mode while allowing the system to cycle between the 16 modes few times in the duration of a production run.

During fall 2018 run period, the Calorimetry Working Group (CALWG) decided to change the pulsing cycle of the BCAL_LED from the previously implemented 16-mode cycle to a two-modes cycle — where all sectors are pulsed simultaneously with 6.25V bias voltage by LEDs on either the upstream and downstream ends of the BCAL. This change aimed to minimize artifacts caused by pulser control boards when switching between pulsing modes, and was applied starting with run 50742 on October 3rd, 2018⁴.

The BCAL_LED monitoring system has been used so far in an offline post-run period configuration. This is mainly due to the low frequency of the LED

³With cost considerations in mind, LEDs of mid-range quality were procured, and these had a light intensity variation between 10-20%.

⁴<https://logbooks.jlab.org/entry/3603335>

pulser triggers⁵, computationally-demanding skimming process required to isolate the BCAL_LED events from other events in the data stream, as well as queues on the JLab compute farm. Section 3.3 details the current operation of a two-staged online monitoring system. The first stage includes a plugin and histograms for experts that would be reviewed every 24 hours during data taking. The second stage would include histograms for experts that would be reviewed after each run period.

Section 3.1 discusses the BCAL_LED readout system, events selection, different triggers which exist in a BCAL_LED skim file and possible filters to distinguish physics from LED triggers. Section 3.2 discusses the software used for the monitoring system. Section 3.3 discusses the different monitoring phases. Section 3.4 discusses current problems we have observed using the monitoring system and histograms used to diagnose it. Section 3.5 presents a study of the mean and width of pedestal in BCAL channels and their dependence on temperature and bias voltage.

3.1 BCAL LED Readout

Pulses from each of the 4 strings in a module can be observed in both up and downstream SiPMs in the corresponding sector. Some optical crosstalk can be observed in adjacent sectors [38]. However, by pulsing one sector at a time in each module, we are able to collect data for that sector without suffering optical crosstalk from adjacent sectors. So, optical crosstalk was ignored for the scope of this study⁶.

LED pulses observed by BCAL SiPM channels are stored into the data stream as (individual end) "hit" and subsequently (two-sided) "point" information following

⁵LED pulser runs usually at 10 Hz which is very low compared to the physics event rate during production runs.

⁶This is true for the 16-mode pulsing cycle which is no longer being used. Further studying of the optical crosstalk is planned for the new two-modes pulsing cycle.

data "event" reconstruction. Pulser data are identified using trigger information (e.g. upstream pulser associated with trigger 0x100, and 0x200 for downstream pulser).

3.1.1 BCAL_LED Events Selection

The event selection for BCAL_LED skim identifies events subject to one of the following conditions:

1. front panel (FP) LED trigger or
2. more than 200 hits in the BCAL or
3. more than 12 GeV energy deposition in the BCAL

When this script is in effect, each of the three conditions filters LED events. Investigating abnormalities in FP triggers during the fall 2018 run period led to a the discovery of a bug in the skim code, which disabled conditions 2 and 3 since the plugin was created⁷. Upon fixing this bug, it was found that some events with Global Trigger Processor (GTP) physics triggers pass through these conditions. These events are a result of FCAL, BCAL or PS GTP triggers. The panels in Fig. 3.5 show FP and GTP triggers for: all events in the LED skim files (top left), events which do not have an FP LED trigger yet they satisfy the 200 hits cut (top right), events which do not have an FP LED trigger yet they satisfy the 12 GeV energy cut (bottom left) and events which do not have a FP LED trigger yet they satisfy both the 200 hits and the 12 GeV energy cuts (bottom right). An example event which made it through these cuts is shown in Fig. 3.6.

Studying the number of hits versus the energy deposition in the BCAL per event shows the leaked events in clear contrast to real LED events. An example energy vs

⁷The trigger_skims plugin was created in May 2016. The bug was discovered in March 2019.

number of hits plot for BCAL LED "SKIM" events (i.e. events with FP LED trigger or 200 BCAL hits or 12 GeV energy) is compared to real LED events in Fig. 3.7. A projection of the number of hits for event an LED skim file is shown in Fig. 3.8. The peak around 1536 hits represents real LED events while the distribution at lower number of hits shows the GTP events leaking into the LED skim. Based on these plots, an improved condition of requiring at least 1200 hits was implemented and the energy condition has been disabled temporarily. In Fig 3.9, we compare between the use of front panel triggers alone and the inclusion of the 1200 hits as an alternative trigger. In the absence of the front panel trigger, the pulser side (upstream or downstream) is decided based on the accumulative pulse peak recorded in all channels on either side of the BCAL, as the side far from the pulser usually records higher pulse peak than the near side ⁸.

⁸Information from this plot is now part of the main online monitoring histograms as a result of efforts by V. Neelamana, A. Somov, M. Dalton and the author.

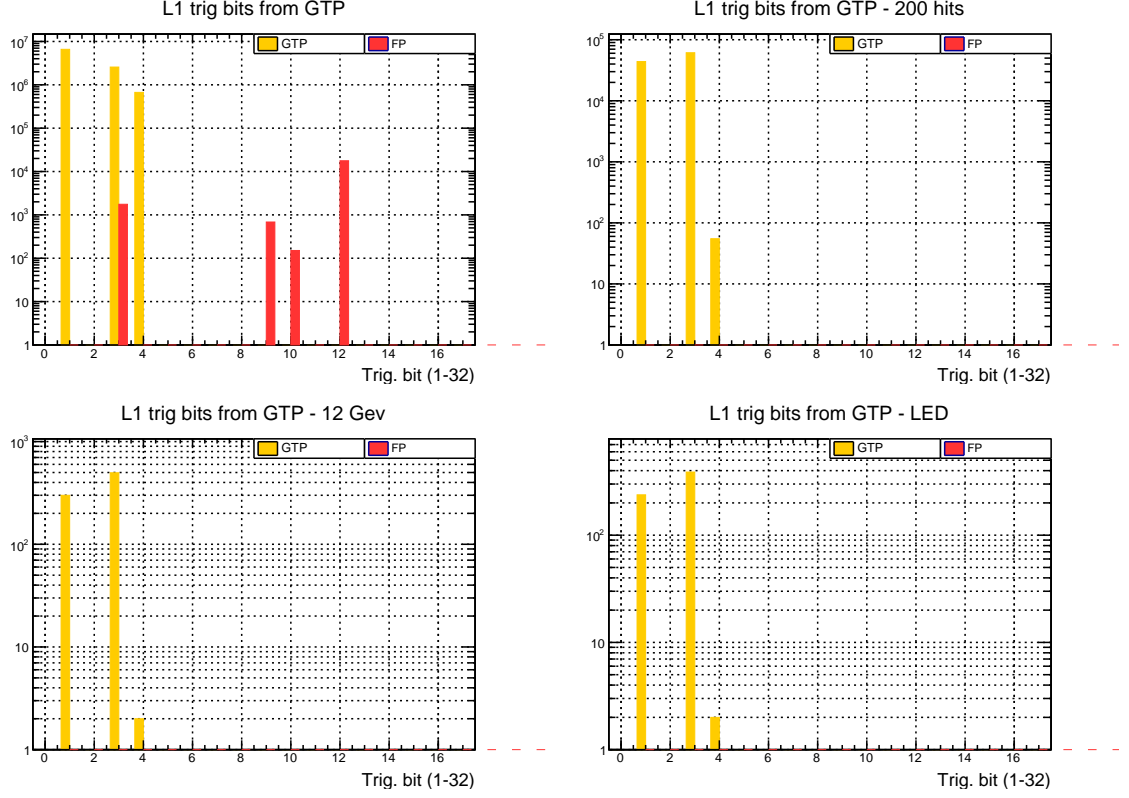


Figure 3.5: Histogram showing triggers for a sample of run 51262. (Top left) Triggers from all events. Yellow bars represent GTP triggers (FCAL, BCAL and PS) while red ones represent FP triggers (FCAL LED, BCAL LED and random). The BCAL LED triggers are represented by triggers 9 and 10 (upstream and downstream respectively), which correspond to "lane" values of 8 and 9 in the trigger/DAQ configuration file. (top right) Triggers of events which do not have an FP LED trigger yet they satisfy the 200-hits cut. (bottom left) Triggers of events which do not have an FP LED trigger yet they satisfy the 12 GeV-energy cut. (bottom right) Triggers of events are shown which do not have a FP LED trigger yet they satisfy either the 200-hits or the 12 GeV-energy cuts (colour online).

BCAL view from downstream looking upstream

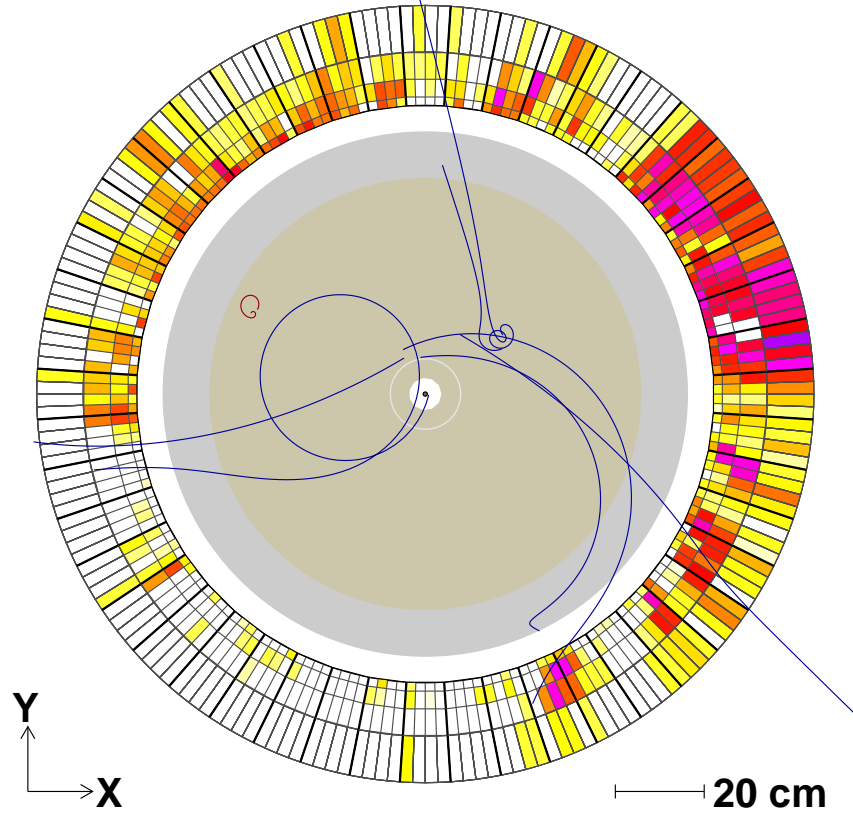


Figure 3.6: An example leaked event identified as an LED event by the skim plugin. Such an event is likely due to a hadronic shower by a cosmic muon, striking the upper right quadrant in this view.

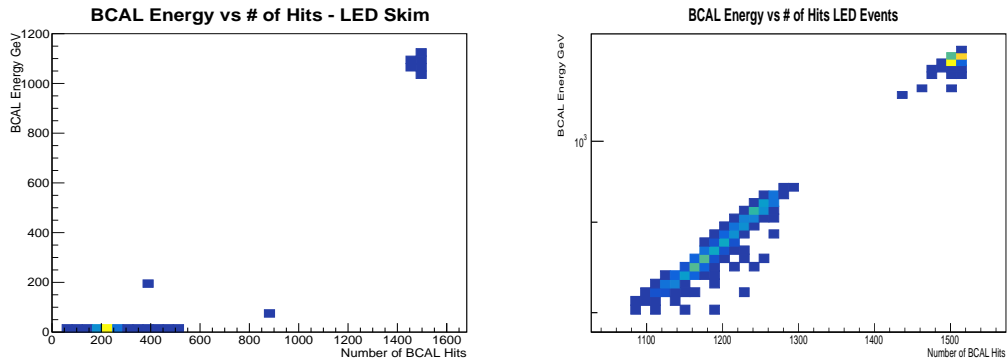


Figure 3.7: Example plots for number of hits versus energy deposition in the BCAL per event, for events identified as LED events by the skim (left) and real LED events (right). The leaked events can be seen in the left panel with relatively lower energies and number of hits. Also, they do not follow the linear relation we see between number of hits and energy for LED events in the right panel (colour online).

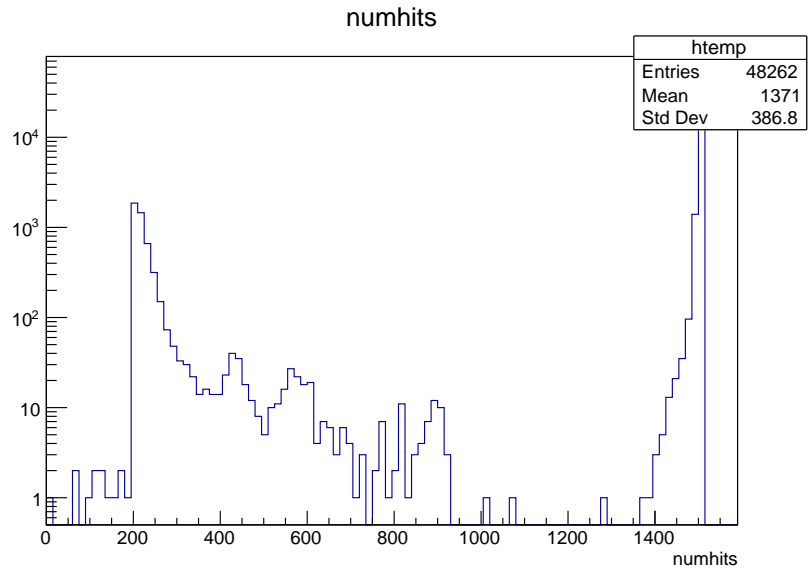


Figure 3.8: The number of hits for events identified as LED events by the skim plugin; this is a projection of the plot in the left panel of Fig. 3.7. The real LED events are indicated by the peak around 1536. The distribution at lower number of hits shows the GTP events leaking into the LED skim.

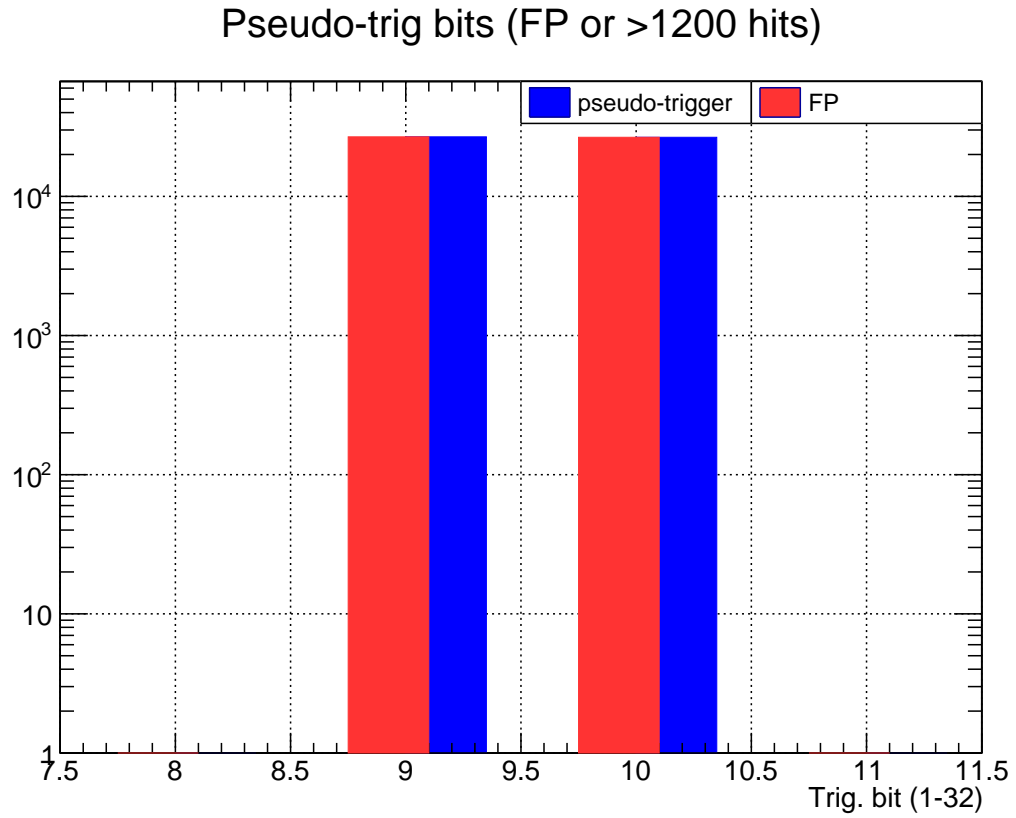


Figure 3.9: Example plot comparing the use of front panel triggers alone (red) and the inclusion of the 1200 hits as an alternative trigger (blue). In this particular run the FP triggers agree with the pseudo-trigger (colour online).

3.2 LED Monitoring Plugin

Monitoring the LED pulse peak⁹ over each run and comparing to previous runs allows the detection of drifts in gains and can be used in correcting the calibration of SiPMs. For that purpose, a plugin (C++ script) was written that loops over raw data and identifies LED events among physics events coming from the LH_2 target or cosmic radiations.

A stack of pedestal¹⁰-subtracted pulse peaks (PSPP) from all channels in the four downstream sectors is shown in Fig. 2.3 as an example. The top band (above 10^2 ADC counts) represents the pulser signal as observed by the respective channels on the same sector. The middle band ($10 - 10^2$ ADC counts) represents crosstalk in the adjacent sectors, while the bottom band (less than 10 ADC counts) represents background (SiPM and electronic noise). Fig. 2.3 shows a single pulser cycle. Starting from the left, Sectors 1-4 upstream (far side) are pulsed with 6.25 V (black-red-green-blue band on the left) with optical crosstalk clear in middle band. Then sectors 1-4 downstream are pulsed with 6.25 V, sectors 1-4 upstream are pulsed with 6 V and finally sectors 1-4 downstream are pulsed with 6 V (black-red-green-blue band on the right). The gap around 15×10^6 represents an increase in the non-LED events rate possibly due to beam fluctuations.

⁹Pulse Peak: the highest sample recorded after threshold crossing within the trigger window [46].

¹⁰Pedestal: the integration over the trigger window of the signal measured when there is no energy deposited in the channel.

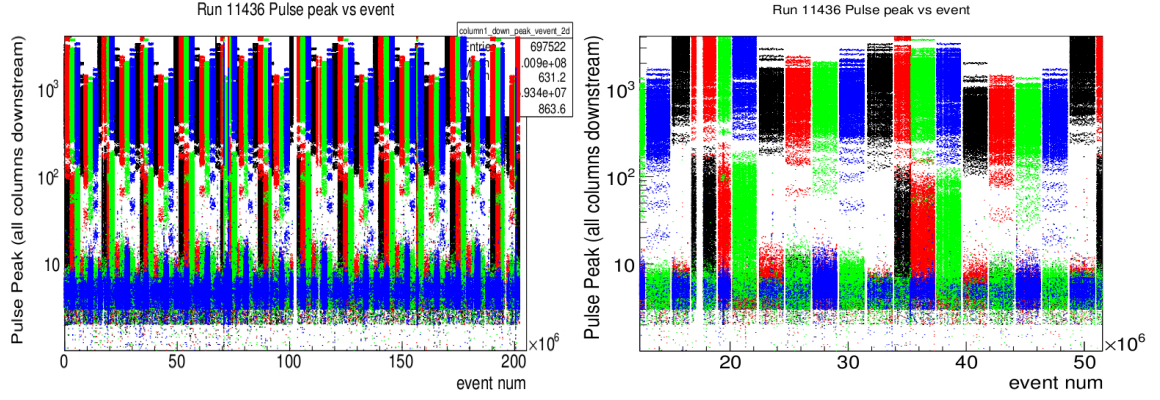


Figure 3.10: (Left) Stack of PSPP over six pulser cycles for all four downstream sectors for run 11436. (Right) A single pulser cycle is shown composed of four groups [43] (colour online).

The average PSPP over all channels in each sector per event allows the identification of different pulser configurations and an example plot is shown in Fig. 3.11. After identification, the average PSPP per pulser configuration for every channel over the event is stored in a file.

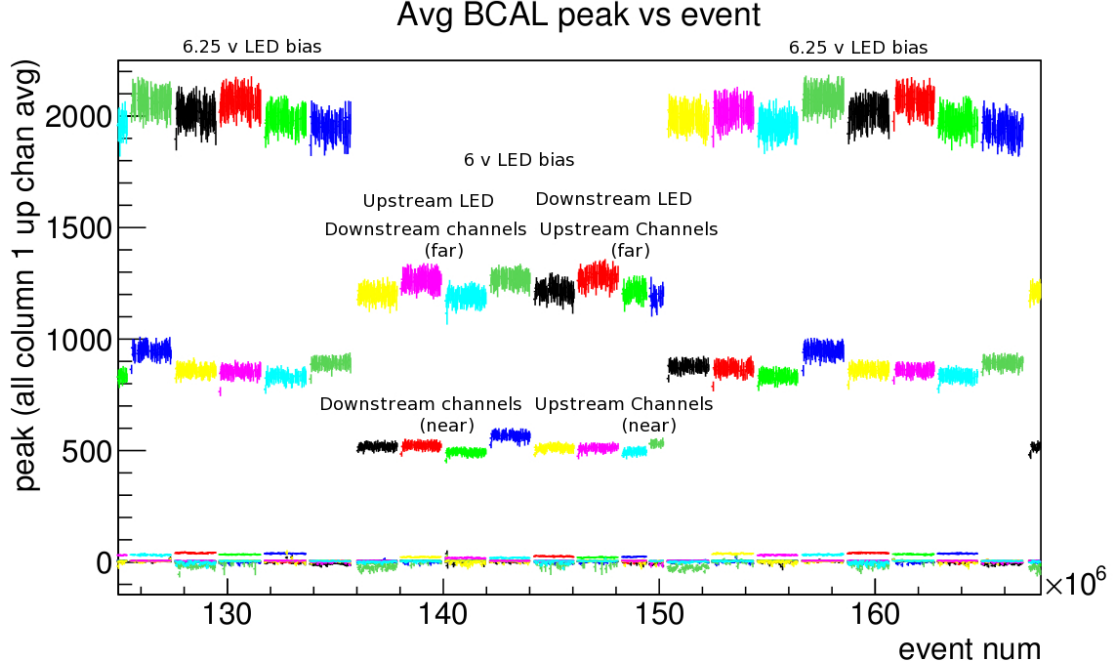


Figure 3.11: Different pulsing configurations as seen by all channels in the BCAL. Colours: yellow through blue represent average PSPP over sectors 1 downstream to sector 4 upstream. PSPP values of 2000, 1200, 900, and 600 are produced by pulsing LEDs with 6.25 V far and near, and 6 V far and near, respectively ¹¹ (colour online).

A plotting macro forms the normalized pulse peak by dividing the average PSPP per configuration for every channel for the targeted run over the average PSPP recorded for this channel over the run period and plots the ratio as shown in Figure 3.12. As can be observed, the majority of the BCAL channels remain stable over long periods of running (less than 1% deviation) with a few outliers in the 1-2% range and fewer still with a deviation more than 2%.

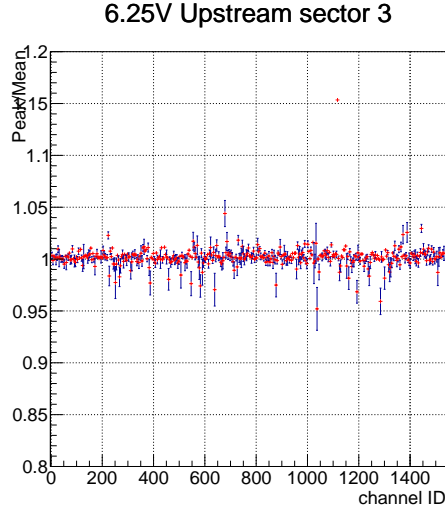


Figure 3.12: A sample normalized pulse peak vs channel ID is shown for the bias of 6.25 V and the upstream pulser configuration over run 11445. [47]

As a further test of the monitoring system, the standard deviation of each channel is studied over all runs in the run period. This is done by collecting the ratios from each channel, as shown in Fig. 3.13. Then, the projection on the Y-axis is taken and fit using a Gaussian distribution Fig. 3.13. The standard deviation of this fit is plotted versus channel ID Fig. 3.14 and the fractional variation¹² is shown in Fig. 3.14. Both demonstrate the stability of the method (LEDs and SiPMs) over large periods of running.

¹²Fractional variation: the ratio of the standard deviation to the mean of the fit

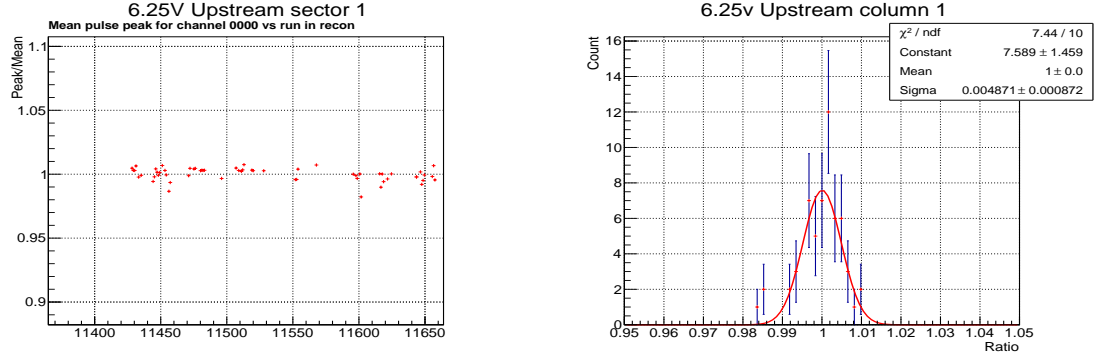


Figure 3.13: (Left) Normalized pulse peak to average ratio vs run number for channel 0 (module 1, layer 1, sector 1 downstream). The ratio is clustered around 1, demonstrating stability over a large number of runs taken over 12 days [47]. (Right) A Gaussian fit of the Y-axis projection of Fig. 3.13 is shown. From this fit the standard deviation and mean are obtained to calculate the fractional variation [47].

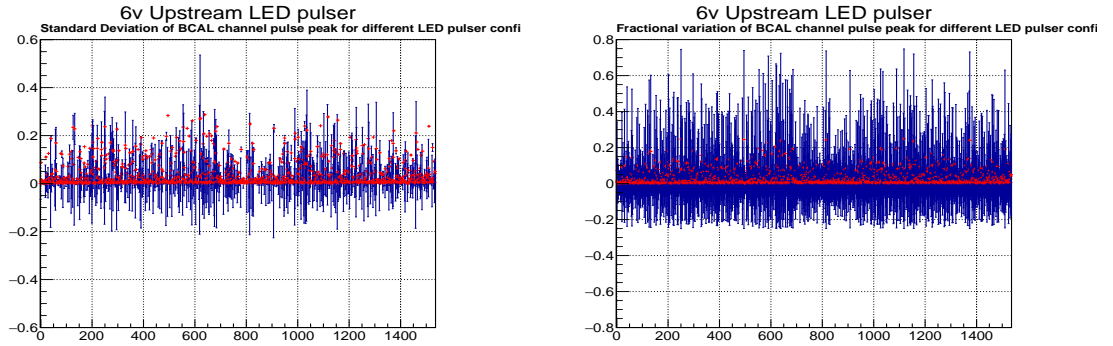


Figure 3.14: (Left) The standard deviation of the normalized pulse peak fit for each channel over spring 2016 runs [47]. (Right) The fractional variance of the normalized pulse peak fit for each channel over spring 2016 runs [47].

3.3 Monitoring Phases

The LED pulser plugin has been used to monitor data starting with the spring 2016 run period offline. The plugin has been tested to work on raw data files directly, which is slow because most of the events in those files are from beam (physics) with a minute fraction (0.025%) coming from the LED pulser. However, faster processing was achieved first by using a skim plugin to identify LED events from raw data files and write them to separate LED data files. As explained in section 3.1.1, identification is done based on the trigger bit. Also, any event with more than 200 BCAL points or integrated energy higher than 12 GeV is identified as a potential LED event.

Most runs exhibit stability in the normalized pulse peak as previously shown in Fig. 3.17. So far, the only problem that has been observed is the deviation of entire LED pulser quadrants as shown in Fig. 3.17. As mentioned previously, we expect this deviation to be the result of problems in LED control system and not in the BCAL SiPM channels as the same effect can be seen for corresponding channels upstream and downstream. The CALWG will assess this issue and determine whether repairs are needed to the control system during a period of experimental shutdown.

The intent for the BCAL_LED plugin is that it can be used for either online or offline monitoring. In this section, we present a two-phased monitoring system for the BCAL_LED system that has been approved and adopted by the CALWG.

- **Phase A, Essentially Online, expert:** At this stage, the monitoring analysis is based on the skim files (usually the first five files of each run). The relative gain and timing are plotted versus the run number for each channel. A separate histogram for each of the two pulsing modes adds up to a total of 3072 histograms. Example plots for expert online monitoring of relative gains are

shown in Fig. 3.15. An expert inspects these histograms within 24 hours from the generation of the skim files.

- **Phase B, Offline, expert:** The offline expert tier would utilize a relative gain monitoring similar to the one shown in Fig. 3.15, extended over the run period. It also includes detailed studies of the SiPMs and LED pulser system to investigate abnormalities and/or radiation damage symptoms appearing in the Phase A monitoring tier. Details on diagnosing the different abnormalities in the BCAL_LED system triggers are presented in section 3.1.1 while details on diagnosing abnormalities in the BCAL_LED bias distribution boards will be discussed in section 3.4.2. Such studies have been carried out by another graduate student in the group [48].

⇓ BCAL Channel vs Run number ⇒

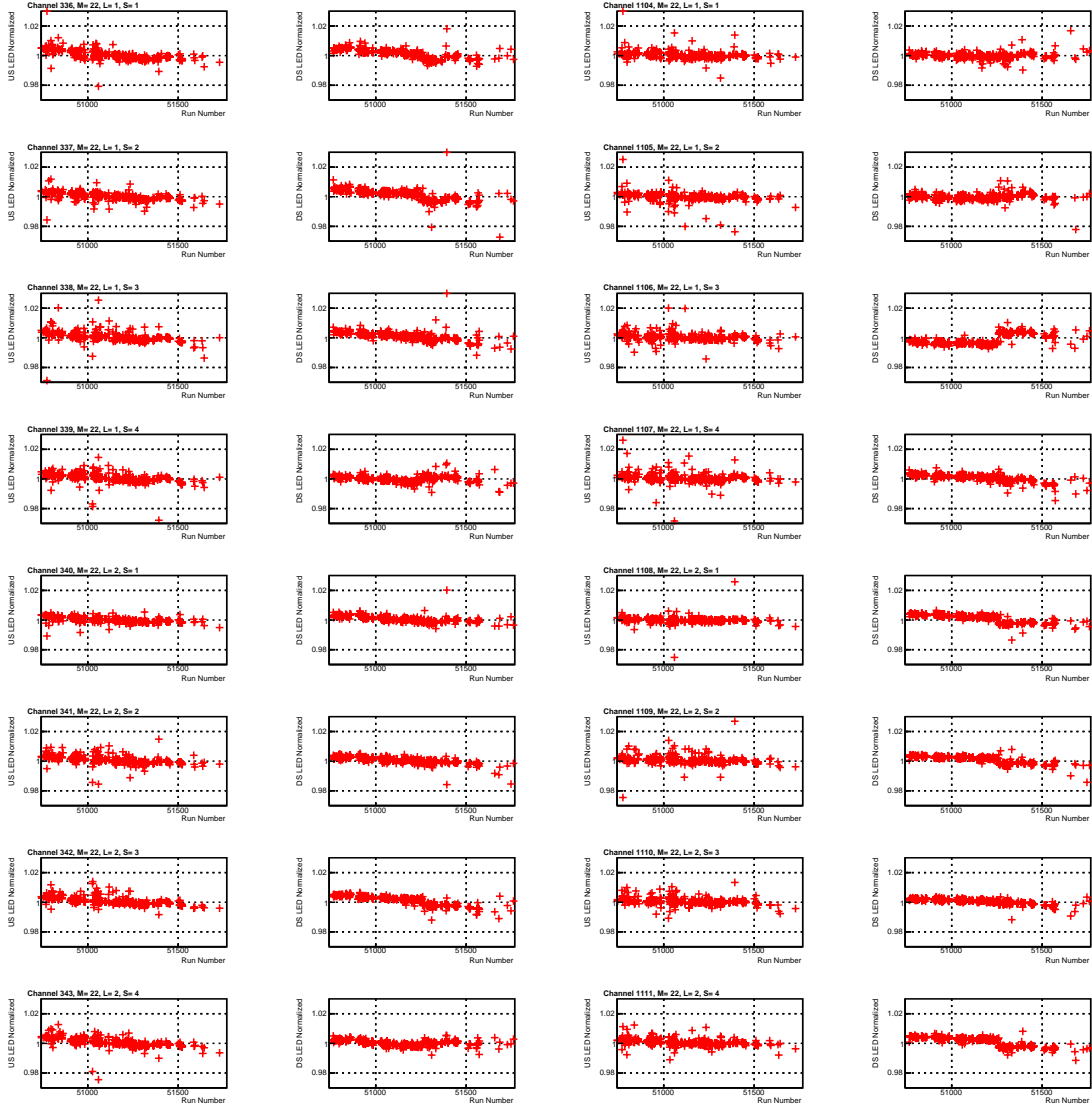


Figure 3.15: An example of Phase A online relative gain monitoring histograms for experts over fall 2018 runs. The relative gain is plotted versus the run number for each channel. Each row represents the change in relative gain for a pair of BCAL channels. The two columns on the left represent the downstream channel relative gain when pulsed by the upstream LED (leftmost column) and downstream LED (middle left column). Similarly, the two columns on the right show the relative gain for the conjugate channel (same module, sector and layer) on the upstream end of the BCAL. In this format, all 1536 channels of the BCAL are summarized in a 96 page file. Phase B monitoring uses an extended version of these plots to study a complete run period.

3.3.1 Online Monitoring

In addition to the two-tiers mentioned in section 3.3, a third-tier online for the shift takers was decided as unfeasible by the CALWG due to reasons aforementioned. Modifications to the pulsing rate could make it usable in the future. If implemented, the BCAL_LED plugin could be used in real time with RootSpy¹³ during runs to monitor the behaviour of SiPMs. A plugin and plotting code were written for monitoring occupancy and time shifts of BCAL channels using LED signals. The information should be concise, therefore the interface would only flag channels which are behaving abnormally; either by a change in the relative gain or timing of the channel. The information would be represented by occupancy-style histograms, one set for amplitudegain and one for timing. An example plot for monitoring relative gain is shown in Fig. 3.16. In the end, the CALWG decided to not implement this third-tier to avoid overloading non-expert shift takers.

¹³RootSpy: A system for the distributed viewing of ROOT histograms [49].

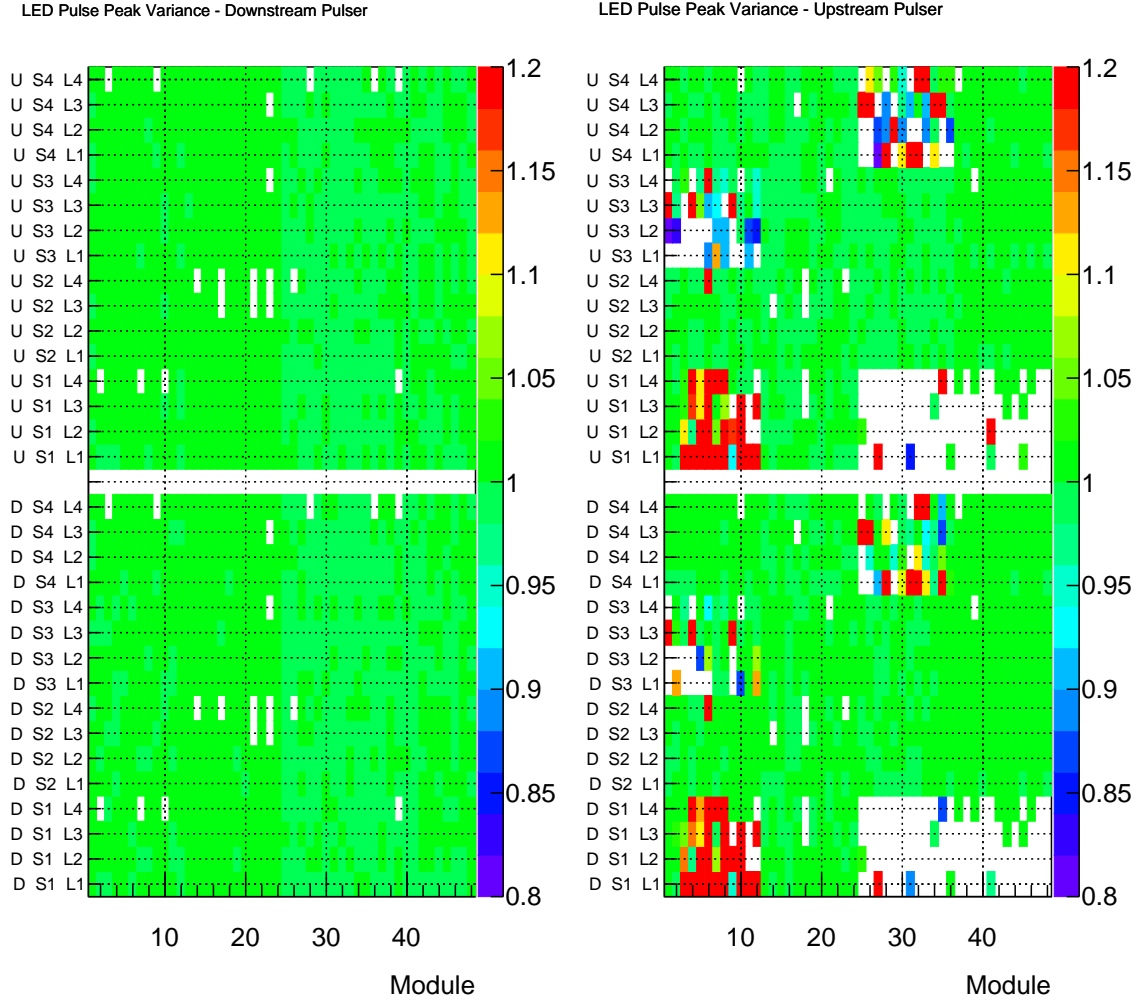


Figure 3.16: An example of the third-tier essentially-online relative gain monitoring histograms for shift takers from run 61624 (spring 2019). This tier was decided unfeasible by the CALWG for reasons mentioned in the text. The color scheme is used to make it easy to see if a channel is behaving as expected or not. Well-behaved channels will have a stable gain over the run period, leading to a relative gain of unity (when compared to the average over the run period) (green). Channels with lower than expected gain will have a relative gain lower than unity (violet - blue). Channels with higher than expected relative gain will be larger than unity (yellow - red). White blocks indicate channels where the LED did not pulse or the channel is dead (colour online).

As a fast visual check, the 16 ratio histograms shown in Fig. 3.12 are superimposed into four histograms with the four colours indicating the different sectors as graphed in Fig. 3.17. This ratio is typically clustered around the value 1. An example of a deviation can be visually detected in Fig. 3.17. In this particular example, quadrants 1, 2 and 4 in sector 1, pulsed with the downstream pulser at 6 V, show deviation from unity. A similar behaviour observed in downstream channels ($0 \leq \text{channel ID} \leq 767$) and upstream channels ($768 \leq \text{channel ID} \leq 1535$) for the same pulser configuration. This "grouped" behaviour of a deviation points to a problem in the bias distribution boards in the pulser and not due to BCAL channel fluctuation. Separate histograms can be accessed for more detailed study.

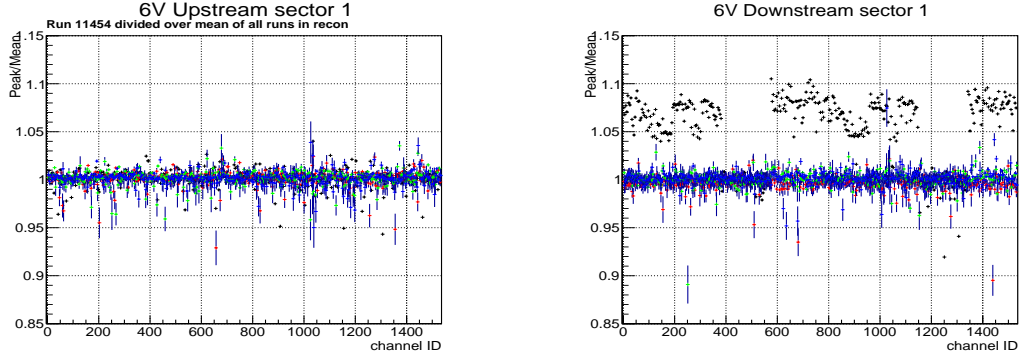


Figure 3.17: (Left) The 16 ratio histograms (a sample is shown in Fig. 3.12) are superimposed into four histograms with four colours indicating different sectors. (Right) Channels with ratios deviating from unity can be visually detected (colour online).

3.4 Known Problems

In this section, we discuss different problems which were detected in the BCAL through the BCAL_LED monitoring system. Section 3.4.1 discusses deviations in SiPMs gains as the main focus of the monitoring system. Section 3.4.2 discusses failures in LED bias distribution boards on a quadrant level. Problems with identification of BCAL_LED events have been discussed in section 3.1.1.

3.4.1 Drifting BCAL Channels

In order to, achieve the main goal of the LED pulser system, which is to detect and verify drifts in the relative gains for BCAL channels, we developed a script to calculate the normalized pulse peak for every channel over the run period. The relative gain (ratio of normalized pulse peaks) between upstream and downstream BCAL channels is used to identify LED pulser fluctuations, such that when the LED pulser signal changes the same effect will be observed by both the upstream and downstream channels. In that case we ignore the fluctuation as it is not a subject of this study, although the assigned coordinator in GlueX would record such cases and decide on

an appropriate action.

On the other hand, observing a drift in the relative gain for far and near LED pulsers confirms that the change is caused by a drift in BCAL channel gain and not a drift in the LED pulser. A script was written that can plot the profile of all 1536 BCAL channels over the run period. Applying a threshold of 1% drift, only 9 channels exceeded that threshold over the spring 2017 run period. A plot representing the worst five drifting channels is shown in Fig 3.18. Each row represents the normalized pulse peak for a pair of BCAL channels. The two leftmost columns show the upstream channel while the two rightmost columns show the downstream channel of the same module, layer and sector. Each channel is pulsed by the upstream pulser on the left and the downstream pulser on the right. The top four rows show that the downstream channels are relatively stable around the unity, while the upstream channels show clear deviations from the unity. The drift is persistent when pulsed by either the upstream and downstream pulsers, which indicates that the drift is in the SiPM gains and not in the pulser signal. The bottom row shows a clear drift in the downstream channel for the upstream pulser while the same channel is stable with the downstream pulser. The upstream channel is stable with both pulsers which indicates the drift is in the downstream SiPM gain. The CALWG decided the SiPM channel represented by the top row in Fig 3.18 is unreliable and has been turned off since.

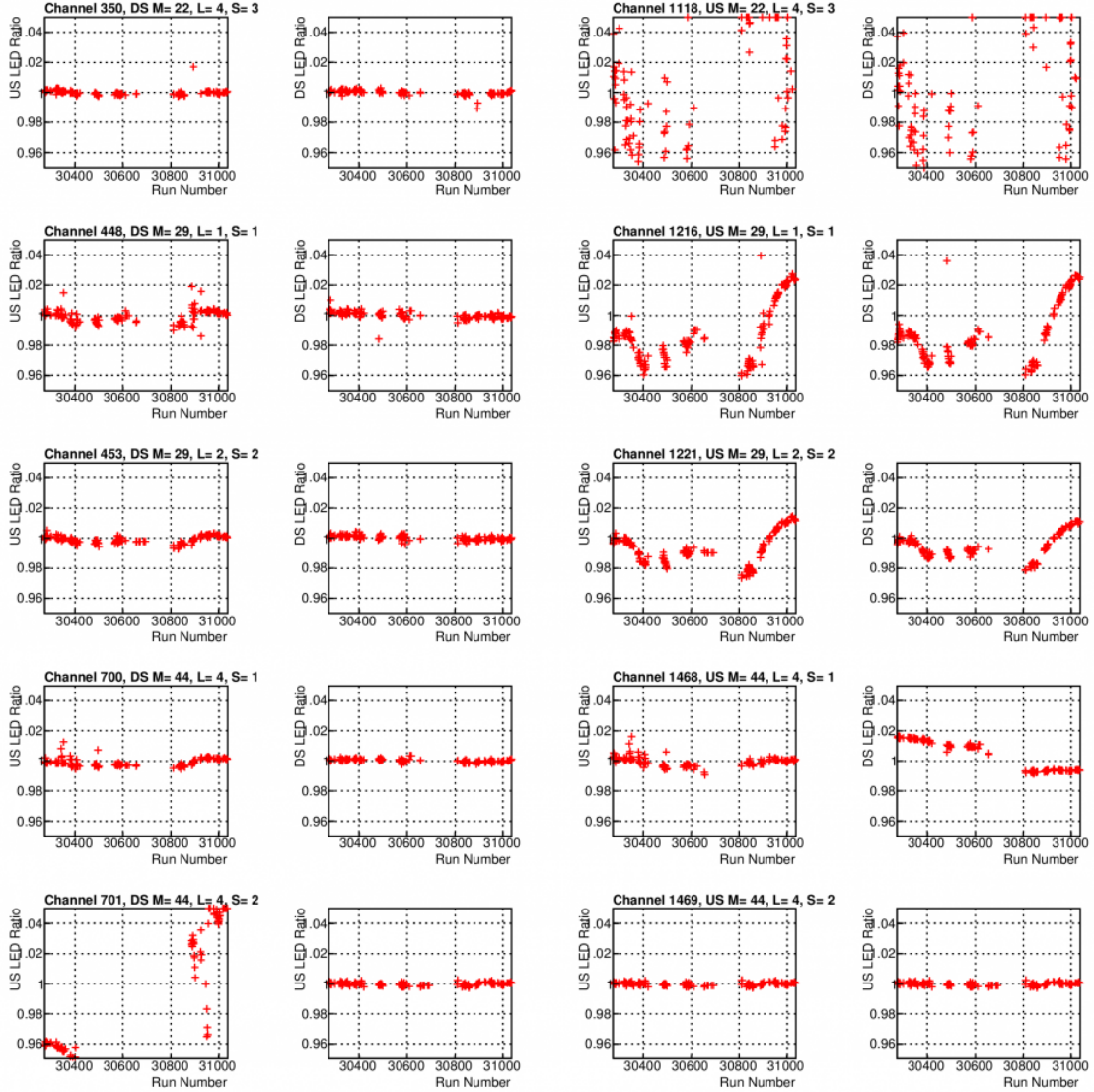


Figure 3.18: The normalized pulse peak profile of five channel pairs is plotted over the spring 2017 run period. Each row represents a pair of channels. The two leftmost columns show the downstream channel while the two rightmost columns show the upstream channel of the same module, layer and sector. Each channel was pulsed by the upstream pulser on left and the downstream pulser on the right [50]. The top four rows show that the downstream channels are relatively stable around the unity, while the upstream channels show clear deviations from the unity. The drift is persistent when pulsed by either the upstream and downstream pulsers, which indicates that the drift is in the SiPM gains and not in the pulser signal. The bottom row shows a clear drift in the downstream channel for the upstream pulser while the same channel is stable with the downstream pulser. The upstream channel is stable with both pulsers which indicates the drift is in the downstream SiPM gain.

Upon studying LED pulser data over the spring 2018 run period data set, a general drift was observed in the normalized pulse peak over the run period. The drift seems to originate from the LED controller and not from the SiPMs, as it manifests in all channels on all pulsing modes and cancels out in the relative gain of a downstream channel to it's conjugate upstream channel. Fig 3.19 shows an example of a downstream channel (channel 203) normalized pulse peak (first row) exhibiting the drift, which cancels in the second row upon dividing over the normalized pulse peak of the upstream conjugate channel (channel 971).

After studying the normalized pulse peaks, the relative gains were studied next. A fluctuation of more than 1% in relative gain can be seen in only three channels as shown in Fig 3.20. The same three channels exhibited fluctuations in spring 2017 run period. All other channels seem to have less than 1% fluctuation over the run period [51].

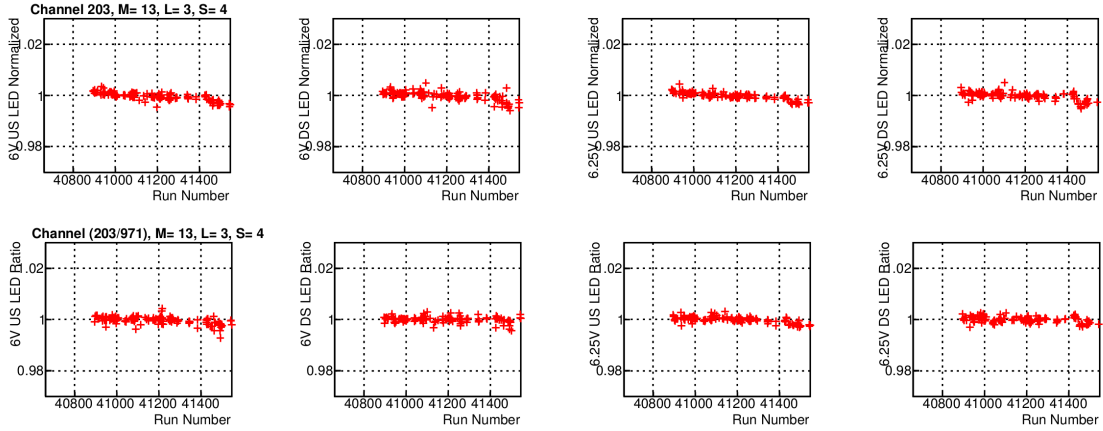


Figure 3.19: A general drift is observed in the pulse peak for the BCAL LED response over spring 2018. The first row represents a downstream channel normalized pulse peak exhibiting the drift which largely cancels in the second row upon dividing over the normalized pulse peak of the upstream conjugate channel [51].

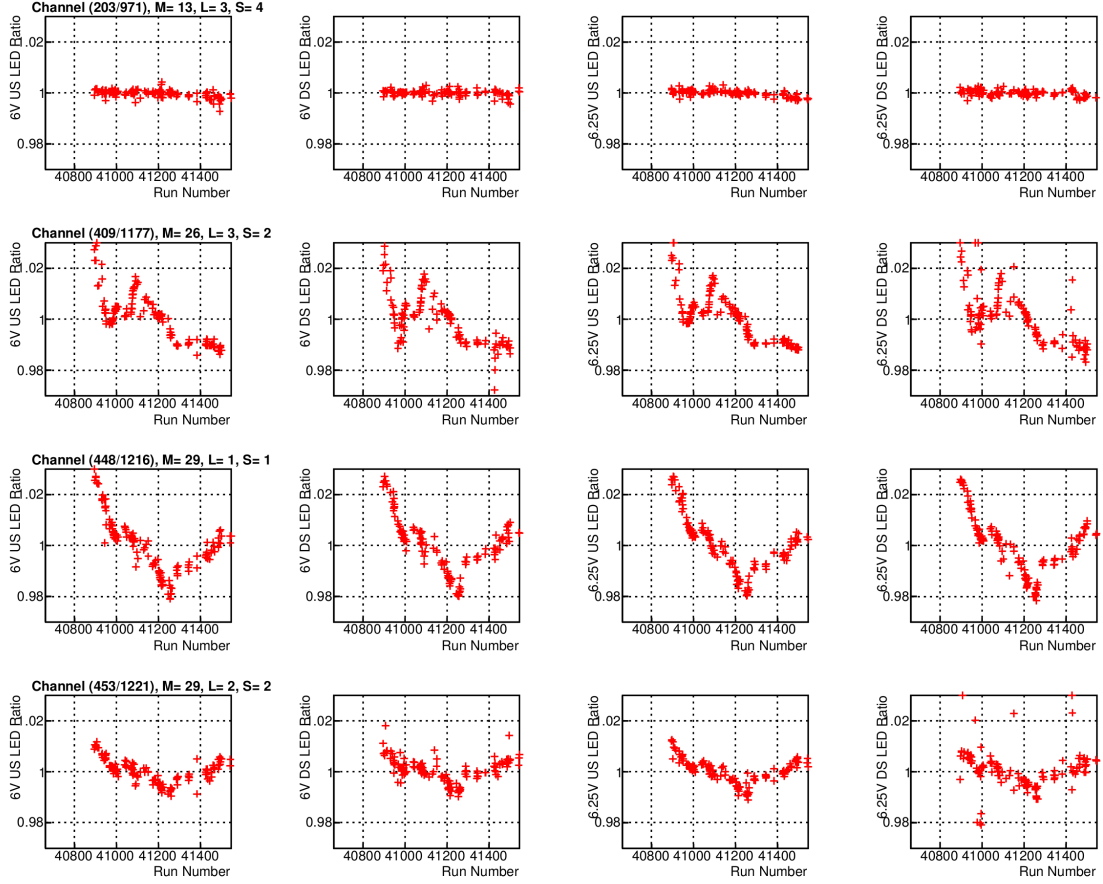


Figure 3.20: The PSPP profile of four channel pairs over spring 2018 run period is graphed. Each row represents the ratio between a pair of channels (downstream/upstream) over the four pulser modes (6 V upstream, 6 V downstream, 6.25 V upstream, 6.25 V downstream). The first row represents a well behaved pair for reference. Rows 2-4 show three pairs with misbehaving channels, yet all within 2% from the unit baseline. [51].

3.4.2 Failing Quadrants

We studied the evolution of number of hits related to LED triggers over the fall 2018 run period. The results show that some quadrants fail to produce a signal indicated by the "quantized" fluctuations in the number of hits. Fig. 3.21 shows a peak at 1536 where all channels are being pulsed with a tail indicating some LED are not firing all the time. A second peak at lower number of hits indicates that one quadrant is failing to produce a signal. This is consistent with the number of channels in each quadrant which is 384 channels (16 channels per each of the 12 modules per each side). We wrote a script which summarizes the occupancy of different quadrants in a single plot. The script checks which quadrants are being pulsed based on occupancy of the majority of channels in that quadrant and compares that to the BCAL_LED trigger. An example plot is shown in Fig. 3.22.

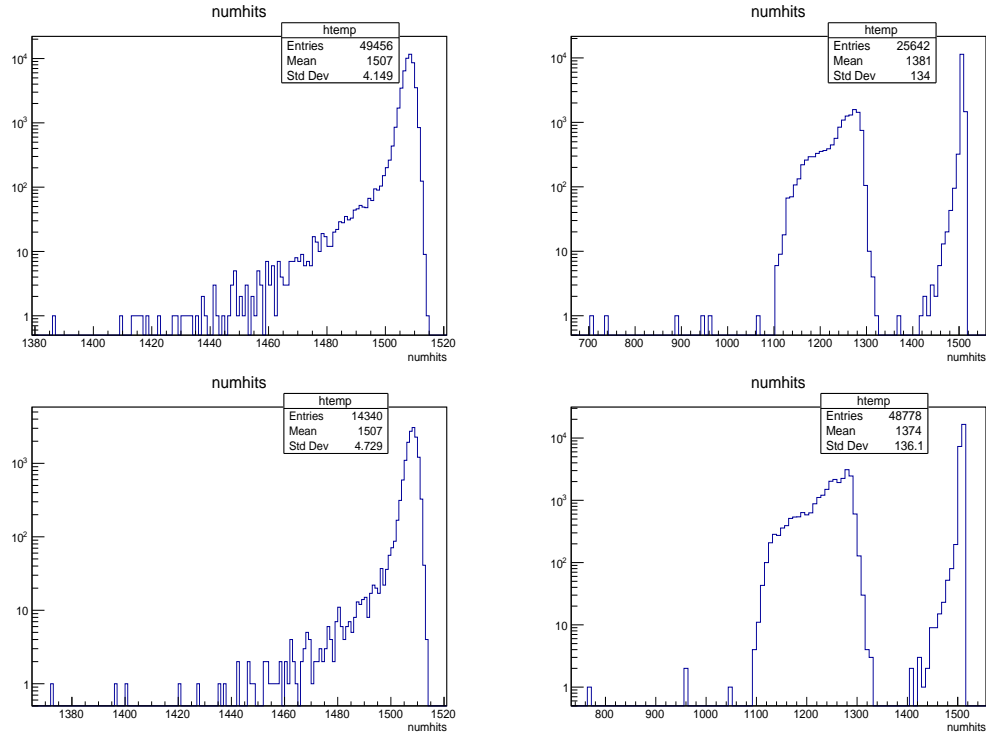


Figure 3.21: Evolution of the number of hits for LED events over the fall 2018 run period. The peak around 1536 indicates that all channels are being pulsed. The tail on the right indicates that sometime few LEDs fail to fire. A second peak at lower number of hits indicates a quadrant is failing to produce a signal.

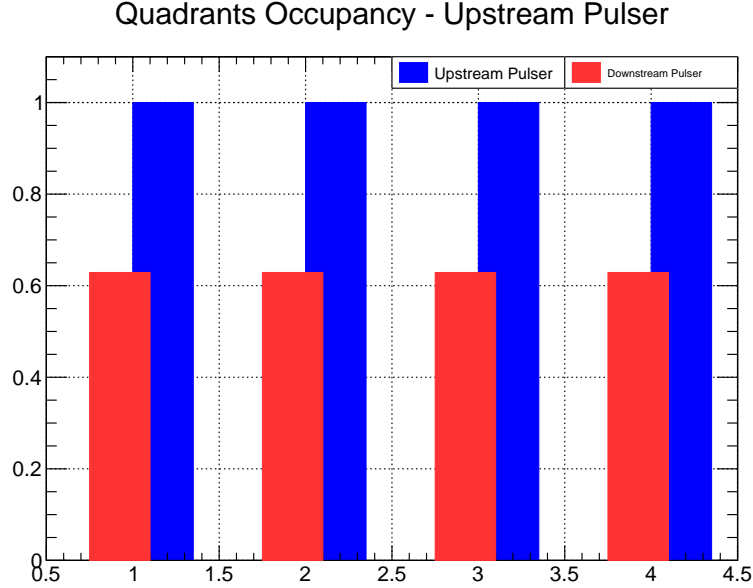


Figure 3.22: Example plots showing the occupancy of different quadrants in the BCAL from run 61580. Occupancy is calculated as the ratio between the number of pulser triggers to the number of events where at least 192 channels (half) in the quadrant record a pulse when a trigger is found for the upstream (blue) and downstream (red) pulsers. As we can see the downstream pulser is failing to pulse all quadrants in $\sim 40\%$ of the events (colour online).

3.5 Pedestal Study

A plugin¹⁴ and plotting scripts were created to study the behaviour of width and mean of pedestals in the BCAL as a function of temperature and SiPM overbias voltage (V_{OB}). A previous study has been done in 2015 [52]. The motivation of the study herein is to see if the SiPMs had degraded since 2015. The study can also guide the experimenters in choosing the optimum values for overbias and temperature for the SiPMs. This plugin can also be used to monitor the overbias-temperature compensation circuits in the SiPM front-board.

The data sets for this analysis include [53]:

1. Dedicated LED runs at 5° , 10° and 18° C with $V_{OB} = 0-2$ V increased in 0.2 V

¹⁴A plugin is a code module which can be used with GlueX software packages to pass user customized commands to the data analysis program.

steps.

2. Runs with LED trigger but LEDs turned off (Pedestal Only).
3. Low voltage (LV) (SiPMs turned off) runs.

An example distribution of pedestals is shown in Fig 3.23, on a linear scale (left) and log scale (right), with the latter showing the small background at higher ADC counts. Distributions are fit using Gaussian functions over a range of four times the value of the Root Mean Square (RMS) centered around the mean of the histogram (range = $[h_{Mean} - 2h_{RMS}, h_{Mean} + 2h_{RMS}]$, where h_{Mean} = histogram mean, h_{RMS} = histogram root mean square).

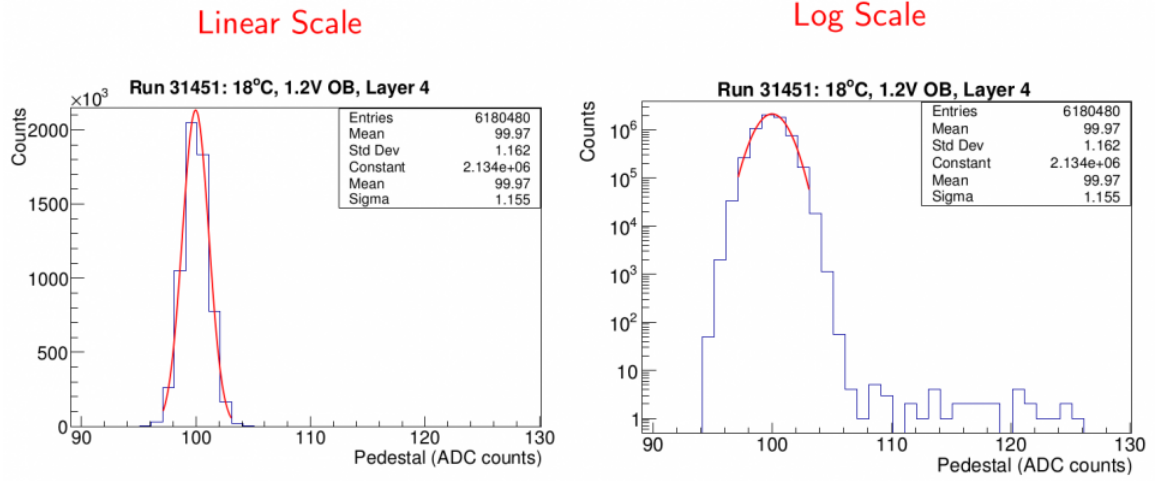


Figure 3.23: Example pedestal distribution and fitting for all channels in layer 4 at 1.2 V overbias and 18° [54] (colour online).

The widths and means of the fits are plotted versus overbias voltage in Fig 3.24. Each graph is fit using a function $W(V_{OB}) = W(V_{OB} = 0) + A_1 e^{(A_1 V_{OB})}$ with A and B as the fitting parameters. An example plot for 10° C is shown. The top two panels show the width and mean for "LEDs on" runs while the bottom two panels show "LEDs off" (Pedestal Only) runs. The left most point indicates LV runs during which the SiPMs

are turned off and the readout is just the current passing through the front-board. Therefore these LV points are excluded from the fits. The pedestal distribution width increases with increasing the overbias as expected. The effect is multiplied with each successive layer within each sector, which is expected as a layer-one channel consists of a single SiPM, a layer-two channel consists of two SiPMs and so on. The pedestal distribution mean starts with inverted behaviour with layer-one higher than layer-two and so on. Then a crossover occurs restoring the normal behaviour. The V_{OB} for crossover depends on temperature.

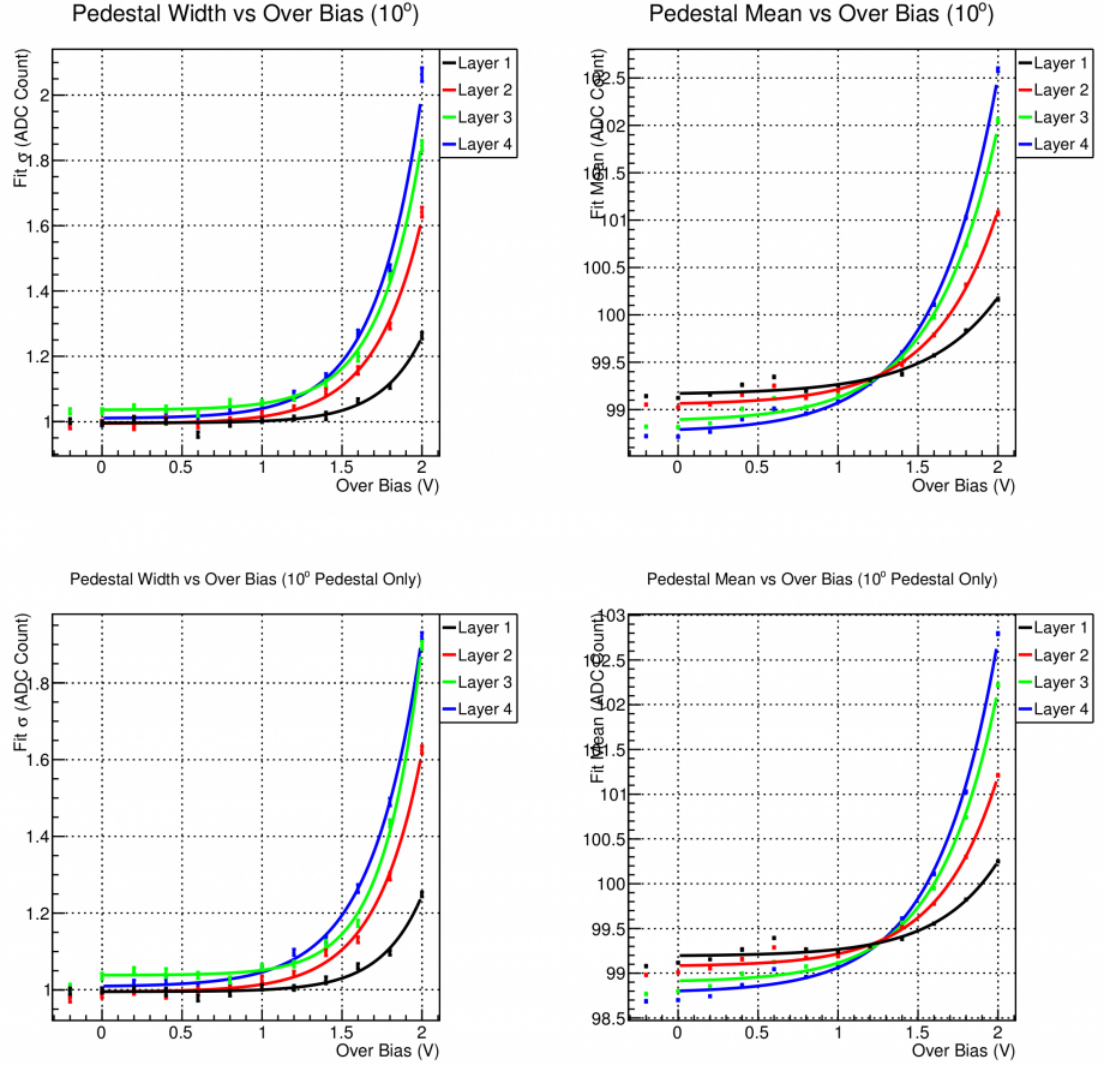


Figure 3.24: Pedestal distribution width and mean versus SiPM overbias at 10°. The top two panels show the width and mean for LEDs on runs while the bottom two panels show LEDs off (pedestal only) runs. The left-most point indicates LV runs and therefore is excluded from the fits [54] (colour online).

The behaviour of pedestal width and mean vs over bias and temperature seems to agree with expectations and the previous study carried out in 2015 and shown in Fig 3.25 ¹⁵.

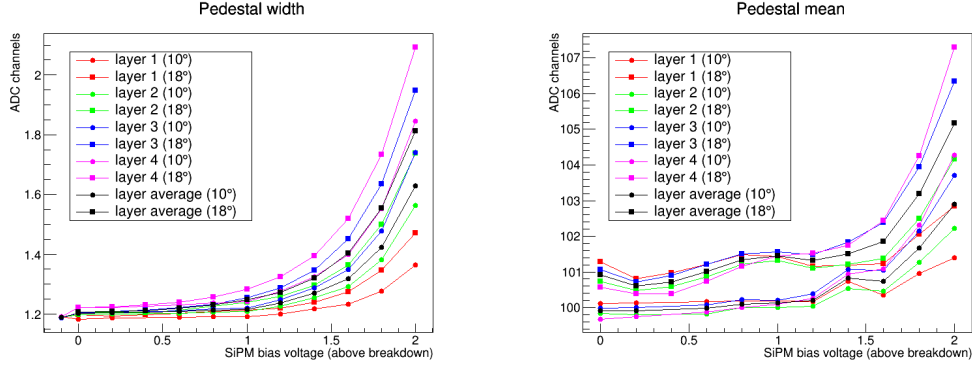


Figure 3.25: Pedestal distribution width (left) and mean (right) versus SiPM overbias at 10 and 18° according the study carried out in 2015 [52] (colour online).

3.6 Conclusions

In this chapter we discussed the BCAL_LED gain monitoring system and efforts to implement it which started in spring of 2016. The system uses LED pulses with controlled bias to monitor gains of SiPM in the BCAL. FP triggers and number of hits in the BCAL are used to identify BCAL_LED events. A monitoring plugin and plotting script were used for offline monitoring of BCAL channels gains since 2016. Few drifting channels have been identified and one channel has been disabled. A two-tier monitoring system was proposed. The system adds a daily expert monitoring of relative gain tier to the end of run period monitoring tier. This system has been implemented for fall 2019, spring 2020 and summer 2020 data taking. We also reported on a bug in the BCAL_LED event selection and an improved filter to exclude GTP physics triggers from leaking to the BCAL_LED data stream. New histograms were developed to monitor BCAL_LED front panel trigger failures and failing quadrants.

¹⁵Members of the group have continued these studies for spring 2020 and will also do for fall 2020.

We also studied the dependence of the width and mean of pedestals in BCAL channels on temperature and SiPM overbias voltage, and this work is ongoing in GlueX.

Chapter 4

Data Analysis

CEBAF typically runs between January and April and for a few more weeks between September and December of each year. These run periods are called the spring and fall periods, respectively. The run conditions vary between and within run periods; however, in general an event (trigger) is recorded when the tagger (TAGH or TAGM) records a hit by a deflected electron in coincidence with energy deposition in a one or more of the detector subsystems (usually PS, BCAL and FCAL). The spring 2016 run period was planned for commissioning the detector, so only opportunistic physics data were recorded during that run period after the commissioning was done. This included data recorded with 0° and 90° beam polarizations and the amorphous radiator. Accelerator problems prevented the collection of physics data during the fall of 2016. The spring 2017 run period was the first production run period during which 50×10^9 triggers were recorded. Two more beam polarizations (-45° and 45°) were introduced in this run period for a total of four beam polarizations, in addition to data recorded with the amorphous radiator. More accelerator problems prevented the collection of physics data during the fall of 2017. During the spring 2018 run period 145×10^9 triggers were recorded with the same four beam polarizations. The fall 2018 run period included the commissioning for the PrimEx experiment, so only 78×10^9 triggers were recorded during this run period. This run period also included

a low beam-energy data set during which the photon beam had a coherent peak at around 7 GeV rather than the nominal coherent peak at around 9 GeV. This low beam energy overlaps with beam energy used in the CLAS experiment which was carried out at Hall B at JLab. Since then, data was taken in spring 2020 and summer 2020. Preliminary GlueX cross-sections from $\gamma p \rightarrow \eta p$ have been extracted and compared to those from CLAS [55].

The data in this thesis include only the spring 2017, spring 2018 and fall 2018 data. In this chapter, the selection of the b_1 events is described, the methodology for extracting the moments, PWAs and cross-section from the data is detailed, and the inputs to the fits are discussed.

4.1 Event Selection

The goal of event selection is to clean the data sample by removing contributions from other decay channels and purifying it by suppressing the background and thereby increasing the signal-to-background ratio. These data samples can then be used to investigate physics observables like cross sections, AMs and PWAs. In order to minimize computational requirements, event selection is divided into two stages. In each stage a number of conditions are applied to the data set to remove events which are unlikely to contain b_1 events. This reduces both the file size and the time needed to process the data. In this thesis we focus on the decay channel of the b_1 with the highest combined branching fraction [5], indicated in parentheses, and referred to as ‘omegapi’. This channel is

$$b_1 \rightarrow \pi^0 \omega, \quad \omega \rightarrow \pi^+ \pi^- \pi^0, \quad \pi^0 \rightarrow 2\gamma$$

$$\text{BR}_{combined} \approx (1.0) \cdot (0.892 \pm 0.007) \cdot (0.98823 \pm 0.00034)$$

4.1.1 Stage I

The selection starts by matching events to the topology of the reaction we are studying. The topology of the $\omega\pi^0$ channel is $p\pi^+\pi^-\pi^0\pi^0$ (the recoil proton, the neutral pion from the b_1 decay and the three pions two charged and one neutral from the ω decay). We are studying exclusive events which means that all final state particles must be detected¹. The choice of studying exclusive events increases signal purity and reduces file size and processing time but it also reduces the number of signal events.

The number of tracks or showers recorded in an event cannot be used alone to exclude events. This becomes clear when we consider that multiple showers could be reconstructed as a single shower if they are close in the calorimeter. Also, spurious showers can be caused by electromagnetic split-offs where a photon or a charged particle generates multiple charged particles in the calorimeter, which are then reconstructed as multiple showers. In order to make sure that we do not discard good events due to such spurious tracks or showers, we apply the default GlueX analysis cut which allows 3 extra charged tracks and 15 extra neutral showers. For each of the events which match this criteria particle combinations (combos) are formed. For the $b_1 \rightarrow \pi^+\pi^-\pi^0\pi^0$ channel, particle combos include two positively-charged tracks (the π^+ and the recoil proton), one negatively-charged track (π^-), and four neutral showers ($2\pi^0 \rightarrow 4\gamma$).

In the first stage, mostly standard GlueX cuts are applied, starting with PID cuts.

¹An inclusive event, on the other hand, means that one or more of the final state particles are not detected directly.

The energy loss of a charged track per unit length (dE/dx) as measured by the CDC is used to identify charged particle species up to $1 \text{ GeV}/c$ in momentum. An example plot in Fig. 2.12 shows dE/dx measured by the CDC as a function of the momentum of the positively charged particle. In this stage, a loose cut is applied to exclude misidentified particles. Positively charged particles with low energy loss compared to the upper proton band are excluded by the cut.

Loose cuts on the invariant mass of the decaying particles follow. These cuts are applied on the b_1 decaying to $\omega\pi^0$, the ω decaying to $\pi^+\pi^-\pi^0$ and the π^0 decaying to 2γ . If the reconstructed invariant mass of the daughters is far from the expected mass of the parent particle, the event is discarded. These cuts also reduce file size and processing time. Equation 4.1 shows these cuts for the decaying b_1 , ω , and π^0 .

$$\begin{aligned}
\text{Decaying } \pi^0 : \quad & 0.08 \text{ GeV} < m_{\pi^0} < 0.19 \text{ GeV} \\
\text{Decaying } \omega : \quad & 0.5 \text{ GeV} < m_{\omega} < 1.1 \text{ GeV} \\
\text{Decaying } b_1 : \quad & 0.5 \text{ GeV} < m_{b_1} < 2.5 \text{ GeV}
\end{aligned} \tag{4.1}$$

The next step is a loose missing mass (MM) cut. MM is the invariant mass difference between the initial and the final state particles. For the $\omega\pi^0$ decay channel it is defined in Eq. 4.2. This cut helps selecting exclusive events. An exclusive event with no extra particles produced should have vanishing MM. However, a loose cut requiring $|\text{MM}^2| < 0.05 \text{ GeV}^2$ is applied. This cut allows exclusive events with excess showers which may be present due to electronic noise or split-offs, but rejects events which are unlikely to be exclusive events.

$$MM^2 = (p_i - p_f)^2 = \left(p_\gamma^{\text{beam}} + p_{\text{proton}}^{\text{target}} - (p_{\text{proton}}^{\text{recoil}} + p_{\pi^+} + p_{\pi^-} + p_{\gamma,1} + p_{\gamma,2} + p_{\gamma,3} + p_{\gamma,4}) \right)^2 \quad (4.2)$$

The last of the cuts in Stage I is a set of particle identification timing (PIDT) cuts. As explained in Ch.2, the accelerator produces beam bunches at intervals of 4 ns. Particles in various detector subsystems need to be matched with the correct RF beam bunch, these cuts help with this matching. These cuts are based on a time of flight each particle would take to reach a detector subsystem, therefore different cuts are applied to select different particle species traveling to different detector subsystems. A summary of the timing cuts used in our analysis is presented in Table 4.1 [56]. Fig. 4.1 shows the Linear momentum distribution of different particles and their time of flight from the spring 2017 run period. Plots representing PIDT cuts for data and MC simulation of the different run periods are represented in App. D. In Sec. 4.2.1 we discuss accidental subtraction, a cut applied to eliminate contributions to the yield by matching particles to the wrong beam bunch.

Particle Species	ST cut	TOF cut	FCAL cut	BCAL cut
Proton	2.5 ns	0.6 ns	2.0 ns	1.0 ns
π^+	2.5 ns	0.5 ns	2.0 ns	1.0 ns
π^-	2.5 ns	0.5 ns	2.0 ns	1.0 ns
γ	—	—	2.5 ns	1.5 ns

Detector Subsystem	ST	TOF	FCAL	BCAL
Timing Resolution	234 ps	105 ps	380 ps	150 ps

Table 4.1: Selection cuts on $|\Delta t_{\text{RF}}|$ for different particle species in ST, TOF, BCAL, and FCAL detector subsystems. A larger cut is used for photons in calorimeters (FCAL and BCAL) due to the time needed for the electromagnetic showers to evolve, shower fluctuations, and the light produced to travel to the photosensors, which could result in a larger $|\Delta t_{\text{RF}}|$; inspection of the BCAL $|\Delta t|$ versus momentum plot in Fig. 4.1 indicates that 1.5 ns is a conservative cut. Typical timing resolutions of the detector subsystems are presented below [57, 58]. In the case of the BCAL, the number shown is the resolution at $E_\gamma=1$ GeV.

4.1.2 Stage II

The second stage of event selection starts with a kinematic fit (KinFit), which combines measured observables (particle positions, momenta, and energies) with a set of conservation laws to calculate a more accurate estimate of the measured observables. As all final state particles momenta and energies are measured in an exclusive event, the KinFit in this case is a χ^2 minimization, where χ^2 is the absolute difference between the measured and fitted observables as shown in Eq. 4.3 [59].

$$\chi^2 = \sum_k \frac{(y_k^{\text{fit}} - y_k^{\text{meas}})^2}{\sigma_k^2} \quad (4.3)$$

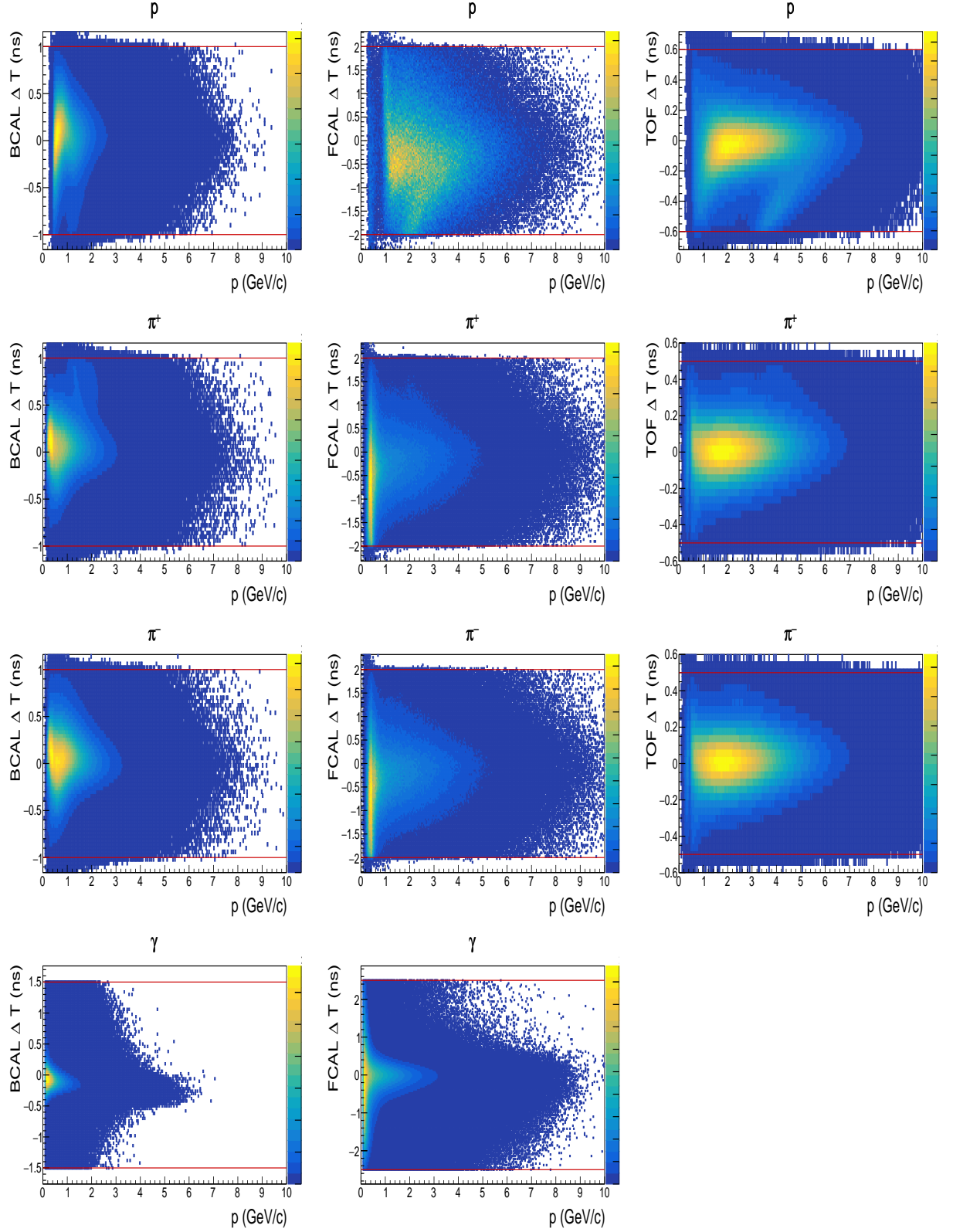


Figure 4.1: Time of flight distribution for the proton, $\pi^+\pi^-$ and γ versus their linear momenta in the BCAL, FCAL and TOF detector subsystems. These plots are produced for with spring 2017 data. The red lines indicate the PIDT selection cuts used in our analysis.

where y_k 's are the measured and fitted observables and σ_k 's are the Gaussian errors on y_k measurement. The KinFit varies the value of each observable to obtain the minimal possible absolute difference between the measured and fitted observables (i.e. minimum χ^2) [59].

In addition to energy and momentum conservation, the KinFit also constrains particles to come from their parent decay vertex and have total invariant mass matching that of the parent. In our case, each of the two photon pairs must originate from a π^0 decay vertex and have the total invariant mass of a π , the two charged pions and a π^0 must trace back to the ω decay vertex and have a total invariant mass matching the invariant mass of the ω . Likewise, the ω and the second π^0 must come from the b_1 decay vertex. While the measured observables may not conform to these constraints due to measurement resolution, missing or misidentified particles, the fitted observables are required to satisfy these constraints.

When the KinFit converges for a particle combo, a confidence level (CL) is calculated and assigned to it. CL quantifies the probability that the minimum χ^2 value for the fit can be produced by a random Probability Distribution Function (PDF). The CL distribution is uniform for a pure signal sample, such that a $\text{CL} > 0.05$ cut will remove 5% of the events in the pure signal sample. Background events tend to converge the fit with a very low CL. Fig. 4.2 is an example, where the b_1 peak in invariant mass of the $\omega\pi^0$ extends to higher CL values, while the backgrounds on the low and high invariant mass sides populates lower CL values. This is why a cut on the low end of CL distribution is a powerful way to eliminate background events while preserving most of the signal events.

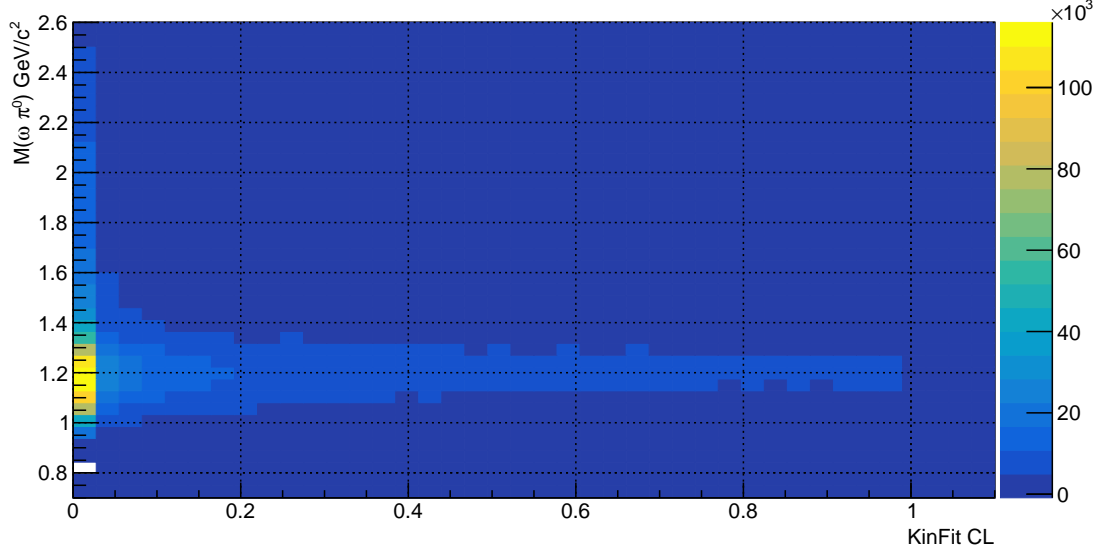


Figure 4.2: The invariant mass of $\omega\pi^0$ after accidentals and ω background subtraction versus the KinFit CL (colour online).

Unfortunately, the optimum CL cut depends on the reaction channel studied. The best cut needs to balance between statistics and purity. A loose CL cut may not eliminate enough background events to obtain a pure enough signal sample for a reliable extraction of physical observables. On the other hand, a tight cut may produce a very pure signal sample, but at the same time discarding a considerable portion of the signal. For the analysis in this thesis, CL cut of 5×10^{-5} is used.

After the KinFit CL cut, a tighter invariant mass cut is applied on the decaying π^0 invariant mass to reject events where the KinFit converged with CL passing the cut but the reconstructed invariant mass is far from the expected value. Therefore a tighter cut is applied on the reconstructed invariant mass of the decaying π^0 's as shown in Eq. 4.4 and Fig. 4.8.

$$\text{Decaying } \pi^0 : \quad 105 \text{ GeV} < m_{\pi^0} < 0.165 \text{ GeV} \quad (4.4)$$

Next, a cut on the beam energy is applied to suppress background arising from baryonic reaction channels. For example the reaction $\gamma p \rightarrow \omega \Delta^+ \rightarrow \omega \pi^0 p$ has the same final state particles as the b_1 decay. Events with beam energy less than 6 GeV are discarded.

Following the beam energy cut, a set of cuts are applied to reject events where the measured observables may suffer from reduced precision of detector subsystems near their edges. The kinematic fit constrains the event vertex to lie within the target volume. However, near the edges a particle may interact with the container material producing complicated reactions and final states, which are not easy to account for. A cut on the z-position of the kinematically-fit vertex is applied to reject events outside a virtual cylinder located fully inside the target by allowing only events with z position between 52-78 cm and a radius less than 1 cm from the target center. These cuts are represented in Fig. 4.3.

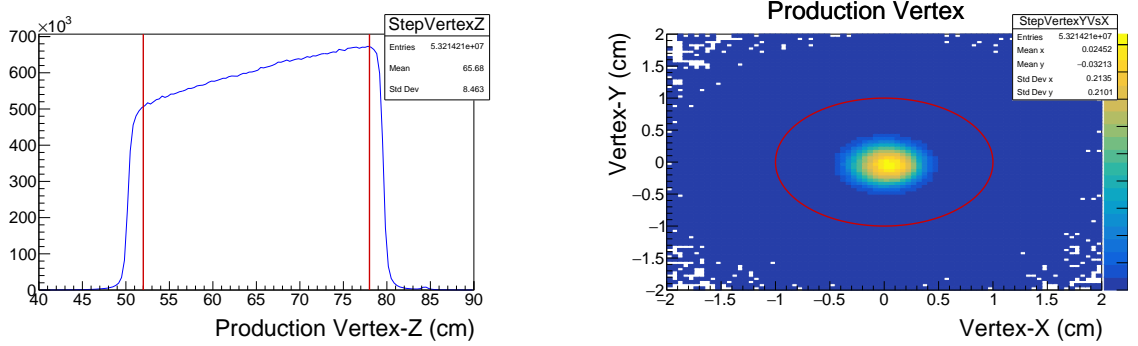


Figure 4.3: (left) The z-position, (right) the x-position versus the y-position of the kinematically-fit vertex. The red lines and the red circle indicate the cut limits (colour online).

The next step in detector edge cuts are cuts on calorimeters edges. Neutral showers may be only partially reconstructed in these regions due to escaping or undetected energy. Therefore, measured observables from these regions are unreliable and events

with showers in these regions are rejected through a set of cuts. This set of cuts are referred to as fiducial cuts. The standard fiducial cuts in GlueX collaboration reject events with neutral showers near the FCAL beam hole, the outer edges of the FCAL and the BCAL on the downstream side as shown in Fig. 4.4. This is done by rejecting events with neutral showers with polar angle θ less than 2.0° and in the $10.3 - 11.9^\circ$ range. These cuts are optimized based on simulation to reject most of the poorly reconstructed showers while keeping most of the signal events.

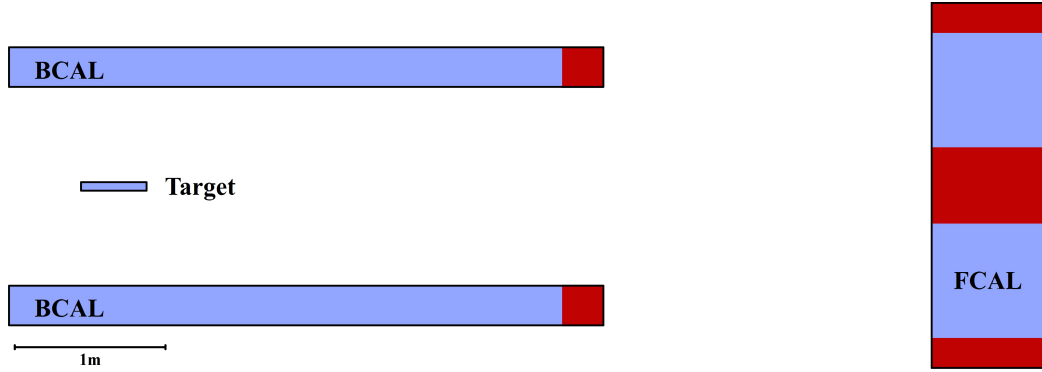


Figure 4.4: A side-view of the GlueX detector representing only the target, BCAL and FCAL. The red regions represent fiducial cuts applied around the beam hole in the FCAL, the edges of the FCAL and the downstream edge of the BCAL. Reconstruction is unreliable in these regions (colour online).

Likewise, a cut is applied on the recoil proton momentum as the reconstruction suffers due to the lack of tracking information from the CDC. A fiducial cut on the proton momentum requires that $P_{\text{recoil}} > 0.25 \text{ GeV}$.

The number of events passing through each of our selection cuts for the spring 2017 run period is presented in Fig. 4.5. The effect of the different selection cuts on the invariant mass of the 4π final state can be observed in Fig. 4.6. The PID cut rejects a lot of the high invariant mass events. The PID ΔT excludes more events at the low invariant mass events. The invariant mass cut highlights the b_1 peak from the

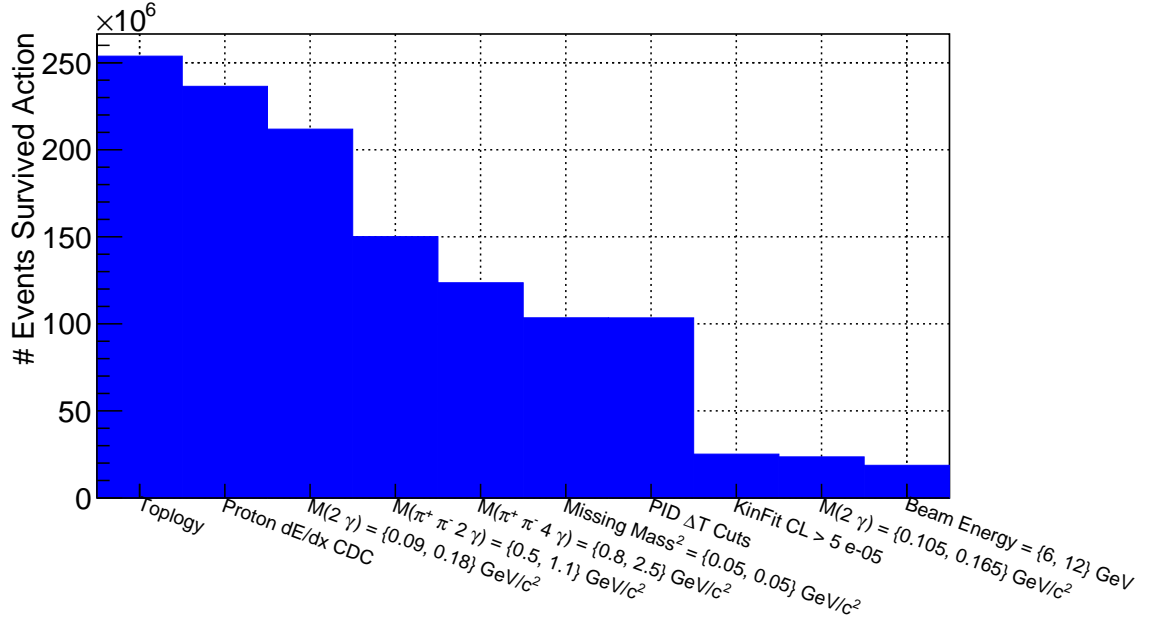


Figure 4.5: The number of events passing through each of the selection cuts in spring 2017 run period.

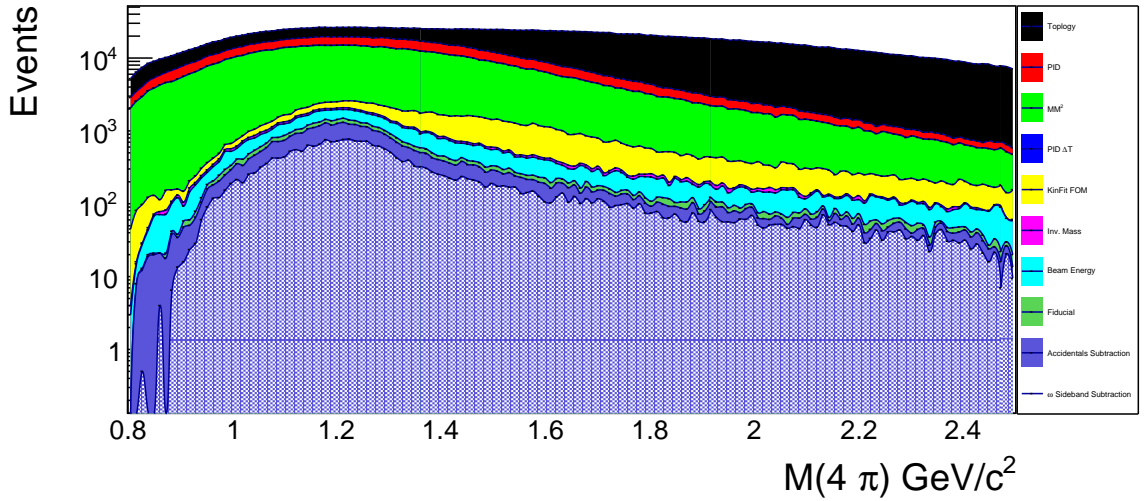


Figure 4.6: Invariant mass spectra of the $\omega\pi^0$. The effect of various cuts on the invariant mass spectra is shown, with the cut names listed on the legend (colour online).

background on either sides. The fiducial cut is more effective at eliminating events far from the b_1 peak. The effect of our selection cuts on the invariant mass of the $\gamma\gamma$

and $\pi^+\pi^-\pi^0$ are presented in App. E. Accidental and ω side band subtractions will be discussed in the following sections.

4.2 Analysis Methodology

Every event is defined by a time window initiated by a trigger identifying the corresponding beam bucket (more details in Sec. 2.5.1. All particles reconstructed within this time window are recorded to this event. A single event could include more than one reaction. Due to the indistinguishability of particles, there is no definite way of verifying which particle is part of which reaction. Apart from obeying physical laws, which is the assumption we enforce by our applying selection cuts, all possible combinations of particle should be considered as a candidate.

In our final state of interest, a particle combination (sometimes referred to as a combo) is formed of a beam photon, proton, π^+ , π^- and two π^0 . A single event contains many particle combination due to extra particles (e.g. two protons are reconstructed as both are possible candidates) or the combinatorics of the four γ which could be arranged in three different ways to form two π^0 . We accept all candidates that pass our cuts and assign to the whole event a weight equal to the reciprocal of the number of candidates.

In the following sections we will discuss weights assigned to each particle combination to account for misidentified beam photons and $\pi^+\pi^+\pi^0$ background under the ω peak.

4.2.1 Accidental Subtraction

As mentioned earlier, contributions to the yield may arise due to matching particles to the wrong beam bunch. A sample Δt_{RF} distribution is shown in Fig. 4.7. The peak central at 0 ns represents the events with the reconstructed using the correct beam bunch (prompt), while peaks on either side represent events assigned to the wrong beam bunch (accidentals). Applying a cut to only allow events from the prompt peak still allows contributions from accidentals to leak under the prompt peak. Therefore, the yield contribution due to accidental beam bunches is calculated and subtracted from the prompt peak yield. In our analysis, 3 accidental beam bunches on either side of the prompt peak are used to estimate the accidentals contribution, thereby excluding the accidental peaks adjacent to the prompt peak as they contain contributions from the prompt peak. Fig. 4.7 shows the cuts applied to define the prompt peak (defined as the range between the green lines) and the accidental peaks (defined as the areas between the red lines). The accidentals contribution is scaled by a factor of $\frac{1}{6}$ as it represents the contribution from 6 accidental peaks. As mentioned previously, the effect of accidental subtraction on the b_1 yield is shown in Fig. 4.6.

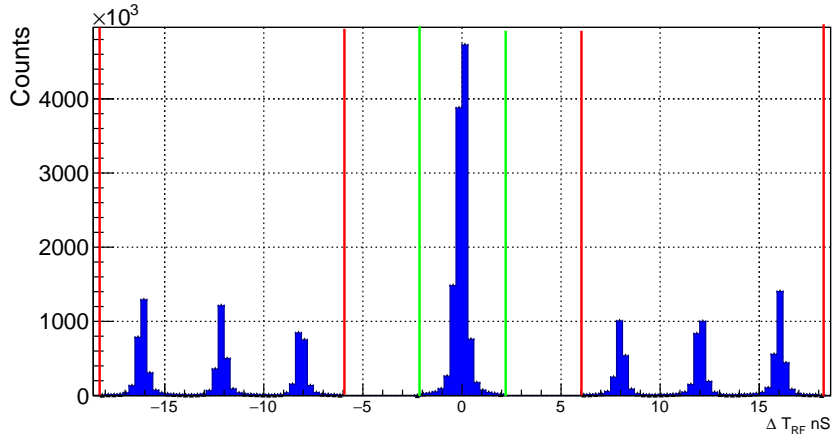


Figure 4.7: Δt_{RF} distribution from data. The prompt peak at 0 ns represents events reconstructed with correct beam bunch with contribution from accidentals. The peaks on either side are used for accidental subtraction, as described in Section 4.2.1. The peaks at ± 4 ns are excluded from the plot and the subtraction to avoid leakage from the prompt peak (colour online).

4.2.2 ω Side-Band Subtraction

Fig. 4.8 presents the invariant mass distributions of the reconstructed $\gamma\gamma$, $\pi^+\pi^-\pi^0$ and $\omega\pi^0$ from spring 2017 data and MC simulations². There is substantial background under the ω peak including misidentified $\rho \rightarrow \pi^+\pi^-$ with a wrong π^0 , $\rho \rightarrow \pi^+\pi^-\pi^0$ and $\omega \rightarrow \pi^+\pi^-\gamma$ with a spurious γ . This background would affect the extraction of physics observables from the yield.

In order to account for the contribution of this background, an invariant mass side-band subtraction is performed. The ω peak is selected to be within three σ of the Gaussian fit, indicated by the red lines. The side-band regions are selected on either side of the ω peak with one σ width and separated from the peak by two σ to reduce leakage of the ω peak to the side bands, indicated by the blue lines. Similarly to the subtraction of accidentals, the contribution of the side bands to the b_1 yield

²Invariant mass plots for spring 2018 and fall 2018 data and MC are presented in the App. C.

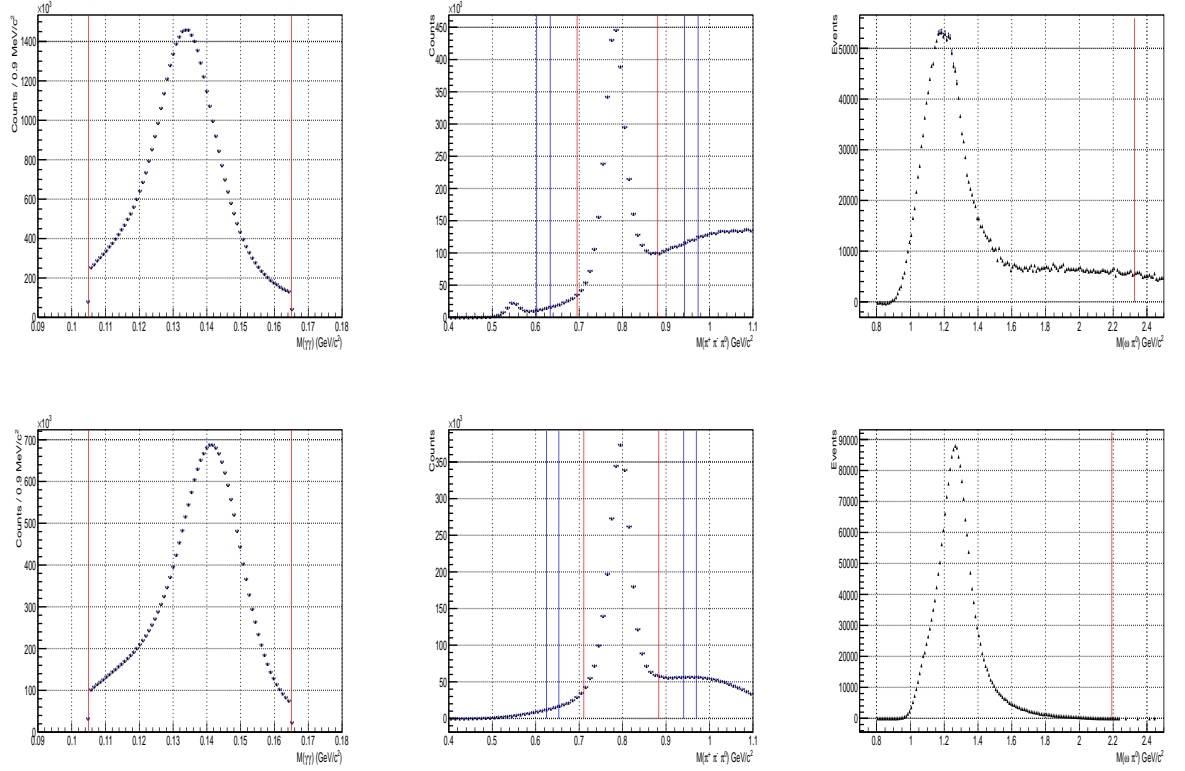


Figure 4.8: Invariant mass of $\gamma\gamma$ (left) after event selection cuts, $\pi^+\pi^-\pi^0$ (middle) after subtracting accidentals and $\omega\pi^0$ (right) after subtracting the accidentals and ω background. The top row is produced with spring 2017 data and the bottom row is produced with MC simulation. The red lines indicate the selection cuts for π^0 , ω and $\omega\pi^0$. The blue lines indicate the side-bands used to calculate the background under the ω peak. The $\omega\pi^0$ range is defined by 8.7σ above and below the b_1 peak.

is calculated and subtracted from the yield calculated from the ω peak. The effect of the side band subtraction is shown in Fig. 4.6. The $\omega\pi^0$ yield before, after and from the ω side band subtraction is shown in Fig. 4.9. This method assumes a linear background, an improved model of the background is needed to introduce more complex background subtraction methods. The systematic uncertainty associated with the location and width of the side-bands is discussed in Ch. 7. The choice of the subtraction method is another source of systematic uncertainty that needs to be studied in the future.

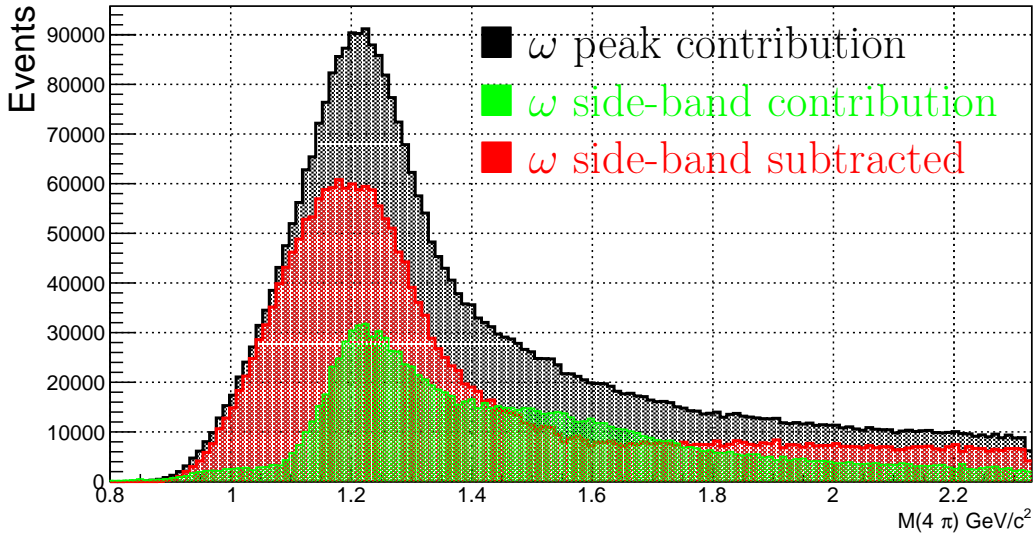


Figure 4.9: Invariant mass of the $\omega\pi^0$. The black curve represents events reconstructed from the ω peak including contribution from the ω side bands. The green curve represents events reconstructed with contribution from the ω side bands. The red curve represents the black curve after side band subtraction (colour online).

4.3 Fit Models

As discussed in Sec. 1.4.3, different models can be used to fit the distribution of the b_1 decay angles. Each model provides insights on a different aspect of the reaction. In the following paragraphs we will discuss the mathematical technique. We will present the two models used to fit the data in the following subsections.

Fitting is done using Minuit2 software [60] with a maximum log-likelihood fitting method. A likelihood function calculates the probability of generating the behaviour of the experimentally measured data by a set of parameterized distributions. The maximum likelihood method aims to find the set of values for the parameters maximizing the likelihood and can be visualized as a peak in the hyper-surface of probability.

As the natural logarithm is a monotonically increasing function, a maximum in the likelihood is a maximum in the log-likelihood, which is typically used in fitting. The log of the likelihood function has an advantage when the sample is made up of independent observations. In that case, the logarithm transforms the product of densities into a sum. This is easier to analyse and also provides better stability as products tend to converge quickly to zero or to infinity, if the average single observation density is less than or greater than 1. Sums on the other hand are more stable. This is important when the maximum likelihood problem is solved numerically on computers where limited machine precision does not allow to distinguish between a very small number and zero and a very large number from infinity.

4.3.1 Angular Moments

The AMs model is based on a set of 25 orthogonal functions which form a basis for the four-dimensional $\omega\pi$ decay angles space. As explained in Sec. 1.4.3, the AMs expansion assumes the spin-parity states allowed for the $\omega\pi$ system to be $J^P = 1^\pm, 0^-$. This assumption is used to truncate the infinite set of AMs to the effectively complete set of 25 AMs mentioned earlier. Being model independent allows the AMs to provide a description of the b_1 decay with no ambiguity.

The model is implemented as PDF to be used with AmpTools [61] software. Generated and accepted flat MC samples are used as input for AmpTools along with the data³. The fit is binned in the $\omega\pi$ invariant mass, Mandelstam-t and beam energy. This is done through a special library which we wrote for this purpose. The fit is performed independently for each of the four beam polarization orientations and for the unpolarized beam.

4.3.2 Partial Waves Amplitudes

The PWAs model is based on a model by members of the JPAC group. The model assumes the $\omega\pi$ system can have total spin up to be $J = 2$, includes partial waves up to D-wave and a fourth order polynomial distribution of the ω 's three pion Dalitz plot. Under these assumptions, the model has 28 fit parameters. This model suffers from the intrinsic ambiguity inherent in the definition of intensity as the square of the amplitude.

Including 0^\pm ⁴, 1^\pm , 2^\pm spin-parity states for the $\omega\pi$ and allowing partial waves $l = 0, 1, 2$ the fit parameters are:

³A more detailed discussion of the MC sample is provided in Ch. 5.

⁴ 0^+ spin-parity state can not decay to $\omega\pi^0$

- 17 Vertices $V_{\lambda\gamma,\Lambda}^i$

$$0^- \rightarrow V_{+1,0}^{0^-}$$

$$1^+ \rightarrow V_{+1,-1}^{1^+}, V_{+1,0}^{1^+}, V_{+1,+1}^{1^+},$$

$$1^- \rightarrow V_{+1,-1}^{1^-}, V_{+1,0}^{1^-}, V_{+1,+1}^{1^-}$$

$$2^+ \rightarrow V_{+1,-2}^{2^+}, V_{+1,-1}^{2^+}, V_{+1,0}^{2^+}, V_{+1,+1}^{2^+}, V_{+1,+2}^{2^+}$$

$$2^- \rightarrow V_{+1,-2}^{2^-}, V_{+1,-1}^{2^-}, V_{+1,0}^{2^-}, V_{+1,+1}^{2^-}, V_{+1,+2}^{2^-}$$

reduced from 36 parameters by using the symmetry $V_{\lambda\gamma,\Lambda}^i = -\tau_e \tau_i (-1)^\Lambda V_{-\lambda\gamma,-\Lambda}^i$ where $\tau_i = \eta_i (-1)^{J_i}$ is the naturality of the $\omega\pi^0$ state, and τ_e is the naturality of the exchange (assumed to be +1).

- 6 real partial wave amplitudes C_l^i ($C_l = 0$ for odd l when $\eta_i = +1$, and for even l when $\eta_i = -1$)

$$0^- \rightarrow C_1^{0^-}$$

$$1^\pm \rightarrow C_1^{1^\pm}, C_0^{1^\pm}, C_2^{1^\pm} \text{ (where } D/S = \frac{C_2^{1^+}}{C_0^{1^+}})$$

$$2^\pm \rightarrow C_1^{2^\pm}, C_2^{2^\pm}$$

- Four Dalitz parameters α, β, γ and δ .
- Beam photon polarization fraction P_γ .

$V_{\lambda\gamma,\Lambda}^i$'s depend on Mandelstam- t , beam energy and $M(\omega\pi^0)$. C_l^i 's depend on $M(\omega\pi^0)$. We are initially limiting the fit to the beam energy coherent peak and a limited Mandelstam- t range. Starting with the b_1 invariant mass peak we can extract the partial waves amplitudes C_l^i 's in different bins of invariant mass. If obtained with acceptable confidence we can fix them for other bins of beam energy and Mandelstam- t and extract the production vertices $V_{\lambda\gamma,\Lambda}^i$.

4.4 Summary

We can abridge the data analysis as selecting events through cuts for: particle identification, selecting invariant mass and beam energy ranges of interest, rejecting erroneously reconstructed events mainly through KinFit and to steer clear of the unreliable regions of the detector. These cuts are followed by by subtractions of events reconstructed using out-of-time beam buckets and the ω background. We presented AM and PWA as two models for the analysis of the $\omega\pi$ channel.

Chapter 5

Monte Carlo Simulations

Before fitting yields obtained from data to extract AMs, SDMEs and PWAs, corrections need to be applied to account for efficiency of the reconstruction and analysis workflow for measuring the b_1 yield. Acceptance is the quantitative measurement of how efficient the reconstruction and analysis are. Studying the acceptance requires a reliable Monte Carlo (MC) sample large enough to populate the multidimensional space of all relevant parameters. In this chapter, we will discuss the procedure followed to create a MC sample, its features, and the acceptance of the yields as calculated using this sample.

5.1 MC Generators

The first stage of creating a MC sample is generating the energy-momentum four-vectors of the initial and final state particles of the reaction. This is done by randomly generating a beam photon energy¹, and the energy-momentum of all final state particles except one, whose four-vector is calculated according to the energy-momentum conservation. As GlueX has a fixed target, we can neglect the thermal energy of the

¹This becomes sufficient by choosing the beam momentum direction as the Z-axis which leads to vanishing components of the beam momentum in directions X and Y and total beam energy matching the momentum component along Z.

proton target².

After generating the set of four-vectors for an event, a weight is calculated based on a PDF. This PDF could be uniform to simulate particles scattering with no resonance (i.e. phase-space) or it could describe the features of a resonance (i.e. signal): the decaying $b_1(1235)$ meson in our case. Following the general concept of a MC simulation, the event is recorded if the weight is larger than a threshold which is generated by a uniform random function. In the following sections, we will discuss the generators used to simulate the $\omega\pi^0$ phase-space.

5.1.1 genr8

genr8 is one of the default generators for MC simulation in GlueX collaboration. It is based on the isobar model which constructs any many-body system as a tree of subsequent two-body decays [64]. For example, the $\omega\pi$ decay of the b_1 meson in the isobar model would be presented by Eq. 5.1:

$$\gamma p \rightarrow p b_1(1235) \rightarrow p[\omega]\pi^0 \rightarrow p[(\rho)\pi^0]\pi^0 \rightarrow p[(\pi^+\pi^-)\pi^0]\pi^0 = p\pi^+\pi^-2\pi^0 \quad (5.1)$$

The isobar model cannot describe the angular distribution of the $b_1(1235)$ final state adequately, so it is limited to simulating phase-space. In order to simulate the decay of the b_1 resonance, a generator which allows a non-uniform PDF is needed. In the following section, we will discuss two such generators used by GlueX collaborators.

5.1.2 gen_amp

gen_amp is one of the default generators for MC simulation in GlueX collaboration. It has the capabilities to generate a phase-space MC sample and allow the users to

²Few meVs for LH_2 target at $\sim 20^\circ$ K (more details in Sec. 2.2).

write their own PDF as an amplitude, which is then used to calculate the weight for each event. However, `gen_amp` uses a one-step decay implementation which generates a non-flat angular distribution for the phase-space of the two-step b_1 decay, as shown in Fig 5.1. The one-step decay implementation assumes that the b_1 decays directly to four pions ($b_1 \rightarrow 4\pi$). Also, generating a four-pion phase-space using `gen_amp` and then employing an accept/reject algorithm to simulate the ω Breit-Wigner peak in the three-pion invariant mass leads to an artificially wide ω peak and a shoulder in the 3π invariant mass as seen in Fig 5.2. This motivated the effort to develop a two-step generator for the $\omega\pi$ channel named `gen_omegapi` which we will discuss in the following section.

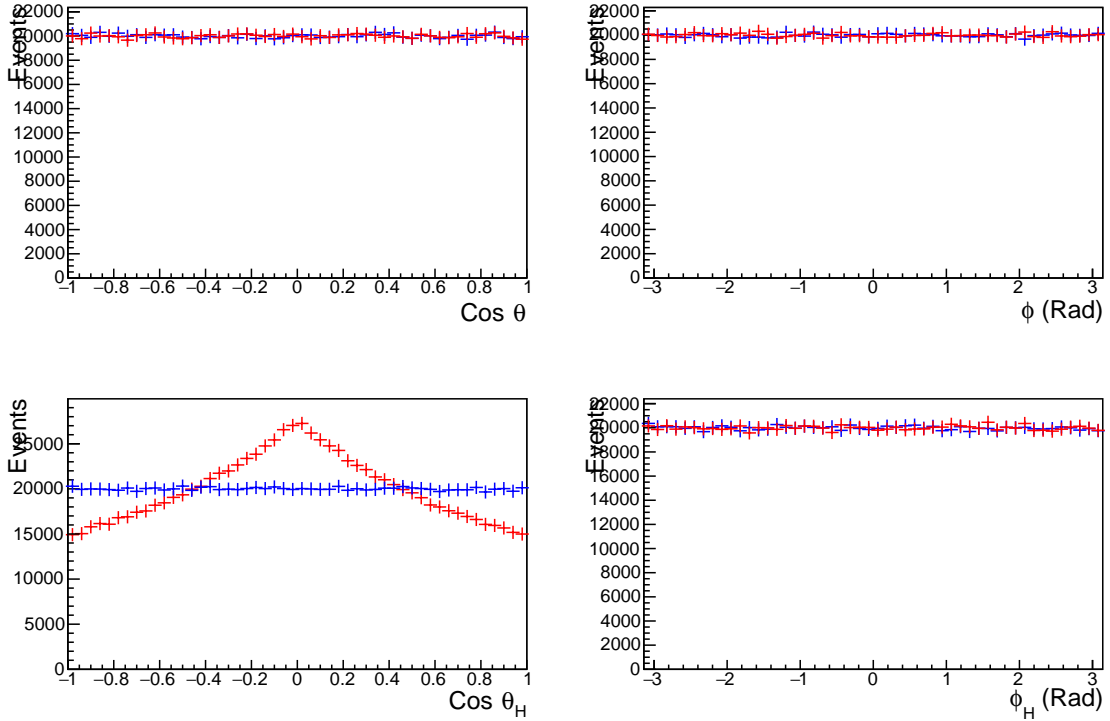


Figure 5.1: Helicity frame angles of the phase-space for the $\omega\pi$ channel as generated by `gen_amp` (red) and `gen_omegapi` (blue). Being in the decaying particle rest frame, the phase-space angular distribution is expected to be flat. We can see the non-flat $\cos \theta_H$ distribution generated by `gen_amp` as a result of the four pion phase-space.

5.1.3 gen_omegapi

The need for a special $\omega\pi^0$ generator arose from the inability of the default MC generators to simulate a b_1 decay or a uniform $\omega\pi^0$ phase-space. In order to rectify this, we wrote a two-step generator for the $\omega\pi$ channel named `gen_omegapi` which generates an ω and a π^0 from a decaying b_1 , randomly selecting the ω rest mass according to a Breit-Wigner distribution with width of 8 MeV [5]. The new generator produces the desired uniform angular distribution of the $\omega\pi$ phase-space with narrow ω invariant mass peak, as shown in Figs 5.1 and 5.2. A comparison between the generators is summarized in Table 5.1. As it was based on `gen_amp`, `gen_omegapi` also allows the user to write their own PDF as an amplitude which is then used to calculate the weight for each event.

gen_omegapi	gen_amp
1. GammaPToXYP ($\gamma p \rightarrow \omega\pi^0 p$) 2. Generate an ω with 8 MeV width Breit Wigner 3. NBodyPhaseSpaceFactory ($\omega \rightarrow 3\pi$) then boost them to the lab frame	1. GammaPToNPartP ($\gamma p \rightarrow 4\pi^0 p$)

Table 5.1: A summary of the algorithms of the two MC generators `gen_omegapi` and `gen_amp`.

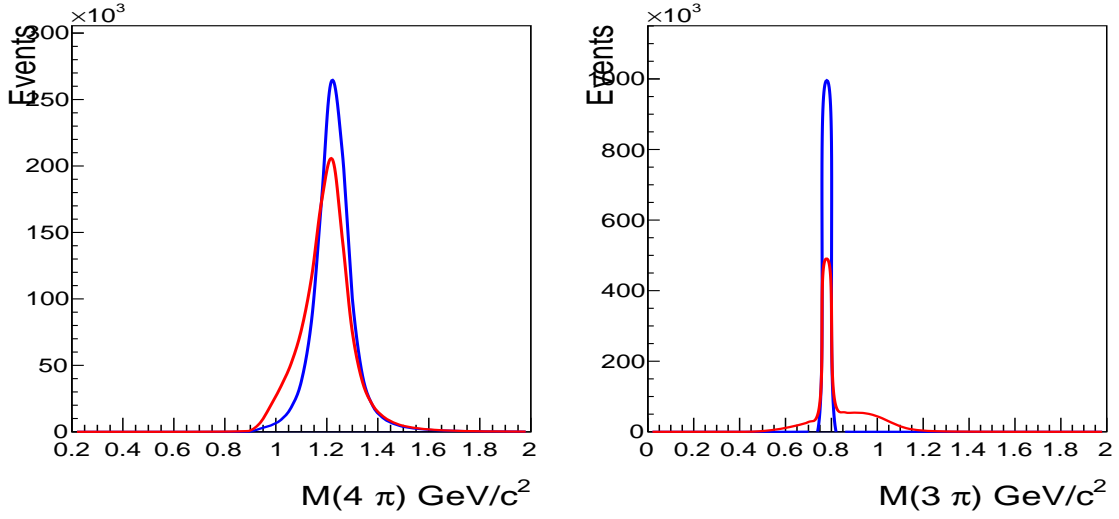


Figure 5.2: Invariant mass of the four-pion (left) and three pions (right) as generated by `gen_amp` (red) and `gen_omegapi` (blue). `gen_amp` produces a wider invariant mass distribution for the three pions with a shoulder around the mass of the η' meson. `gen_omegapi` produces realistic shapes for both distributions.

5.2 Amplitudes

As mentioned earlier, MC generators simulate an isotropic phase-space of the final state particles without a resonance. In order to simulate a b_1 resonance decaying into an $\omega\pi^0$ system, a PDF is needed to sculpt the phase-space. In this section, we will be discussing the two PDFs we wrote to simulate the features of a b_1 meson decay.

5.2.1 Angular Moments Model

The first PDF we wrote is based on the AMs expansion presented by a Berkeley Group-A experiment and used by them [21], the Omega-Photon collaboration [17] and the SLAC-H Collaboration [18] and described in Sec. 1.4.3. This amplitude was submitted to the collaboration software repository (following approval by experts) and can be used with both `gen_amp` (the default collaboration MC simulation generator) and the special `gen_omegapi` generator to simulate the $\omega\pi$ channel based on fit parameters obtained from the data. As mentioned earlier, events with $b_1(1235)$ final

state particles are generated randomly by `gen_amp` and their kinematics are used as input for the amplitude library, which based on these observables calculates the decay angles and returns a weight (i.e. amplitude) for that event. In our efforts to optimize the amplitude generator, we adapted the code to run on graphical processing units (GPU) using the CUDA platform [62].

This amplitude library assumes resonances with spin-parity of $J^P = 1^\pm, 0^-$. The amplitude is fine-tuned with 22 configuration parameters which are obtained by fitting the data to a set of 25 AMs using a separate Minuit [60] script. This amplitude library allows the use of AmpTools³ [61] as an alternative way to fit the data. The fit parameters can be used to calculate the SDMEs⁴ when represented as a sum of the AMs.

5.2.2 Partial Waves Amplitudes Model

This PDF is based on the model provided members of the JPAC group and on which a detailed description was presented in Sec. 1.4.3.2 and Sec. 4.3.2. This amplitude is compatible with both `gen_amp`, `gen_omegapi` and AmpTools. The current PWA implementation allows the $\omega\pi^0$ system to have total spin up to 2 and includes partial waves up to D-Wave ($l = 2$). This is based on results from previous experiments where they found no considerable contribution from higher partial waves. Currently, the model has 28 fitting parameters. The model could be extended to include more spin-parity states and higher order partial waves if the current implementation is not capable to reproduce the experimental observations adequately. Due to time limitation, this model has not been used to produce MC samples for our studies. However,

³A collection of libraries for performing unbinned maximum likelihood fits to data using a set of interfering amplitudes.

⁴The spin-density matrix describes the polarization of the b_1 meson. It can be generally represented by $\rho(b_1) = T\rho(\gamma)T^\dagger$. Where T is the b_1 production matrix and $\rho(\gamma)$ is the spin-density matrix of the beam photon [23].

a demonstration of a fit using this model on experimental data will be presented in Sec. 6.3.

5.3 Acceptance

After the generation step, the MC sample is passed through a Geant4 [63] simulation of the full GlueX detector, which records the final state particles as hits in the various detector subsystems. These hits are then smeared to simulate readout resolution. At this stage the MC sample is converted into experimental data format but is otherwise identical to generated MC. We refer to MC sample at this stage as "thrown" and it is used as the denominator for calculating acceptance. The thrown MC sample is then plugged in the same analysis workflow detailed in Ch. 4 as the experimental data. The MC sample surviving all the reconstruction and analysis cuts is referred to as "accepted". The ratio between the number of accepted MC events to the number of thrown MC events should be equal to the ratio between the events we observe in real data to the total events (events detected plus events lost due to detector inefficiency or cuts). It provides quantitative information on the reconstruction (detector solid angle and efficiency) and cuts application in the analysis. Also, a non-uniform acceptance could indicate a bias introduced by selection cuts or detector inefficiency.

The acceptance study used in this work is based on MC samples of 10^8 $\omega\pi$ events for each of the spring 2017 and fall 2018 run periods and a MC of 35×10^6 $\omega\pi$ events sample for the spring 2018 run period. These samples were generated using the `gen_omegapi` generator, discussed in previous section, and then passed through the data analysis pipeline. The acceptance is calculated by dividing the number of accepted events over the number of thrown events per bin. This method is used to calculate the acceptance in bins of $b_1(1235)$ invariant mass, decay angles, Mandelstam-t

and beam energy. Separate MC samples are used to ensure that each sample reproduces the run period conditions (e.g. beam current and detector calibration).

Fig. 5.3 shows the thrown and accepted yield in bins of $\omega\pi^0$ mass. Compared to the thrown MC sample on the left, the accepted MC sample on the right shows a slight modulation caused by the ω side band subtraction. Dividing these two histograms produces the acceptance in bins of $\omega\pi^0$ mass as presented in Fig. 5.4. The yield obtained from the data is divided by the acceptance to calculate the acceptance-corrected yield. Fig. 5.5 presents the yield in bin of $\omega\pi$ invariant mass from data on before and after acceptance correction is applied. The same procedure is employed to apply acceptance corrections on the yield when studying the other variables.

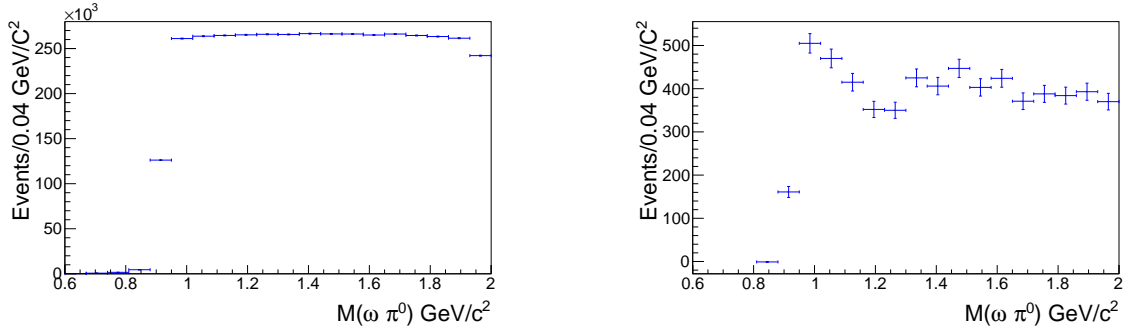


Figure 5.3: Invariant mass of the $\omega\pi^0$ for the thrown (left) and accepted (right) MC sample.

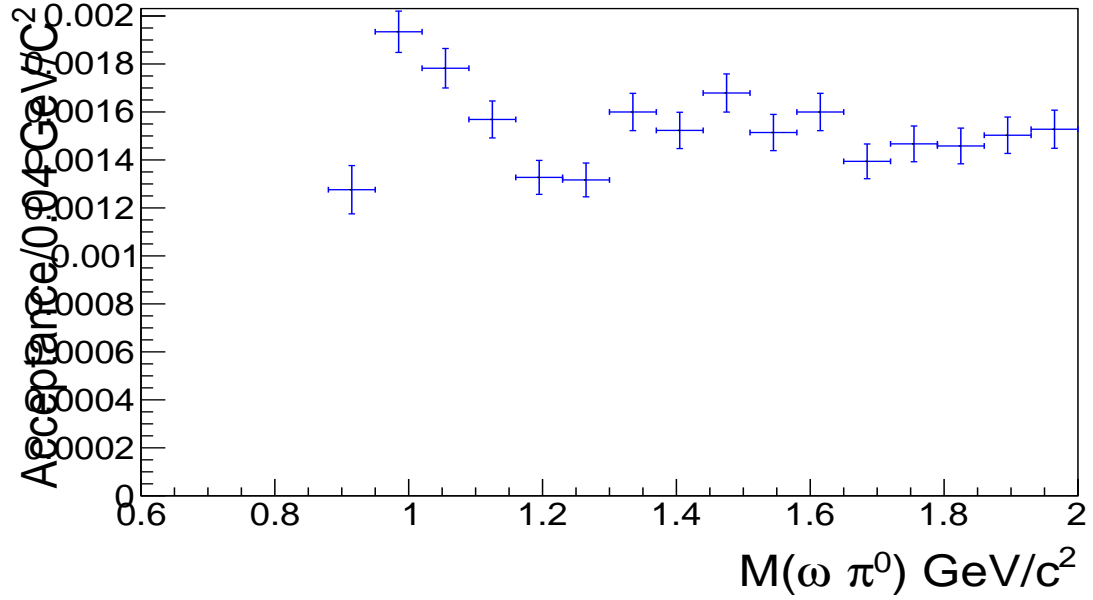


Figure 5.4: The acceptance as a function of the $\omega\pi^0$ invariant mass.

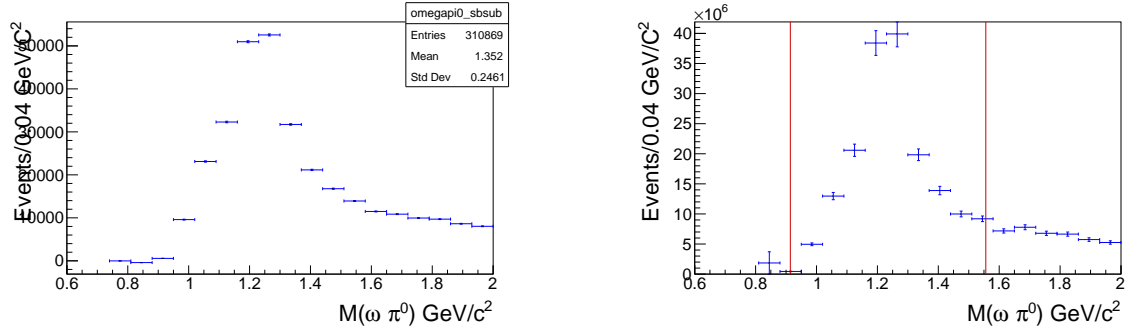


Figure 5.5: Invariant mass of the $\omega\pi^0$ from data before (left) and after applying acceptance correction (right). The red lines define the b_1 peak cut used to extract the angular distribution.

Likewise, Fig. 5.6 demonstrates the thrown yield in bins of helicity frame angles for the b_1 peak. A Gaussian fit of the b_1 peak for is used to set a cut for the b_1 peak with three standard deviations above and below the mean as shown in Fig. 5.5, this is done independently for each run period and MC sample. As discussed earlier, the angular distribution is expected to be flat in the rest frame of the decaying particle:

in the rest frame and in the absence of a resonance, all directions are equally probable. The accepted yield in bins of helicity frame angles for the b_1 peak is shown in Fig. 5.7. A rise is seen in the accepted MC for the ω azimuthal angle $\phi = 0$. This is reflected in the acceptance as seen in Fig. 5.8. Relatively small fluctuations can be seen in acceptance of different angles. However, the acceptance is essentially flat otherwise. The yield in bins of helicity frame angles for the b_1 peak from data is shown in Fig. 5.9. Dividing these histograms produces the acceptance-corrected yield seen in Fig. 5.10. The dip in the yield for ω polar angle at $\theta = 0$ ($\cos\theta = 1$) is concealed by acceptance. We do see the effect of the fluctuations we observed in the acceptance on these histograms. However, the general features of the angular distribution are preserved after applying acceptance correction.

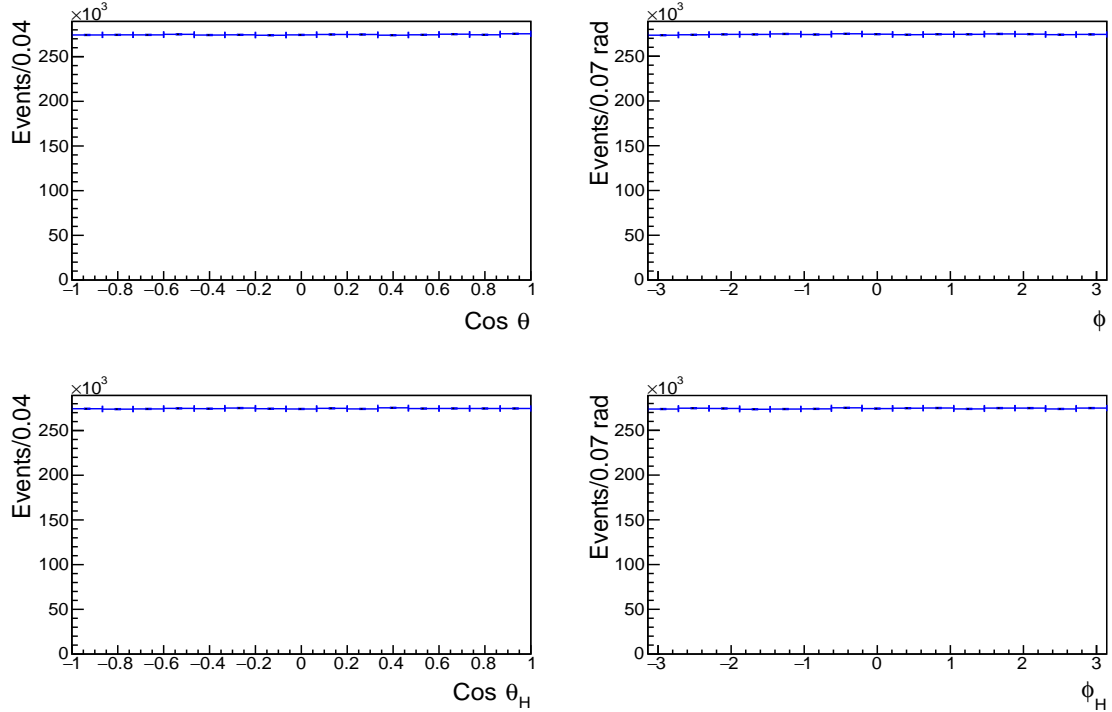


Figure 5.6: Thrown helicity frame angles of the phase-space for the $\omega\pi$ channel as generated by gen_omegapi. The phase-space angular distribution is uniform as expected in the decaying particle rest frame.

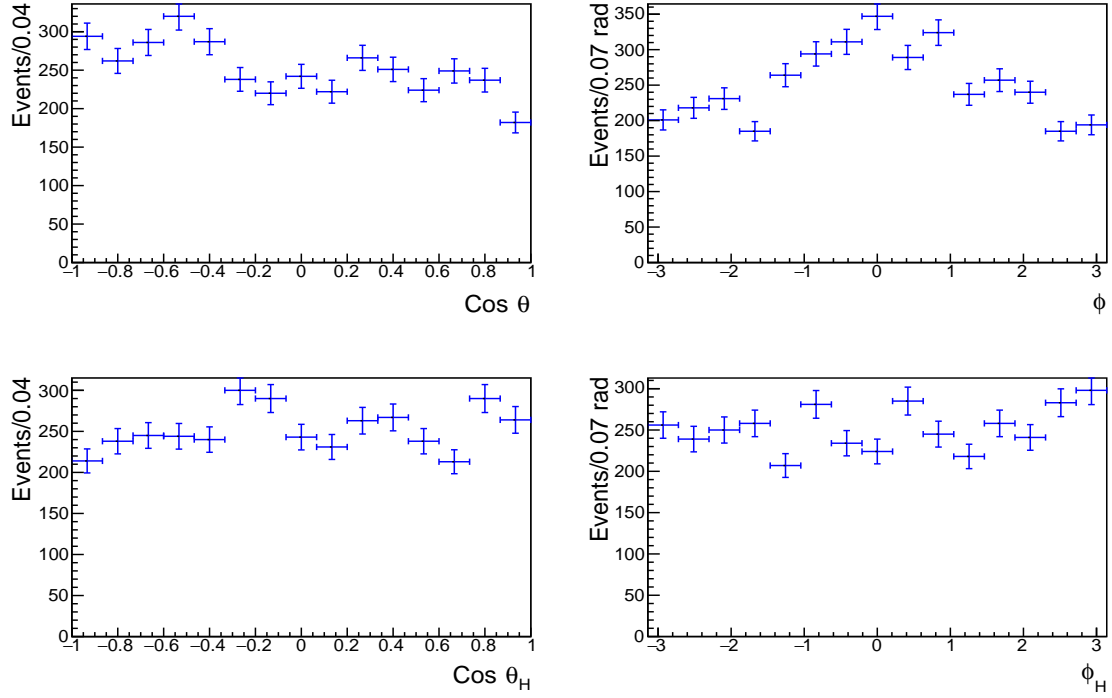


Figure 5.7: Accepted helicity frame angles for the b_1 peak for the $\omega\pi$ channel as generated by gen_omegapi.

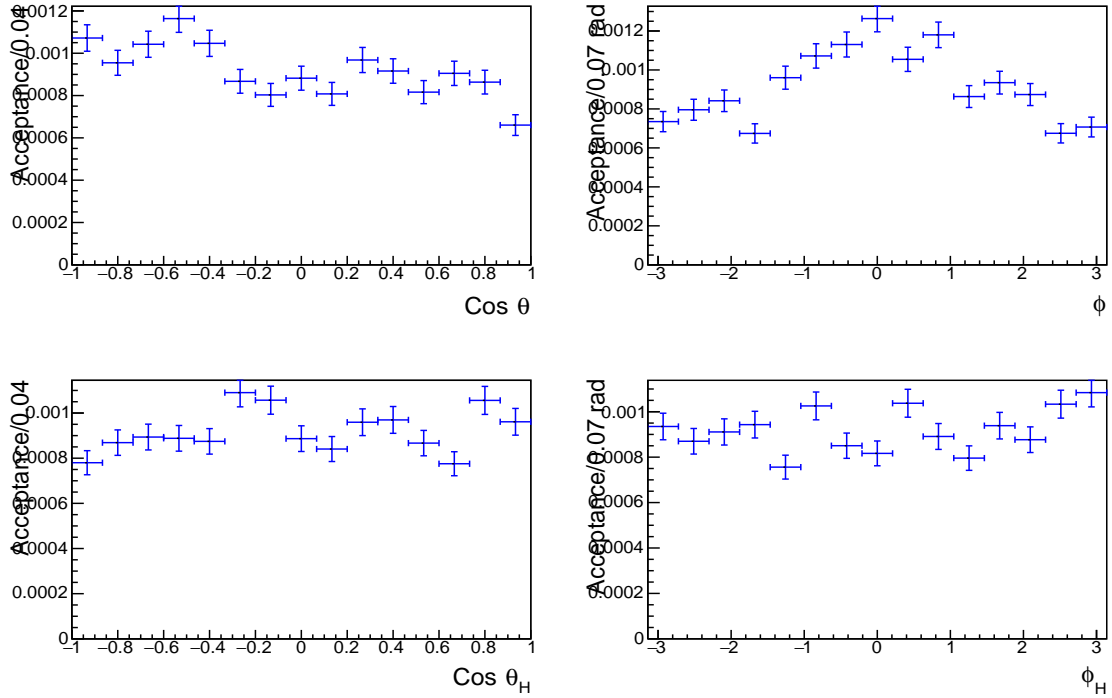


Figure 5.8: Acceptance as a function of the helicity frame angles for the b_1 peak for the $\omega\pi$ channel.

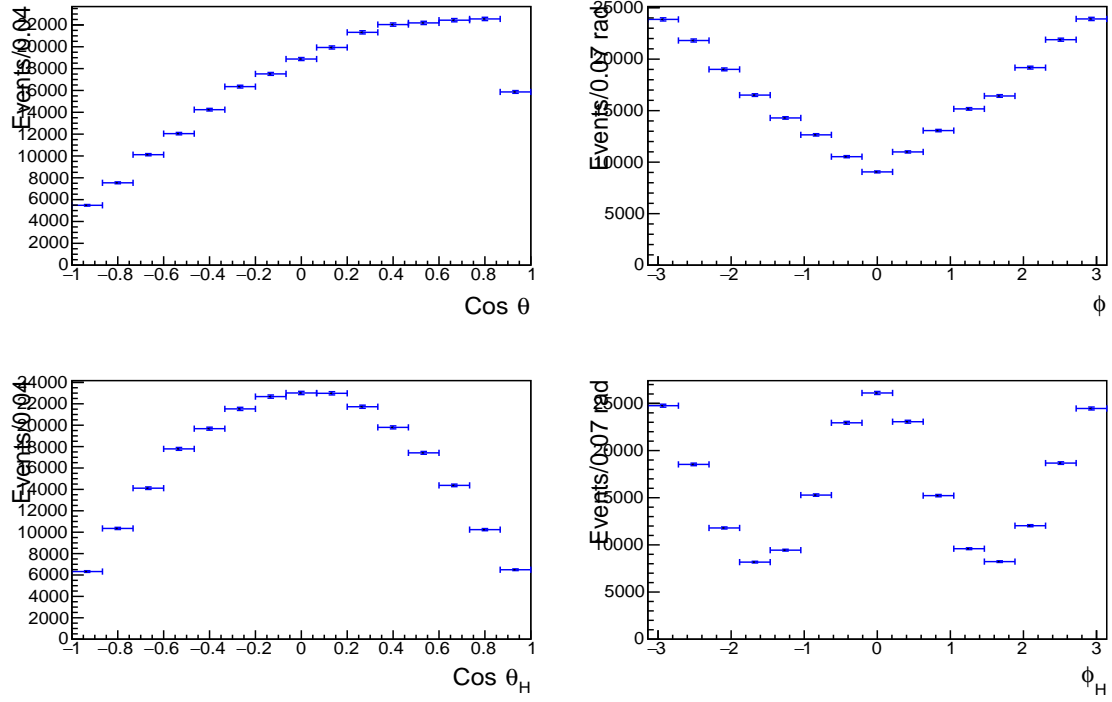


Figure 5.9: Helicity frame angles for the b_1 peak for the $\omega\pi$ channel from data.

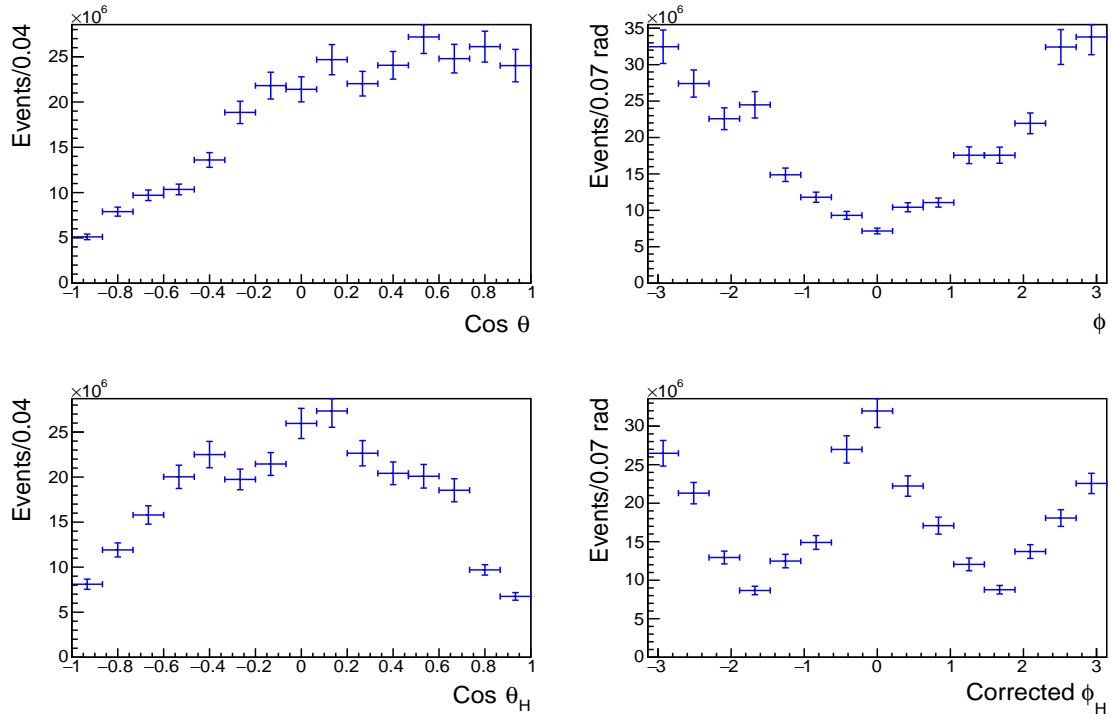


Figure 5.10: Acceptance-corrected helicity frame angles for the b_1 peak for the $\omega\pi$ channel.

5.4 Summary

In this chapter we surveyed relevant MC generators used in GlueX collaboration and we introduced *gen_omegapi* as a dedicated generator we developed to better model the $\omega\pi$ channel. Then, we presented our implementation of the AM and PWA models in the generators and fit framework. Finally, we summed up our efforts in optimizing the MC to studying the acceptance of the $\omega\pi$ channel.

Chapter 6

Results

Our aim is to characterize the $\omega\pi^0$ decay channel of the b_1 meson as a necessary step on the route to a spin-parity analysis and search for potential exotic resonances in the $b_1\pi^0$ decay channel. This makes a complete PWA analysis of the $\omega\pi^0$ decay channel our ultimate goal. It is also important to understand the efficiency of our detector and reconstruction pipeline on the distribution of the b_1 in Mandelstam variables and decay angles.

Previous studies of the $\omega\pi^0$ decay channel has been limited by small data sample. As we will demonstrate in the following sections, the data sample collected in GlueX offer orders of magnitude higher statistics. The size of our data set allows access to AM analysis, PWA analysis, differential and total cross-sections. Due to the time limitations of this study, we will provide a proof of concept for the extraction of AM and PWA and focus on the total and differential cross-sections along with few additional experimental observables, which offer insights into the $\omega\pi$ decay channel.

6.1 Moments

The AM analysis method is advantageous as it requires no theoretical model for any reaction channel, including the b_1 that is the channel of interest in this work, as that could potentially bias the interpretation of the extracted results, if the model is

not on sound footing. Although models are under development by theorists, many of their inputs and details need to be vetted by comparison to data before being adopted. Also, SDMEs can be extracted from an AMs fit, as detailed in previous studies [17, 21]. To this end, a set of 25 moments corresponding to spin-parity states 0^- , 1^- and 1^+ and interference between them is used as orthogonal basis for an expansion of the invariant mass and angular distributions for the b_1 decay. The moments $H_\alpha^\pm(\Omega, \Omega_H)$ are defined as the experimental averages of the product of two Wigner D-functions [17, 18, 21, 22]. As generalized spherical harmonics, Wigner D-functions form a complete basis set for the expansion in angles θ, ϕ, θ_H and ϕ_H . In this expansion, the moments are expressed as:

$$H_{lmLM}^\pm(\Omega, \Omega_H) = 1/2 \operatorname{Re}\{D_{Mm}^L(\theta, \phi, 0)D_{m0}^l(\theta_H, \phi_H, 0) \pm (-1)^{L+M}D_{Mm}^L(\theta, \phi, 0)D_{m0}^l(\theta_H, \phi_H, 0)\} \quad (6.1)$$

where L is the total angular momentum of the $\omega\pi^0$ system and M is its z-component, l and m are the total angular momentum and z component of the quantum state basis on which the $\omega\pi^0$ state is projected [22], $\Omega = (\theta, \phi)$, $\Omega_H = (\theta_H, \phi_H)$ are the four angles describing the decay in the helicity frame, as shown in Fig 1.8, and $D_{ij}^k(\theta, \phi)$ are Wigner D-functions¹. Normalizing $H_{0000}^+ = 1$ means that H_{0000}^+ is the invariant mass of the $\omega\pi$ and sets the normalization constant of the moments to:

$$C_\alpha = \frac{\iint [H_{lmLM}^\pm(\Omega, \Omega_H)]^2 d\Omega d\Omega_H}{(4\pi)^2} = \frac{1}{(2l+1)(2L+1)(2-\delta_{m0})(2-\delta_{M0})} \quad (6.2)$$

¹ $D_{mm'}^j(\alpha, \beta, \gamma) = e^{-im\alpha} d_{mm'}^j(\beta) e^{-im'\gamma}$
 $d_{mm'}^j(\beta) = \sum_k (-1)^k \frac{\sqrt{(j+m)!(j-m)!(j+m')!(j-m')!}}{(j-m'-k)!(j+m-k)!k!(k+m'-m)!} \cos^{2j+m-m'-2k}(\frac{\beta}{2}) \sin^{2k+m'-m}(\frac{\beta}{2})$

Figs 6.1, 6.2 and 6.3 show the extracted moments from the data of the $\omega\pi$ channel as a function of the $\omega\pi$ invariant mass and Mandelstam-t, which, as mentioned previously, is defined as the four momentum transferred squared from the beam photon to the recoil proton, and is given by the equation $t^2 = (p_\gamma - p_{b_1})^2 = (p_{recoil} - p_{target})^2$. The same moments are projected onto the invariant mass axis and shown in App. A. The projections from the Omega-Photon collaboration paper are shown in App. B for comparison. Our results present much higher statistics when compared to the Omega-Photon collaboration data. The moments are similar qualitatively to the Omega-Photon collaboration fit, except for moments $H^+(0022)$, $H^+(2022)$, $H^+(0021)$, $H^+(2021)$, $H^+(2221)$, $H^+(2121)$ and interference moments $H^-(0010)$, $H^-(0011)$, $H^-(2010)$, which show a significant deviation from the Omega-Photon collaboration fit. However, our results are not corrected for acceptance. A more detailed comparison is part of the future work passed to other members of the research group.

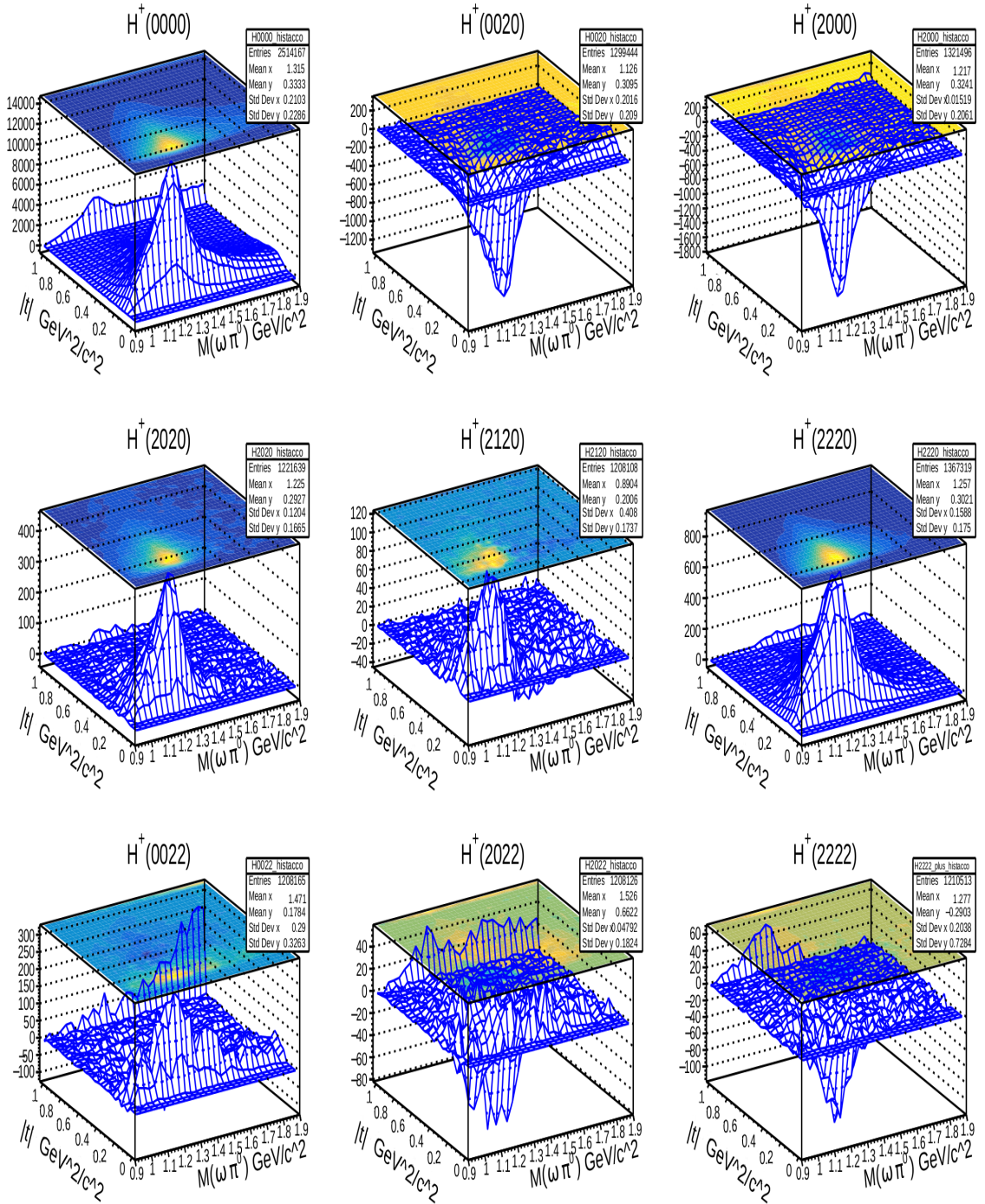


Figure 6.1: Extracted moments of the $\omega\pi$ channel as a function of the $\omega\pi$ invariant mass and Mandelstam- t .

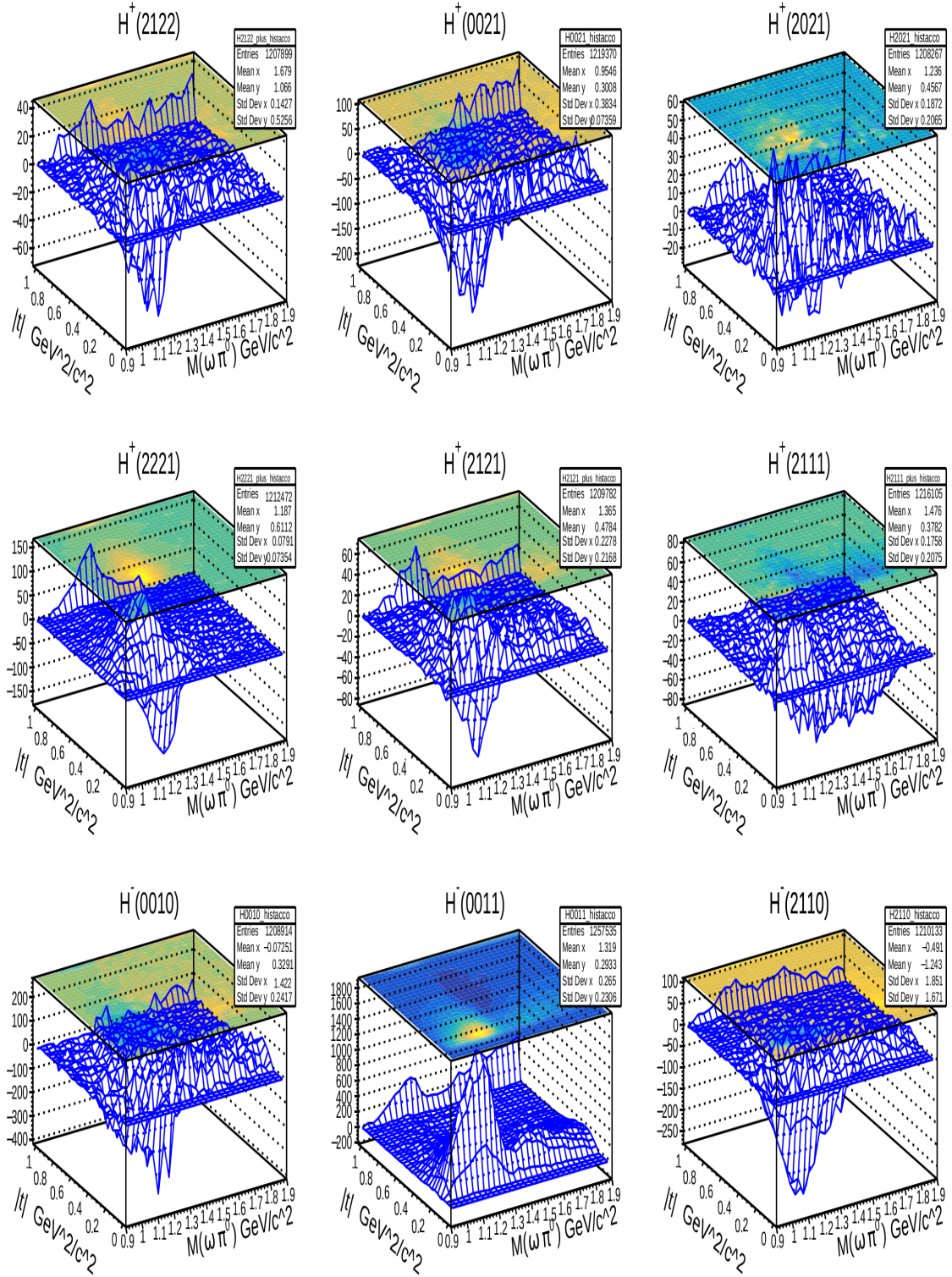


Figure 6.2: Extracted moments of the $\omega\pi$ channel as a function of the $\omega\pi$ invariant mass and Mandelstam- t .

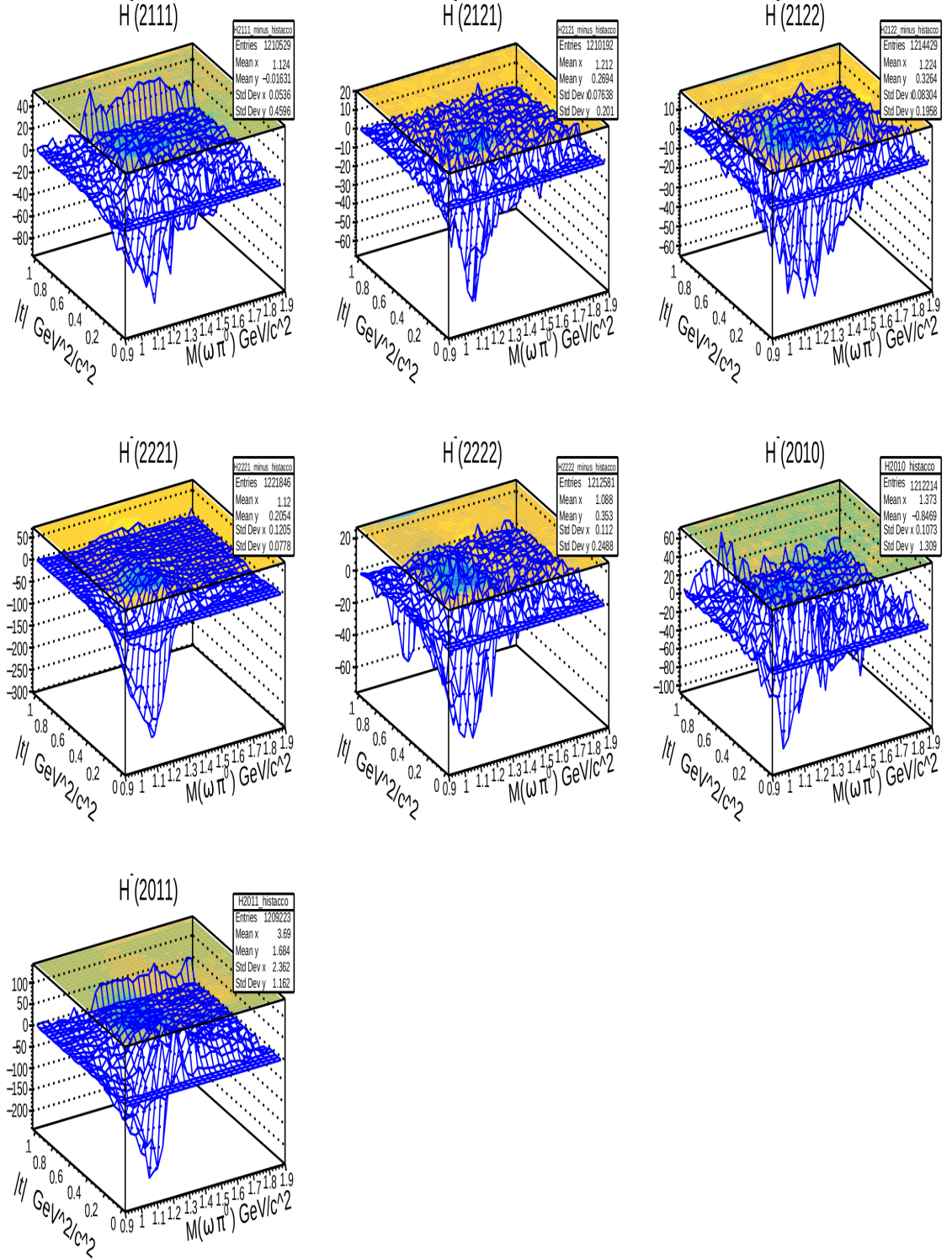


Figure 6.3: Extracted moments of the $\omega\pi$ channel as a function of the $\omega\pi$ invariant mass and Mandelstam- t .

Before we can fit the moments from Figs. 6.1, 6.2 and 6.3 to extract SDMEs we need to apply acceptance corrections. This requires a reliable MC sample large enough to study the efficiency of the reconstruction and cuts for measuring moments in all possible parameters. The parameters which could affect the moments are eight: the four angles describing the reaction in helicity frame, the invariant masses of ω and $\omega\pi$, Mandelstam variables t and s . Mandelstam- s is defined as the four momentum squared of all initial or final state particles, and is given by the equation $s^2 = (p_\gamma + p_{target})^2 = (p_{b_1} + p_{recoil})^2$, which is the square of the beam energy at the relativistic limit. This high dimensionality of the problem means that a straight forward scaling of histograms by efficiency will not be easy.

A possible way to overcome the high dimensionality of the acceptance is applying the acceptance on an event by event basis. AmpTools is a library developed by members of Indiana University to facilitate performing unbinned maximum likelihood fits in the sum of moments of experimental data to probability distribution functions (PDFs) and is used by many members of the GlueX collaboration [61]. We adapted our amplitude generator to work with AmpTools; even though the code is largely written, it is still in testing mode, meaning that debugging is still required. However, the current version of AmpTools does not include full implementation to fit moments; however this is planned by the developers. Our work on extracting the moments and implementing the necessary libraries paves the way for fitting the acceptance corrected moments in the future.

6.2 Additional Experimental Observables

Parallel to our efforts to pursue a full analysis of the $b_1 \rightarrow \omega\pi$ angular distribution in moments or partial wave basis, extraction of few other interesting observables is

possible by studying angular distributions. Here we present a helicity (see Sec. 1.4.2) conservation test based on the b_1 production angle and an extraction of the helicity amplitudes by studying the yield as a function of one of the four helicity-frame angles.

6.2.1 S-Channel Helicity Conservation

The helicity conservation model states that in the helicity frame, the density matrices $\rho^{0,\pm 1}$ are independent of the production angle Φ [18, 23], which is defined as the angle between the resonance-recoil plane and the beam polarization plane. This offers a test for helicity conservation by studying the production angle of the b_1 .

The most general form for the yield as a function of the production angle Φ is given by

$$I(\Phi) = \frac{1}{2\pi} [a + b \cos(2(\Phi)) + c \sin(2(\Phi))] \quad (6.3)$$

The imposition parity conservation (see Sec. 1.2) leads to $c = 0$ [23]. In addition, helicity conservation demands $b = 0$. If satisfied together, we expect a flat angular distribution. Previous measurement by the SLAC-H group found $b = -0.36 \pm 0.08$ [18] as shown in Fig. 6.4. Their results concluded that the b_1 is produced by a non-helicity conserving mechanism.

Fits of the distribution of Φ with b as a free parameter for the four beam polarizations of GlueX (0° , 90° , -45° and 45°) are presented in Figs. 6.5, 6.6 and 6.7 for the spring 2017, spring 2018 and fall 2018 run periods, respectively. All the fits show significant deviation from the flat distribution predicted by the s-channel helicity conservation [17, 18], indicating that the b_1 is produced by a non-helicity conserving mechanism. A summary of the fit results along with the fit's χ^2/NDF is presented

in Table. 6.1. Our results average to -0.169 ± 0.002 which does not agree with results from SLAC-H experiment. However, our results confirm that the b_1 is produced by a non-helicity conserving mechanism and offer much higher statistics compared to the SLAC-H group.

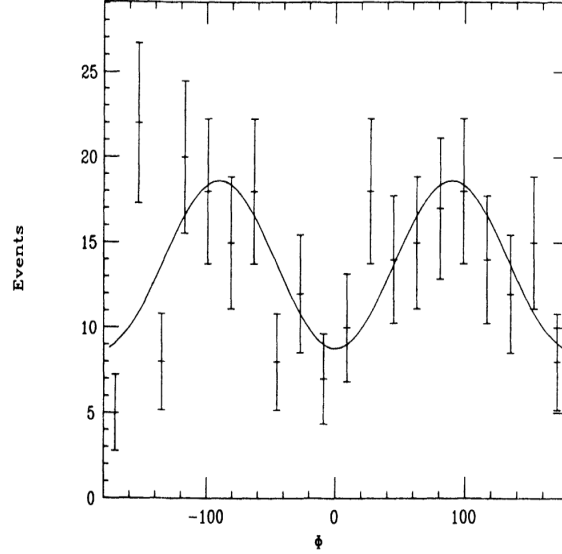


Figure 6.4: Yield of the $b_1(1235)$ meson as a function of the production angle Φ . SLAC-H collaboration data and fit [18].

Fall 2018 Sp. 2018 Sp. 2017	Pol. Angle	b	χ^2/NDF	SCHC χ^2/NDF
	0°	-0.1745	7/18	122/19
	90°	-0.1662	11/18	113/19
	45°	-0.1518	5/18	91/19
	-45°	-0.1745	15/18	126/19
	0°	-0.1578	6/18	42/19
	90°	-0.1792	5/18	56/19
	45°	-0.1842	6/18	57/19
	-45°	-0.1675	5/18	47/19
	0°	-0.1653	16/18	134/19
	90°	-0.1721	11/18	158/19
	-45°	-0.1575	10/18	109/19
	45°	-0.1786	7/18	115/19
	GlueX Average	-0.169 ± 0.002		
	0° (SLAC-H)	-0.36 ± 0.08	24/18	45/19

Table 6.1: Fit results of the b_1 meson yield as a function of production angle.

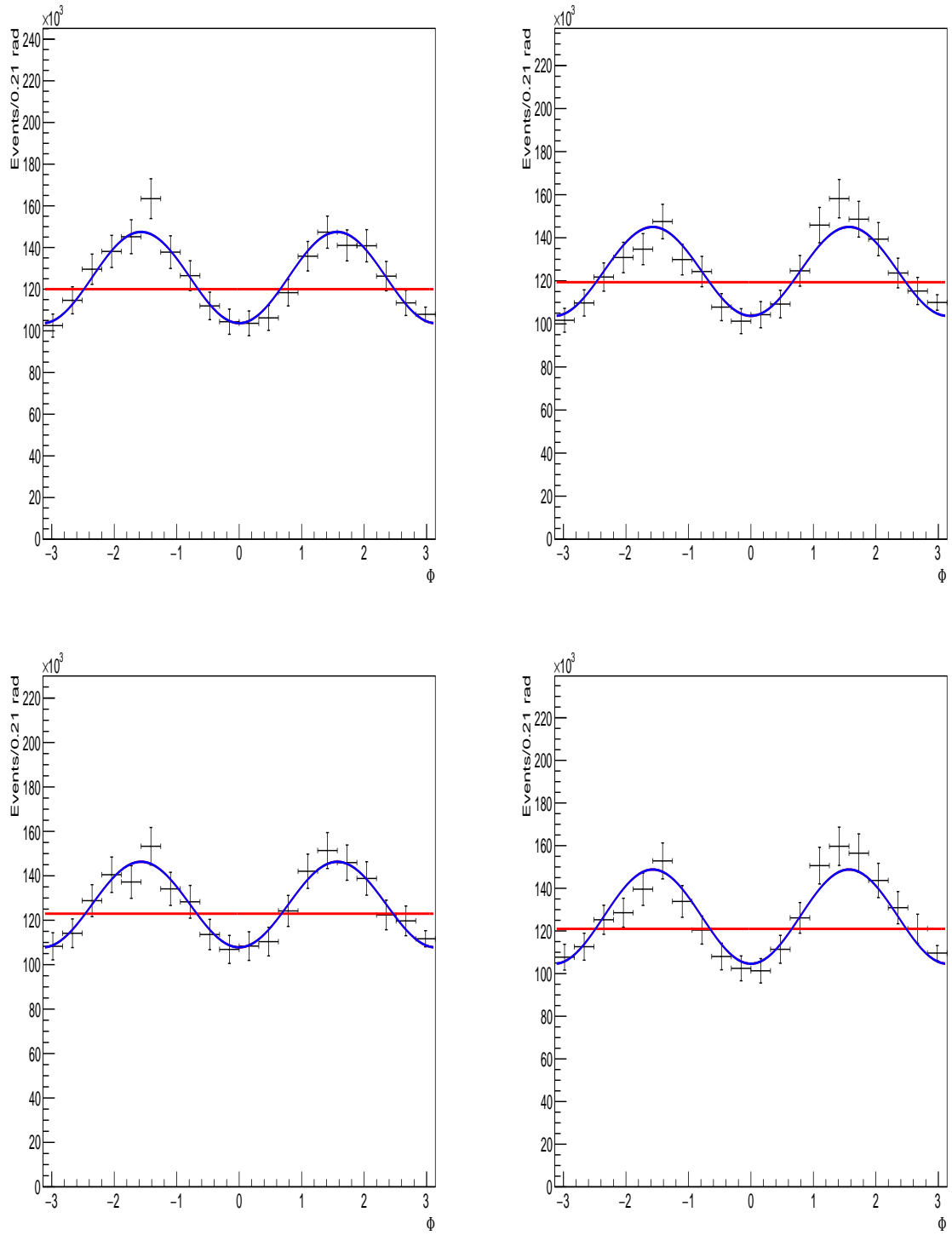


Figure 6.5: Yield of the $b_1(1235)$ meson as a function of the production angle Φ based on spring 2017 data and fit over the coherent peak ($8.2 < E_{beam} < 8.8 \text{ GeV}$). (top left) 0° polarization beam. (top right) 90° polarization beam. (bottom left) -45° polarization beam. (bottom right) 45° polarization beam. The red line represents the helicity conservation assumption. Error bars represent only statistical error. (color online)

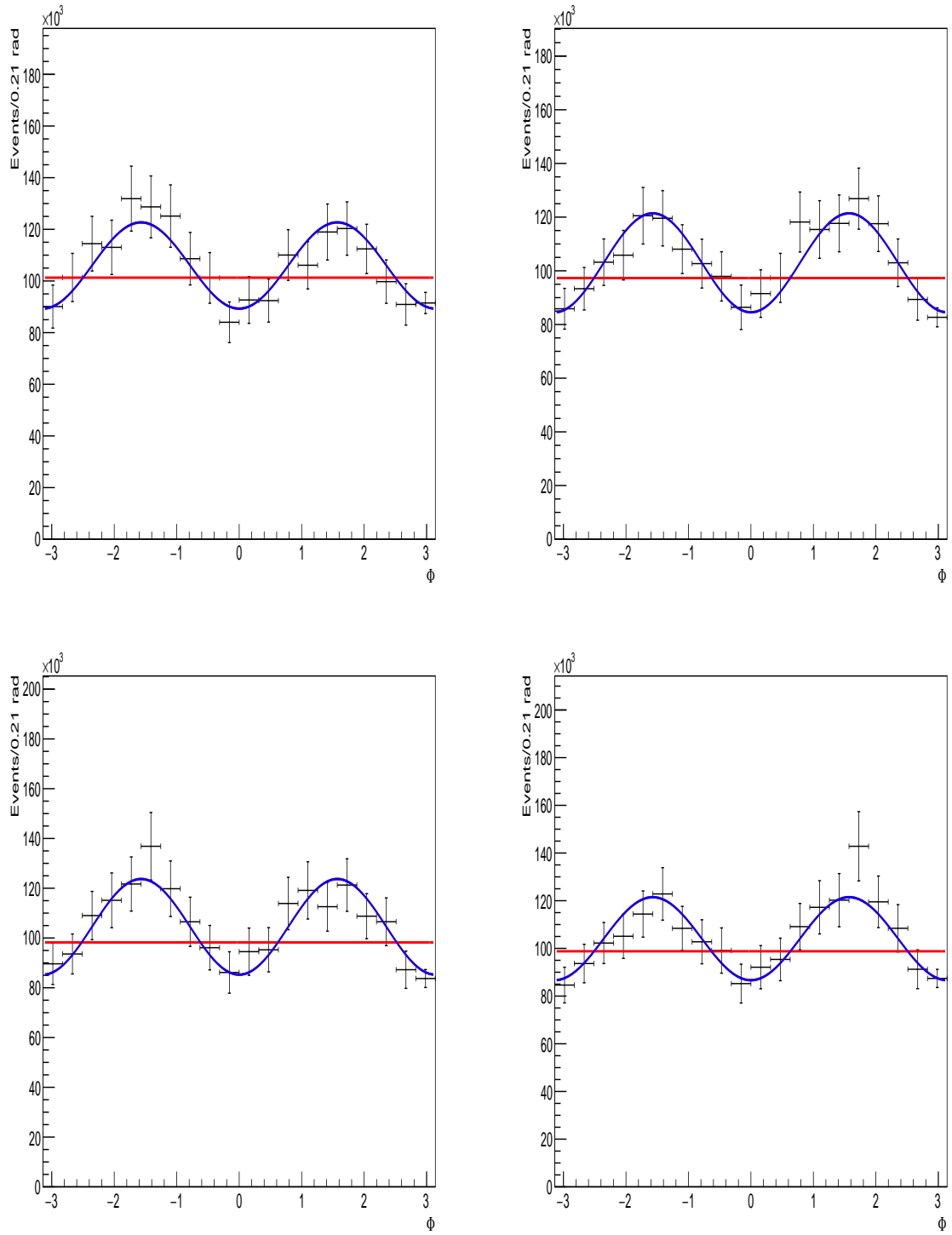


Figure 6.6: Yield of the $b_1(1235)$ meson as a function of the production angle Φ based on spring 2018 data and fit over the coherent peak ($8.2 < E_{beam} < 8.8 \text{ GeV}$). (top left) 0° polarization beam. (top right) 90° polarization beam. (bottom left) -45° polarization beam. (bottom right) 45° polarization beam. The red line represents the helicity conservation assumption. Error bars represent only statistical error. (color online)

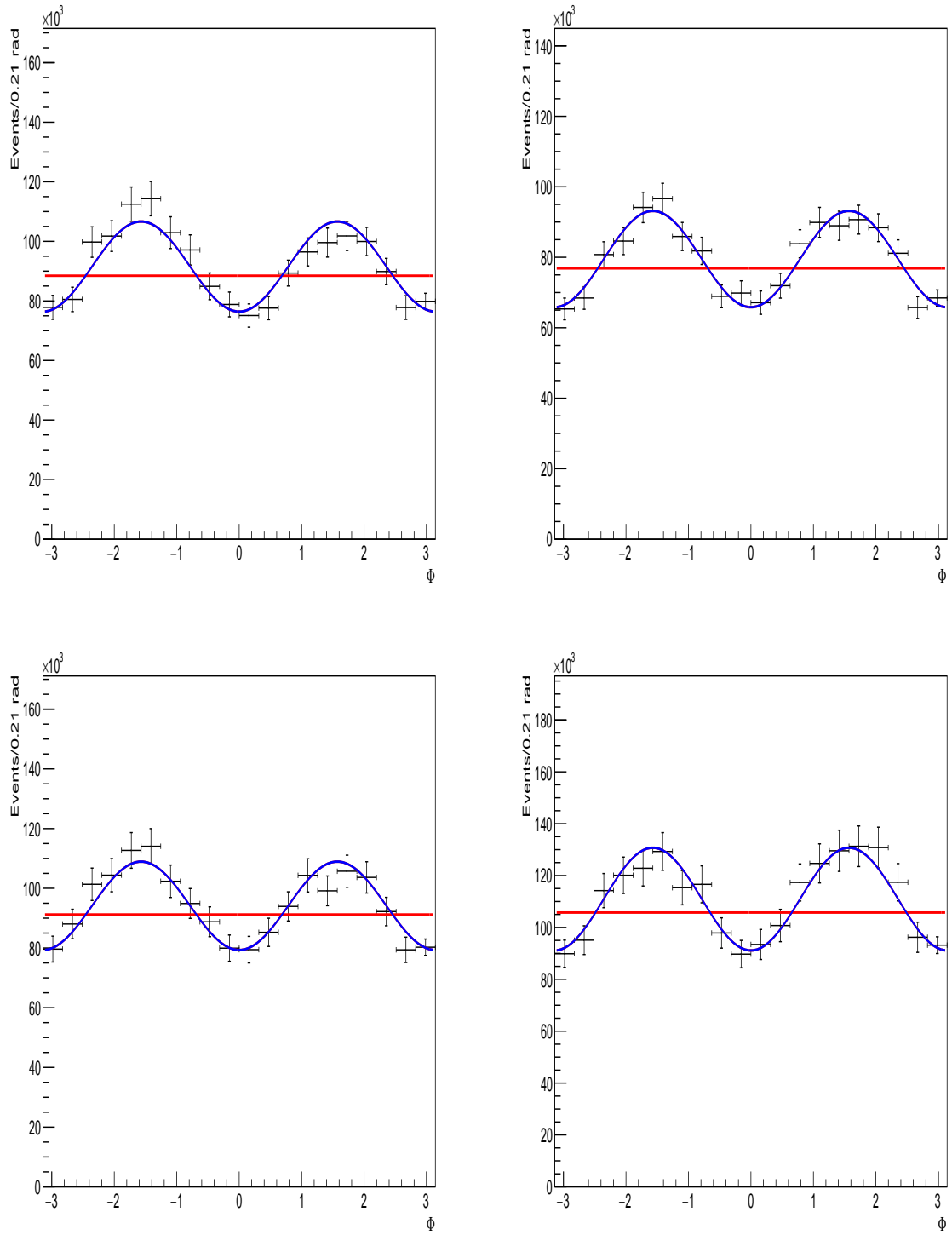


Figure 6.7: Yield of the $b_1(1235)$ meson as a function of the production angle Φ based on fall 2018 data and fit over the coherent peak ($8.2 < E_{beam} < 8.8 \text{ GeV}$). (top left) 0° polarization beam. (top right) 90° polarization beam. (bottom left) -45° polarization beam. (bottom right) 45° polarization beam. The red line represents the helicity conservation assumption. Error bars represent only statistical error. (color online)

6.2.2 Helicity Amplitudes of the ω

The angular distribution of $\cos(\theta_H)$ depends only on the decay properties of a given spin-parity state and not on the details of its production [18]. This offers a direct measurement of the contribution of each helicity amplitude by fitting the distribution using the function

$$\frac{dN}{d\cos(\theta_H)} = \frac{3N}{2}(|F_0|^2 \cos^2 \theta_H + |F_1|^2 \sin^2 \theta_H) \quad (6.4)$$

where F_λ is the decay amplitude for an ω of helicity λ , N is the number of events and unitarity requires that $|F_0|^2 + 2|F_1|^2 = 1$. This means that for a pure $J^P = 1^\pm$ state we would have $|F_1|^2 = 0.5$ and $|F_0|^2 = 0$.

The extracted b_1 yield as a function of the ω polar angle θ_H is shown in Fig. 6.8 as calculated based on data from the run periods spring 2017, spring 2018 and fall 2018. Our three data sets agree with each other, and the fits result in similar values for $|F_1|^2$. A summary of the fit results is presented in Table 6.2. Further work is needed to improve the subtraction of the contributions from the background under the b_1 peak. Averaging the results from these three data sets leads to $|F_1|^2 = 0.3037 \pm 0.0003$. The results from the SLAC-H and Omega-Photon collaboration shown in Fig. 6.9. Our results offer much higher statistics even within each run period. Fit results from the SLAC-H group are presented in Table. 6.3 along with expected $|F_1|^2$ values for $J^P = 0^-$, $J^P = 1^-$ states and a b_1 with a $D/S = 0.26 \pm 0.035$. They reported $|F_1|^2 = 0.383 \pm 0.029$ [18] which did not allow them to rule out a $J^P = 1^-$ state with a $J^P = 0^-$ background as an alternative to the expected $|F_1|^2 = 0.437 \pm 0.012$ of the b_1 meson. Our averaged results do not agree with results from the SLAC-H group. Also, our results do not agree with the expected $|F_1|^2$ of the b_1 meson. We expect that improved results could be attained by improved treatment of the background

under the b_1 peak.

GlueX Data Set	$ F_1 ^2$
Spring 2017	0.306 ± 0.017
Spring 2018	0.300 ± 0.027
Fall 2018	0.305 ± 0.015
Average	0.3037 ± 0.0003

Table 6.2: Helicity amplitudes as calculated through a fit over the distribution of the decay angle $\cos(\theta_H)$.

SLAC-H Data Set	$ F_1 ^2$
Data	0.383 ± 0.029
0^-	0.000
1^-	0.500
$b_1(D/S = 0.26 \pm 0.035)$	0.437 ± 0.012

Table 6.3: Comparison of helicity amplitudes as calculated through different models and data, as reported by the SLAC-H group [18].

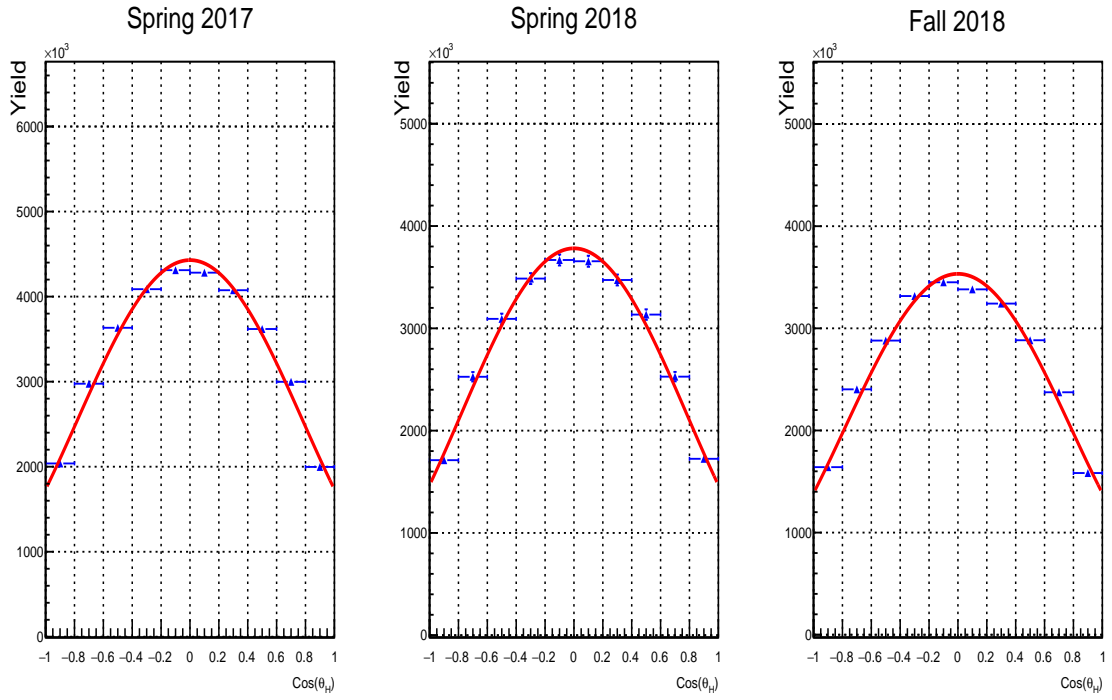


Figure 6.8: Yield and fit of the $b_1(1235)$ meson as a function of θ_H , the polar decay angle of the ω meson. (left) Spring 2017, (middle) Spring 2018, (right) fall 2018.

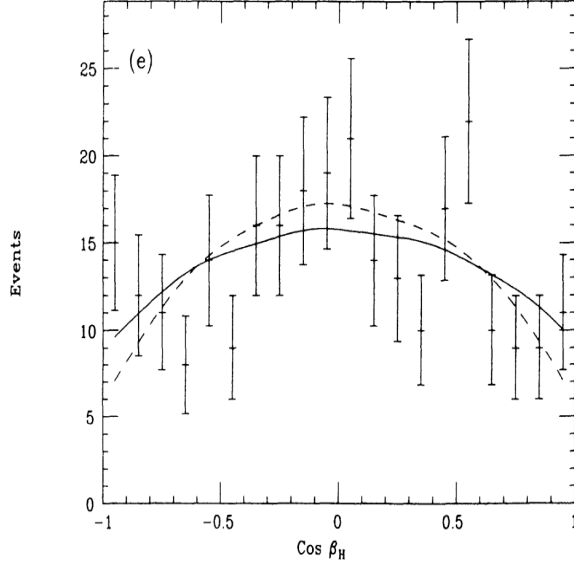


Figure 6.9: Yield of the $b_1(1235)$ meson as a function of θ_H , the polar angle of the ω meson decay plane. SLAC-H collaboration Data, fit (solid curve) and results from the Omega-Photon collaboration (dashed curve) [17, 18].

6.3 Partial Wave Amplitudes

Based on communications with the JPAC theory group, a partial wave amplitudes model developed by them for the $\omega\pi^0$ decay channel has been implemented into AmpTools software. The model implemented includes states with spin up to 2. Due to the complexity of partial wave amplitude ambiguity a complete study of the $\omega\pi^0$ decay channel will likely continue beyond the Ph.D. defence. A demonstration fit based on this model is presented here.

The plots included represent an AmpTools fit over the spring 2017 run period polarized beam data. The fit parameters depend on the beam energy, Mandelstam- t , and the invariant mass of the $\omega\pi^0$. The fit is binned in these three variables. The example fit here was restricted to the bin defined by the coherent peak beam energy range $[8.2, 8.8] \text{ GeV}$, the b_1 peak in the invariant mass range with a width of $0.142 \text{ GeV}/c^2$ and Mandelstam- t limited to the range $[0.1, 0.3] \text{ GeV}^2/c^4$. This restriction was

for reasons of expediency in testing the model. Additional restrictions were placed on other observables and parameters in order to test the general features of the model and simplify initial comparisons.

The fit is performed assuming a 1^+ spin-parity state with a Breit-Wigner invariant mass distribution with mass $M(b_1) = 1.235 \text{ GeV}/c^2$ and width $\Gamma(b_1) = 0.142 \text{ GeV}/c^2$ with a fixed D-wave/S-wave ratio $= 0.27$ (C_2^{1+}/C_0^{1+}) (following the b_1 listing in the PDG [5]), an orbital- $l = 0$ between the ω and the π^0 , a uniform background and polarization fraction $= 0.4$ (Pol. Frac.) for polarization angle $= 0^\circ$ (Pol. Angle). The imaginary part of the production amplitudes describes the phase difference between them. This is why one of the production amplitudes (traditionally the one with the largest magnitude) can be chosen to be real (i.e. phase set to zero) without loss of generality. Based on test fits we chose to set $V_{+1,0}^{1+}$ to be real. The production amplitude for the uniform background can be chosen to be real as interference of the background with other terms is not expected. Fit constants and parameters are summarized in Table. 6.4.

Constants					
Parameter	Value	Constant	Parameter	Value	Constant
$M(b_1)$	$1.235 \text{ GeV}/c^2$	Yes	$\Gamma(b_1)$	$0.142 \text{ GeV}/c^2$	Yes
$M(\omega)$	$0.782 \text{ GeV}/c^2$	Yes	$\Gamma(\omega)$	$0.008 \text{ GeV}/c^2$	Yes
Pol. Angle	0°	Yes	Pol. Frac.	0.4	Yes
C_0^{1+}	1.0	Yes	C_2^{1+}	0.27	Yes
Breit-Wigner orbital- l between ω and π^0				0	Yes
Production Amplitudes					
$Re(V_{+1,-1}^{1+})$	372.42	No	$Im(V_{+1,-1}^{1+})$	2.22	No
$Re(V_{+1,0}^{1+})$	-596.19	No	$Im(V_{+1,0}^{1+})$	0.0	Yes
$Re(V_{+1,+1}^{1+})$	120.56	No	$Im(V_{+1,+1}^{1+})$	7.71	No
Re(Uniform)	499.48	No	Im(Uniform)	0.0	Yes

Table 6.4: Parameters and constants used in the fit.

The plots from this initial, restrictive pass through the data are produced for the

combined S, D and uniform components of the fit (Fig. 6.10), the S-wave component of the fit (Fig. 6.11), the D-wave component of the fit (Fig. 6.12), the phase space MC (generated and accepted) scaled by the S-wave component (Fig. 6.13), the D-wave component (Fig. 6.14), and the combined S, D and uniform components of physics model (Fig. 6.15). The points represent the data, yellow histograms represent generated phase space MC scaled by the physics model while green histograms represent accepted phase space MC scaled by the physics model.

Fig. 6.10 shows that most histograms of the accepted MC scaled by the S+D waves physics model can qualitatively fit the data distribution for the $M(\omega\pi^0)$, Mandelstam-t, the decay angles of the ω 's three daughter pions ($\cos\theta_H$, ϕ_H) and $M(\pi^+\pi^-\pi^0)$. It does capture the general behaviour for the ω decay angles (θ , ϕ) but it needs more work. However, the production angle looks inverted. This issue is being investigated ². Figs. 6.11 and 6.12 indicate how much of the b_1 decays through the S-wave or the D-wave and how the different waves affect the angular distribution. S-wave alone can not reproduce the non flat angular distribution of the data (except for ϕ_H), while D-wave alone would produce a heavily modulated $\cos\theta$ and $\cos\theta_H$ distributions.

Next steps include fitting with free D/S ratio and/or polarization fraction. The D/S ratio is specially important in recent LQCD calculations as the $\omega \pi^0$ is the simplest non-trivial decay channel (decays to a vector and a pseudoscalar), which can be observed and LQCD calculations are possible for a meson decay. On the other hand, calculations for the $\rho \pi$ vector and pseudoscalar decay channel are too complicated while the $\phi \pi$ decay channel is suppressed [65]. Then a search for the optimum bases for the fit should follow. This is conducted by systematically switching production amplitudes on and check if that improves the fit. An ambiguity arises if more than

²This issue was caused by a bug in the configuration file used in the fit and is now resolved.

one set of amplitudes can produce equally acceptable fits for the data. Steps have been taken over the past few months, to transfer this work to another graduate student in the group.

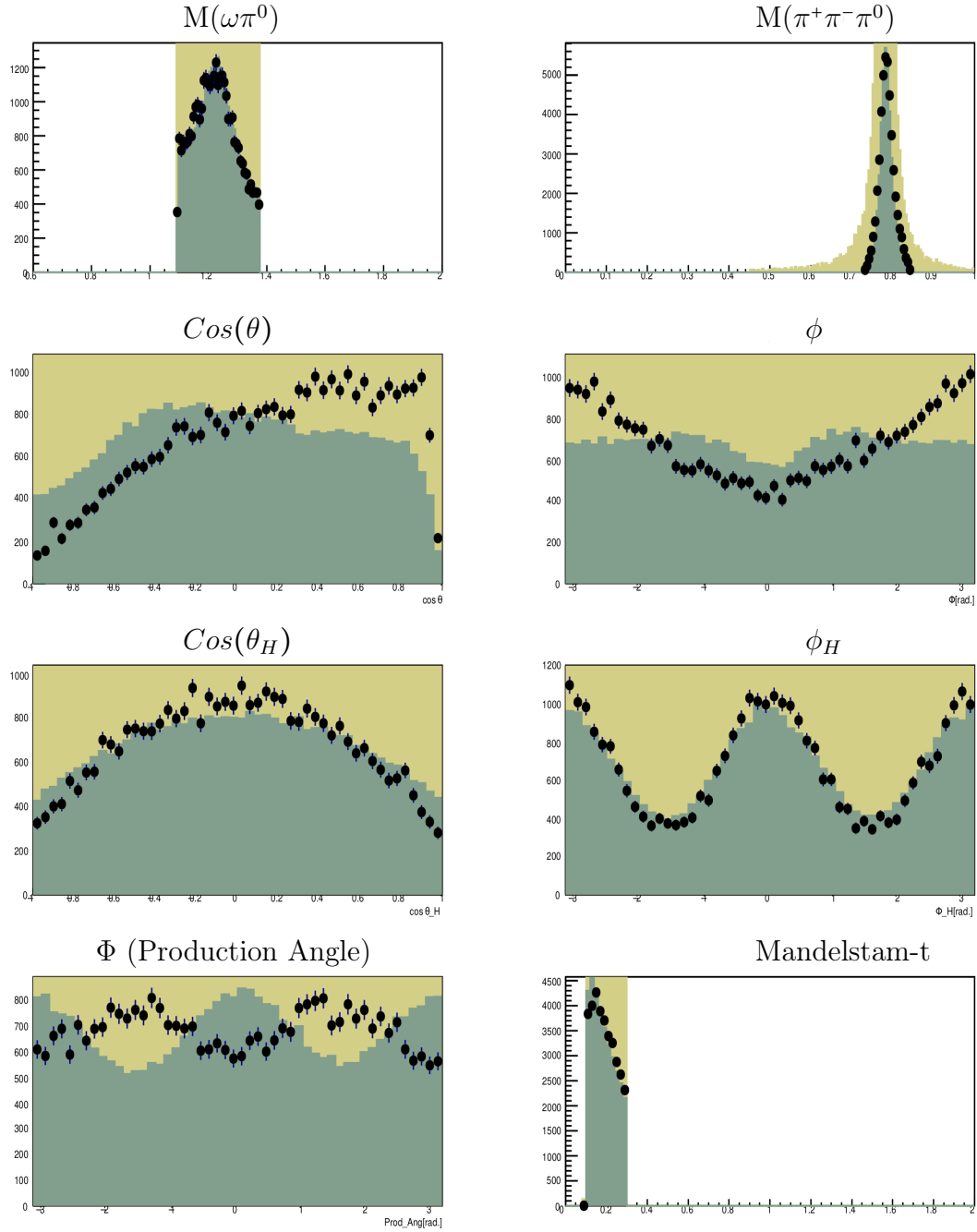


Figure 6.10: Combined S, D and uniform components of the AmpTools fit. The points represent the data, yellow histograms represent generated MC scaled by the physics model while green histograms represent accepted MC scaled by the physics model.

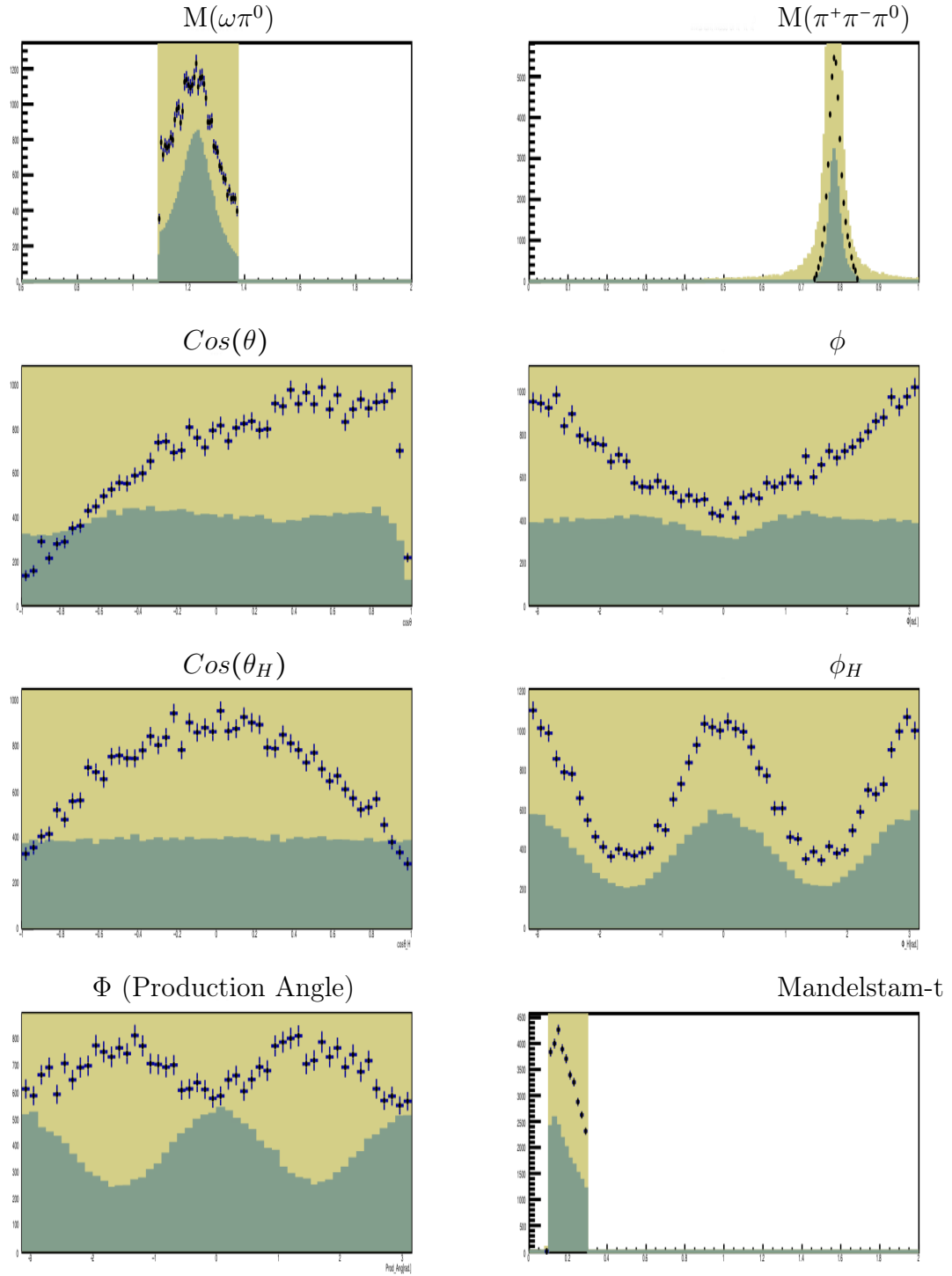


Figure 6.11: S-wave component of the AmpTools fit. The points represent the data, yellow histograms represent generated MC scaled by the physics model while green histograms represent accepted MC scaled by the physics model.

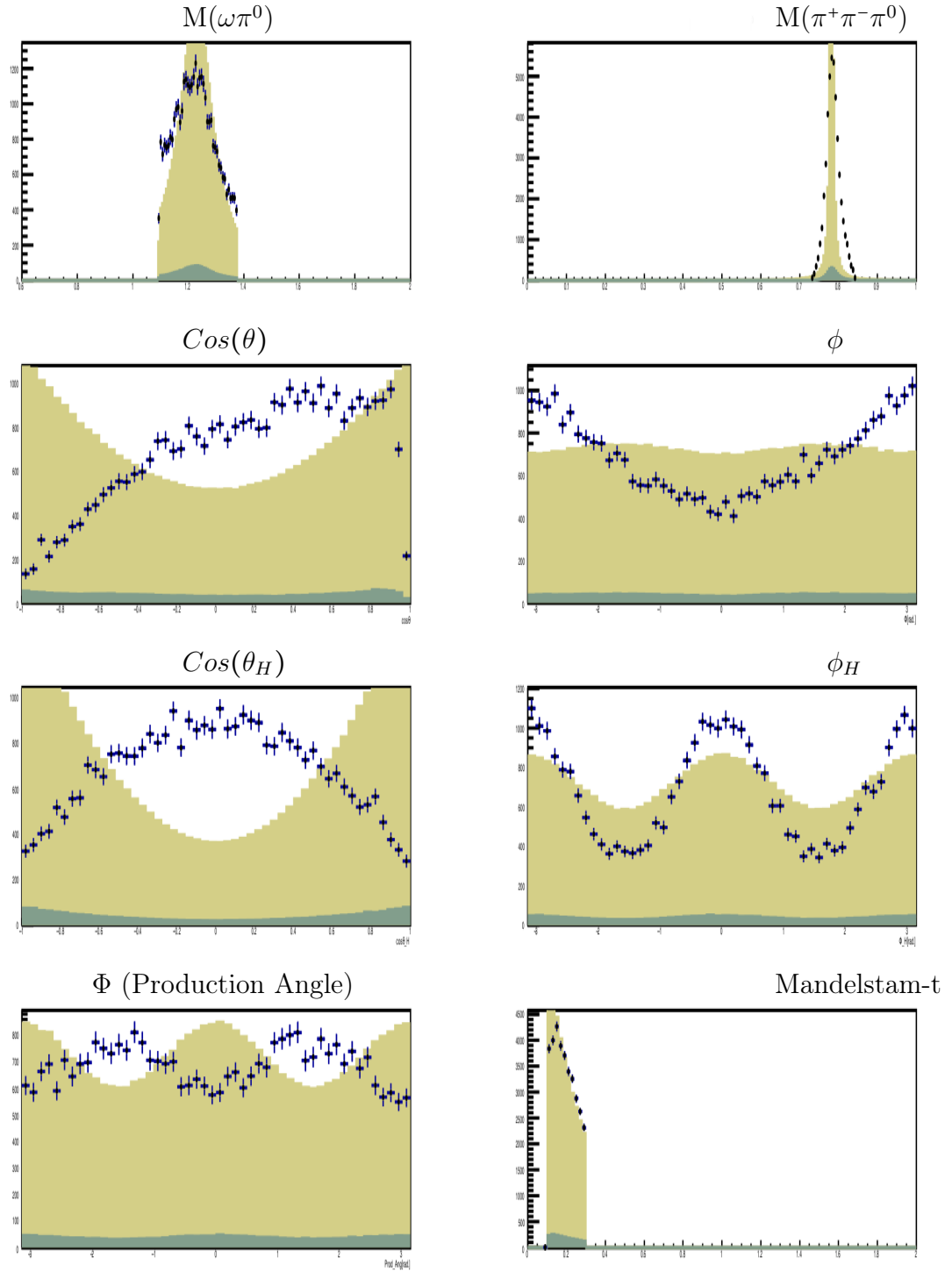


Figure 6.12: D-wave component of the AmpTools fit. The points represent the data, yellow histograms represent generated MC scaled by the physics model while green histograms represent accepted MC scaled by the physics model.

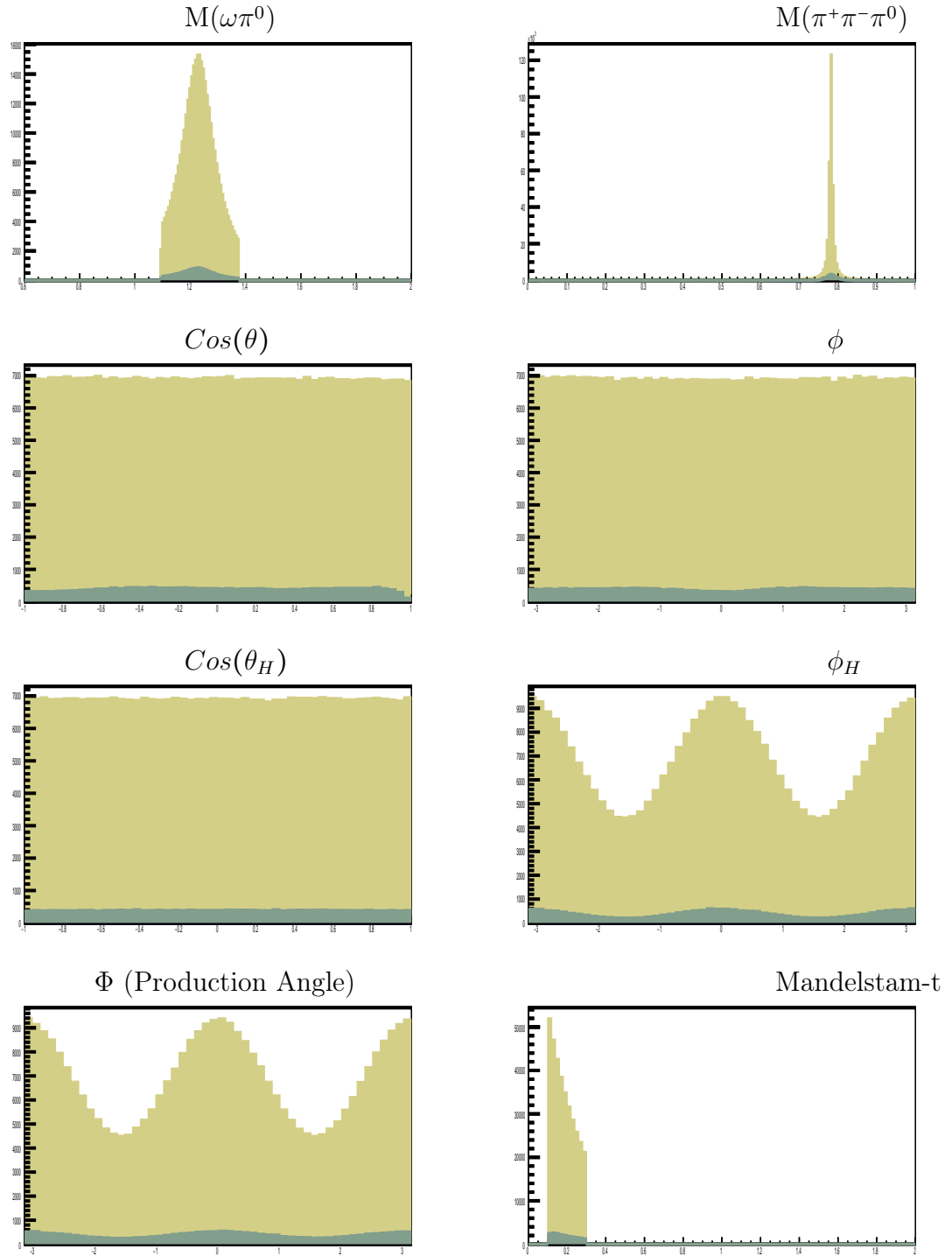


Figure 6.13: Generated phase space MC scaled by the the S-wave component of the physics model.

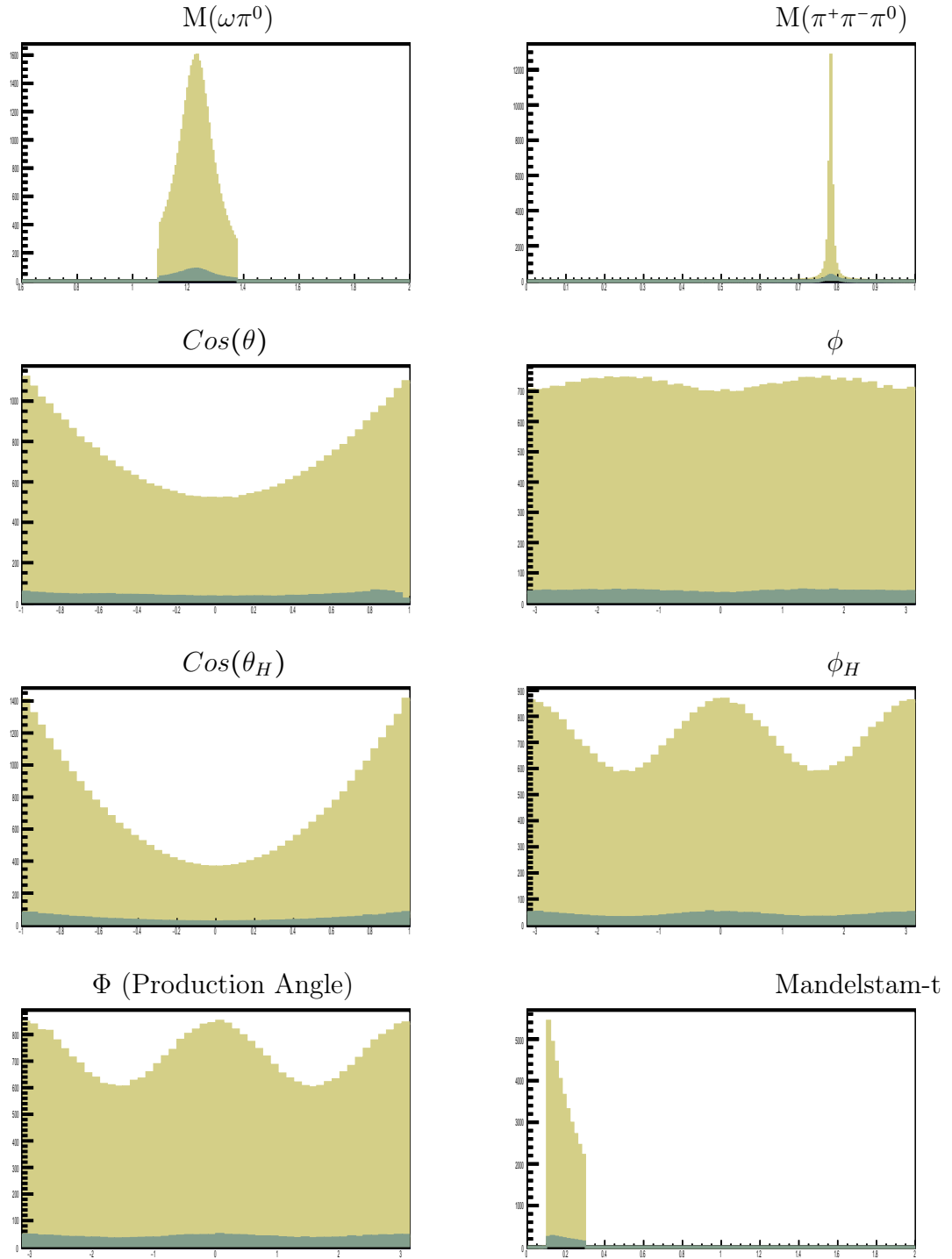


Figure 6.14: Generated phase space MC scaled by the the D-wave component of the physics model.

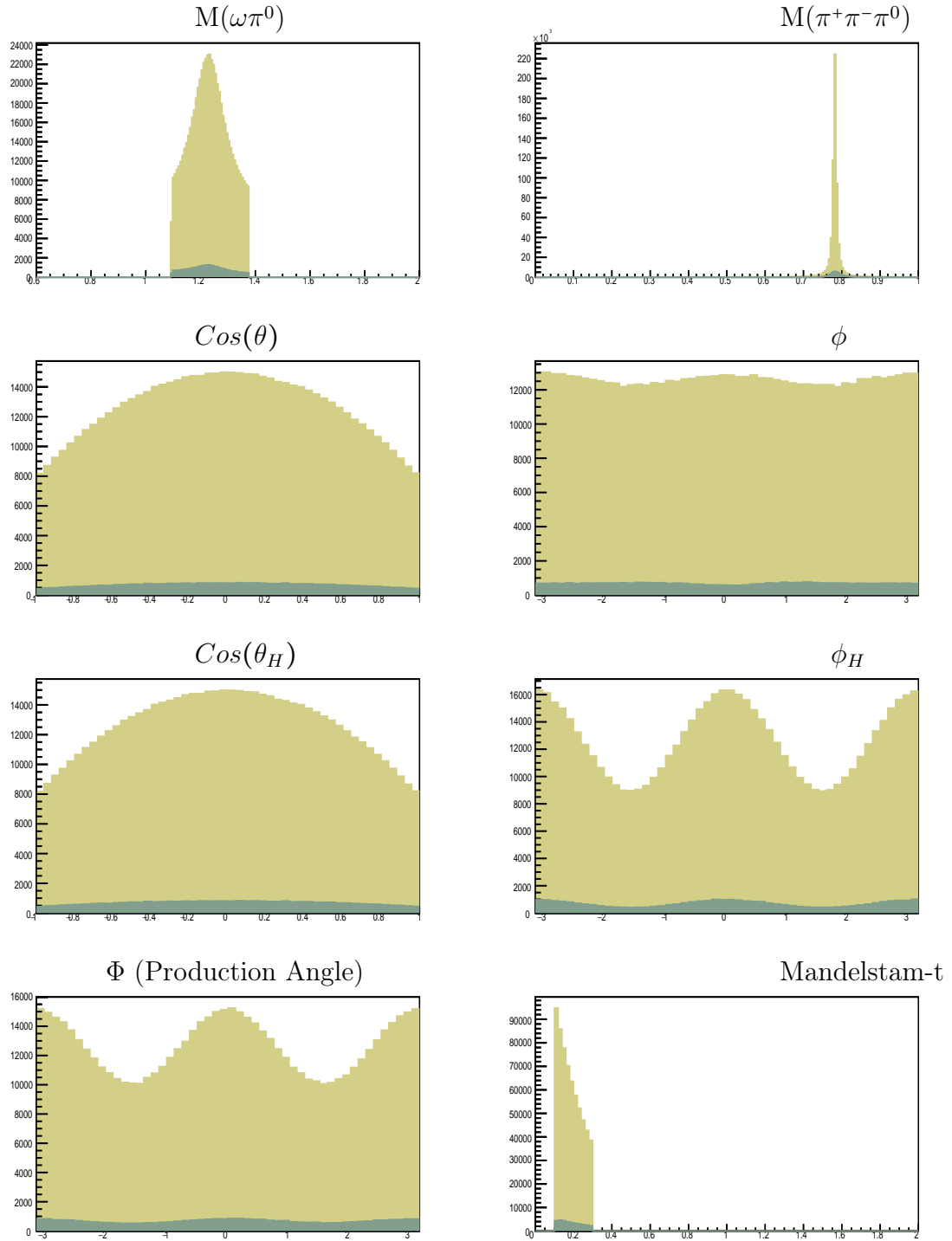


Figure 6.15: Generated phase space MC (yellow) and accepted phase space MC (green) scaled by the physics model.

6.4 Inclusive Cross-section for $\omega\pi^0$

The total cross-section (σ) of a reaction is a measure of probability that this reaction will take place in a collision of the initial state particles. The total cross-section is calculated as the number of events detected (N) divided over the detector efficiency (ϵ) times the beam luminosity (L).

$$\sigma = \frac{N}{\epsilon \times L} \quad (6.5)$$

The efficiency can be divided into tagging (beam tagger) and non-tagging (detector) efficiencies, and then the total photoproduction cross-section for the $\omega\pi^0$ could be calculated in bins of beam energy according to the following equation:

$$\sigma = \frac{N}{\epsilon_{non-tag} \times Tagged\ Flux \times Target\ Thickness} \quad (6.6)$$

In this equation, we assume 0.892 as the branching ratio for the ω decay to $\pi^+\pi^-\pi^0$ and 0.98823 as the branching ratio for the π^0 decay to 2γ [5].

Fig. 6.16 shows the different histograms used to calculate the total cross-section. From left to right: the top row represents the generated and accepted MC and the efficiency, which is the ratio between the two. The bottom row represents the yield from the data, the tagged flux as calculated by the PS (see Sec. 2.1.3) and the flux normalized yield, which is the ratio between the two. The total cross-section is the ratio between the flux normalized yield and the efficiency, scaled by the target thickness and branching ratios. Known artifacts show around the range of the tagger microscope in both the efficiency and flux normalized yield (see Sec. 2.1.1). The efficiency does not match for the three run periods. These features are being investigated by others in the collaboration. The total cross-section for the photoproduction of the

$\omega\pi^0$ is shown in Fig. 6.17. We compare our results with previous experiments in Fig. 6.18, and we can see that our results are consistent with those in our energy range. A few systematic checks are reported in Ch. 7 to ensure the stability of the total cross-section.

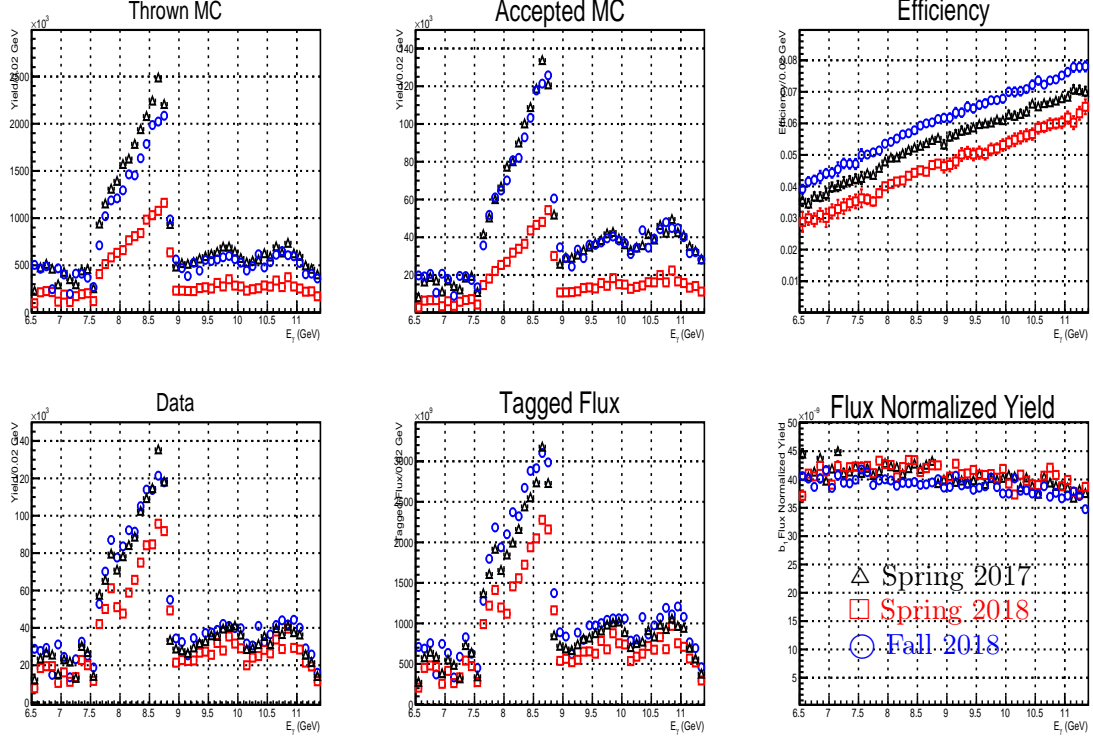


Figure 6.16: Calculating total cross-section of the $\omega\pi^0$ based on data from spring 2017 (Δ), spring 2018 (\square) and fall 2018 (\circ) run periods. Starting from top left the graphs show generated MC, accepted MC, efficiency, yield, tagged beam flux and flux normalized yield. Error bars represent only statistical error. (color online)

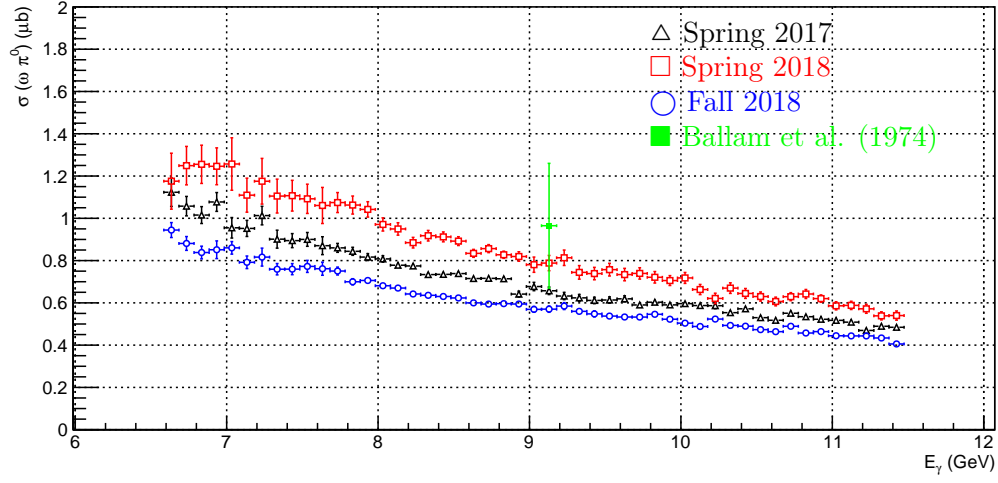


Figure 6.17: Our $\omega\pi^0$ total cross-section results calculated based on data from spring 2017 (Δ), spring 2018 (\square) and fall 2018 (\circ) run periods. Results from previous experiments: (green) Ballam et al. and references therein [16]. Error bars represent only statistical error. (color online)

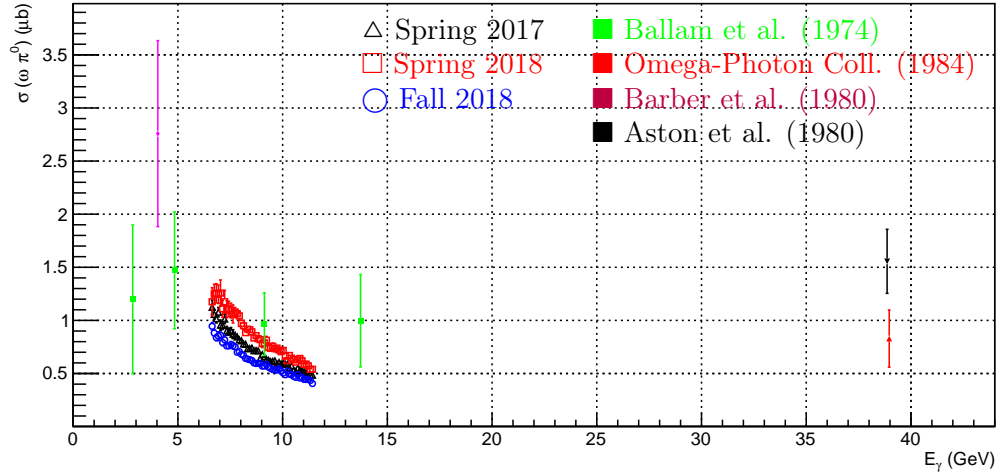


Figure 6.18: Our $\omega\pi^0$ total cross-section results calculated based on data from spring 2017 (Δ), spring 2018 (\square) and fall 2018 (\circ) run periods. Results from previous experiments: (green) Ballam et al. and references therein [16], (purple) Barber et al. [66], (black) Aston et al. [67], (red) The Omega-Photon collaboration [17]. Error bars represent only statistical error. (color online)

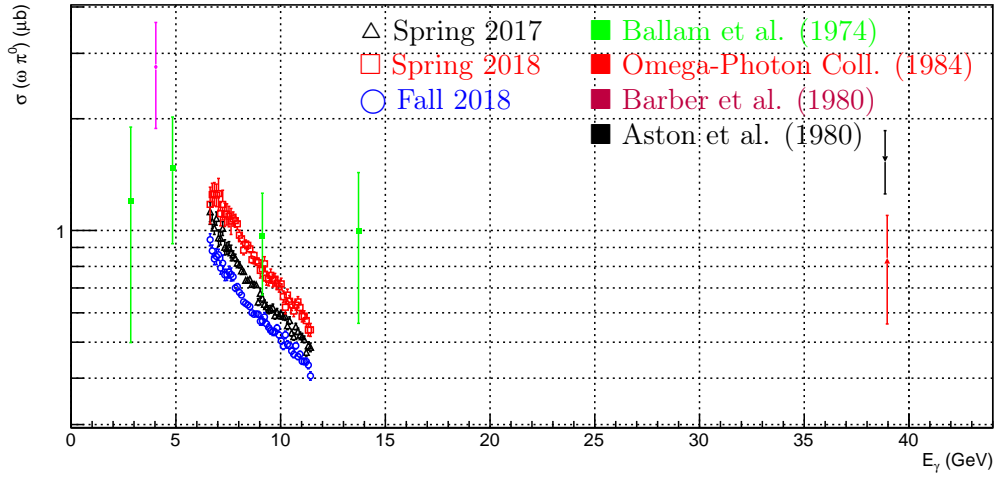


Figure 6.19: Our $\omega\pi^0$ total cross-section results calculated based on data from spring 2017 (Δ), spring 2018 (\square) and fall 2018 (\circ) run periods. Results from previous experiments: (green) Ballam et al. and references therein [16], (purple) Barber et al. [66], (black) Aston et al. [67], (red) The Omega-Photon collaboration [17]. Error bars represent only statistical error. (color online)

6.5 Differential Cross-section for $\omega\pi^0$

The differential cross-section ($\frac{d\sigma}{dt}$) of a reaction is a measure of probability that this reaction will take place in a collision of the initial state particles for a specific four momentum transfer (t) range. It can be calculated by dividing Eqs. 6.5 and 6.6 over dt leading to the following equations.

$$\frac{d\sigma}{dt} = \frac{N}{\epsilon \times L \times dt} \quad (6.7)$$

$$\frac{d\sigma}{dt} = \frac{N}{\epsilon_{non-tag} \times Tagged\ Flux \times Target\ Thickness \times dt} \quad (6.8)$$

The differential cross-section for the photoproduction of the $\omega\pi^0$ is shown in Fig. 6.20 in 5 beam energy bins. Our results from different runs periods do not align, specially at high Mandelstam- t . We see a spike in the differential cross-section in the all beam energy bins at low t . Fig. 6.21 presents the same data plotted on a log scale where

we see the change in the slope of the distribution, and use a sum of two exponential functions for fitting. The mean slope for $0.25 < |t| < 95.0 \text{ GeV}^2/c^2$ is -5.24 ± 0.04 which is consistent with a peripheral production mechanism yet does not agree with the slope of -5 reported by the Omega-Photon Collaboration [17]. The mean slope for $0.95 < |t| < 2.0 \text{ GeV}^2/c^2$ is -1.24 ± 0.05 . This change in slope indicates different production mechanisms. A summary of the fit results is presented in Table. 6.5. Calculations of the differential cross-section at high Mandelstam-t is limited by statistics of our MC simulation. A MC simulation with equal number of events in bins of Mandelstam-t would address that. Also, collaborators are working on supporting simulations with a sum of two Mandelstam-t slopes. Systematic checks are needed to ensure the stability of the differential cross-section.

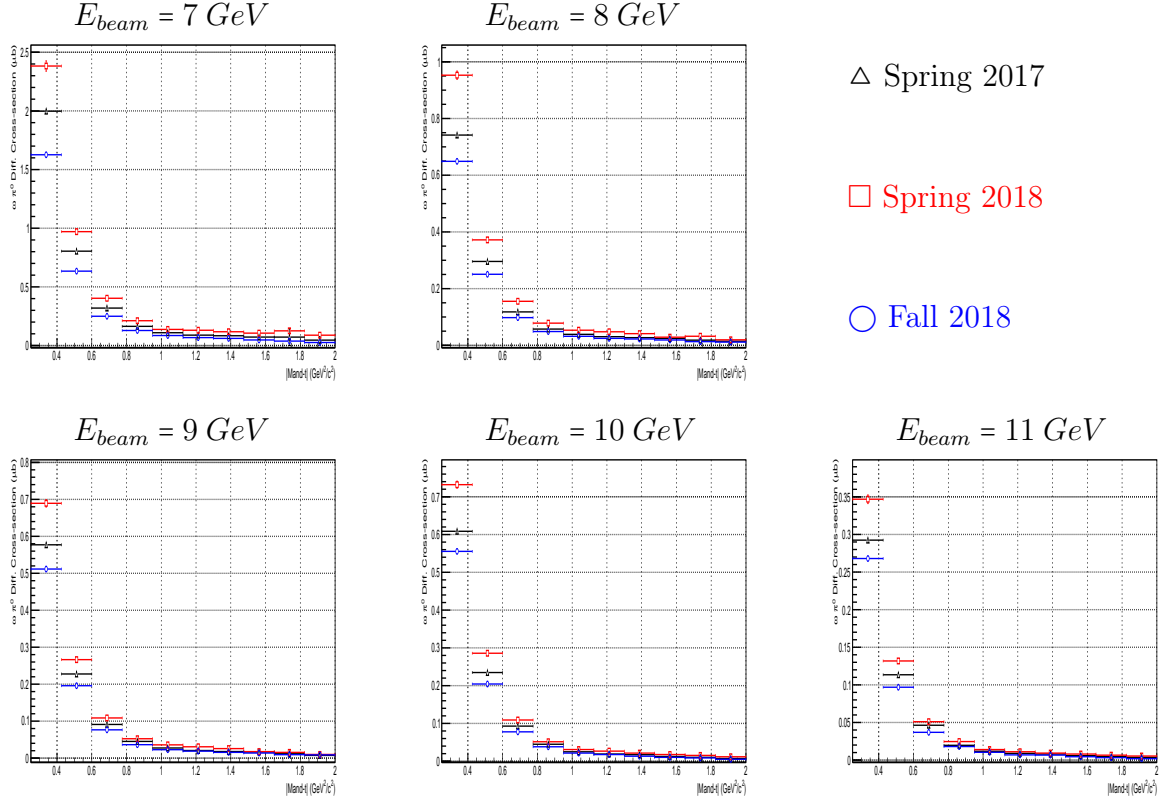


Figure 6.20: Our $\omega\pi^0$ differential cross-section results in different beam energy bins. Calculated based on data from spring 2017 (black), spring 2018 (red) and fall 2018 (blue) run periods. Our results from different runs periods do not align, specially at low Mandelstam- t . We see a spike in the differential cross-section in the 11 GeV beam energy bin at low t . Error bars represent only statistical error. (color online)

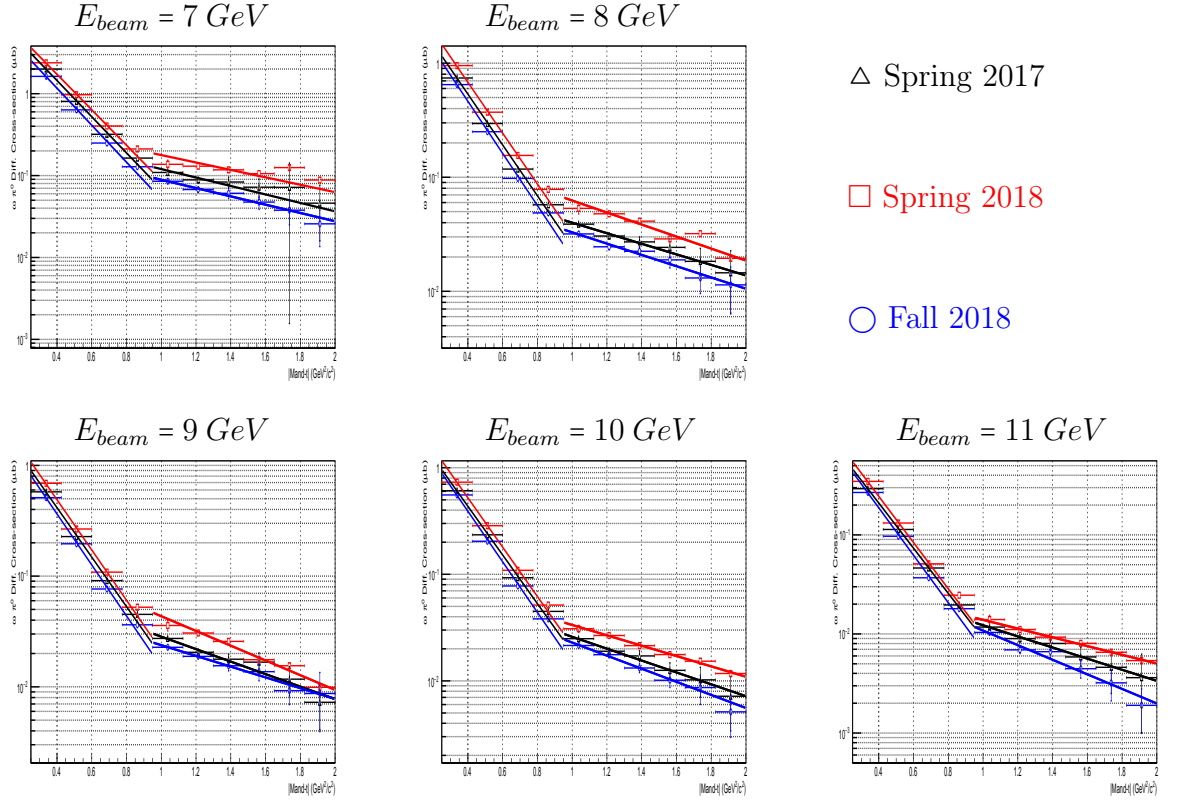


Figure 6.21: Exponential fit of our $\omega\pi^0$ differential cross-section results on semi-log plots are shown in different beam energy bins, calculated based on data from spring 2017 (black), spring 2018 (red) and fall 2018 (blue) run periods. Our results from different runs periods do not align. The distribution is fitted to the sum of two exponential functions. The mean slope is -5.24 ± 0.04 for $0.25 < |t| < 0.95 \text{ GeV}^2/c^2$ and -1.24 ± 0.05 for $0.95 < |t| < 2.0 \text{ GeV}^2/c^2$. A summary of the fit results is presented in Table. 6.5. Error bars represent only statistical error. (color online)

	E_γ	$0.25 < t < 0.95$	$0.95 < t < 2.0$
Sp. 2017	7	-5.09 ± 0.05	-1.2 ± 0.3
	8	-5.13 ± 0.03	-1.1 ± 0.2
	9	-5.15 ± 0.04	-1.3 ± 0.2
	10	-5.26 ± 0.04	-1.3 ± 0.2
	11	-5.25 ± 0.05	-1.3 ± 0.3
Sp. 2018	7	-4.99 ± 0.09	-1.04 ± 0.05
	8	-5.13 ± 0.08	-1.21 ± 0.04
	9	-5.22 ± 0.07	-1.53 ± 0.04
	10	-5.33 ± 0.06	-1.12 ± 0.05
	11	-5.37 ± 0.08	-1.02 ± 0.08
Fall 2018	7	-5.20 ± 0.04	-1.2 ± 0.2
	8	-5.26 ± 0.03	-1.1 ± 0.2
	9	-5.30 ± 0.03	-1.1 ± 0.2
	10	-5.46 ± 0.04	-1.4 ± 0.2
	11	-5.51 ± 0.05	-1.7 ± 0.2
	GlueX	-5.24 ± 0.04	-1.24 ± 0.05

Table 6.5: Fit results of the $\omega\pi^0$ differential cross-section in different bins of photon beam energy for Spring 2017, Spring 2018 and Fall 2018 run periods. The mean fit slope and error are calculated over all beam energies and run periods.

6.6 Summary

We established foundations for extracting and fitting the $\omega\pi$ channel in AMs basis. Our extracted AMs qualitatively agree with results from the Omega-Photon collaboration improve on their statistics. More work is needed by our collaborators to finalize the fitting algorithm for the acceptance corrected angular moments.

We constructed a framework for extracting partial waves amplitudes for the $\omega\pi^0$ channel up to spin 2. This was demonstrated by an example fit which reproduces the main features of a $J^P = 1^+$ state with a 0.27 D/S waves ratio as expected for the b_1 meson. A search for the optimum basis set and for ambiguities in the fit is needed to extract the partial wave amplitudes. These efforts have been handed over to another member of the Regina group.

We studied the s-channel helicity conservation of the $b_1(1235)$ meson photoproduction in the three run periods. Our results indicate that the b_1 meson is produced by a non-helicity-conserving mechanism. This agrees with conclusions from the SLAC-H experiment. However, our fit results exceed their statistics by four orders of magnitude and extend to three more beam polarization configurations.

We extracted the helicity amplitudes of the $b_1(1235)$ meson using data from GlueX three run periods. Our fit average is $|F_1|^2 = 0.3037 \pm 0.0003$ which does not agree with the $|F_1|^2 = 0.437 \pm 0.012$ expected for the b_1 meson. Also, our results do not agree with the SLAC-H collaboration results. More work on excluding background contributions under the b_1 peak could help improving our results.

We extracted the $\omega\pi^0$ cross-section in the beam energy range 6.5-11.4 GeV based on data from GlueX three run periods. Our results agree with previous experiments and improve on their statistics. More work is needed to amalgamate the three run periods. An amplitude analysis would allow isolating the b_1 cross-section.

We extracted the $\omega\pi^0$ differential cross-section in the Mandelstam-t range 0.25-2.0 GeV/c^2 in five beam energy bins based on data from GlueX three run periods. Our results are fitted with two exponential decay functions indicating two different production mechanisms. In the 0.25-0.95 GeV/c^2 Mandelstam-t range, the average slope is -5.24 ± 0.04 which indicates a peripheral production mechanism and is very close but does not agree with the slope of -5 reported by the Omega-Photon experiment [17]. In the 0.95-2.0 GeV/c^2 Mandelstam-t range, the average slope is -1.24 ± 0.05 . Our results improve on the statistics of previous experiments yet more work is needed to merge the three run periods.

Chapter 7

Systematic Studies

Based on our choices for event selection and analysis method we presented our results with statistical errors in Ch. 6. In this chapter, we will discuss studies on the key systematics of our event selection and analysis. The goal of these studies is to bestow more confidence on our results and to estimate systematic errors as guidance on possible bias in our analysis.

As detailed in Ch. 4, our event selection is based on a set of cuts used to select events with the correct topology and reject background events. A systematic check could be done by varying these cuts from the nominal value to a tighter (allowing fewer events) or looser (allowing more events) value and study how much the final results changes. The change in the final result could be used as an estimate for systematic uncertainty coupled with the application of this cut.

Following the GlueX collaboration guidelines for systematic studies [69], we explore cut values to the level where the event yield is varied by no more than $\pm 5\%$, to avoid an adverse impact to the statistics of our channel. In our studies, we add independent systematic error contributions in quadrature and add dependent systematic

error contributions linearly ¹. The total systematic error is added to the statistical error in quadrature.

In this chapter, we will discuss our choice for the most significant potential sources of systematic uncertainty in our event selection. Then we will present our studies on the systematic uncertainty associated with these cuts on the cross-section and differential cross-section of the $\omega\pi^0$.

7.1 Potential Sources of Systematic Error

Observing how the cross-section is calculated in Eq. 6.6 and substituting for the detector acceptance $\epsilon_{non-tag} = \frac{Accepted\ MC}{Thrown\ MC}$ we get:

$$\sigma = \frac{Thrown\ MC}{Tagged\ Flux \times Target\ Thickness} \times \frac{N}{Accepted\ MC} \quad (7.1)$$

As most of our analysis cuts only affect the yield from the data (N) and the accepted MC, it follows that, useful guidance on potential sources for systematic uncertainty can be derived by comparing the effect of a cut on the yield of the $\omega\pi^0$ final state in data and accepted MC, which we call the efficiency of that cut. Fig. 7.1 shows the efficiency ratio of our analysis cuts based on data from the Spring 2017 run period and signal MC. The efficiency of a cut is calculated by dividing the yield obtained by applying all our analysis cuts over the yield obtained by relaxing one cut and applying all the remaining analysis cuts.

$$Cut\ Efficiency = \frac{Yield\ (all\ cuts\ applied)}{Yield\ (one\ cut\ relaxed)} \quad (7.2)$$

¹A full covariance matrix or a calculation of correlation coefficients were beyond the scope of this thesis due to time constraints. These will be investigated in the future by another graduate student in the group.

The efficiency ratio is then calculated by dividing the efficiency of the cut in data over the efficiency of the cut in signal MC.

$$Efficiency\ Ratio\ (cut) = \frac{Cut\ Efficiency\ (Data)}{Cut\ Efficiency\ (MC)} \quad (7.3)$$

Most of the cuts have $100 \pm 1\%$ efficiency, which indicates that these cuts have the same effect on the data and signal MC ensemble.

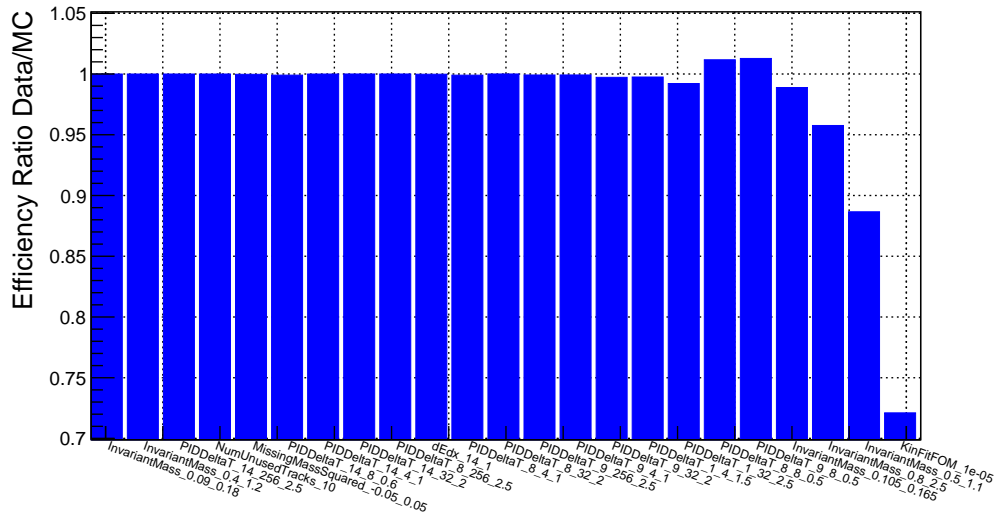


Figure 7.1: The efficiency ratio of our analysis cuts on the yield of $\omega\pi^0$ in data and signal MC. Least efficient cuts are the particular KinFit FOM cut and the invariant mass cuts on the $\pi^+\pi^-\pi^0$ and $\omega\pi^0$ respectively. The rest of the cut have $100 \pm 1\%$ efficiency.

The cuts with lowest efficiencies are:

1. KinFit FOM Cut (eff = 72%)
2. $\pi^+\pi^-\pi^0$ Invariant Mass Cut (eff = 89%)
3. $\omega\pi^0$ Invariant Mass Cut (eff = 95.8%)

In the following sections we will study the systematic uncertainty associated with these cuts. The rest have a very small effect on the efficiency and thus their contribution to the systematic error was deemed as negligible for this analysis.

7.2 $\omega\pi$ Cross-section Systematic Studies

In this section we will study the effect of the KinFit FOM, $\pi^+\pi^-\pi^0$ and $\omega\pi^0$ invariant mass cuts on the cross-section of the $\omega\pi^0$. Each cut is changed independently and the cross-section of the $\omega\pi^0$ is calculated in bins of beam energy for the three run periods.

7.2.1 Kinematic Fit FOM Cut Study

The KinFit FOM for a particle combination is a value between 0 and 1 quantifying the likelihood of that particle combination to describe a real event. A higher FOM indicates that the particle combination is more likely to be a true signal event.

The KinFit FOM cut is changed from the nominal 5×10^{-5} cut to a looser cut of 10^{-5} and a tighter cut of 2.4×10^{-4} . These cuts represent variation of $\pm 5\%$ of the data statistics. For each cut value, the $\omega\pi^0$ cross-section is calculated for the three run periods in bins of beam energy. In each bin, the maximum change in the cross-section is used as an estimate for the systematic error in that bin. The statistical error is added to the systematic error in quadrature to form the total error in each bin.

The $\omega\pi^0$ cross-section with systematic error, as calculated from the KinFit FOM cut scan, is shown in the top panel of Fig. 7.2. The systematic error is drawn in violet while the total error is drawn in green. The systematic error is very small such that it is hard to see on the graph. The bottom left panel of Fig. 7.2 shows the relative systematic (in violet) and statistical (in blue) errors. The bins of the for spring 2018 and fall 2018 run periods are shifted along the x-axis for clarification this is more clear in the zoomed portion shown in the bottom right panel. The relative systematic error is less than ± 0.01 , which is small compared to the relative statistical error.

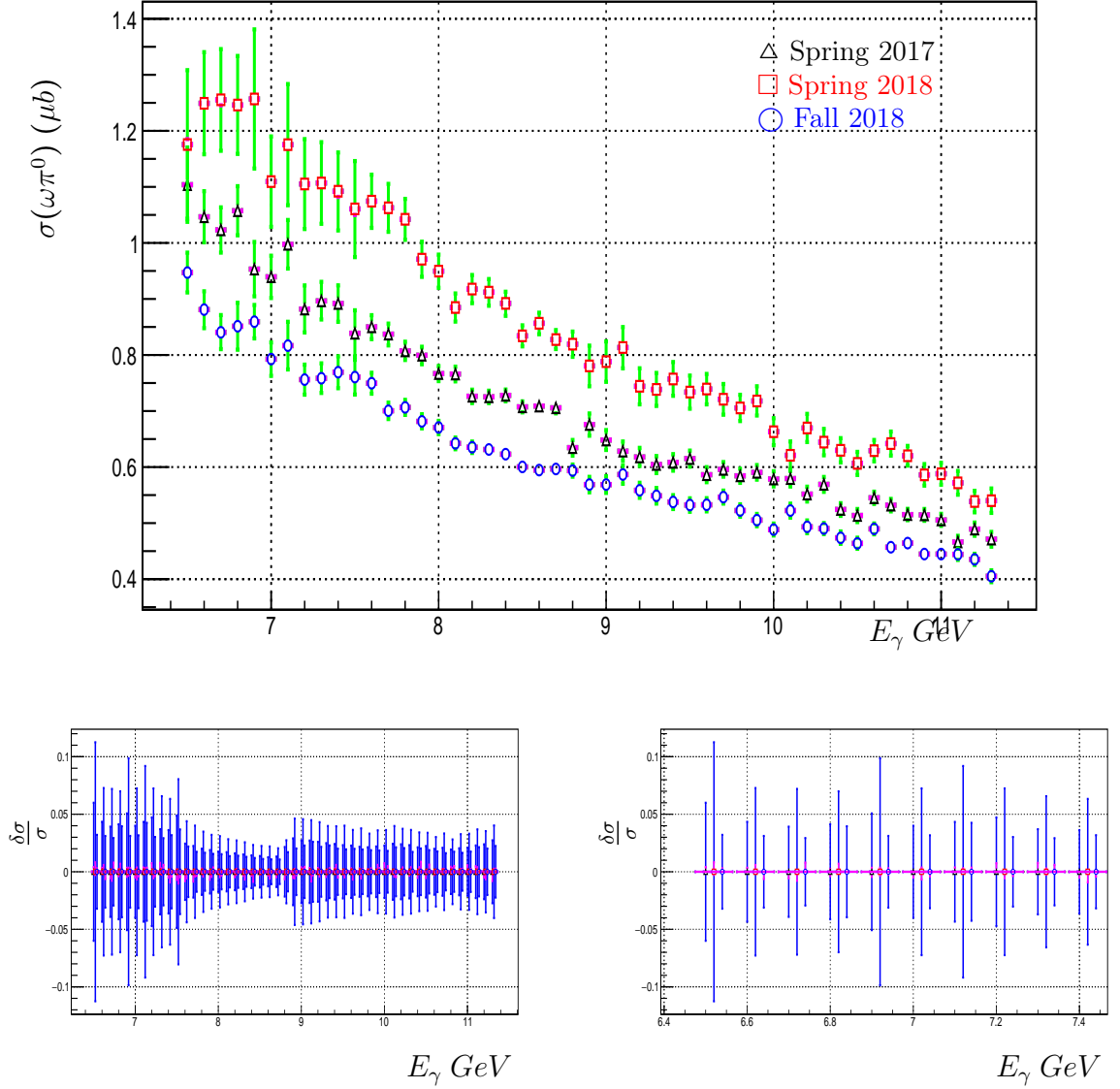


Figure 7.2: (top) The $\omega\pi^0$ cross-section with the systematic error calculated for the three run periods by changing the KinFit FOM cut from 10^{-5} to 10^{-4} . The systematic error is added in quadrature to the statistical error to form the total error for each bin. The systematic error is drawn in violet while total error is shown in green. (bottom left) The relative statistical (blue) and systematic (violet) errors for the $\omega\pi^0$ cross-section. Data points for spring 2018 and fall 2018 run periods are shifted along the x-axis for clarification. (bottom right) A zoomed portion of the lower side of the energy range showing the relative statistical and systematic errors.

7.2.2 $\pi^+\pi^-\pi^0$ Invariant Mass Cut Study

As discussed in Ch. 4, the $\pi^+\pi^-\pi^0$ invariant mass cut selects candidates with invariant mass in the ω peak. The ω peak is defined based on the width of the Briet-Wigner fit of the peak. The cut scan varies the width of the ω peak. As explained in Ch. 4, varying the ω peak width also changes the width and location of the ω -side-band used for background subtraction.

The nominal width of the ω peak in this analysis is 3σ above and below the ω . The cut scan varies the width of the ω peak from 2.6σ to 3.43σ above or below the ω peak, which corresponds to $\pm 5\%$ change in the statistics of our channel. For each peak width, the background is subtracted based on the ω -side-bands and the $\omega\pi^0$ cross-section is calculated for the three run periods in bins of beam energy. In each bin, the maximum change in the cross-section is used as an estimate for the systematic error in that bin. The statistical error is added to the systematic error in quadrature to form the total error in each bin.

The $\omega\pi^0$ cross-section with systematic error, as calculated from the $\pi^+\pi^-\pi^0$ invariant mass cut scan, is shown in top panel of Fig. 7.3. The systematic error is drawn in violet while total error is shown in green. The systematic error is visible on few bins specially on the low beam energy side and for spring 2018 run period. The bottom left panel of Fig. 7.3, shows the relative systematic (in violet) and statistical (in blue) errors. The bins of the for spring 2018 and fall 2018 run periods are shifted along the x-axis for clarification. This is more clear in the zoomed portion shown in the bottom right panel. The relative systematic error is mostly less than ± 0.05 , except for the lowest bin of spring 2018 run period where it reaches 0.08. The relative systematic error is considerable compared to the relative statistical error. We expect the systematic error is mostly on the positive side due to the cut variation allowing

more background around the ω peak into the cross-section calculation.

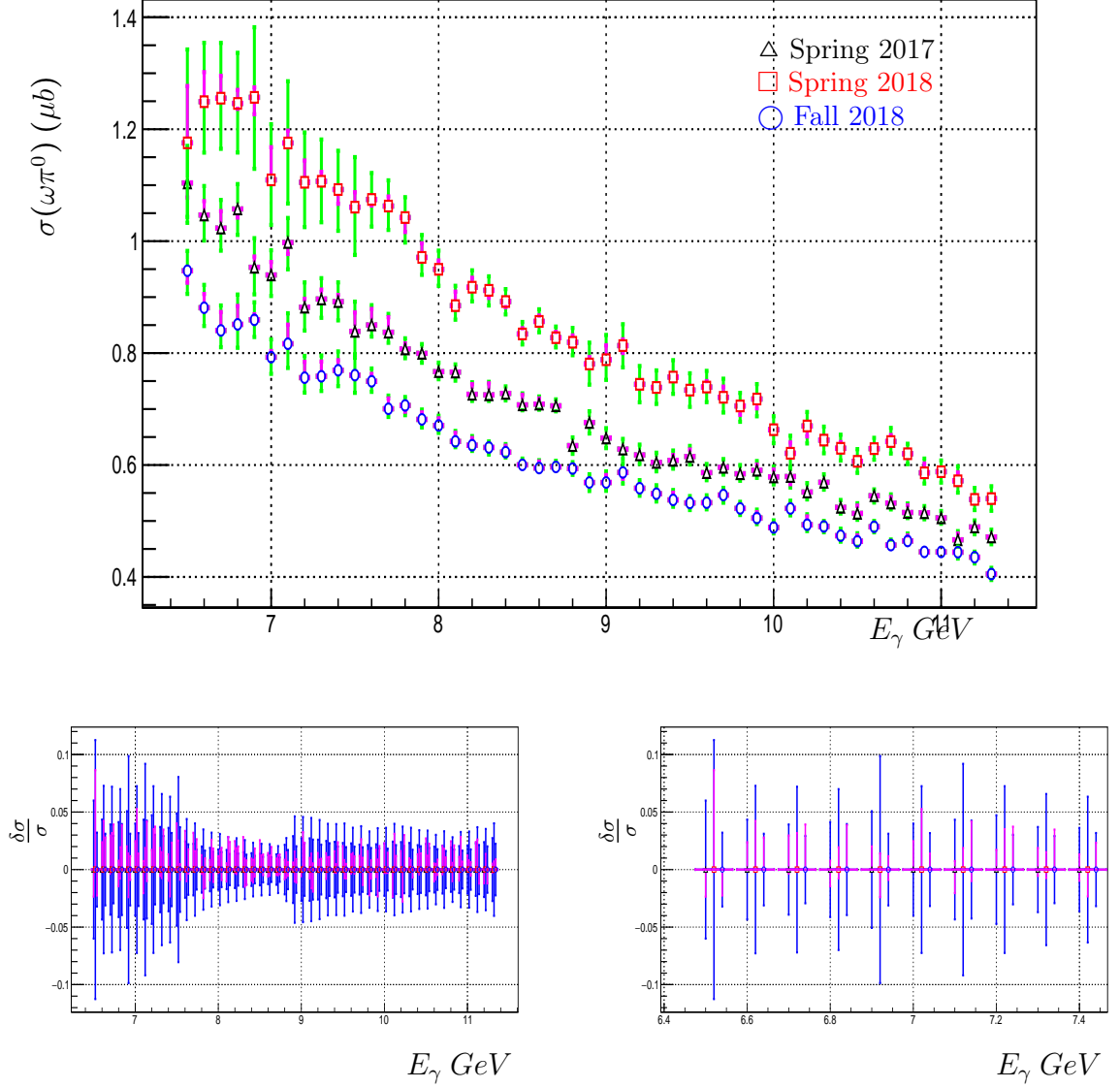


Figure 7.3: (top) The $\omega\pi^0$ cross-section with systematic error calculated for the three run periods by changing the width of the ω peak from 2.6σ to 3.43σ above and below the ω peak. The systematic error is added in quadrature to the statistical error to form the total error for each bin. The systematic error is drawn in violet while total error is shown in green. (bottom left) The relative statistical (blue) and systematic (violet) errors for the $\omega\pi^0$ cross-section. Data points for spring 2018 and fall 2018 run periods are shifted along the x-axis for clarification. (bottom right) A zoomed portion of the lower side of the energy range showing the relative statistical and systematic errors.

7.2.3 $\omega\pi^0$ Invariant Mass Cut Study

The $\omega\pi^0$ invariant mass cut selects a range for the inclusive cross-section calculation. The nominal cut includes all $\omega\pi$ candidates with 8.7σ above and below the b_1 peak into the $\omega\pi^0$ cross-section calculation.

As a systematic check, the $\omega\pi^0$ invariant mass cut is changed to a looser cut of 15σ and a tighter cut of 7.2σ above and below the b_1 peak. This change in $\omega\pi^0$ invariant mass range changes the statistics by $\pm 5\%$. Using this cut, the $\omega\pi^0$ cross-section is calculated for the three run periods in bins of beam energy. In each bin, the maximum change in the cross-section is used as an estimate for the systematic error in that bin. The statistical error is added to the systematic error in quadrature to form the total error in each bin.

The $\omega\pi^0$ cross-section with systematic error, as calculated from the $\omega\pi^0$ invariant mass cut scan, is shown in the top panel of Fig. 7.4. The systematic error is drawn in violet while the total error is shown in green. The graph shows that the $\omega\pi^0$ invariant mass cut introduces small but noticeable systematic uncertainty to our $\omega\pi^0$ cross-section calculation over the beam energy range. The bottom left panel of Fig. 7.4, shows the relative systematic (in violet) and statistical (in blue) errors. The bins of the spring 2018 and fall 2018 run periods are shifted along the x-axis for clarification. This is more clear in the zoomed portion shown in the bottom right panel. The relative systematic error is mostly less than ± 0.03 . The relative systematic error is considerable compared to the relative statistical error. We expect the systematic error to be always on the positive side due to the cut variation affecting mostly far ends of the $\omega\pi^0$ invariant mass where our simulation (which is mostly b_1) fades much faster than the data.

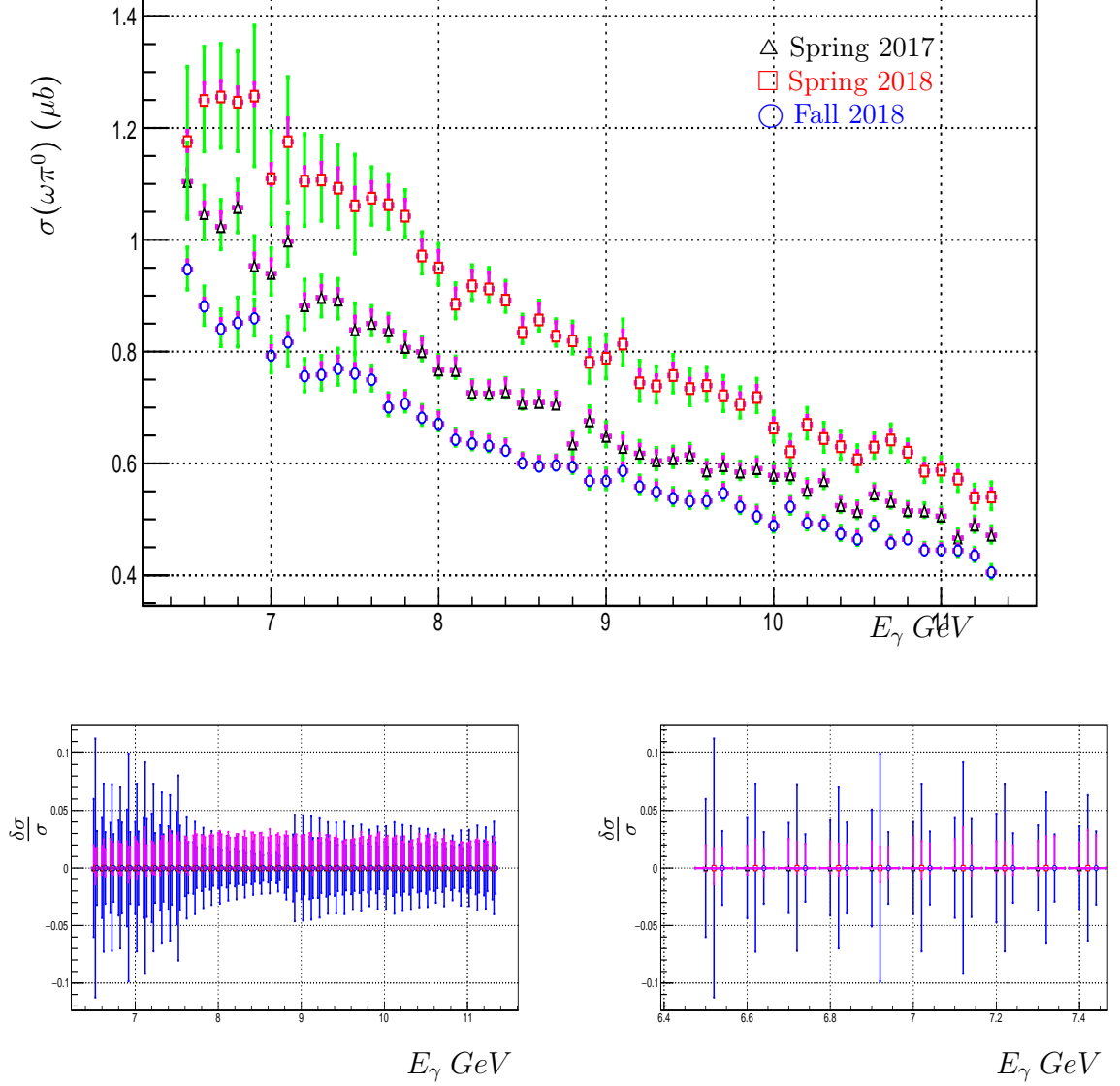


Figure 7.4: (top) The $\omega\pi^0$ cross-section with systematic error calculated for the three run periods by changing the $\omega\pi^0$ invariant mass cut. The systematic error is added in quadrature to the statistical error to form the total error for each bin. The systematic error is drawn in violet while total error is shown in green. (bottom left) The relative statistical (blue) and systematic (violet) errors for the $\omega\pi^0$ cross-section. Data points for spring 2018 and fall 2018 run periods are shifted along the beam energy axis for clarification. (bottom right) A zoomed portion of the lower side of the energy range showing the relative statistical and systematic errors.

7.2.4 $\omega\pi$ Cross-section Combined Systematic Error

As the KinFit exerts pulls on the invariant masses of the $\pi^+\pi^-\pi^0$ and $\omega\pi^0$ candidates, we expect the systematic errors associated with KinFit and invariant mass cuts to be correlated. Following the GlueX collaboration systematics guidelines [69], the combined systematic error is calculated by adding the systematic errors of the KinFit FOM, the $\pi^+\pi^+\pi^0$ and the $\omega\pi^0$ invariant mass cuts linearly.

The top panel of Fig. 7.5 shows the $\omega\pi^0$ cross-section for the three run periods in bins of beam energy. For each bin, the combined systematic error is calculated by adding the systematic errors in the bin linearly. The statistical error is added to the combined systematic error in quadrature to form the total error in each bin. The combined systematic error is drawn in violet while total error is shown in green. The graph shows that by linearly adding the systematic uncertainty for the KinFit FOM, the $\pi^+\pi^+\pi^0$ and the $\omega\pi^0$ invariant mass cuts, the systematic uncertainty on our $\omega\pi^0$ cross-section calculation we see small yet noticeable systematic error across the beam energy range. The bottom left panel of Fig. 7.5, shows the relative combined systematic (in violet) and statistical (in blue) errors. The bins of the spring 2018 and fall 2018 run periods are shifted along the x-axis for clarification. This is more clear in the zoomed portion shown in the bottom right panel. The relative combined systematic error is mostly less than ± 0.06 . The relative combined systematic error is comparable to the relative statistical error.

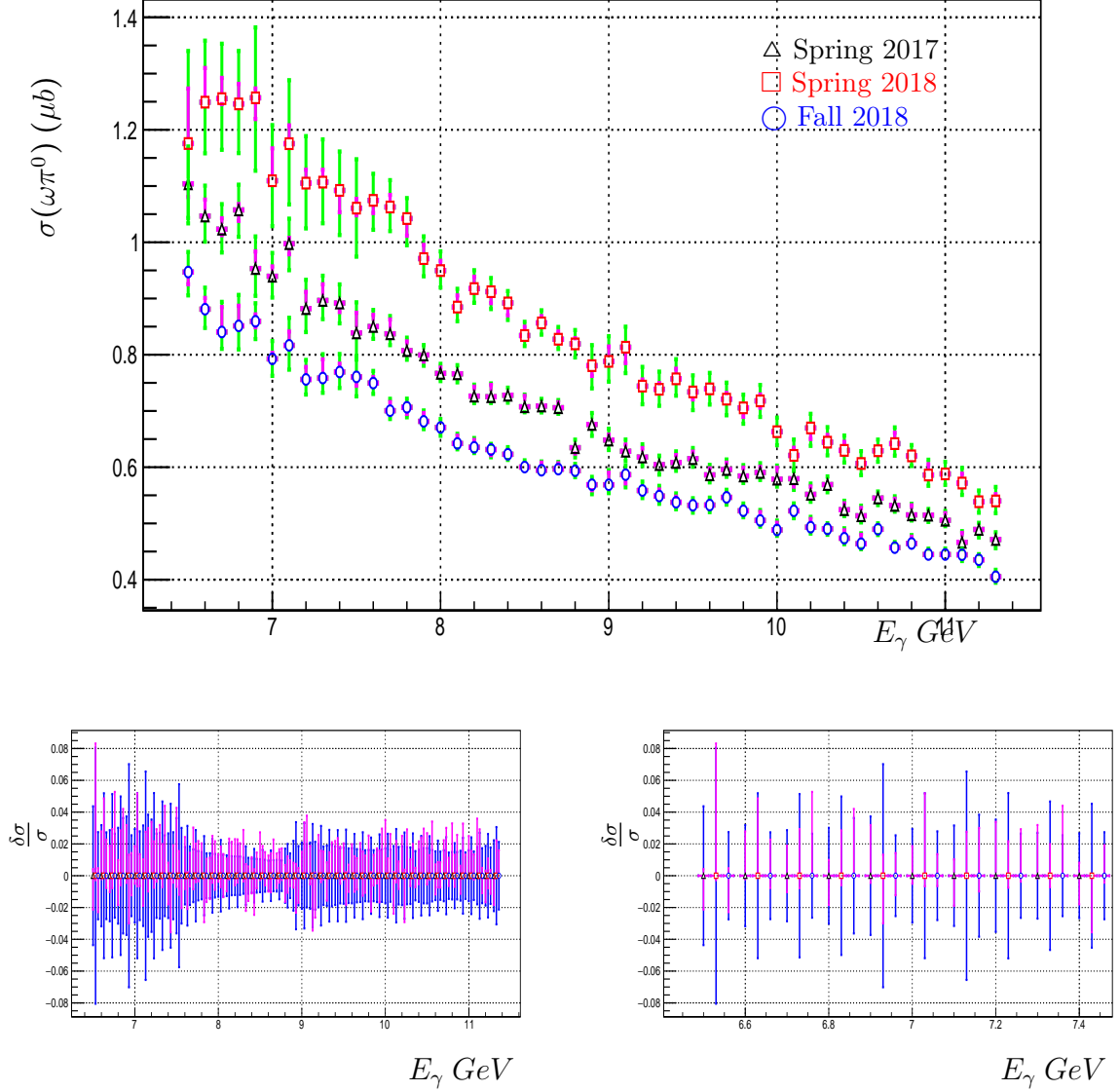


Figure 7.5: (top) The $\omega\pi^0$ cross-section with combined systematic error calculated for the three run periods by linearly adding the systematic errors for the KinFit FOM, $\pi^+\pi^-\pi^0$ and the $\omega\pi^0$ invariant mass cuts. The combined systematic error is added in quadrature to the statistical error to form the total error for each bin. The systematic error is drawn in violet while total error is shown in green. (bottom left) The relative statistical (blue) and combined systematic (violet) errors for the $\omega\pi^0$ cross-section. Data points for spring 2018 and fall 2018 run periods are shifted along the x-axis for clarification. (bottom right) A zoomed portion of the lower side of the energy range showing the relative statistical and combined systematic errors.

7.3 $\omega\pi$ Differential Cross-section Systematic Studies

In this section we study the effect of the KinFit FOM, $\pi^+\pi^-\pi^0$ and $\omega\pi^0$ invariant mass cuts on the differential cross-section of the $\omega\pi^0$. Each cut is changed independently and the differential cross-section of the $\omega\pi^0$ is calculated in bins of Mandelstam-t for five beam energy bins and the three run periods.

7.3.1 Kinematic Fit FOM Cut Study

In order to estimate the systematic uncertainty for the $\omega\pi^0$ differential cross-section, we follow the same procedure as in Sec. 7.2.1. The KinFit FOM cut is changed from the nominal 5×10^{-5} cut to a looser cut of 10^{-5} and a tighter cut of 2.4×10^{-4} . These cuts represent variation of $\pm 5\%$ of the data statistics. For each cut value, the $\omega\pi^0$ differential cross-section is calculated for the three run periods in five bins of beam energy. In each bin for Mandelstam-t, the maximum change in the differential cross-section is used as an estimate for the systematic error in that bin. The statistical error is added to the systematic error in quadrature to form the total error in each bin.

The $\omega\pi^0$ differential cross-section with systematic error, as calculated from the KinFit FOM cut scan, is shown in Fig. 7.6. The systematic error is drawn in violet while total error is shown in green. The bins for the spring 2018 and fall 2018 run periods are shifted along the x-axis for clarification. The systematic error is small such that it can not be seen. The same plots on log scale are represented in Fig. 7.7. The relative systematic (in violet) and statistical (in blue) errors are shown in Fig. 7.8. The relative systematic error is mostly less than 0.1. The relative systematic error is more considerable for bins at the higher end of the Mandelstam-t range where we expect statistical effects of our cuts to be more relevant, as evident by the

larger relative statistical error in these bins.

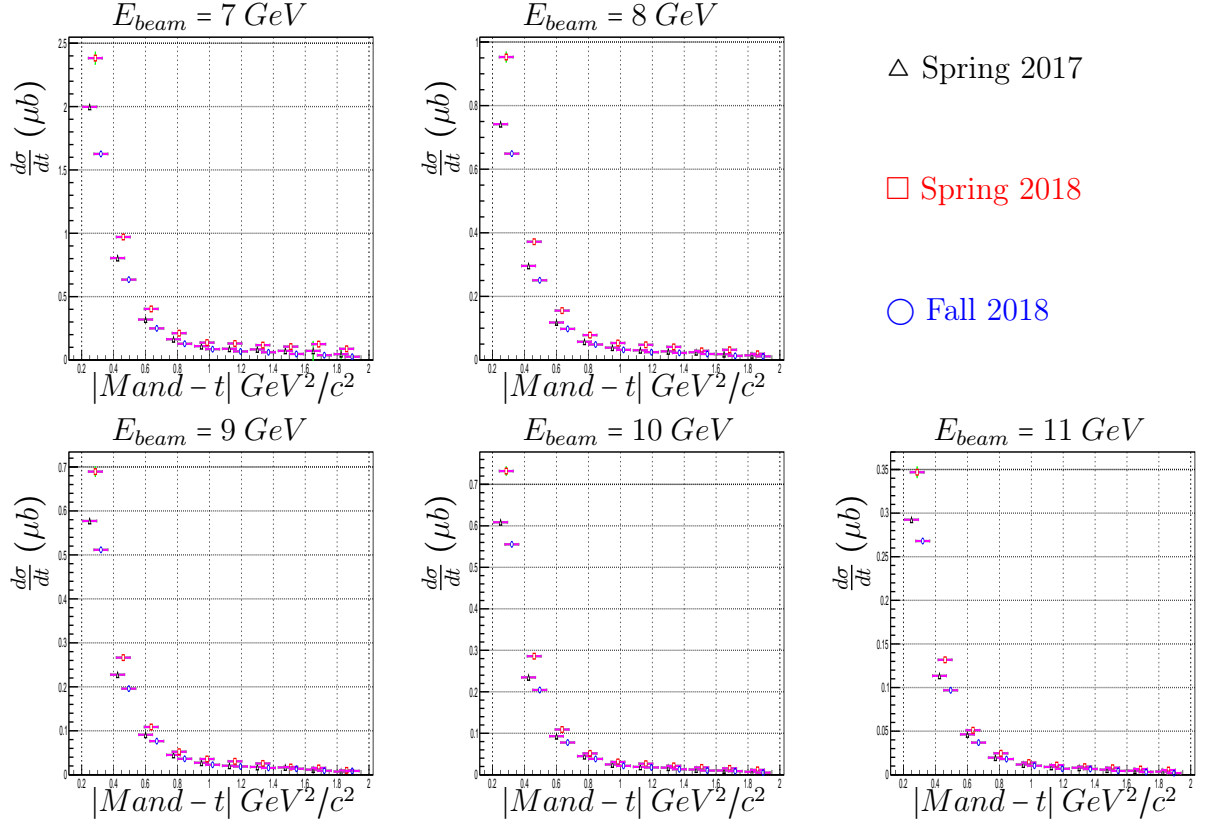


Figure 7.6: The $\omega\pi^0$ differential cross-section with systematic error calculated for changing the KinFit FOM cut from 10^{-5} to 24×10^{-5} . The systematic error is added in quadrature to the statistical error to form the total error for each bin. The systematic error is drawn in violet while total error is shown in green. Spring 2018 and Fall 2018 data points are shifted along the beam energy axis for clarification.

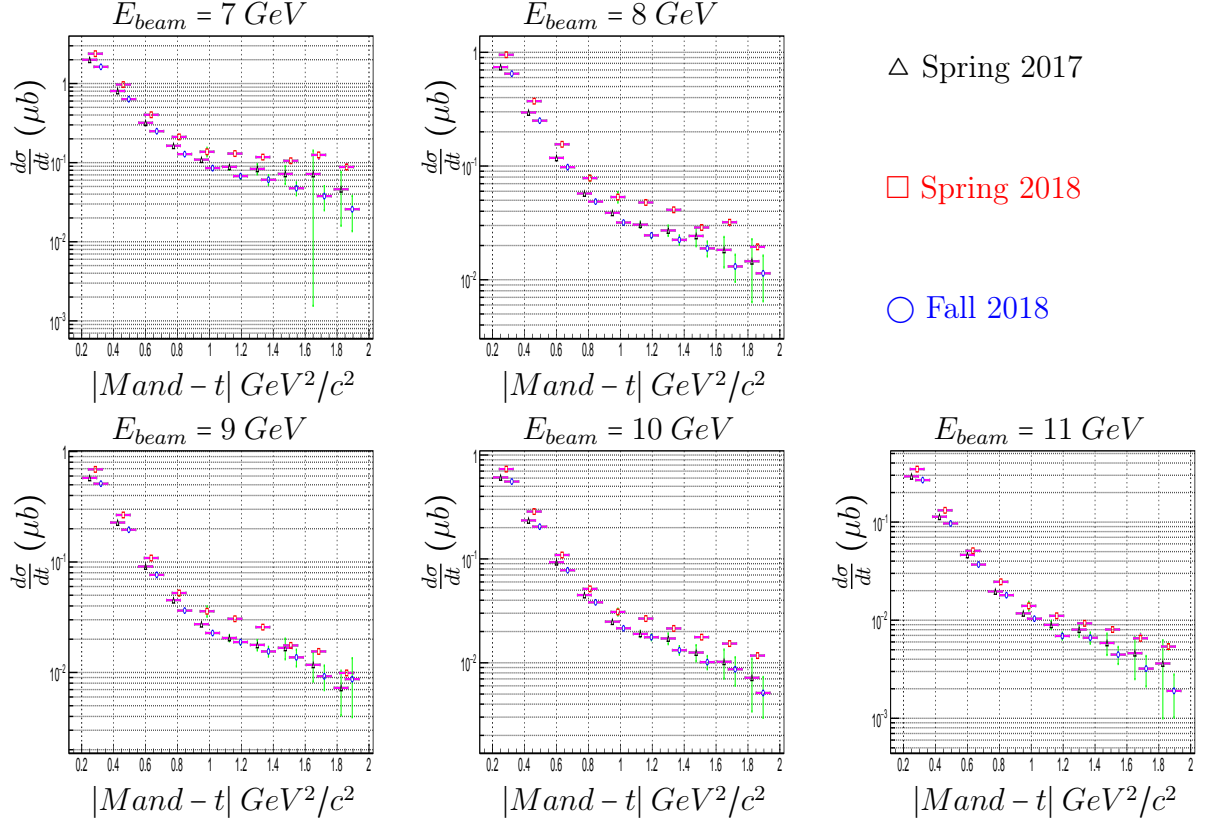


Figure 7.7: The $\omega\pi^0$ differential cross-section with systematic error calculated by changing the KinFit FOM cut from 10^{-5} to 24×10^{-5} . The systematic error is added in quadrature to the statistical error to form the total error for each bin. The systematic error is drawn in violet while total error is shown in green. Spring 2018 and Fall 2018 data points are shifted along the beam energy axis for clarification.

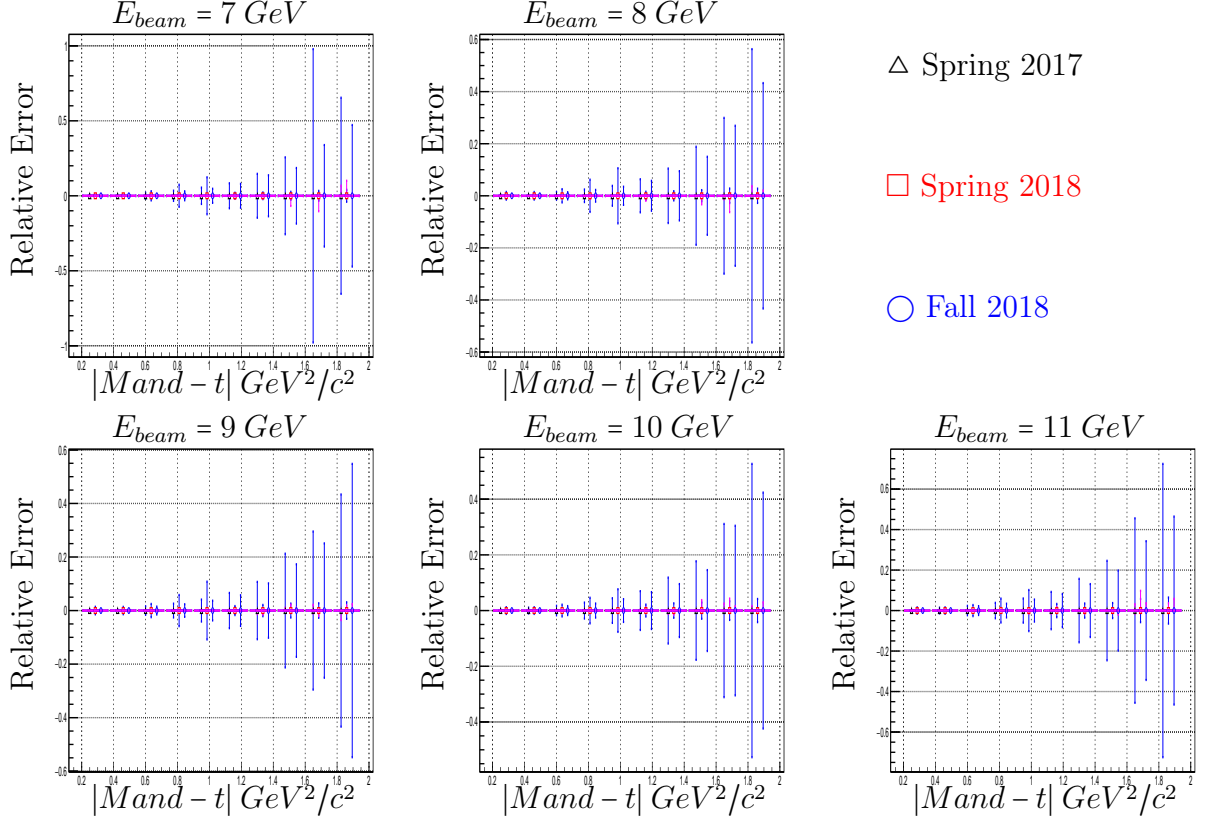


Figure 7.8: The relative statistical (blue) and systematic (violet) error for the $\omega\pi^0$ differential cross-section over the three run periods in five beam energy bins. The systematic error is calculated by changing the KinFit FOM cut from 10^{-5} to 24×10^{-5} .

7.3.2 $\pi^+\pi^-\pi^0$ Invariant Mass Cut Study

Following the same technique explained in Sec. 7.2.2, the $\pi^+\pi^-\pi^0$ cut scan varies the width of the ω peak from the nominal width of the ω peak of 3σ above and below the ω , to a looser cut of 3.43σ and a tighter cut of 2.6σ above or below the ω peak, which corresponds to a $\pm 5\%$ change in the statistics of our channel. For each peak width, the background is subtracted based on the ω -side-bands and the $\omega\pi^0$ differential cross-section is calculated for the three run periods in five bins of beam energy. In each Mandelstam- t bin, the maximum change in the differential cross-section is used as an estimate for the systematic error in that bin. The statistical error is added to the systematic error in quadrature to form the total error in each bin.

The $\omega\pi^0$ differential cross-section with systematic error, as calculated from the $\pi^+\pi^-\pi^0$ invariant mass cut scan, is shown in Fig. 7.9. The systematic error is drawn in violet while total error is shown in green. The bins for the spring 2018 and fall 2018 run periods are shifted along the x-axis for clarification. The systematic error is small such that it can not be seen for most of the bins. The same plots on log scale are represented in Fig. 7.10. The relative systematic (in violet) and statistical (in blue) errors are shown in Fig. 7.11. The relative systematic comparable and sometimes higher than the relative statistical error yet mostly less than 0.2. The relative systematic error is more considerable for bins at the higher end of the Mandelstam-t range and higher beam energy bins where the statistical effects of the cut are more relevant, as evident by the larger relative statistical error in these bins.

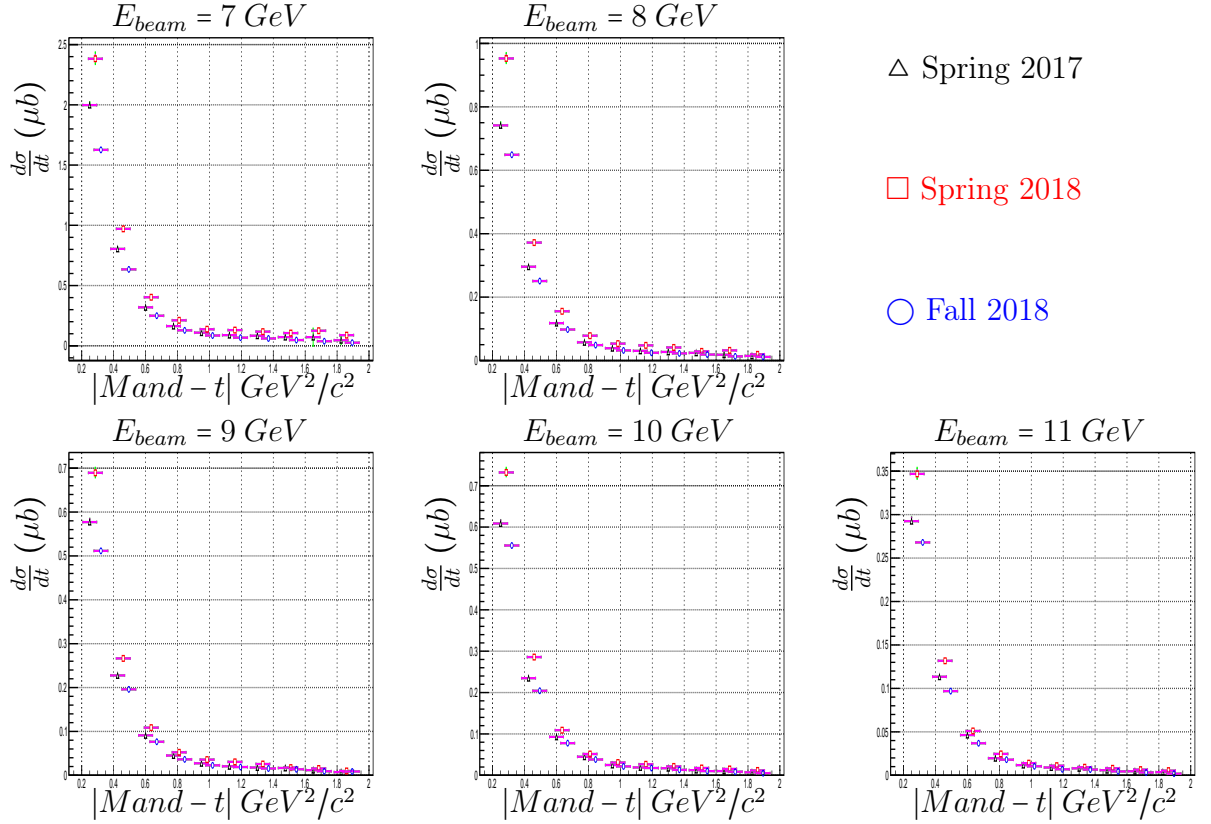


Figure 7.9: The $\omega\pi^0$ differential cross-section with systematic error calculated for the three run periods in five beam energy bins by changing the $\pi^+\pi^-\pi^0$ invariant mass cut. The systematic error is added in quadrature to the statistical error to form the total error for each bin. The systematic error is drawn in violet while total error is shown in green. Spring 2018 and Fall 2018 data points are shifted along the beam energy axis for clarification.

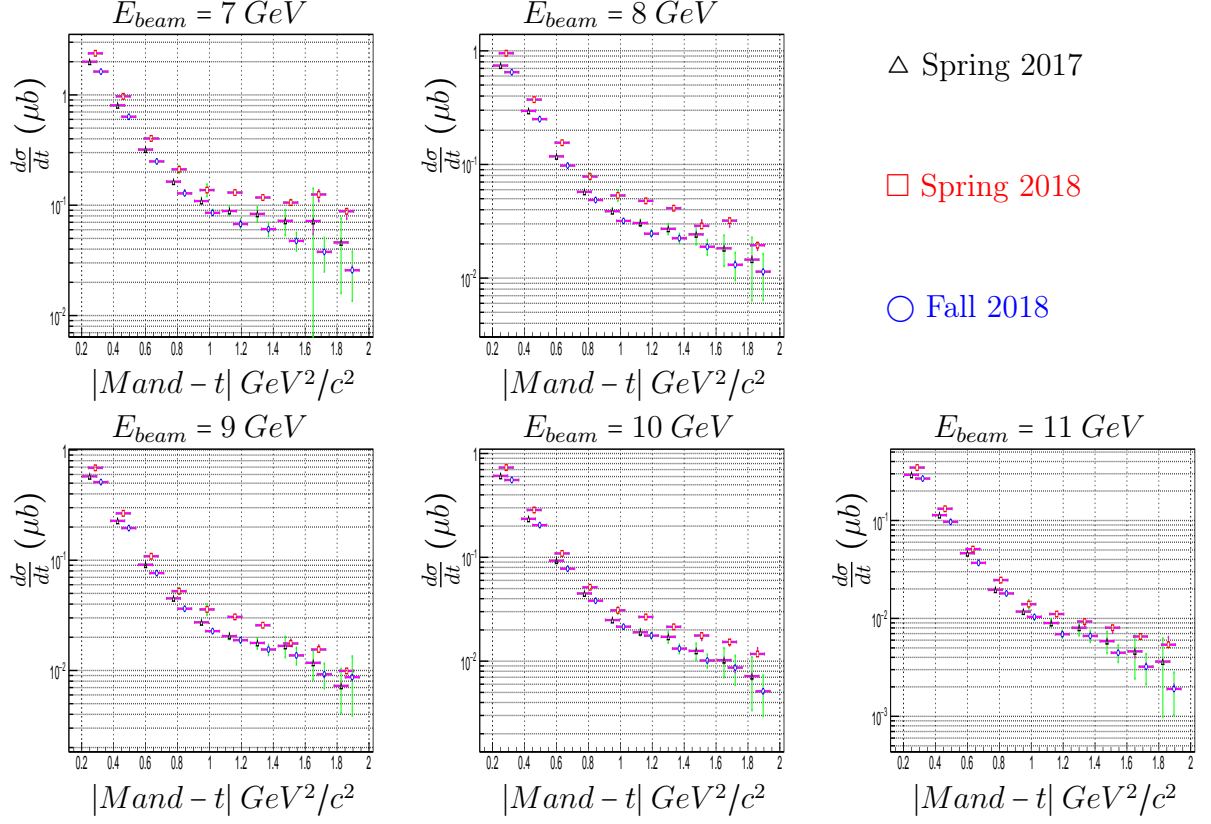


Figure 7.10: The $\omega\pi^0$ differential cross-section with systematic error calculated for the three run periods in five beam energy bins by changing the $\pi^+\pi^-\pi^0$ invariant mass cut. The systematic error is added in quadrature to the statistical error to form the total error for each bin. The systematic error is drawn in violet while total error is shown in green. Spring 2018 and Fall 2018 data points are shifted along the beam energy axis for clarification.

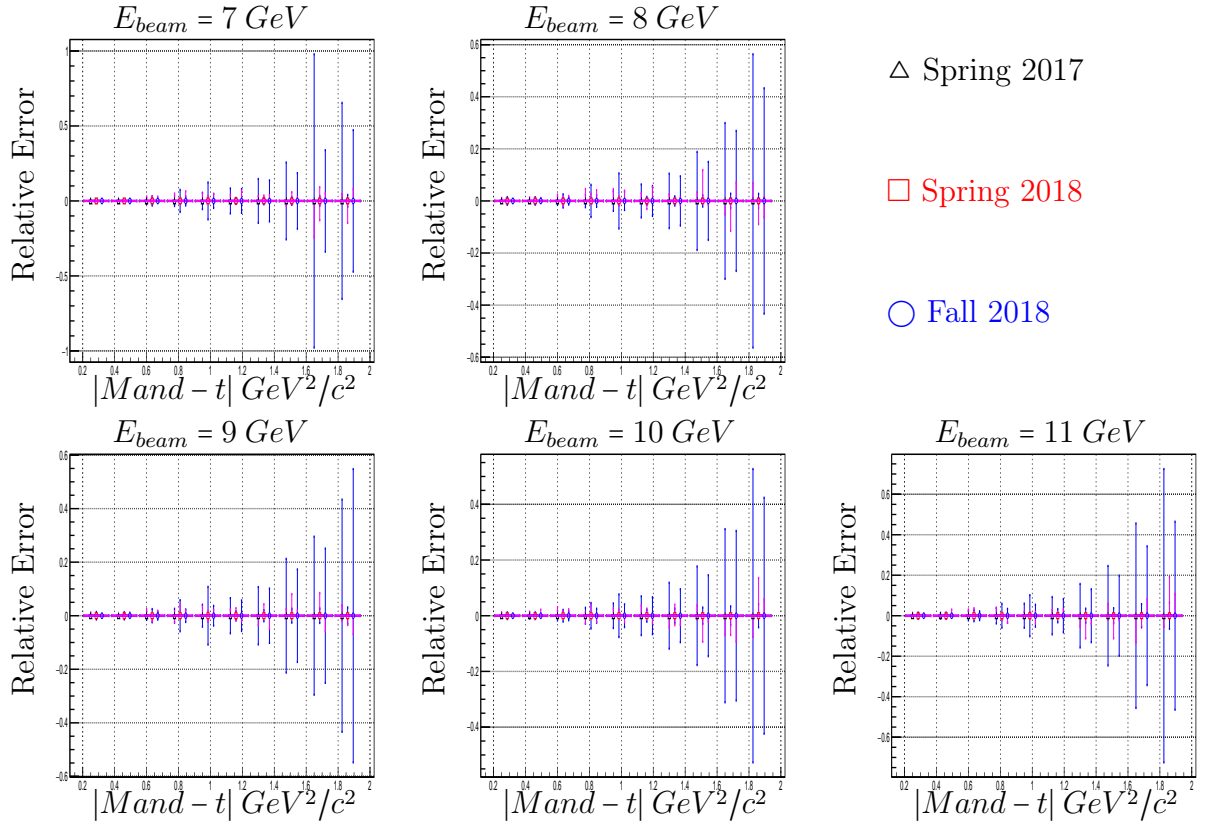


Figure 7.11: The relative statistical (blue) and systematic (violet) error for the $\omega\pi^0$ differential cross-section over the three run periods in five beam energy bins. The relative systematic error is calculated by changing the $\pi^+\pi^-\pi^0$ invariant mass cut.

7.3.3 $\omega\pi^0$ Invariant Mass Cut Study

Similar to the algorithm used in Sec. 7.2.3, we changed the cut on the $\omega\pi^0$ invariant mass from the nominal cut of 8.7σ above and below the b_1 peak, to a looser cut of 15σ and a tighter cut of 7.2σ above and below the b_1 peak. This cut change corresponds to a change in $\omega\pi^0$ yield from data by $\pm 5\%$. Using this cut, the $\omega\pi^0$ differential cross-section is calculated for the three run periods in five bins of beam energy. In each bin, the maximum change in the differential cross-section is used as an estimate for the systematic error in that bin. The statistical error is added to the systematic error in quadrature to form the total error in each bin.

The $\omega\pi^0$ differential cross-section with systematic error, as calculated from the $\omega\pi^0$ invariant mass cut scan, is shown in Fig. 7.12. The systematic error is drawn in violet while the total error is shown in green. The bins for the spring 2018 and fall 2018 run periods are shifted along the x-axis for clarification. The systematic error is small such that it can not be seen for most of the bins. The same plots on log scale are represented in Fig. 7.13. The relative systematic (in violet) and statistical (in blue) errors are shown in Fig. 7.14. The relative systematic is quite large and mostly higher than the relative statistical error yet mostly less than 0.2. The relative systematic error is more considerable for bins at the higher end of the Mandelstam-t range and higher beam energy bins where the statistical effects of the cut are more relevant, as evident by the larger relative statistical error in these bins. Similar to the effect seen on cross-section calculation, the relative systematic error is mostly in the positive direction due to the cut variation affecting mostly far ends of the $\omega\pi^0$ invariant mass where our simulation (which is mostly b_1) fades much faster than the data.

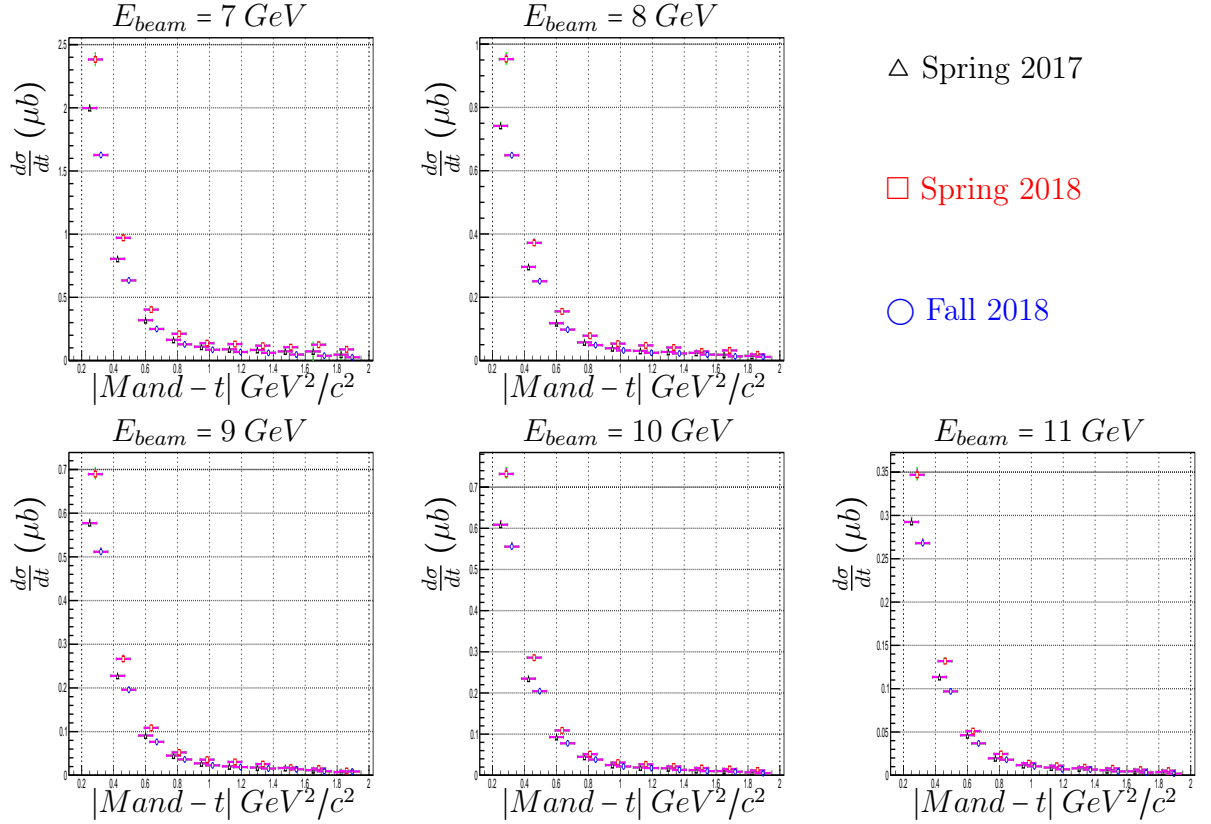


Figure 7.12: The $\omega\pi^0$ differential cross-section with systematic error calculated for the three run periods in five beam energy bins by changing the $\omega\pi^0$ invariant mass cut. The systematic error is added in quadrature to the statistical error to form the total error for each bin. The systematic error is drawn in violet while total error is shown in green. Spring 2018 and Fall 2018 data points are shifted along the beam energy axis for clarification.

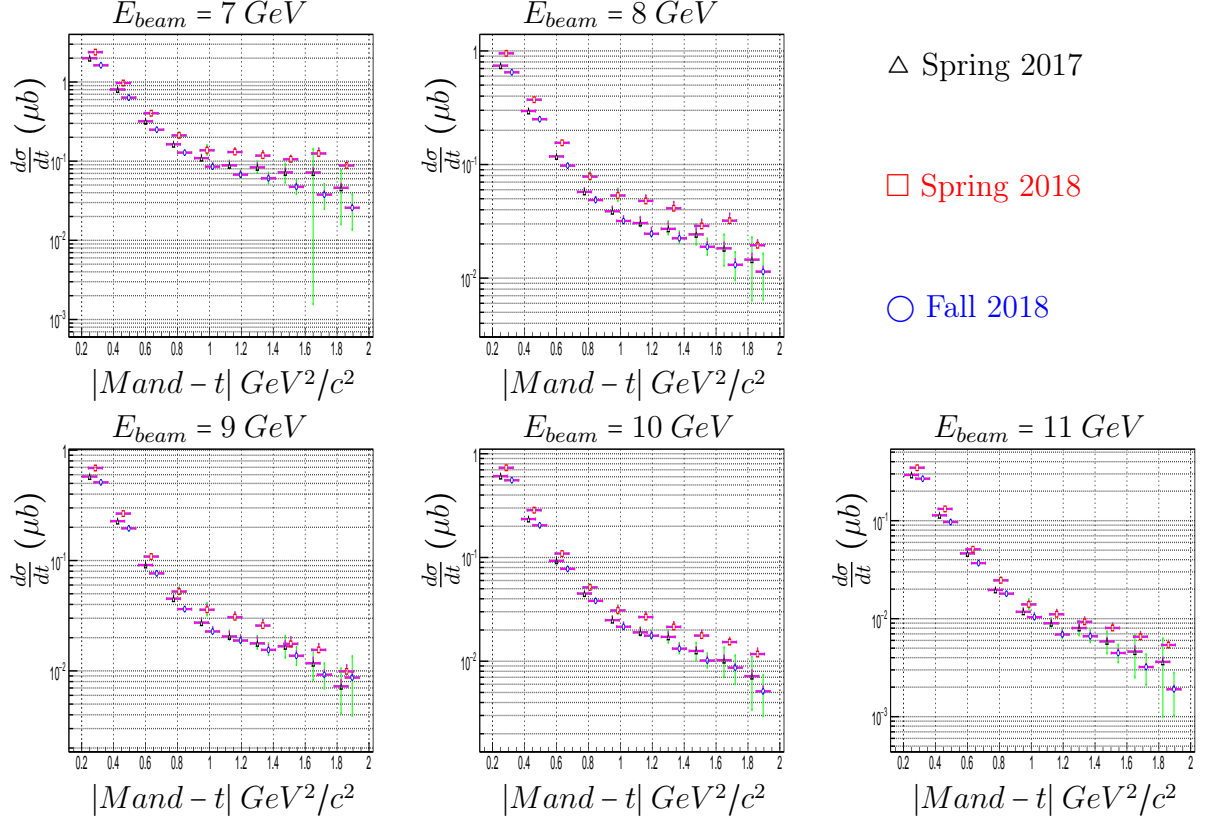


Figure 7.13: The $\omega\pi^0$ differential cross-section with systematic error calculated for the three run periods in five beam energy bins by changing the $\omega\pi^0$ invariant mass cut. The systematic error is added in quadrature to the statistical error to form the total error for each bin. The systematic error is drawn in violet while total error is shown in green. Spring 2018 and Fall 2018 data points are shifted along the beam energy axis for clarification.

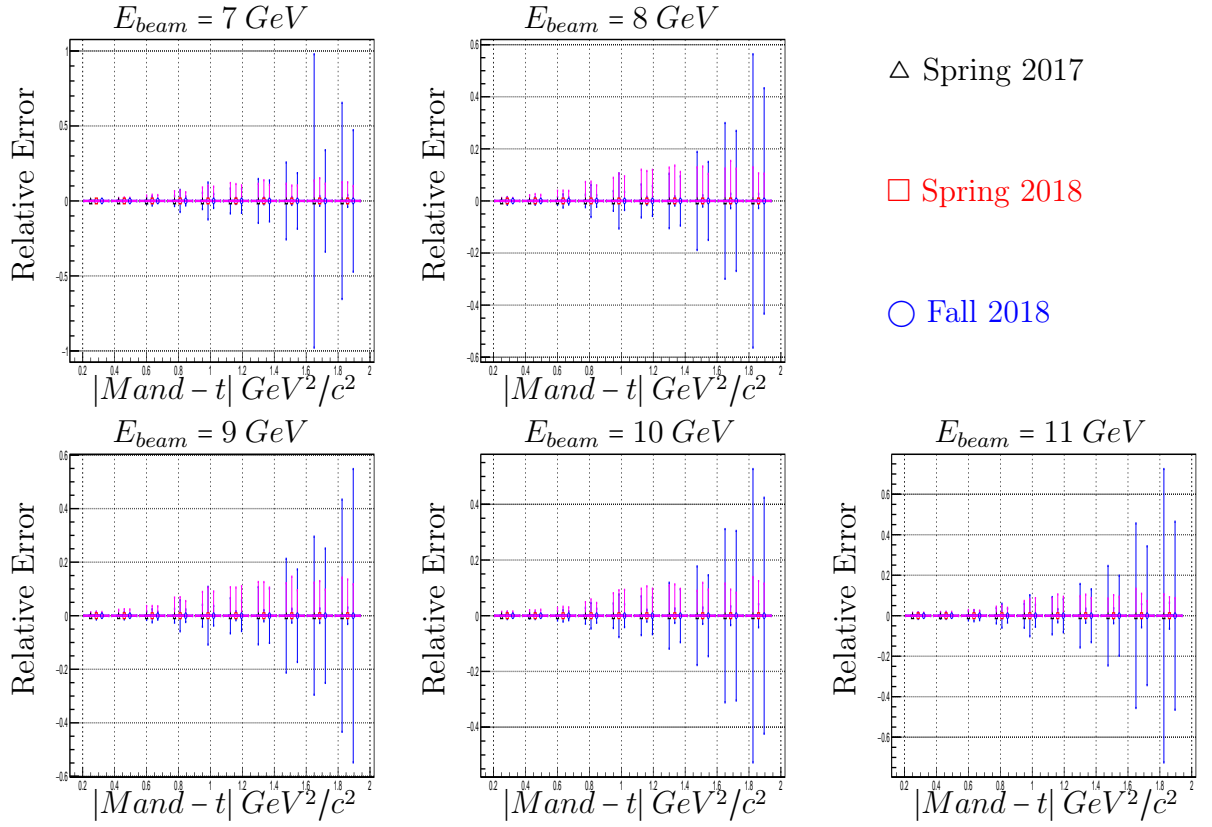


Figure 7.14: The relative statistical (blue) and systematic (violet) error for the $\omega\pi^0$ differential cross-section over the three run periods in five beam energy bins. The systematic error is calculated by changing the $\omega\pi^0$ invariant mass cut.

7.3.4 Combined Systematic Error for the $\omega\pi$ Differential Cross-section

As we mentioned in Sec. 7.2.4, we expect the systematic errors associated with KinFit and invariant mass cuts to be correlated. The combined systematic error therefore, is calculated by adding the systematic errors of the KinFit FOM, the $\pi^+\pi^+\pi^0$ and the $\omega\pi^0$ invariant mass cuts linearly.

Fig. 7.15 shows the $\omega\pi^0$ differential cross-section for the three run periods in five bins of beam energy. For each bin, the combined systematic error is calculated by adding the systematic errors in the bin linearly. The statistical error is added to the combined systematic error in quadrature to form the total error in each bin. The combined systematic error is drawn in violet while total error is shown in green. The bins for the spring 2018 and fall 2018 run periods are shifted along the x-axis for clarification. The combined systematic error is small such that it can not be seen for most of the bins. The same plots on log scale are represented in Fig. 7.16. The relative combined systematic (in violet) and statistical (in blue) errors are shown in Fig. 7.17. The relative combined systematic is quite large and mostly higher than the relative statistical error yet mostly less than 0.2. The relative combined systematic error is more considerable for bins at the higher end of the Mandelstam- t range and higher beam energy bins where the statistical effects of the cut are more relevant, as evident by the larger relative statistical error in these bins. Also, the fact that the effect is more noticeable for spring 2018 run period which has lower statistics.

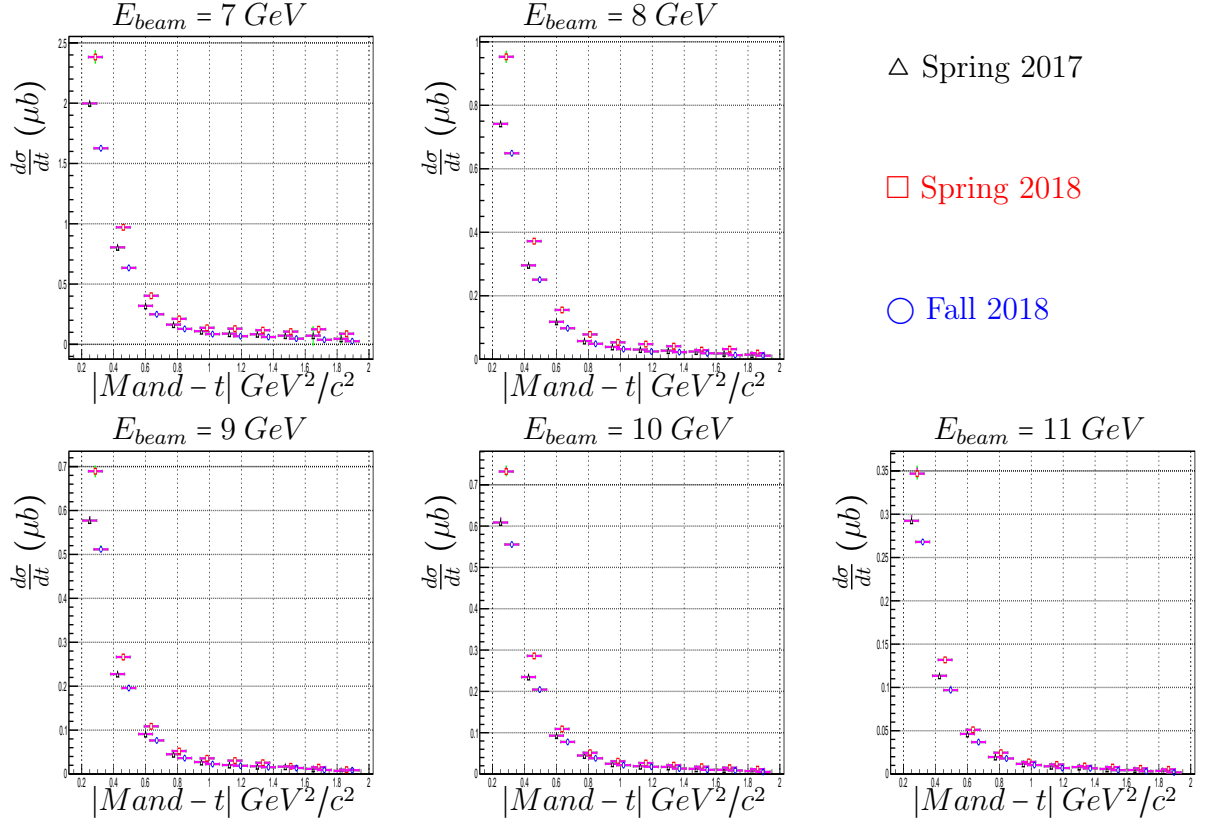


Figure 7.15: The $\omega\pi^0$ differential cross-section with combined systematic error calculated for the three run periods in five beam energy bins by linearly adding the systematic errors for the KinFit FOM, $\pi^+\pi^-\pi^0$ and the $\omega\pi^0$ invariant mass cuts. The combined systematic error is added in quadrature to the statistical error to form the total error for each bin. The combined systematic error is drawn in violet while total error is shown in green. Spring 2018 and Fall 2018 data points are shifted along the beam energy axis for clarification.

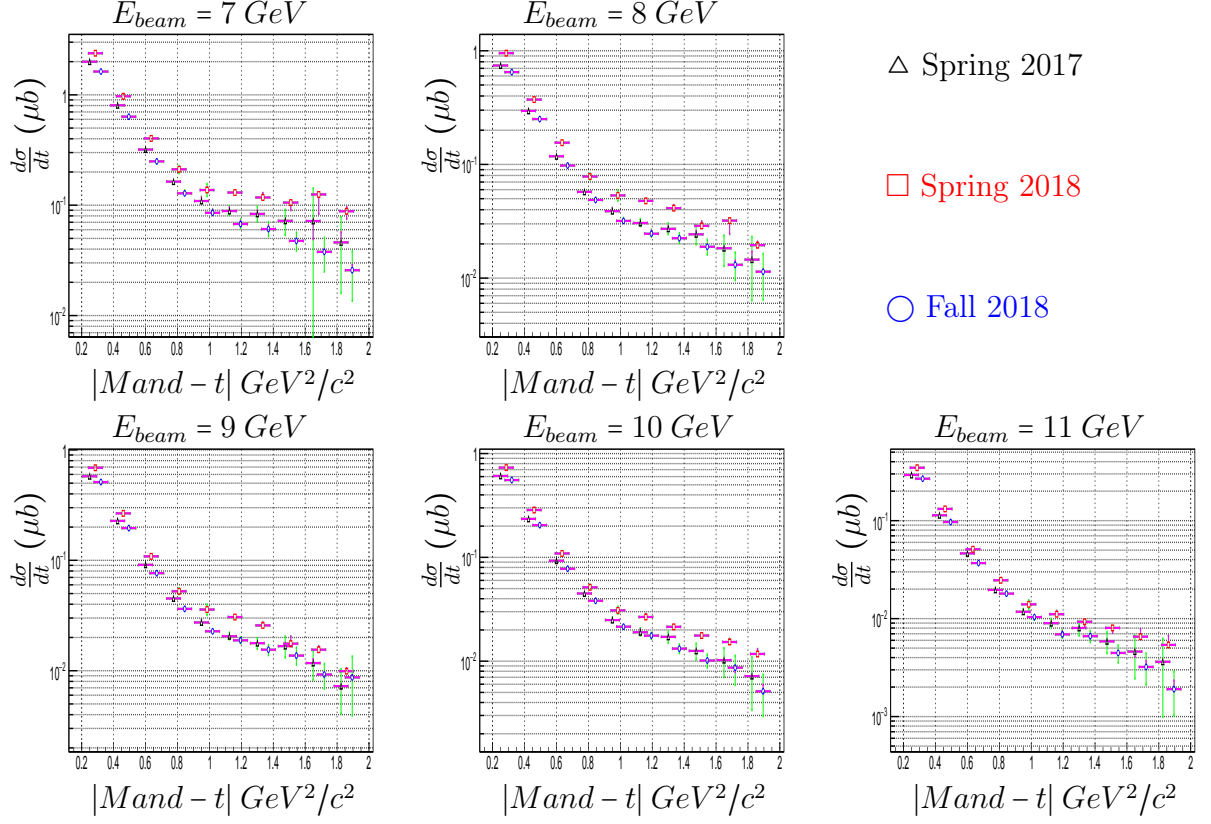


Figure 7.16: The $\omega\pi^0$ differential cross-section with combined systematic error calculated for the three run periods in five beam energy bins by linearly adding the systematic errors for the KinFit FOM, $\pi^+\pi^-\pi^0$ and the $\omega\pi^0$ invariant mass cuts. The combined systematic error is added in quadrature to the statistical error to form the total error for each bin. The combined systematic error is drawn in violet while total error is shown in green. Spring 2018 and Fall 2018 data points are shifted along the beam energy axis for clarification.

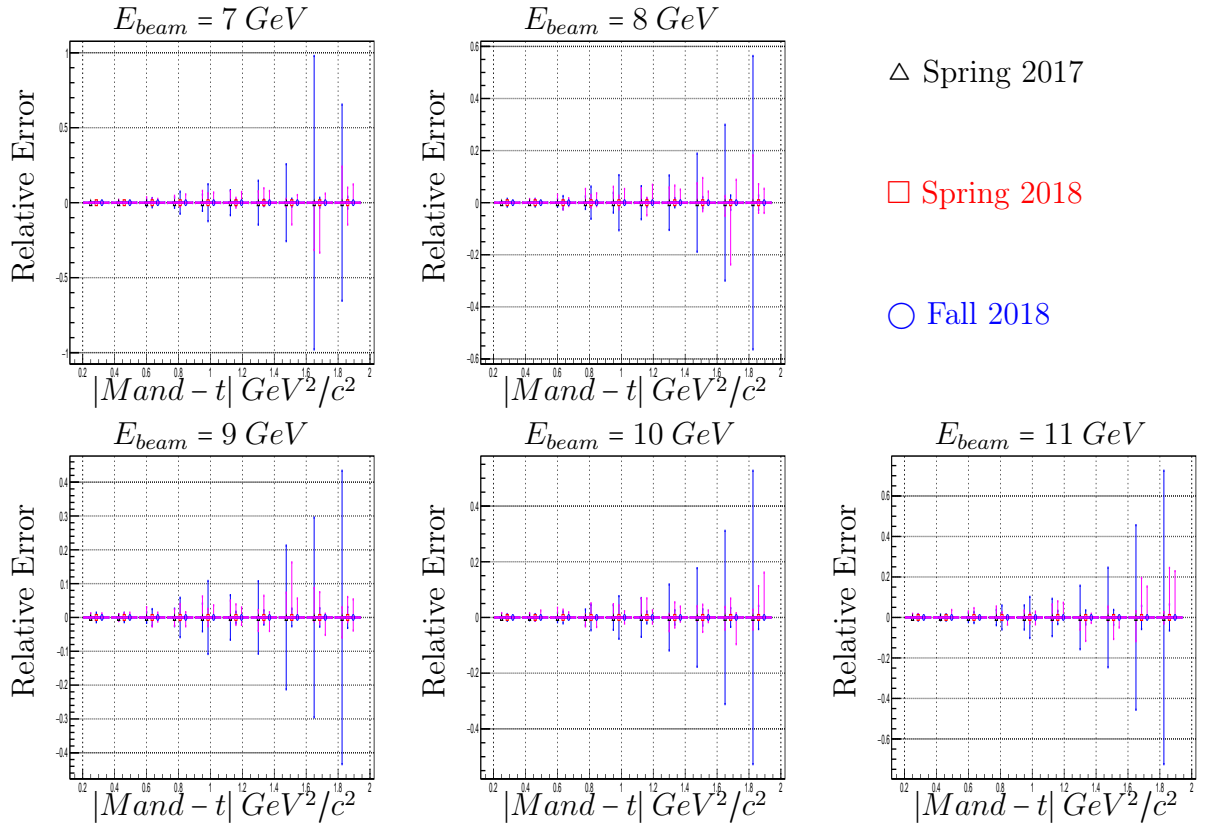


Figure 7.17: The relative statistical (blue) and combined systematic (violet) errors for the $\omega\pi^0$ differential cross-section over the three run periods in five beam energy bins. The combined systematic error is calculated by linearly adding the systematic errors for the KinFit FOM, $\pi^+\pi^-\pi^0$ and the $\omega\pi^0$ invariant mass cuts for each bin.

7.4 Summary

In this chapter, we discussed few potential sources for systematic errors in the calculation of the $\omega\pi^0$ cross-section and differential cross-section. We performed a systematic check on the KinFit FOM, the $\pi^+\pi^-\pi^0$ and the $\omega\pi^0$ invariant mass cuts. We showed that the $\omega\pi^0$ cross-section mostly less than 5% combined systematic error for most of the beam energy range. The differential cross-sections suffer much higher combined systematic error specially at high beam energy and Mandelstam-t yet mostly less than 20%². Further systematic checks are necessary in the future to gain confidence in the stability of $\omega\pi^0$ cross-section and differential cross-section over other facets of the analysis method.

²At present the discrepancy in acceptance between the different run periods is less than 48% and is not included as a systematic uncertainty as we expect this discrepancy to be resolved soon.

Chapter 8

Conclusions and Future Work

In this thesis we presented our efforts as part of the GlueX collaboration at JLab. The principal goal of the GlueX experiment is to study the meson spectra with a focus on exotic states for which the b_1 meson is a potential gateway as it appears in the decay of the lightest exotic multiplet π_1 . Our efforts included service work for the Barrel Calorimeter subsystem and physics analysis of the $\omega\pi^0$ channel as the dominant decay channel for the b_1 meson.

We developed and used software to monitor and detect drifts and fluctuations in the gains of the BCAL channels in Hall D during data collection starting in spring 2017, based on LED pulsers. Code and scripts were also developed to study the behaviour of width and mean of pedestal and PSPP in the BCAL as a function of run conditions. The behaviour of pedestal width and mean agrees with expectations and previous studies, and provides a useful tool for experimenters in diagnosing potential issues with the operation of the BCAL SiPMs or LED system during operations.

We presented our data analysis workflow to select events through cuts for particle identification, invariant mass selection and beam energy ranges of interest, rejecting erroneously reconstructed events mainly through KinFit and fiducial cuts to steer

clear of the unreliable regions of the detector. These cuts are followed by by subtractions of events reconstructed using out-of-time beam buckets and the ω background. We presented AM and PWA as two models for the analysis of the $\omega\pi$ channel.

An AM expansion model for the $\omega\pi$ decay channel was implemented as a software library for MC simulation and analysis. The library has been used to simulate the $\omega\pi^0$ decay channel of the b_1 meson. Further development is planned to use the library to fit the data. AMs has been extracted from the data. Preliminary comparison shows qualitative similarities with extracted AM by previous experiments and offer much higher statistics.

A PWA model for the $\omega\pi$ decay channel was implemented as a software library for MC simulation and analysis. The library was used for a proof of concept fit of a data sample. This fit demonstrates that the model is capable of describing the invariant mass, angular and Mandelstam-t distributions of the decay. A fix to address the production angle distribution is underway, followed by a search for ambiguities in the partial waves base set.

Software was developed to simulate the two-step decay process of the $\omega\pi$ decay channel. The software was used to simulate the $\omega\pi$ flat phase space in the helicity frame. Combined with the AMs library mentioned above, the software was used to simulate the decay of the b_1 meson. The software solved shortcomings of single-step decay simulators and is compatible with PWAs library for future use. This software is currently part of the GlueX software repository and is being used by other collaborators.

The conservation of s-channel helicity in the photoproduction of the b_1 was studied

through the distribution of the production angle. The distribution exhibits deviation from the SCHC condition. Fits over four beam polarization directions and three run periods align with $b = -0.169 \pm 0.002$. Our results are supported with much higher statistics yet they do not align with -0.36 ± 0.08 reported by a previous experiment. Our results indicate that the b_1 is produced by a non-s-channel helicity mechanism. Better $\omega\pi^0$ background suppression would improve our confidence in the result.

The helicity amplitude for $\omega\pi$ decay channel of the b_1 was extracted through the distribution of the azimuthal decay angle of the daughter ω meson in the helicity frame of the parent b_1 meson. The distribution improves on statistics of previous measurements. Average of the fit of over the three run periods yields $|F_1|^2 = 0.3037 \pm 0.0003$ which does not agree with the $|F_1|^2 = 0.437 \pm 0.012$ expected helicity amplitude of a b_1 meson with $D/S = 0.26 \pm 0.035$ or a previous measurements of $|F_1|^2 = 0.383 \pm 0.029$. Improved $\omega\pi^0$ background subtraction could improve the results.

The cross-section of the $\omega\pi^0$ photoproduction was extracted as function of the beam energy for the three GlueX run periods to be of the order of $1 \mu\text{b}$. Our results agree with previous experiments and present much higher statistics compared to them. An improved calibration of the beam photon tagger could suppress deviations in the cross-section. It could also improve the agreement between the three run periods, along with improved simulation and selection cuts.

The differential cross-section of the $\omega\pi^0$ photoproduction was extracted as a function of Mandelstam- t in five bins of beam energy. Fits of the distribution indicate the presence of two production processes with average slopes of $p_1 = -5.24 \pm 0.04$ for the $0.25 < -t < 0.95 \text{ GeV}^2/c^2$ range and $p_2 = -1.24 \pm 0.05$ for the $0.95 < -t < 2.0 \text{ GeV}^2/c^2$ range. These slopes are very close to previous measurements and improve on their

statistics.

We presented a systematic check for the effect of KinFit FOM, $\pi^+\pi^-\pi^0$ and $\omega\pi^0$ invariant mass cuts on the $\omega\pi^0$ cross-section and differential cross-section. The combined systematic error was estimated to be mostly less than 5% for the cross-section and affecting the lower side of beam energy range. For the differential cross-section the combined systematic error was estimated to be mostly less than 20% and affecting the higher side of the Mandelstam-t range and beam energy.

The following tasks have been handed over to other graduate students in the group:

- Monitoring and detecting drifts in gains of the BCAL channels.
- Applying acceptance corrections to the experimental AMs in seven dimensional space.
- Development of PWA software for $\omega\pi$ channel.

Bibliography

- [1] M. Gell-Mann, ‘The Eightfold Way: A Theory of Strong Interaction Symmetry.’ California Institute of Technology, USA 1961.
- [2] M. Gell-Mann, ‘The Symmetry Group of Vector and Axial Vector Currents.’ Physics **1**, 63 1964.
- [3] G. Zweig, ‘An SU(3) Model for Strong Interaction Symmetry and its Breaking.’ CERN, CERN-TH-412 1964.
- [4] W. A. Bardeen, H. Fritzsch and M. Gell-Mann., ‘Scale and Conformal Symmetry in Hadron Physics’ Wiley 1973.
- [5] M. Tanabashi et al. (Particle Data Group). ‘The Review of Particle Physics’ Physical Review D, 2018.
- [6] J. J. Dudek, R. G. Edwards, P. Guo, and C. E. Thomas, ‘Toward the Excited Isoscalar Meson Spectrum from Lattice QCD.’ Physical Review D **88**, 094505 2013.
- [7] N. Isgur, and J. Paton, ‘Flux-tube model for hadrons in QCD.’ Physical Review D **31**, 1985.
- [8] A. Chodos, R. L. Jaffe, K. Johnson, C. B. Thorn, and V. F. Weisskopf, ‘New extended model of hadrons.’ Physical Review D **9**, 1985.
- [9] J.M. Cornwall and A. Soni, ‘Glueballs as bound states of massive gluons.’ Physics Letters B **120**, 1983.
- [10] Z. H. Li, U. Lombardo, H. J. Schulze, and W. Zuo, ‘Nuclear Three-Body Force from the Nijmegen Potential.’ Exotic States of Nuclear Matter, 2008.
- [11] C.A. Meyer and E. S. Swanson, ‘Hybrid Mesons.’ Progress in Particle and Nuclear Physics **82**, 21 2015.
- [12] J. J. Dudek, ‘The lightest hybrid meson supermultiplet in QCD.’ Physical Review D **84**, 074023 2011.
- [13] P. R. Page, E. S. Swanson, and A. P. Szczepaniak, ‘Hybrid meson decay phenomenology.’ Physical Review D **59**, 034016 1999.

- [14] N. Isgur, R. Kokoski, and J. E. Paton, ‘Gluonic Excitations of Mesons: Why They Are Missing and Where to Find Them.’ *Physical Review Letters* **54**, 869 1985.
- [15] A. J. Woss, J. J. Dudek, R. G. Edwards, C. E. Thomas and D. J. Wilson, ‘Decays of an exotic 1^{-+} hybrid meson resonance in QCD’, [arXiv:2009.10034 [hep-lat]].
- [16] J. Ballam et al. ‘A search for B and $\rho'(1250)$ production in the reaction $\gamma\rho \rightarrow \rho\pi^+\pi^- + \text{neutrals}$ at 2.8, 4.7 and 9.3 GeV’, *Nuclear Physics B*, **76**, 1974.
- [17] M. Atkinson *et al.* [Omega Photon], ‘A Spin Parity Analysis of the $\omega\pi^0$ Enhancement Photoproduced in the Energy Range 20-GeV to 70-GeV’, *Nuclear Physics B* **243**, 1-28 1984.
- [18] J. E. Brau et al. ‘Production and decay properties of the $\omega\pi^0$ state at 1250 MeV/c² produced by 20-GeV polarized photons on hydrogen’, *Physical Review D* **37**, 1988.
- [19] M. Swat. A. P. Szczepaniak. ‘Role of photoproduction in exotic meson searches’, *Physics Letters B* **516**, 72-76 2001.
- [20] V. Devanathan, ‘Angular Momentum Techniques in Quantum Mechanics’, Springer Science & Business Media, 1999.
- [21] S. U. Chung, et al. ‘Spin Parity Analysis of the B Meson’ *Physical Review D* **11**, 2426 1975.
- [22] S. Chung, ‘Spin Formalisms’, BNL PREPRINT, 2014.
- [23] K. Schilling and G. Wolf. ‘How to analyse vector-meson production in inelastic lepton scattering.’ *Nuclear Physics B*, 61:381 – 413, 1973.
- [24] Jefferson Lab. ‘Pre-Conceptual Design Report for The Science and Experimental Equipment for The 12 GeV Upgrade of CEBAF.’ June 10, 2003.
- [25] H. Al Ghouli, E. G. Anassontzis, F. Barbosa, et al. ‘First results from the gluex experiment.’ AIP Conference Proceedings, 1735, 2016.
- [26] A. W. Sàenz and H. Überall, *Coherent Radiation Sources*. Berlin Heidelberg: Springer-Verlag 1985
- [27] R. T. Jones, ‘Intense Beams of Polarized and Nearly Monochromatic Photons from Coherent Bremsstrahlung.’ University of Connecticut, USA, web 1997
- [28] B. Pratt. ‘Diamond Radiator Fabrication, Characterization and Performance for the GlueX Experiment.’ PhD thesis, University of Connecticut, 2017.
- [29] GlueX Collaboration. ‘Hall D/Gluex technical design report.’ GlueX-doc-2442, 2016.

- [30] A. Barnes. ‘Development of the tagger microscope & Analysis of Spin Density Matrix Elements in $\gamma p \rightarrow \phi p$ for the GlueX Experiment.’ PhD thesis, University of Connecticut, 2017.
- [31] M. Dugger et al. ‘Design and construction of a high-energy photon polarimeter.’ Nuclear Instruments and Methods in Physics Research Section A, vol. 867, 2017.
- [32] GlueX Collaboration. ‘Measurement of the beam asymmetry Σ for π^0 and η photoproduction on the proton at $E_\gamma = 9$ GeV,’ Physical Review C, vol. 95, no. 042201, 2017.
- [33] F. Barbosa, C. Hutton, A. Sitnikov, A. Somov, S. Somov, and I. Tolstukhin, ‘Pair Spectrometer Hodoscope for Hall D at Jefferson Lab.’ Nuclear Instruments and Methods A, 795, 376 2015
- [34] GlueX Collaboration. ‘The technical construction report’. GlueX-doc-2511, 2016.
- [35] Y. V. Haarlem et al. ‘The GlueX central drift chamber: Design and performance’, Nuclear Instruments and Methods in Physics Research Section A, vol. 622, pp. 142–156, 2010.
- [36] L. Pentchev et al. ‘Studies with cathode drift chambers for the GlueX experiment at Jefferson Lab’, Nuclear Instruments and Methods in Physics Research Section A, vol. 845, pp. 281–284, 2017.
- [37] D. S. Carman and S. Taylor, ‘Hall D Forward Drift Chamber Technical Design Report.’ Jefferson Lab, VA 2008
- [38] E.G. Anassontzis, P. Ioannou, C. Kourkouvelis, et al. ‘Relative gain monitoring of the GlueX calorimeters’. Nuclear Instruments and Methods in Physics Research Section A, 738:41-49, 2014.
- [39] T. D. Beattie, A. M. Foda, C. Henschel, S. Katsaganis, S. Krueger, G. J. Lolos, Z. Papandreou, E. L. Plummer, I. A. Semenova and A. Y. Semenov, *et al.* ‘Construction and Performance of the Barrel Electromagnetic Calorimeter for the GlueX Experiment’, Nuclear Instruments and Methods in Physics Research Section A **896**, 24-42 (2018).
- [40] E. Pooser. ‘The GlueX Start counter & Beam asymmetry Σ in single π^0 photoproduction.’ PhD thesis, Florida International University, 2016.
- [41] GlueX Wiki contributors, ‘Time-of-Flight.’ On the public GlueX Wiki at <https://halldweb.jlab.org/wiki/index.php/Time-of-Flight> (last modified June, 2018
- [42] S. Denisov et al. ‘Characteristics of the TOF counters for GlueX experiment’, Nuclear Instruments and Methods in Physics Research Section A, vol. 494, pp. 495–499, 2002.

- [43] A. M. Foda. ‘Progress on BCAL LED Monitoring Plugin.’ Jefferson Lab Electronic Logbook.
- [44] E. Smith. ‘New pulser script to cycle through BCAL LED configurations.’ Jefferson Lab Electronic Logbook.
- [45] A. M. Foda. ‘LED Bias Scan & Cross Talk Runs’ Jefferson Lab Electronic Logbook.
- [46] E. Jastrzembski and H. Dong. ‘Summary of FADC250 Operating Modes.’
- [47] A. M. Foda. ‘Calorimetry Meeting Sept 22nd, 2016’, GlueXWiki.
- [48] S. Shooberta, V. Neelamana, A. M. Foda, Z. Papandreou, ‘BCAL LED Monitoring Fall 2018’, HallD DocDB: <https://halldweb.jlab.org/doc-public/DocDB/ShowDocument?docid=4640>
- [49] GlueX Collaboration. RootSpy.
- [50] A. M. Foda. ‘BCAL gain drifts.’ Jefferson Lab Electronic Logbook.
- [51] A. M. Foda. ‘Spring 2018 LED - 3 Reoccurring Bad Channels.’ Jefferson Lab Electronic Logbook.
- [52] M. Dalton. ‘Plots of BCAL pedestal width and mean for bias scan at 10 and 18 degrees C.’ Jefferson Lab Electronic Logbook.
- [53] T. Beattie. ‘Run list for May 2017 LED studies.’ Jefferson Lab Electronic Logbook.
- [54] A. M. Foda. ‘BCAL pedestal width and mean for bias scan at 5, 10 and 18 degrees C.’ Jefferson Lab Electronic Logbook.
- [55] M. Kamel, ‘Eta Photo-production differential Cross Sections for DNP2020’, HallD DocDB: <https://halldweb.jlab.org/doc-private/DocDB/ShowDocument?docid=4701>
- [56] GlueX Wiki contributors, ‘Spring 2017 Analysis Launch Cuts.’ Public GlueX Wiki.
- [57] S. Adhikari *et al.* [GlueX], ‘The GlueX beamline and detector’, Nuclear Instruments and Methods in Physics Research Section A **987**, 164807 (2021).
- [58] N. S. Jarvis, C. A. Meyer, B. Zihlmann, M. Staib, A. Austregesilo, F. Barbosa, C. Dickover, V. Razmyslovich, S. Taylor and Y. Van Haarlem, *et al.* ‘The Central Drift Chamber for GlueX’, Nuclear Instruments and Methods in Physics Research Section A **962**, 163727 (2020).
- [59] D. Keller, ‘Techniques in Kinematic Fitting.’ CLAS-NOTE 2010-015, web 2010

- [60] F. James, ‘MINUIT, Function Minimization and ERROR Analysis’, Version 94.1, CERN program Library long writeup D506.
- [61] M. Shepherd et al., ‘AmpTools’ <https://github.com/mashephe/AmpTools>
- [62] NVIDIA Corporation, ‘CUDA Zone - NVIDIA Developer’ <https://developer.nvidia.com/cuda-zone>
- [63] GEANT
R. Brun and F. Carminati, CERN Program Library Long Writeup W5013, 1993 (unpublished).
- [64] Paul M. Eugenio, ‘GENR8: A General Monte Carlo Event Generator’, HallD DocDB <https://halldweb.jlab.org/doc-public/DocDB/ShowDocument?docid=11>
- [65] Woss, Antoni J. et al. ‘ b_1 resonance in coupled $\pi\omega$, $\pi\phi$ scattering from lattice QCD’ Physics Review D, 100, 5, 2019.
- [66] D. P. Barber et al. ‘Photoproduction of $\rho'(1.2)$ and $\rho'(1.6)$ in the final states $\pi^+ \pi^- \pi^+ \pi^-$ and $\pi^+ \pi^- \pi^0 \pi^0$ ’ Zeitschrift für Physik, c, 4, 169, 1980.
- [67] D. Aston et al. ‘Observation of an $\omega\pi^0$ state of mass 1.25 GeV produced by photons of energy 20–70 GeV’, Physics Letters B **92** 1980. erratum: Physics Letters B, **95**, 1980.
- [68] M. Nozar *et al.* [E852], ‘A Study of the reaction $\pi^- p \rightarrow \omega\pi^- p$ at 18 GeV/c: The D and S decay amplitudes for $b_1(1235) \rightarrow \omega\pi$,’ Physics Letters B **541**, 35-44 2002.
- [69] GlueX Collaboration, ‘Guidance on Systematic Errors’, GlueX Wiki: https://halldweb.jlab.org/wiki-private/index.php/Guidance_on_systematic_errors

Appendix A

Extracted Angular Moments from 2017 GlueX Data

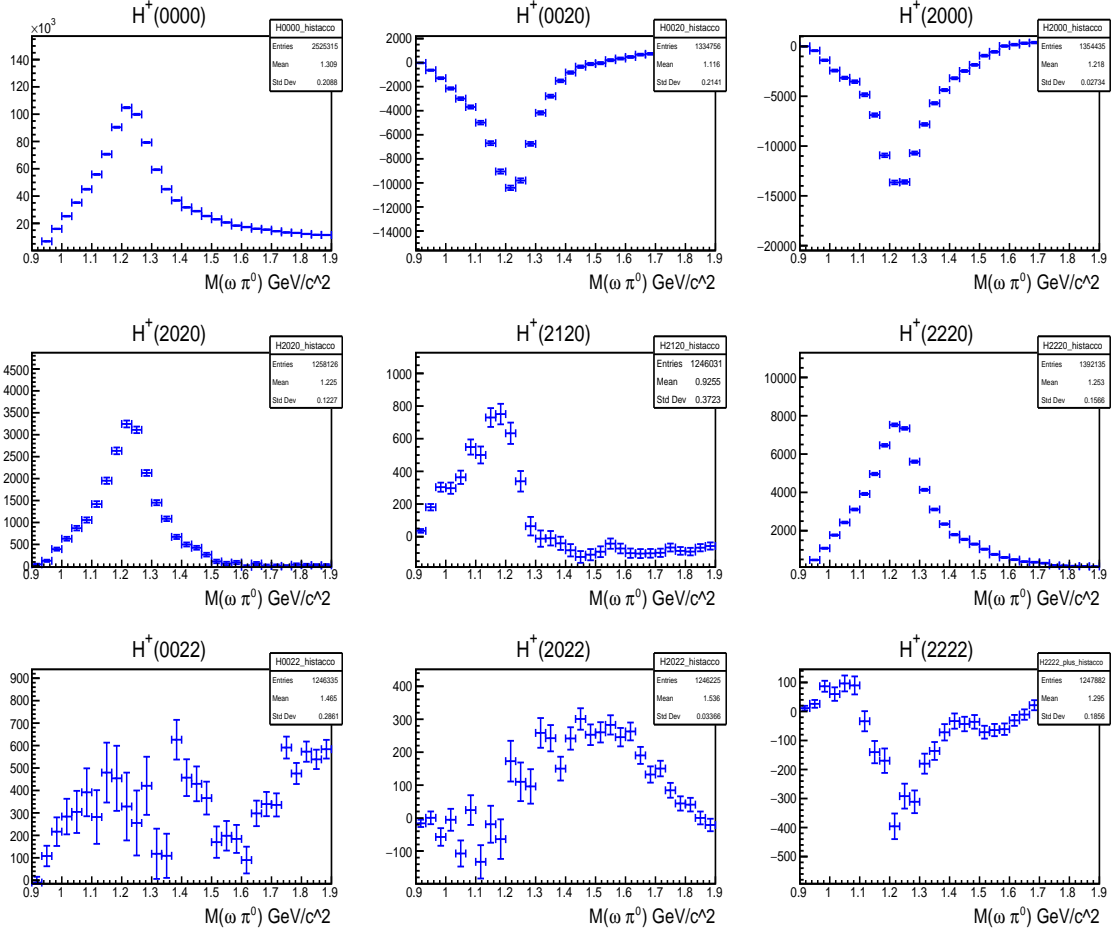


Figure A.1: Extracted moments of the $\omega\pi$ channel as a function of the $\omega\pi$ invariant mass.

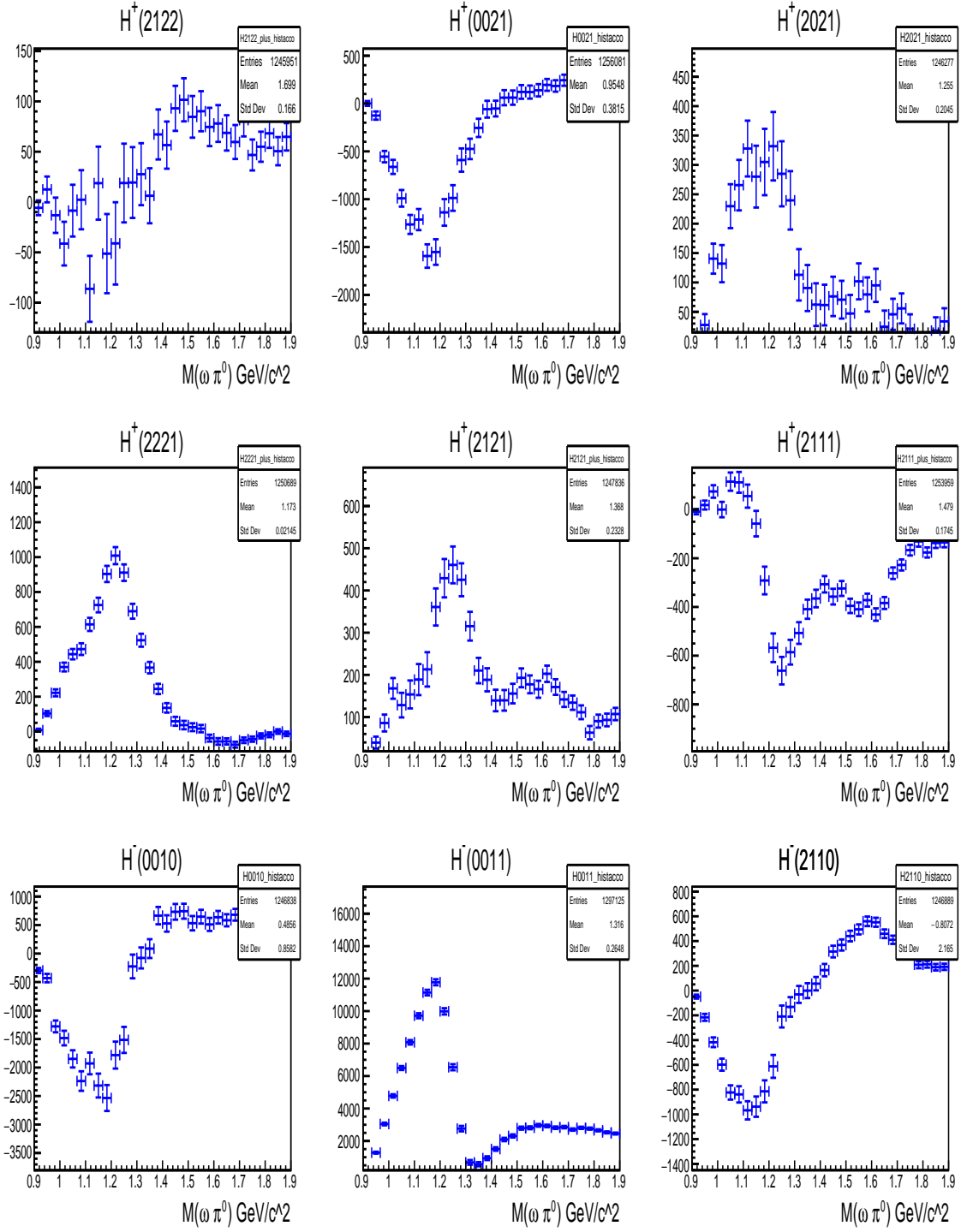


Figure A.2: Extracted moments of the $\omega\pi$ channel as a function of the $\omega\pi$ invariant mass.

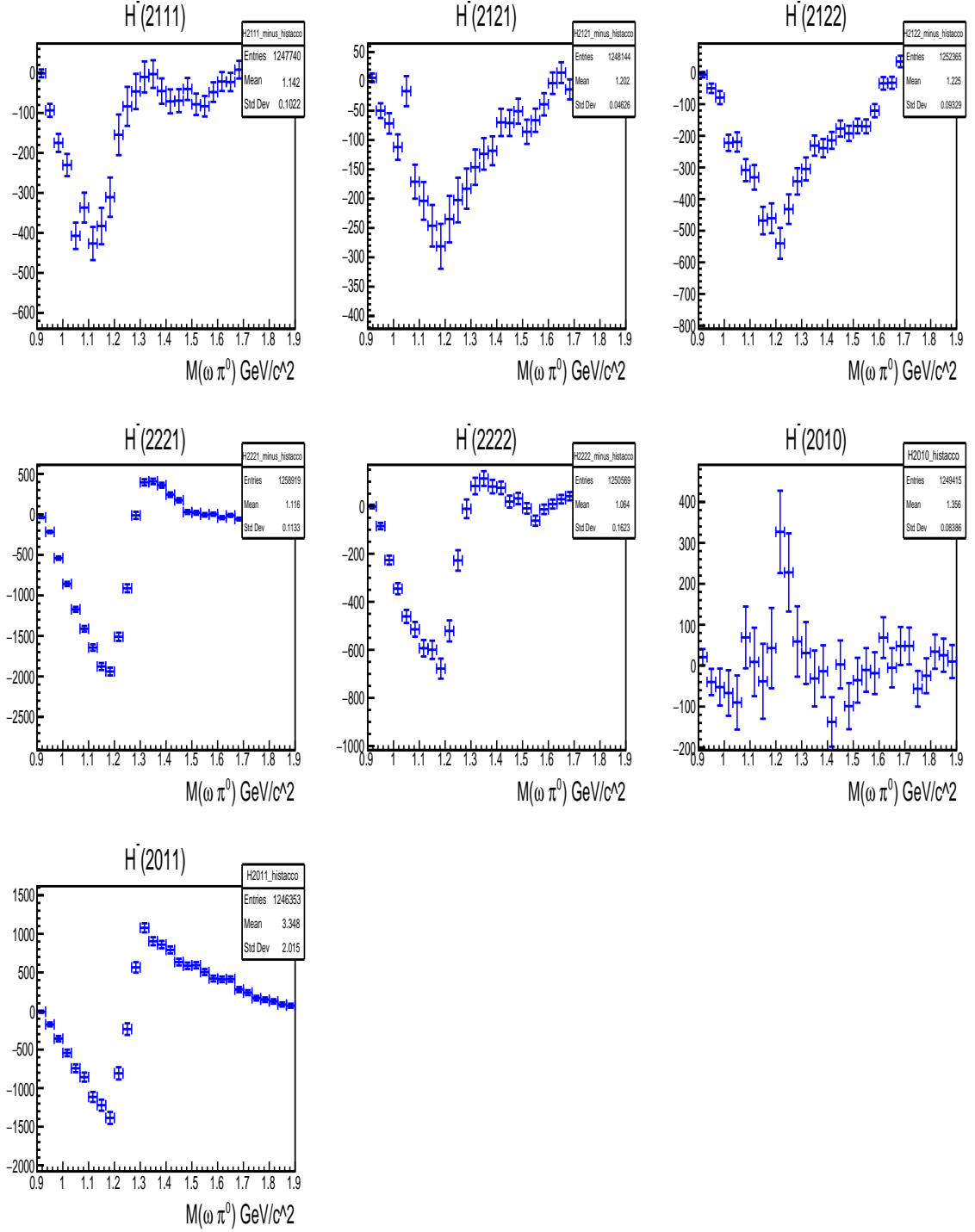


Figure A.3: Extracted moments of the $\omega\pi$ channel as a function of the $\omega\pi$ invariant mass.

Appendix B

Angular Moments Extracted by The Omega-Photon Collaboration

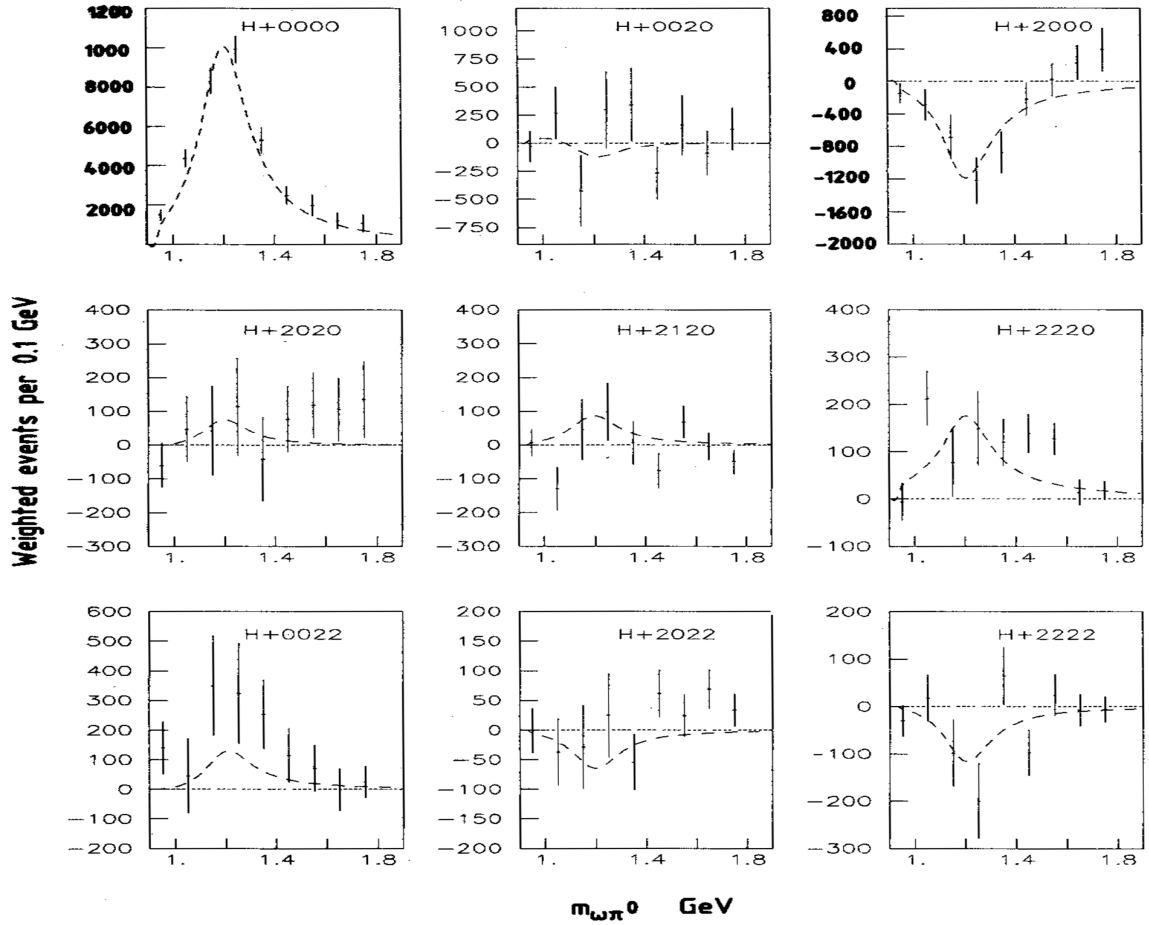


Figure B.1: Moments of the $\omega\pi$ channel as a function of the $\omega\pi$ invariant mass. Markers represent acceptance corrected moments. Lines represent the fit.

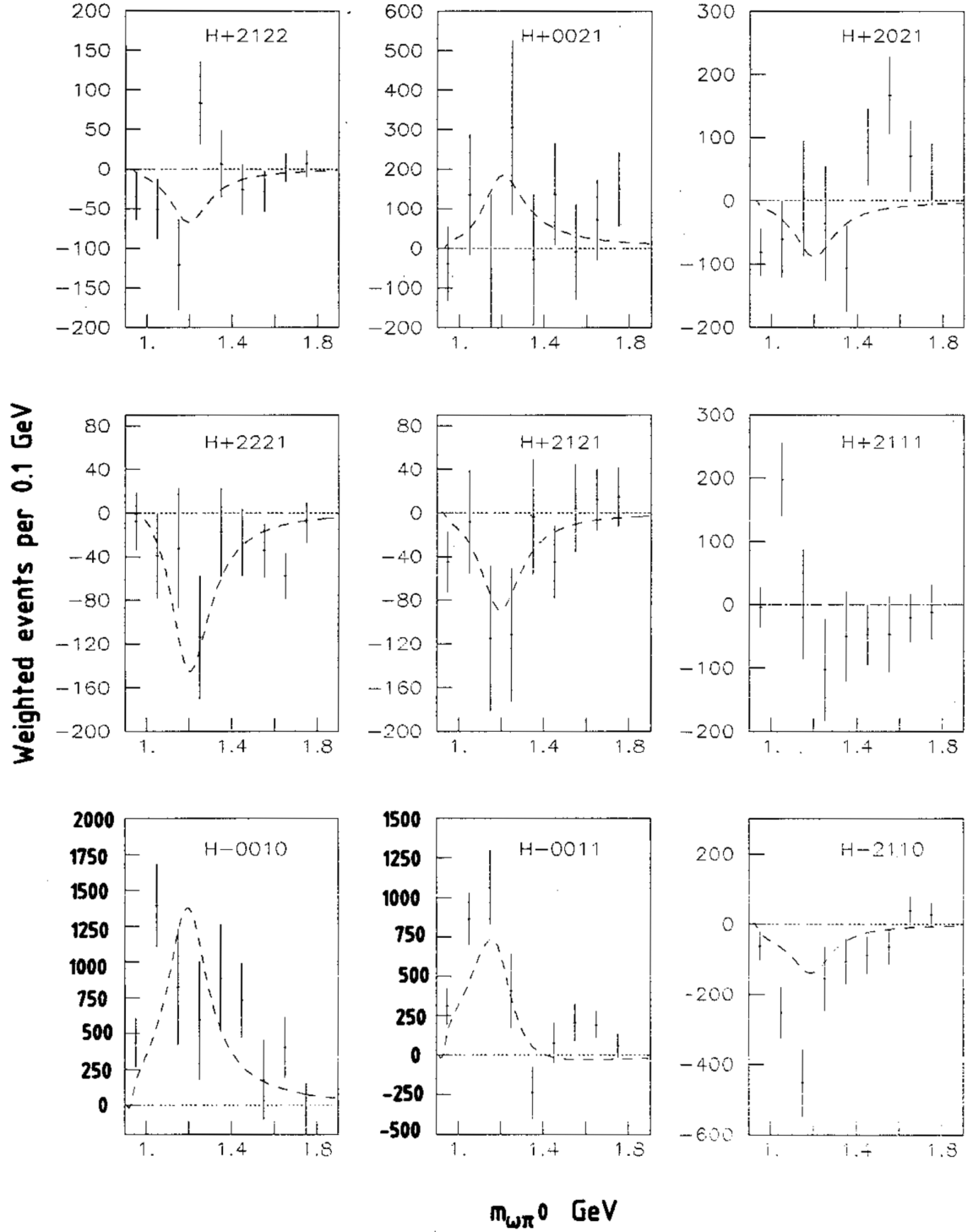


Figure B.2: Moments of the $\omega\pi$ channel as a function of the $\omega\pi$ invariant mass. Markers represent acceptance corrected moments. Lines represent the fit.

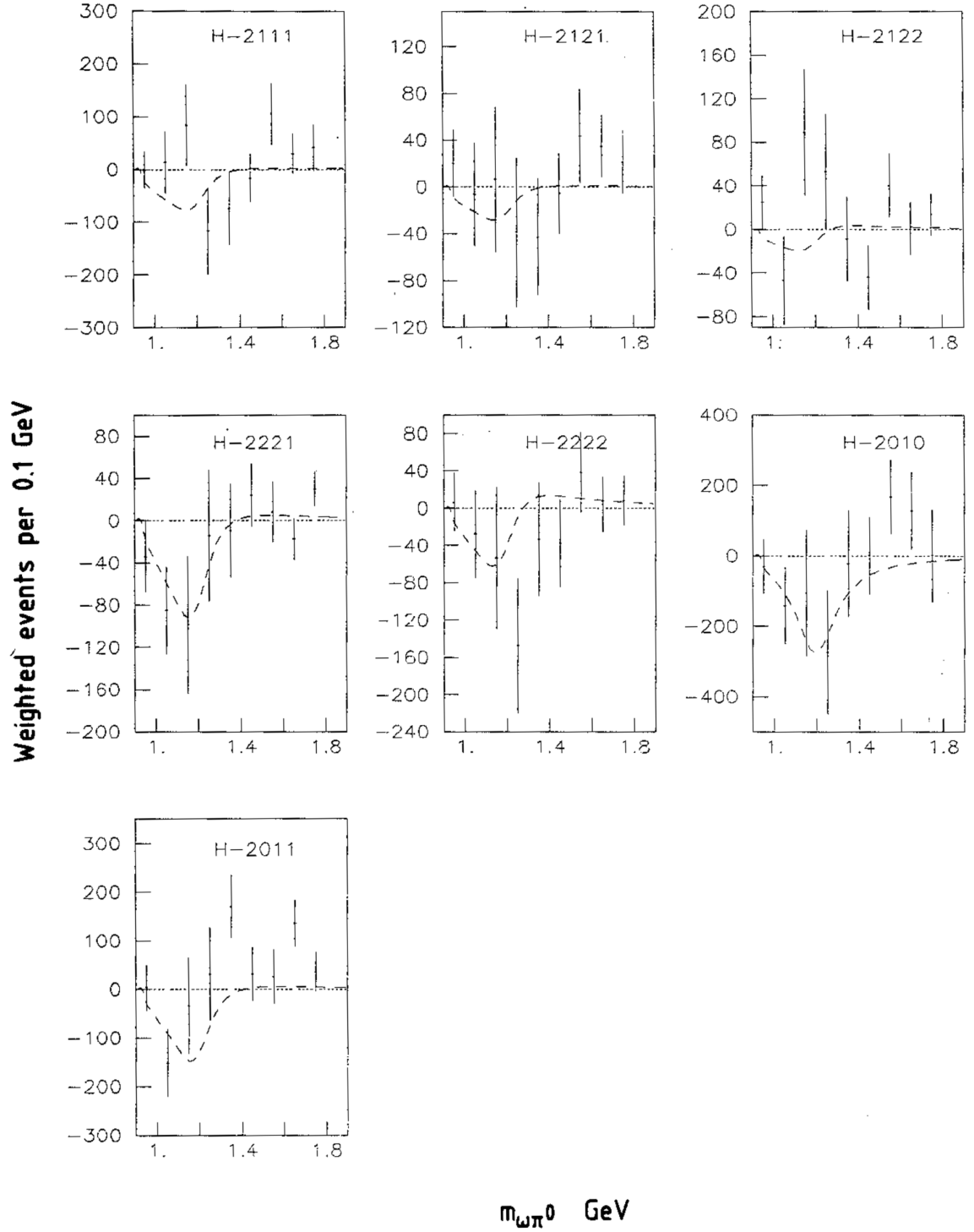


Figure B.3: Moments of the $\omega\pi$ channel as a function of the $\omega\pi$ invariant mass. Markers represent acceptance corrected moments. Lines represent the fit.

Appendix C

Invariant Masses

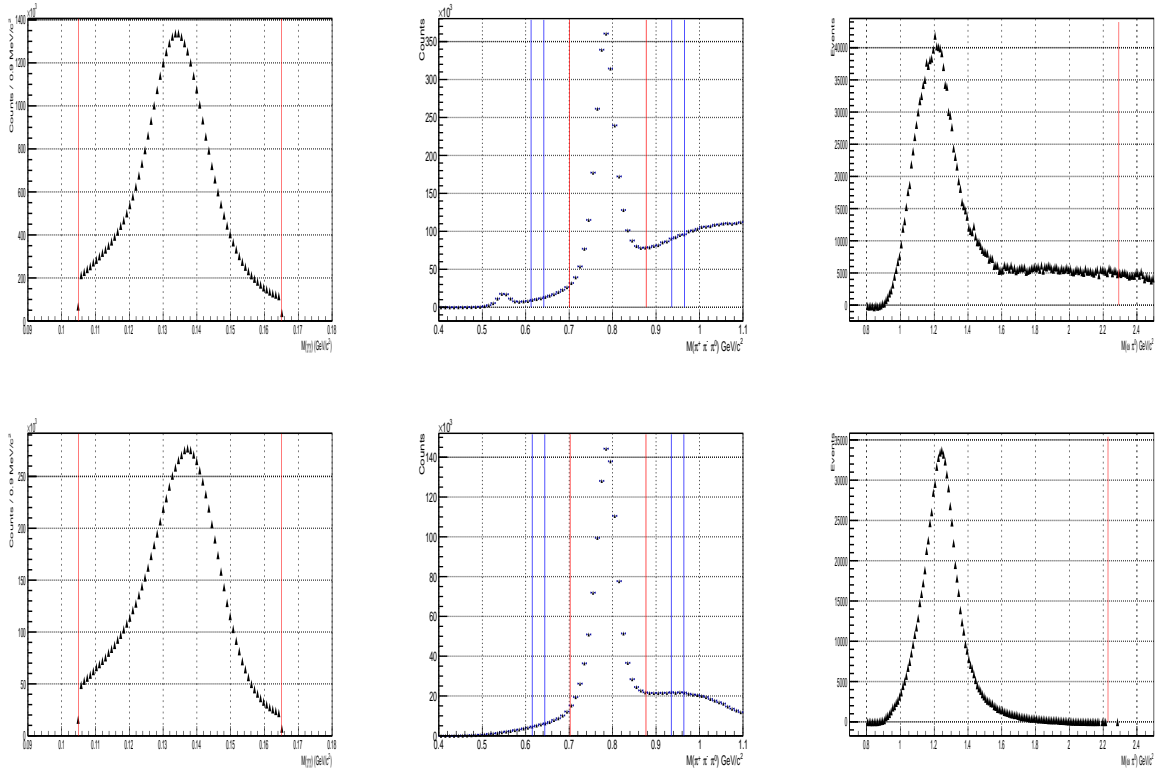


Figure C.1: Invariant mass of $\gamma\gamma$ (left) after event selection cuts, $\pi^+\pi^-\pi^0$ (middle) after subtracting accidentals and $\omega\pi^0$ (right) after subtracting the accidentals and ω background. The top row is produced with spring 2018 data and the bottom row is produced with MC simulation. The red lines indicate the selection cuts for π^0 , ω and $\omega\pi^0$. The blue lines indicate the side-bands used to calculate the background under the ω peak. The $\omega\pi^0$ range is defined by 8.7σ above and below the b_1 peak.

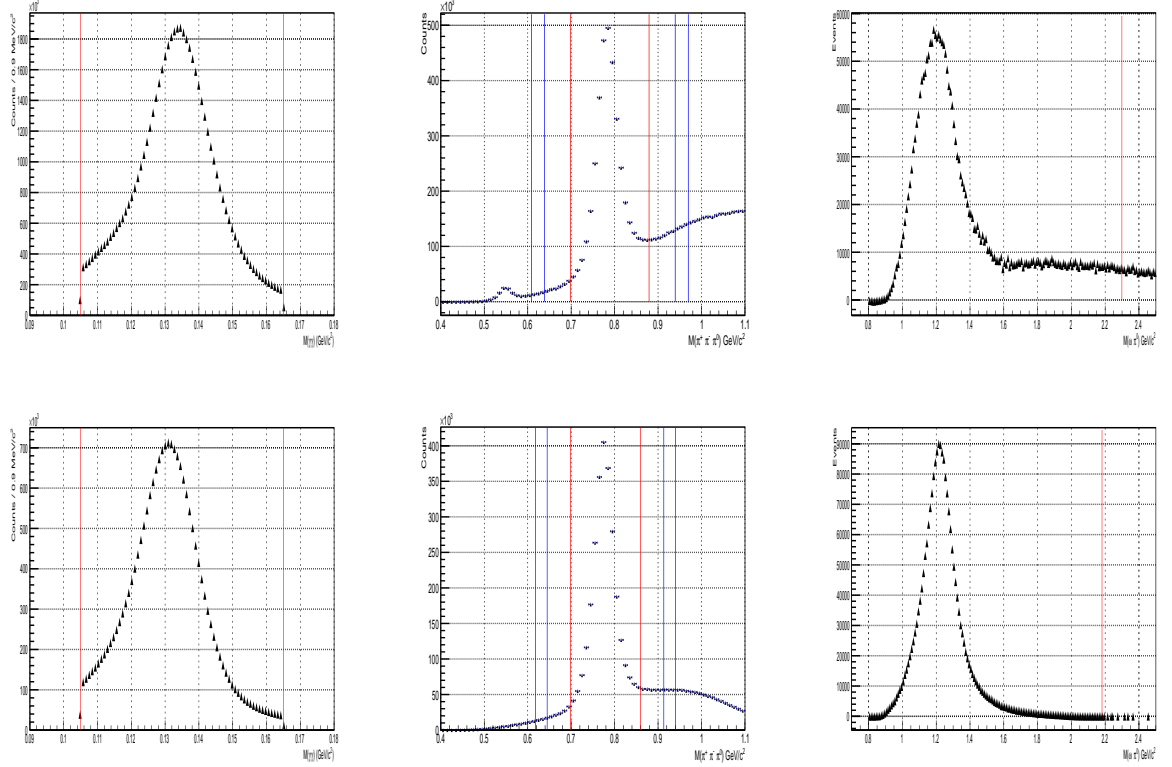


Figure C.2: Invariant mass of $\gamma\gamma$ (left) after event selection cuts, $\pi^+\pi^-\pi^0$ (middle) after subtracting accidentals and $\omega\pi^0$ (right) after subtracting the accidentals and ω background. The top row is produced with fall 2018 data and the bottom row is produced with MC simulation. The red lines indicate the selection cuts for π^0 , ω and $\omega\pi^0$. The blue lines indicate the side-bands used to calculate the background under the ω peak. The $\omega\pi^0$ range is defined by 8.7σ above and below the b_1 peak.

Appendix D

Particle Identification Timing Cuts

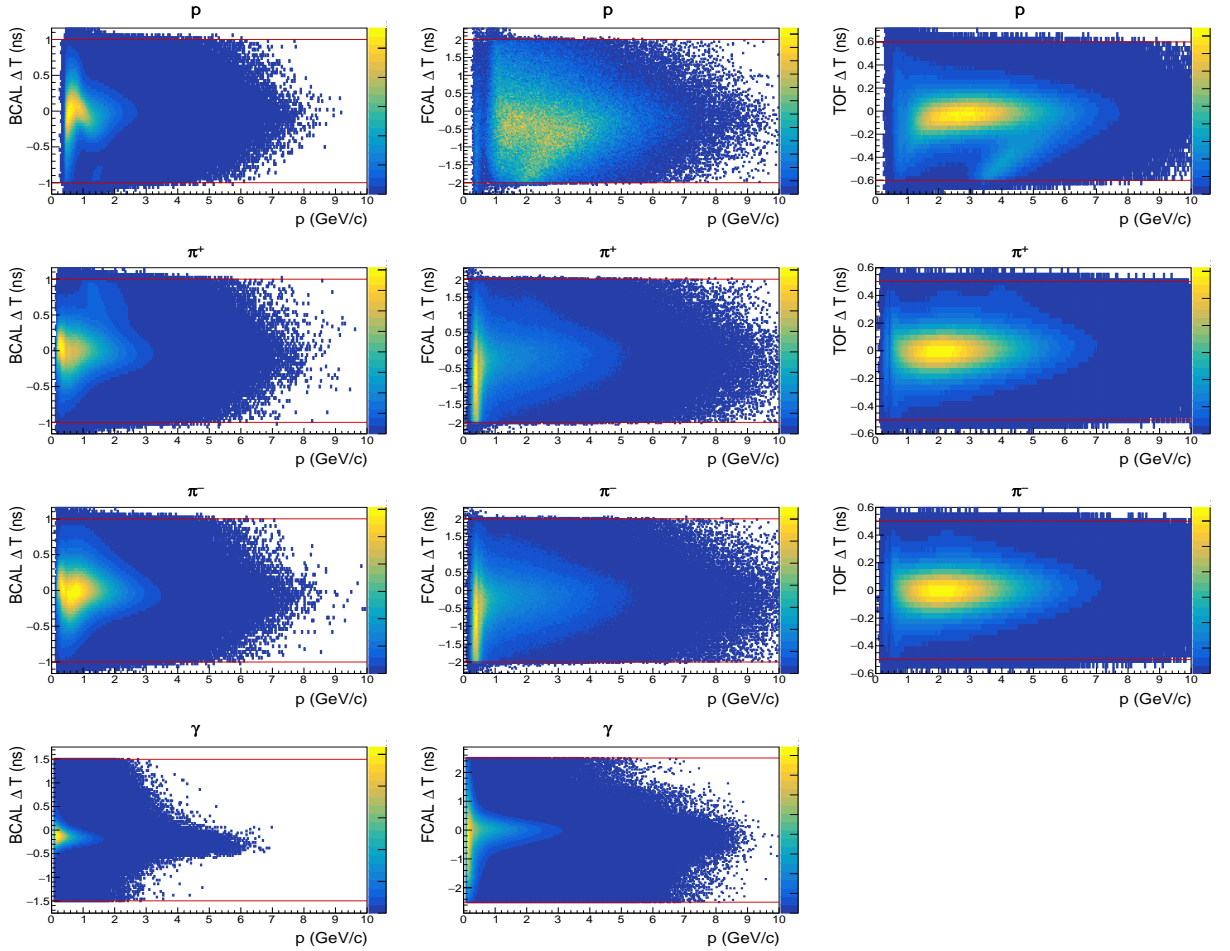


Figure D.1: Time of flight distribution for the proton, $\pi^+\pi^-$ and γ versus their linear momenta in the BCAL, FCAL and TOF detector subsystems. These plots are produced for with data from spring 2018 run period. The red lines indicate the PIDT selection cuts used in our analysis.

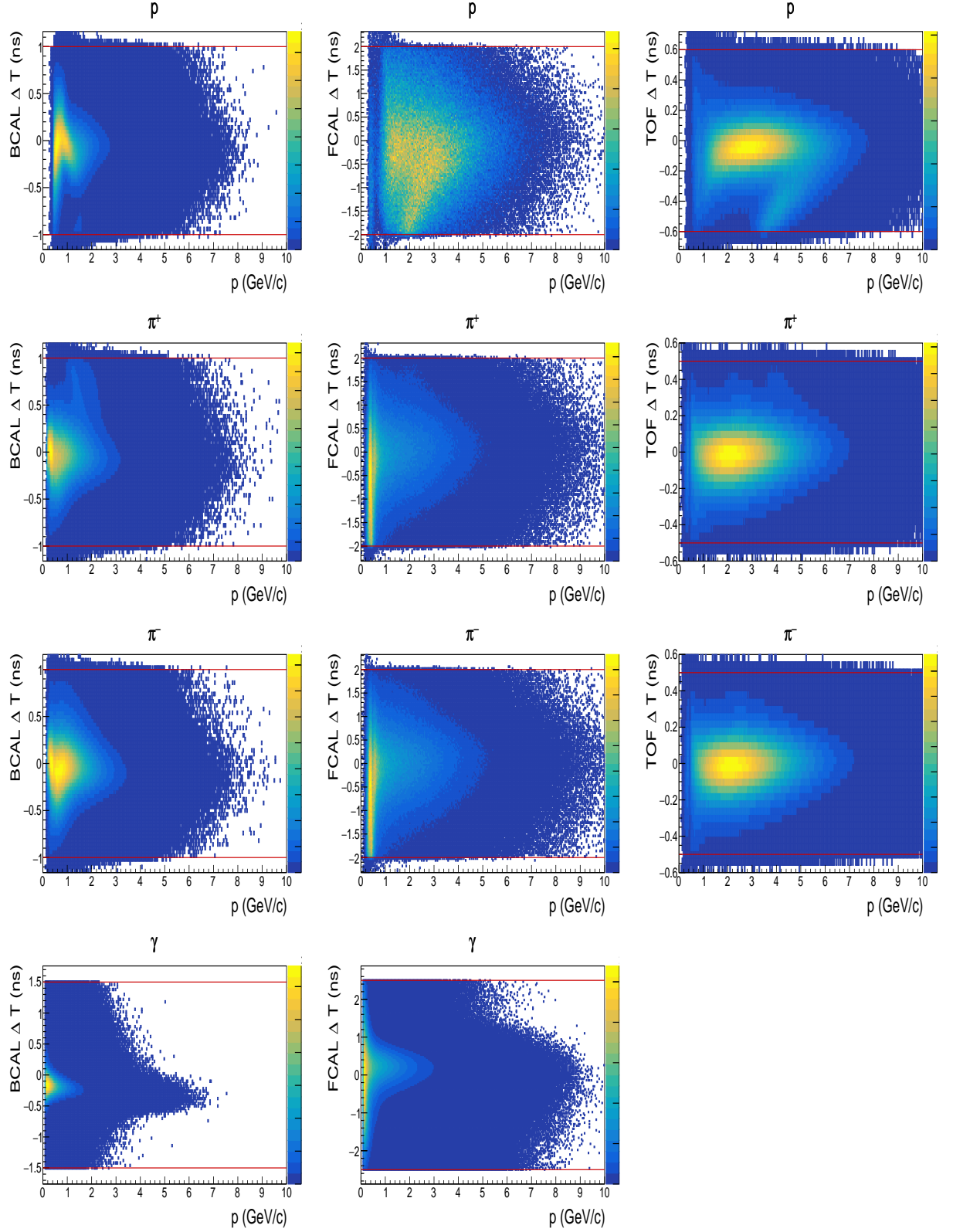


Figure D.2: Time of flight distribution for the proton, $\pi^+\pi^-$ and γ versus their linear momenta in the BCAL, FCAL and TOF detector subsystems. These plots are produced for with data from fall 2018 run period. The red lines indicate the PIDT selection cuts used in our analysis.

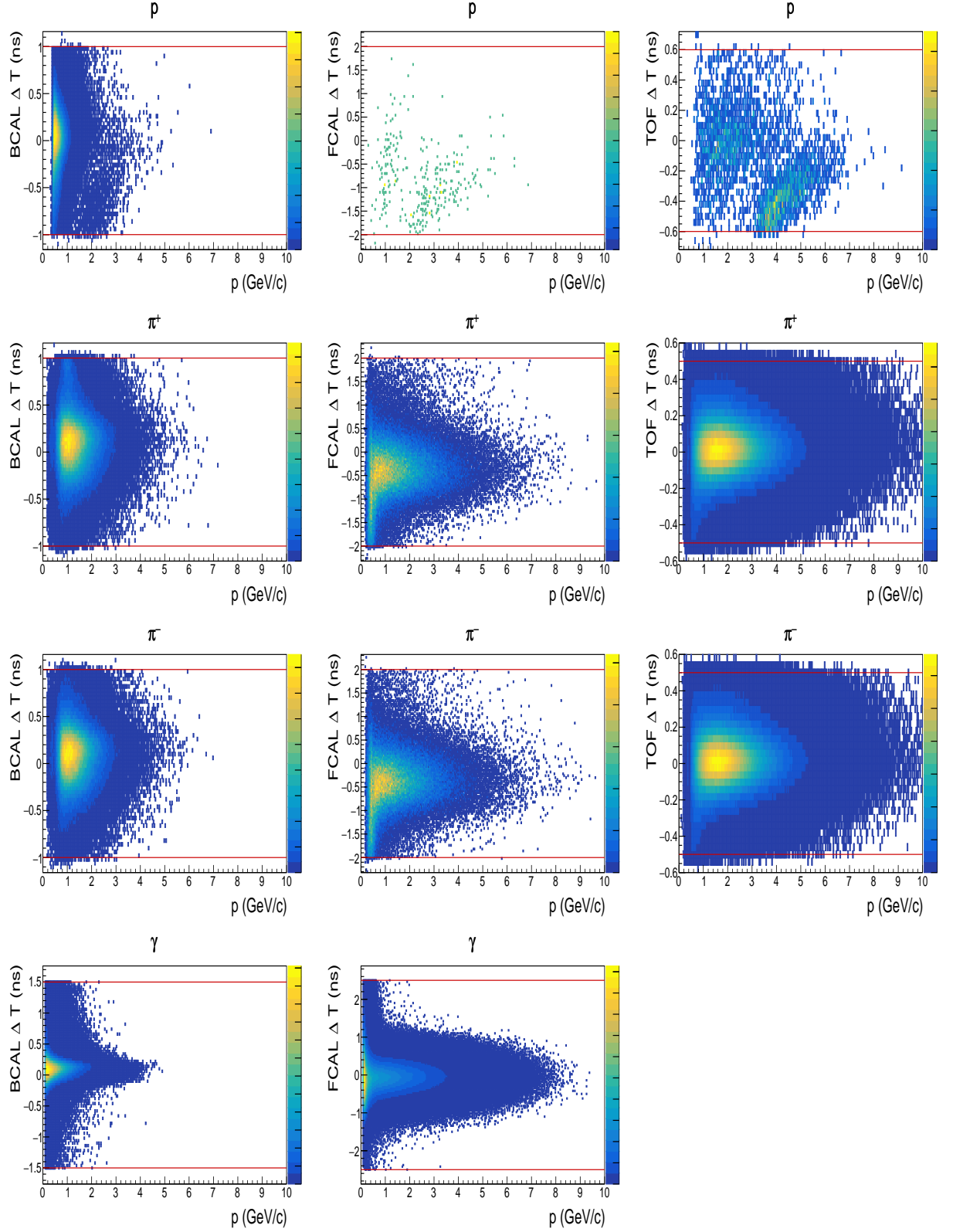


Figure D.3: Time of flight distribution for the proton, $\pi^+\pi^-$ and γ versus their linear momenta in the BCAL, FCAL and TOF detector subsystems. These plots are produced for with MC simulation for spring 2017 run period. The red lines indicate the PIDT selection cuts used in our analysis.

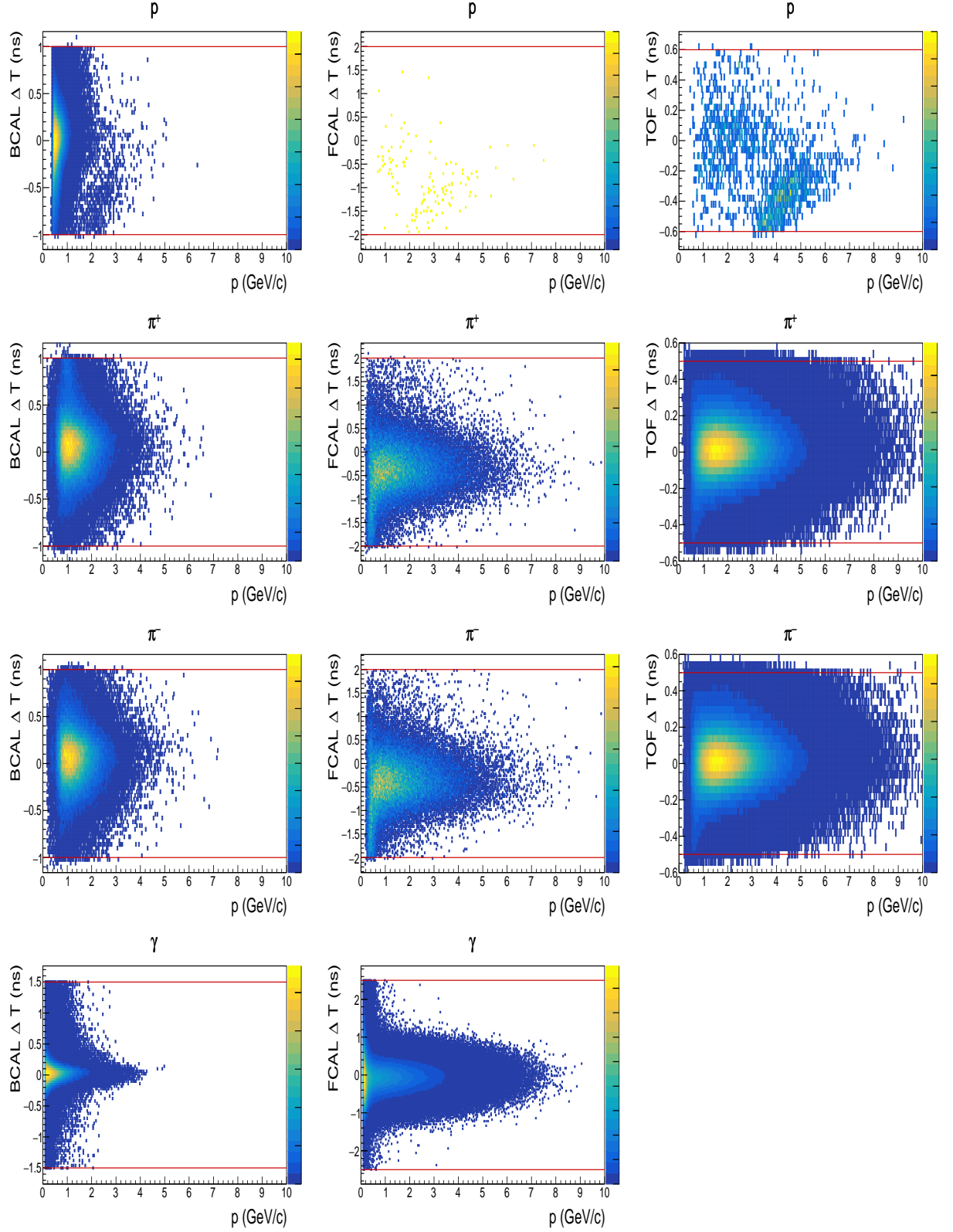


Figure D.4: Time of flight distribution for the proton, $\pi^+\pi^-$ and γ versus their linear momenta in the BCAL, FCAL and TOF detector subsystems. These plots are produced for with MC simulation for spring 2018 run period. The red lines indicate the PIDT selection cuts used in our analysis.

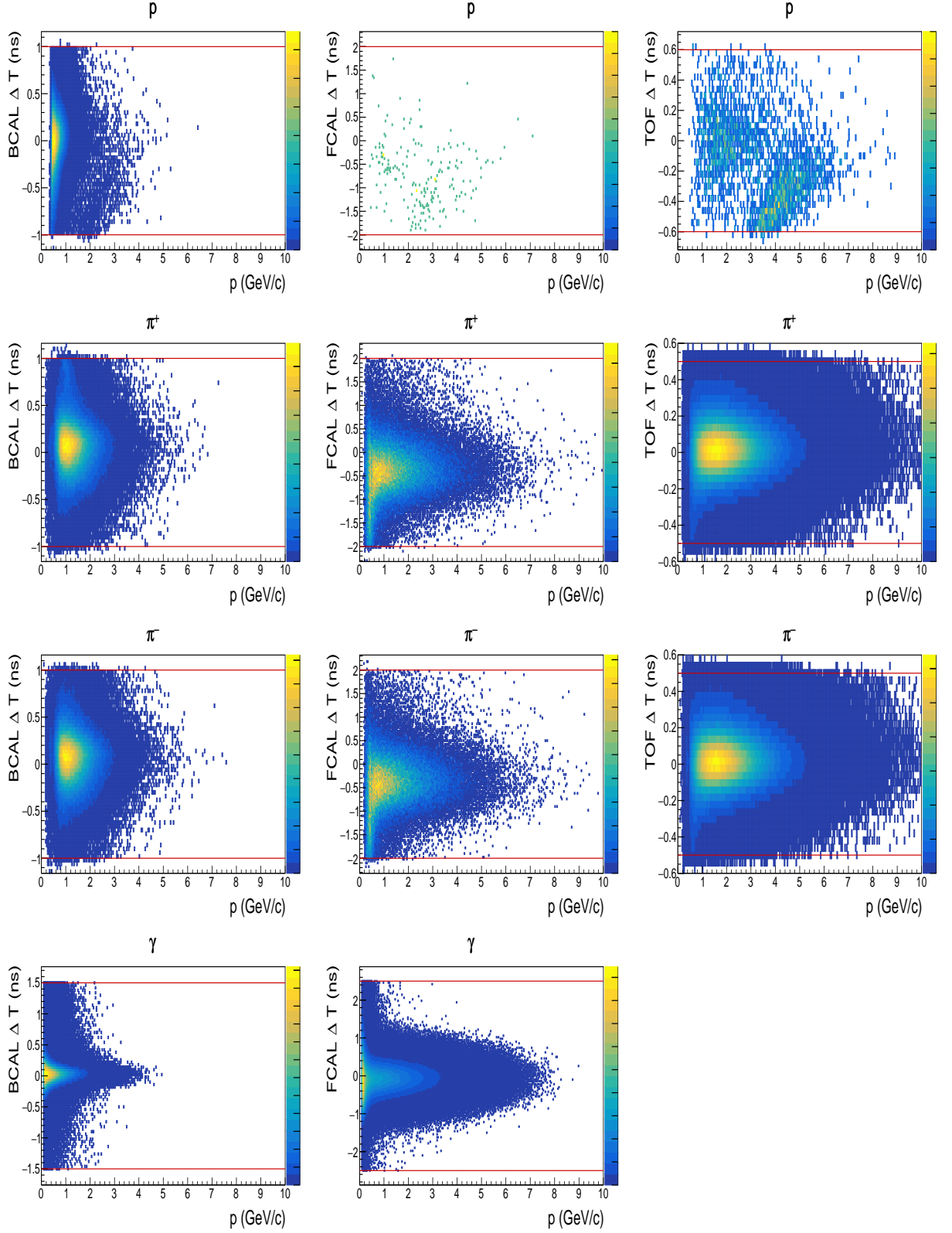


Figure D.5: Time of flight distribution for the proton, $\pi^+\pi^-$ and γ versus their linear momenta in the BCAL, FCAL and TOF detector subsystems. These plots are produced for with MC simulation for fall 2018 run period. The red lines indicate the PIDT selection cuts used in our analysis.

Appendix E

Invariant Mass Plots

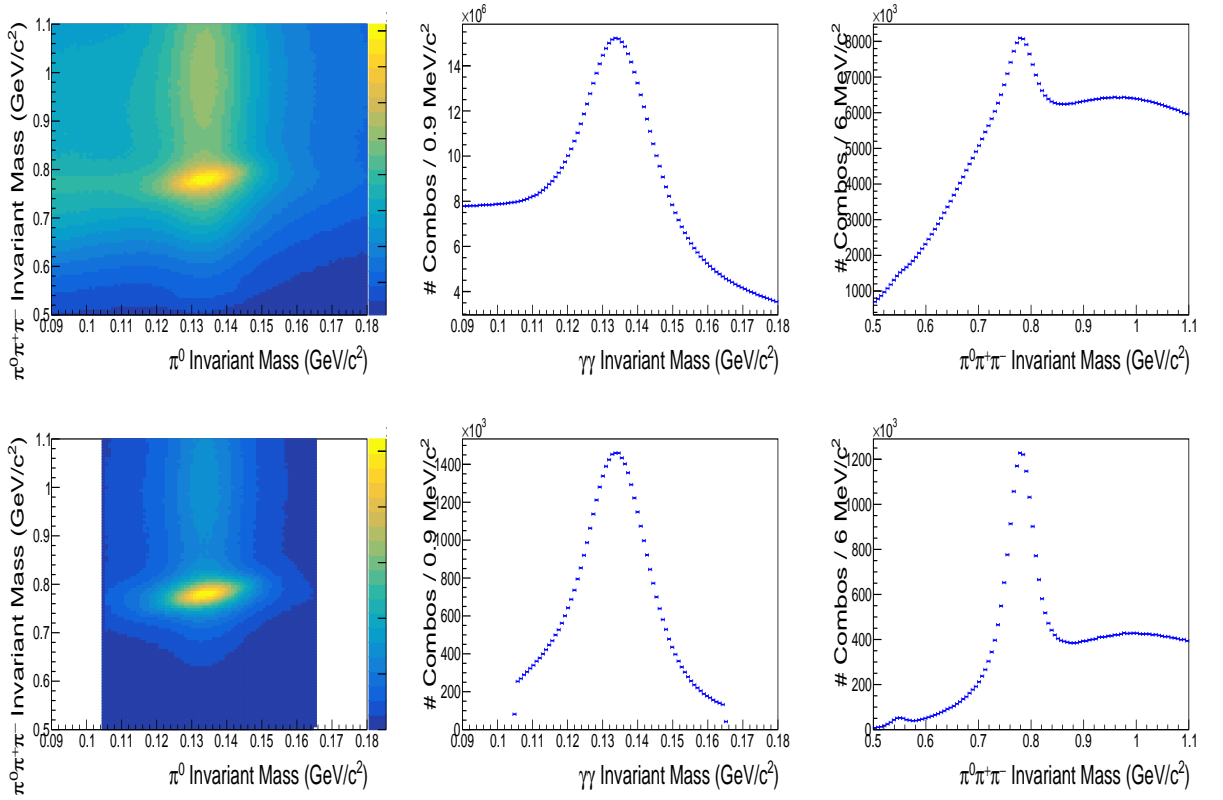


Figure E.1: The invariant mass of $\gamma\gamma$ versus the invariant mass of $\pi^+\pi^-\pi^0$ (right) and their projection on the both axes, before applying our selection cuts (top row) and after applying our selection cuts (bottom row). No background (accidentals or ω side-band) subtractions were applied on these plots. These plots are produced with spring 2017 data. Significant background to the ω peak is present, as clear by the $\eta(548)$ peak.

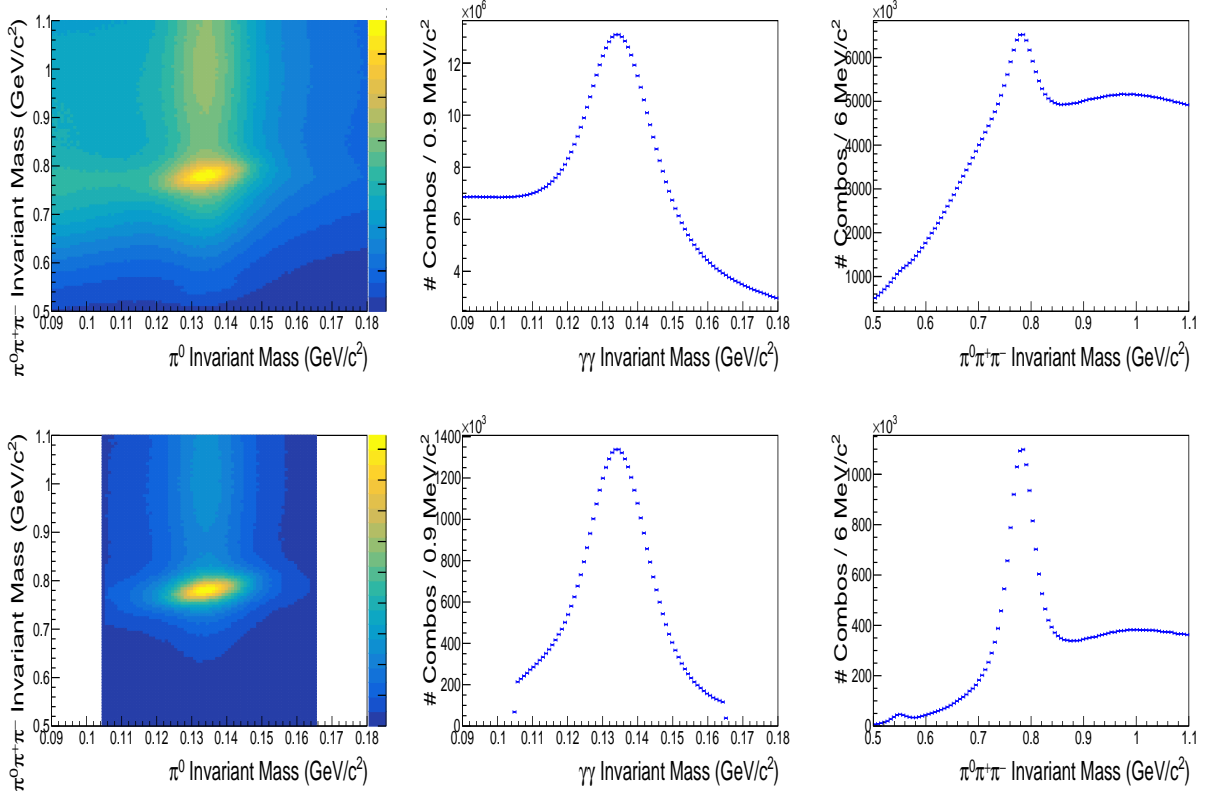


Figure E.2: The invariant mass of $\gamma\gamma$ versus the invariant mass of $\pi^+\pi^-\pi^0$ (right) and their projection on the both axes, before applying our selection cuts (top row) and after applying our selection cuts (bottom row). No background (accidentals or ω side-band) subtractions were applied on these plots. These plots are produced with spring 2018 data. Significant background to the ω peak is present, as clear by the $\eta(548)$ peak.

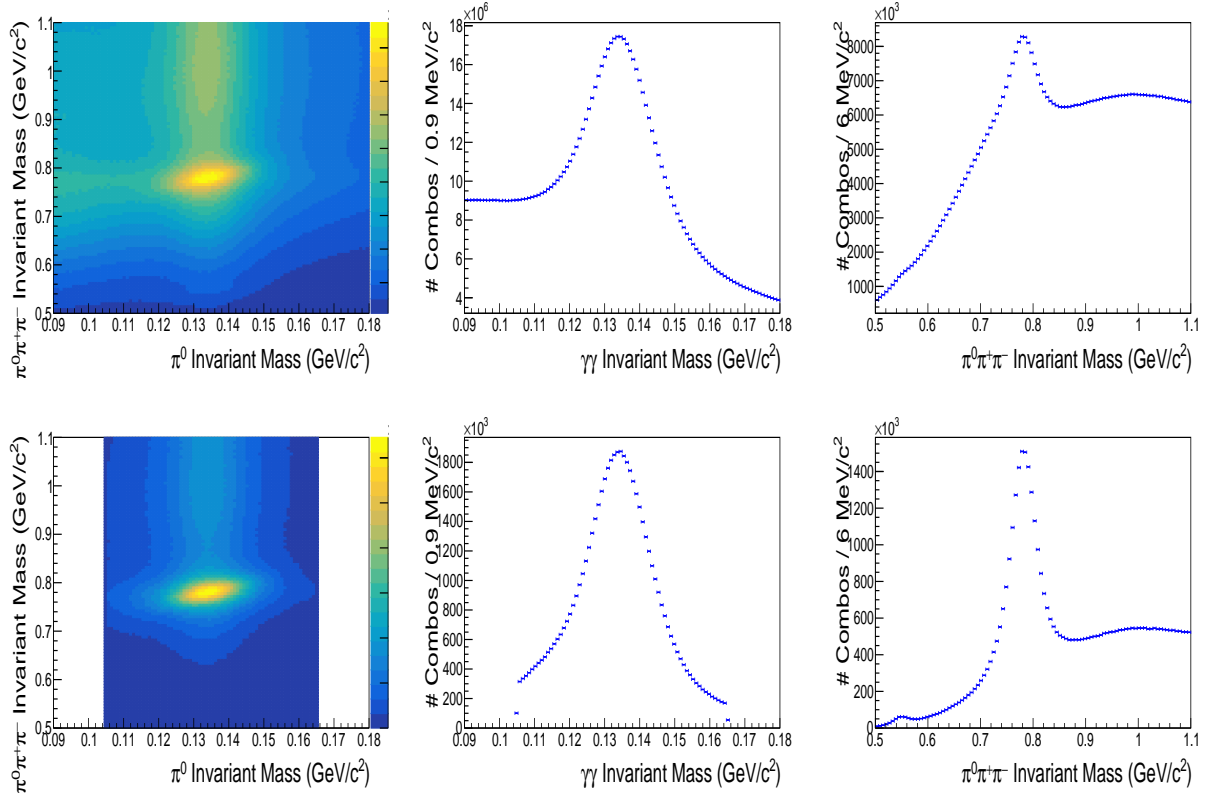


Figure E.3: The invariant mass of $\gamma\gamma$ versus the invariant mass of $\pi^+\pi^-\pi^0$ (right) and their projection on the both axes, before applying our selection cuts (top row) and after applying our selection cuts (bottom row). No background (accidentals or ω side-band) subtractions were applied on these plots. These plots are produced with fall 2018 data. Significant background to the ω peak is present, as clear by the $\eta(548)$ peak.

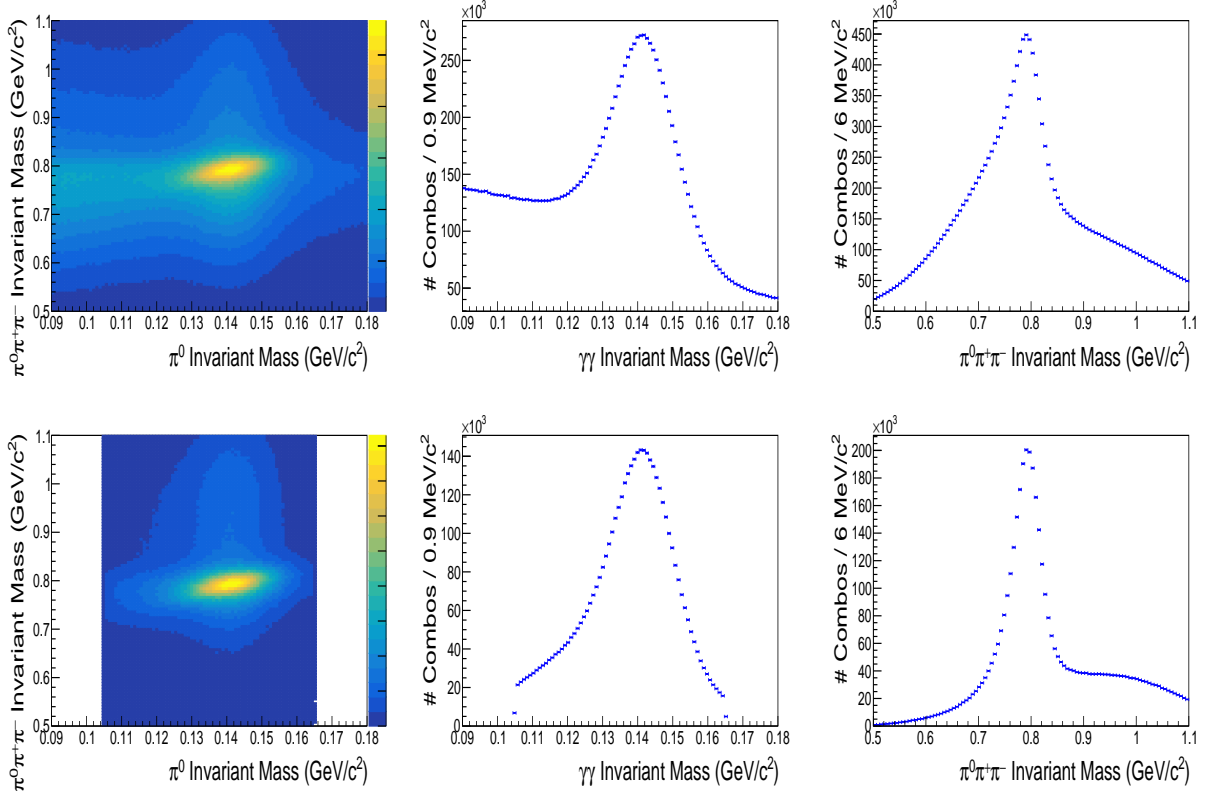


Figure E.4: The invariant mass of $\gamma\gamma$ versus the invariant mass of $\pi^+\pi^-\pi^0$ (right) and their projection on the both axes, before applying our selection cuts (top row) and after applying our selection cuts (bottom row). No background (accidentals or ω side-band) subtractions were applied on these plots. These plots are produced with spring 2017 MC simulation. Only $\omega\pi^0$ events are include in the simulation. The background is significantly lower compared to data and arises from wrongly reconstructed events.

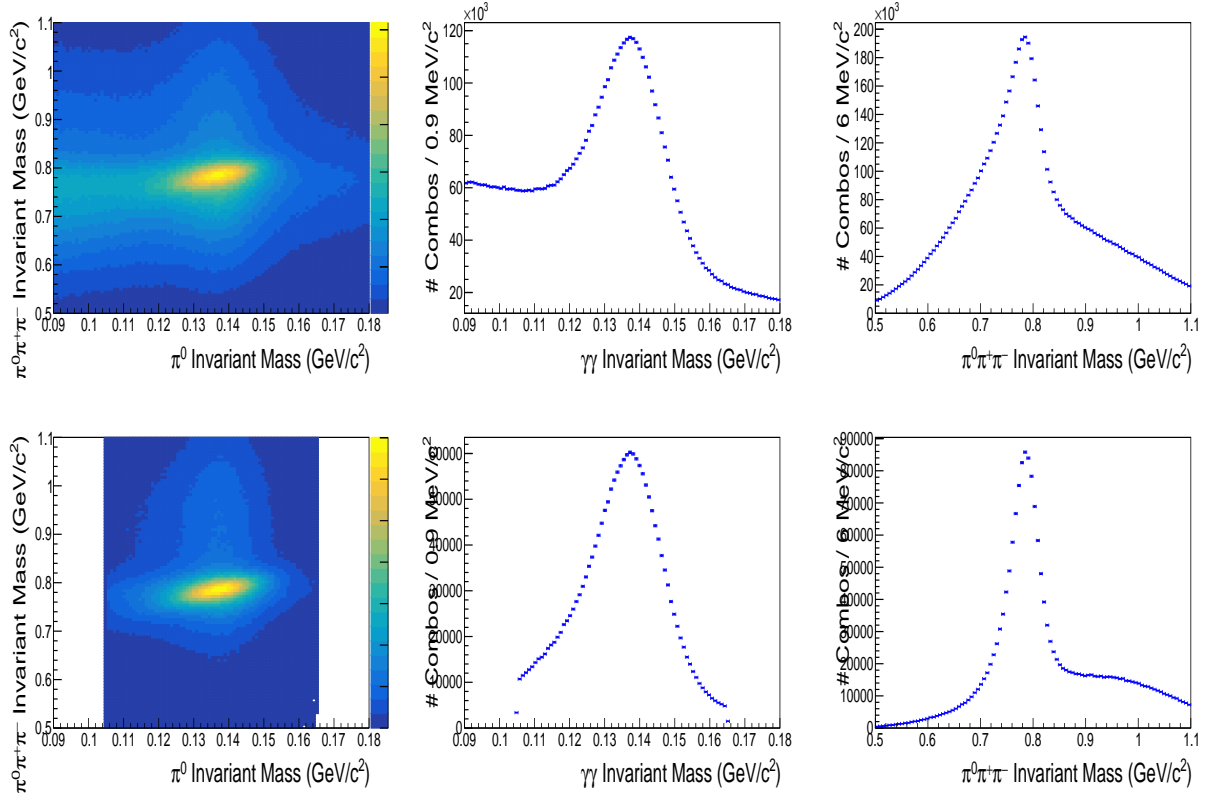


Figure E.5: The invariant mass of $\gamma\gamma$ versus the invariant mass of $\pi^+\pi^-\pi^0$ (right) and their projection on the both axes, before applying our selection cuts (top row) and after applying our selection cuts (bottom row). No background (accidentals or ω side-band) subtractions were applied on these plots. These plots are produced with spring 2018 MC simulation. Only $\omega\pi^0$ events are include in the simulation. The background is significantly lower compared to data and arises from wrongly reconstructed events.

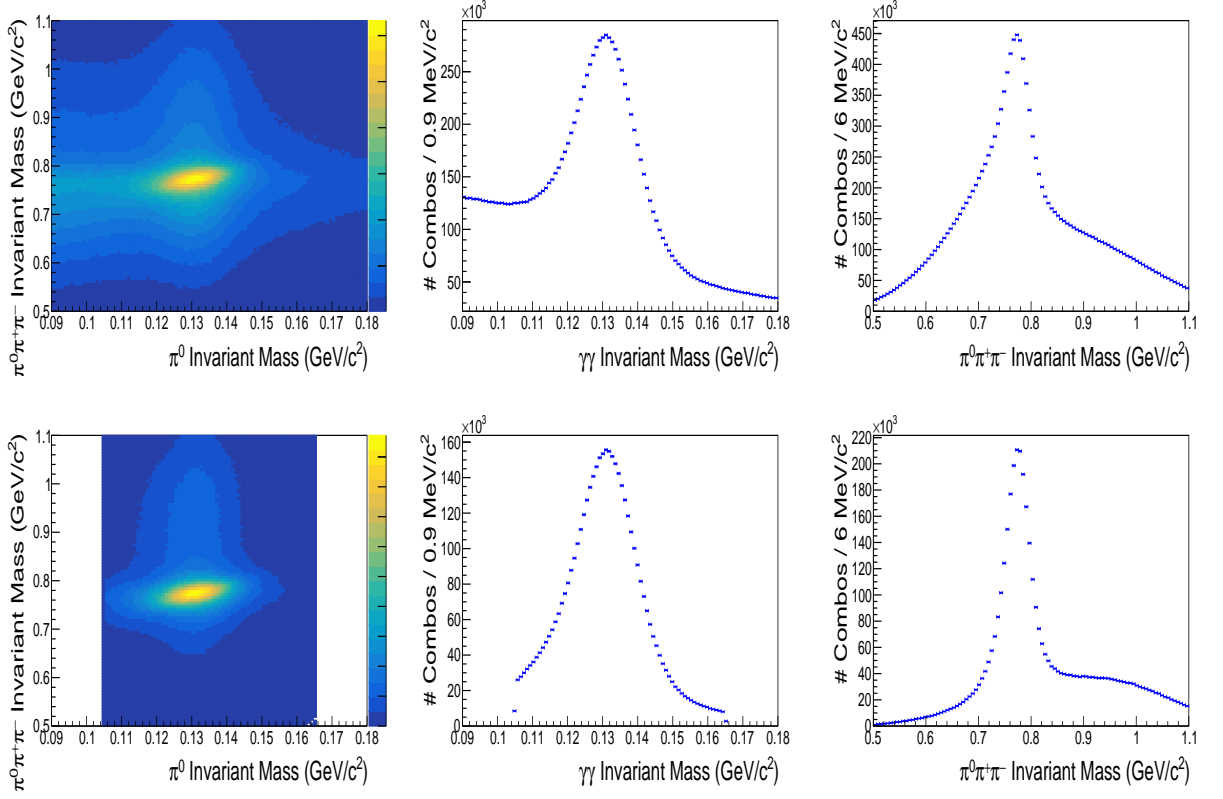


Figure E.6: The invariant mass of $\gamma\gamma$ versus the invariant mass of $\pi^+\pi^-\pi^0$ (right) and their projection on the both axes, before applying our selection cuts (top row) and after applying our selection cuts (bottom row). No background (accidentals or ω side-band) subtractions were applied on these plots. These plots are produced with fall 2018 MC simulation. Only $\omega\pi^0$ events are include in the simulation. The background is significantly lower compared to data and arises from wrongly reconstructed events.